

Interactions of 3 nm, 8 nm, and 15 nm gold particles with human alveolar epithelial cells: A microscopy study

Dissertation

zur Erlangung des Grades

des Doktors der Naturwissenschaften

der Naturwissenschaftlich-Technischen Fakultät III

Chemie, Pharmazie, Bio- und Werkstoffwissenschaften

der Universität des Saarlandes

von

Katharina Böse

Saarbrücken

17.10.2013

Tag des Kolloquiums: 10.12.2013

Dekan: Prof. Dr. V. Helms

Berichterstatter: Prof. Dr. A. K. Kiemer

Prof. Dr. I. Bernhardt

Vorsitz: Prof. Dr. G. Jung

Akad. Mitarbeiter: Dr. A. Kraegeloh

„Mit dem Wissen wächst der Zweifel.“

-Johann Wolfgang von Goethe-

Table of contents

SUMMARY	1
ZUSAMMENFASSUNG.....	1
1. GENERAL INTRODUCTION	2
1.1 Nanoparticles	2
1.1.1 <i>Nanomaterials - A definition</i>	2
1.1.2 <i>Gold nanoparticles</i>	3
1.1.2.1 <i>Optical properties and applications</i>	3
1.1.2.2 <i>Chemical properties and applications</i>	5
1.1.2.3 <i>Toxicity of gold nanoparticles</i>	5
1.2 The human lung	7
1.2.1 <i>Structure and function</i>	7
1.2.2 <i>Particle-lung interactions and particle-induced lung inflammation</i>	9
1.2.3 <i>Nanoparticle-lung interactions</i>	10
1.2.4 <i>Nanoparticle exposure to human lung cells</i>	10
1.2.4.1 <i>Particle dosage</i>	10
1.2.4.2 <i>Particle stability and protein corona</i>	11
1.3 Intracellular transport	12
1.3.1 <i>Endo- and exocytic transport</i>	12
1.3.2 <i>Microtubules - Structure and function</i>	13
1.3.3 <i>Interactions of nanoparticles with microtubules</i>	14
1.4 Imaging at the nanoscale level	15
1.4.1 <i>Fluorescence microscopy and its limitations</i>	15
1.4.2 <i>Stimulated emission depletion (STED) microscopy</i>	17
1.4.3 <i>Electron microscopy</i>	19
1.5 Objective of the thesis	21
1.6 References	22
2. INTERACTIONS OF 3 NM, 8 NM, AND 15 NM GOLD PARTICLES WITH A549 CELLS.....	29
2.1 Introduction	29
2.2 Experimental section	31
2.2.1 <i>Gold nanoparticle synthesis</i>	31
2.2.2 <i>Characterization of gold nanoparticles</i>	32
2.2.3 <i>Cell culture</i>	32
2.2.4 <i>Exposure of cells to gold nanoparticles and polymer</i>	32
2.2.5 <i>Nocodazole treatment</i>	33

2.2.6 Sample preparation for STED and confocal microscopy	33
2.2.6.1 Preparation of gold nanoparticles	33
2.2.6.2 Preparation of A549 cells	33
2.2.7 STED and confocal microscopy.....	35
2.2.7.1 Imaging of gold nanoparticles	35
2.2.7.2 Imaging of A549 cells	35
2.2.8 Widefield microscopy	35
2.2.9 Image processing and image analysis	36
2.2.10 Preparation of A549 cells for SEM and TEM.....	36
2.2.11 SEM and TEM imaging of A549 cells.....	38
2.2.12 Cytotoxicity and cell proliferation assays.....	38
2.2.12.1 Cell seeding and exposure to nanoparticles	38
2.2.12.2 WST-1 assay.....	39
2.2.12.3 BrdU assay	39
2.2.13 Assay data analysis	39
2.3 Results.....	40
2.3.1 Characterization of fluorescently labeled gold nanoparticles	40
2.3.2 Confocal and STED microscopy of fluorescently labeled gold nanoparticles.....	43
2.3.3 The intracellular distribution of gold particles in relation to the tubulin cytoskeleton.....	47
2.3.4 The intracellular distribution of gold nanoparticles in relation to the Golgi.....	50
2.3.5 Localization of gold nanoparticles inside the nucleus of A549 cells.....	52
2.3.6 Changes in the morphology of nuclei of A549 cells after exposure to gold nanoparticles	56
2.3.7 Effects of gold nanoparticles on the microtubule structure.....	57
2.3.8 Cytotoxicity testing of gold nanoparticles	59
2.3.8.1 WST-1 assay.....	59
2.3.8.2 BrdU assay	61
2.3.8.3 Cellular morphology.....	63
2.3.9 Inhibition of microtubule-mediated transport by nocodazole treatment.....	64
2.3.10 Electron microscopy of gold nanoparticles and cytoskeletons of A549 cells.....	66
2.3.10.1 SEM analyses	66
2.3.10.2 TEM analyses	70
2.4 Discussion.....	73
2.4.1 The intracellular distribution of gold nanoparticles in A549 cells.....	73
2.4.1.1 Gold nanoparticle distribution in relation to the tubulin cytoskeleton.....	73
2.4.1.2 Gold nanoparticle distribution in relation to the Golgi	74
2.4.1.3 Gold nanoparticle distribution in relation to the cell nucleus	75
2.4.2 Genotoxicity of gold nanoparticles.....	76
2.4.3 Cytotoxicity of gold nanoparticles	76
2.4.4 The influence of gold nanoparticles on the cellular structure involving microtubules	81
2.4.5 Gold nanoparticle transport along microtubules	82
2.5 Conclusion.....	83
2.6 References.....	84
Appendix.....	89

3. BLEBBING OF A549 CELLS CAUSED BY NANOPARTICLE EXPOSURE	95
3.1 Introduction	95
3.2 Experimental section	97
3.2.1 Nanoparticle synthesis and characterization	97
3.2.2 Expression of a GFP fusion protein in A549 cells for live cell imaging	97
3.2.2.1 Transformation of <i>E. coli</i>	97
3.2.2.2 Colony polymerase chain reaction (PCR).....	97
3.2.2.3 Gel electrophoresis	98
3.2.2.4 Plasmid propagation and isolation.....	99
3.2.2.5 UV spectrophotometric measurements of purified plasmid DNA	99
3.2.2.6 Transfection of A549 cells with pAcGFP1-Mem.....	99
3.2.2.7 Establishment of stable A549 pAcGFP1-Mem cells.....	99
3.2.3 Cell culture of A549 cells	100
3.2.4 Sample preparation for confocal microscopy	100
3.2.4.1 Exposure of cells to nanoparticles	100
3.2.4.2 Immunostaining.....	100
3.2.5 Sample preparation for live cell confocal microscopy.....	101
3.2.5.1 Exposure of cells to nanoparticles	101
3.2.5.2 Exposure of cells to fluorescent dextran	101
3.2.6 Confocal microscopy	101
3.2.6.1 Imaging of fixed cell samples.....	101
3.2.6.2 Live cell imaging.....	102
3.2.7 Deconvolution and image processing	102
3.3 Results.....	103
3.3.1 Characterization of nanoparticles.....	103
3.3.2 Establishment and characterization of A549 pAcGFP1-Mem cells	103
3.3.3 Characterization of cell blebbing	105
3.3.3.1 Cell blebbing caused by gold nanoparticles of different sizes	105
3.3.3.2 Cell blebbing caused by nanoparticle composition.....	105
3.3.4 Cell blebbing and cell movement - formation of lamellipodia	107
3.3.5 Cell blebbing and macropinocytosis	110
3.3.5.1 The use of labeled dextran to identify macropinosomes	110
3.3.5.2 Gold nanoparticle transport via macropinosomes.....	111
3.3.5.3 Uptake of gold nanoparticles by macropinocytosis	113
3.4 Discussion.....	116
3.4.1 Cell blebbing and cell movement.....	116
3.4.2 Cell blebbing and macropinocytosis	117
3.5 Conclusion	118
3.6 References.....	119

4. A CORRELATIVE ANALYSIS OF GOLD NANOPARTICLES INTERNALIZED BY A549 CELLS.....	121
4.1 Introduction	121
4.2 Experimental section.....	123
4.2.1 Gold nanoparticle synthesis.....	123
4.2.2 Characterization of gold nanoparticles.....	123
4.2.3 Cell culture	124
4.2.4 Preparation of silicon nitride microchips and cell seeding.....	124
4.2.5 Exposure of cells to nanoparticles.....	124
4.2.6 Immunostaining	124
4.2.7 Confocal laser scanning microscopy (CLSM).....	125
4.2.8 Scanning transmission electron microscopy (STEM) of hydrated samples in the ESEM (wet STEM) .	125
4.2.9 TEM imaging.....	125
4.3 Results.....	126
4.3.1 Properties of gold nanoparticles.....	126
4.3.2 Localization of Atto 647N fluorescence signals by CLSM.....	127
4.3.3 Correlative imaging of cell samples by electron microscopy.....	130
4.3.4 Correlation of fluorescence signals with positions of gold nanoparticles.....	131
4.4 Discussion.....	136
4.4.1 Particle dosage for microscopy studies of nanoparticle-cell interactions.....	136
4.4.2 The use of CLEM for investigating nanoparticle-cell interactions.....	137
4.4.3 Influence of sample preparation on CLEM.....	139
4.5 Conclusion.....	140
4.6 References.....	141
Appendix.....	145
LIST OF ABBREVIATIONS	150
LIST OF PUBLICATIONS.....	152
CURRICULUM VITAE	154
ACKNOWLEDGEMENTS.....	156

Summary

The inhalation of nanoparticles can cause interactions with pulmonary structures. Human alveolar epithelial cells type II organize the alveolar epithelium and thus can be regarded as barrier against pulmonary nanoparticle uptake. Within the present work, interactions of differently sized gold nanoparticles with A549 cells, a model for type II human alveolar epithelial cells, were studied. The intracellular location of the fluorescently labeled gold particles was analyzed by STED (stimulated emission depletion) and electron microscopy. Gold nanoparticles were detected inside the cell nucleus and the Golgi complex. A nanoparticle accumulation was observed at the perinuclear region. The association of gold nanoparticles and cytoskeletal filaments indicated an active intracellular nanoparticle transport. A vesicle-based transport of gold nanoparticles was revealed by live cell imaging. Besides the intracellular particle location, an impact of gold nanoparticles on cell viability and cell proliferation was studied. Cell-based assays revealed a different cytotoxic potential of the gold nanoparticle sizes used. The last part of the work describes the development of an approach of correlative light and electron microscopy (CLEM) for studying nanoparticle-cell interactions. The used method allowed for a correlative imaging of the nanoparticle fluorescence in relation to the nanoparticle core.

Zusammenfassung

Die Inhalation von Nanopartikeln kann eine Interaktion mit pulmonalen Strukturen zur Folge haben. Humane alveolare Typ II Epithelzellen kleiden die Lungenbläschen aus und stellen dadurch eine wichtige Barriere für das Eindringen von Nanopartikel in die Lunge sowie in den menschlichen Organismus dar. Die vorliegende Arbeit befasst sich deshalb mit der Interaktion von Goldnanopartikeln verschiedener Größe mit A549 Zellen, einem Modellsystem für humane alveolare Typ II Epithelzellen. Die zelluläre Lokalisation der fluoreszenzmarkierten Goldpartikel wurde durch hochauflösende Mikroskopiemethoden, wie STED (stimulated emission depletion) - Mikroskopie und Elektronenmikroskopie bestimmt. Die Nanopartikel konnten im Zellkern sowie im Golgi - Apparat nachgewiesen werden. Die Akkumulation der Partikel in Zellkernnähe sowie die Assoziation von Goldnanopartikeln mit dem Zytoskelett ließen außerdem einen aktiven intrazellulären Nanopartikeltransport vermuten. Ein Vesikel-basierter Transport der Goldnanopartikel konnte durch Lebendzellmikroskopie bestätigt werden. Neben der Partikellokalisierung wurde die Auswirkung der Goldnanopartikel auf die Vitalität und Proliferation von A549 Zellen untersucht. Die eingesetzten Zell-basierten Assays zeigten ein unterschiedliches zytotoxisches Potential der verwendeten Partikelgrößen. Den Abschluss der Arbeit bildete die Entwicklung eines korrelativen Mikroskopieansatzes, der die Detektion der Nanopartikelfluoreszenz in Abhängigkeit des Partikelkerns erlaubte.

1. General introduction

1.1 Nanoparticles

1.1.1 Nanomaterials - A definition

Materials on the nanoscale (1-100 nm) are designated as nanomaterials. The term “nano” originates from the Greek word *nanos*, dwarf, and denotes the small size of nanomaterials. Structures with nanometer dimensions are synthesized because of their special physical and chemical properties, which are not present in the same material of larger dimensions. A well-known example is the use of nano-sized titanium dioxide (TiO₂) or zinc oxide (ZnO) in sunscreens. TiO₂ and ZnO absorb UV light, thereby providing UV protection. In contrast to microsized TiO₂ and ZnO, TiO₂ and ZnO nanoparticles are transparent and thus are gladly used in sunscreens to gain a less opaque cream (Smijts and Pavel 2011). The array of products containing engineered nanomaterials has extended to almost all sectors of daily life. Nanosized silica acts as anti-caking or clearing agent and is supplemented to food products (Dekkers *et al.*, 2011). Nanosilver is used as packaging material due to its antimicrobial activity (Wijnhoven *et al.*, 2009). Also gold nanoparticles are extensively used, predominately within the biomedical sector (Lévy *et al.*, 2010). The rapid development of nanotechnology calls for definitions (European Union 20/10/2011) that help to distinguish between bulk and nanomaterial as well as to differentiate between diverse kinds of nanomaterials (*Figure 1*). In general, nanomaterials can be divided into single nano-objects or nano-structured materials (ISO/TS 80004-1:2010). Nano-structured materials have structural elements with dimensions in the range of 1 - 100 nm (ISO/TS 80004-4:2011), e.g. nano-structured surfaces. In contrast, single nano-objects are materials with one, two, or three dimensions of the material itself in the nanometer range. Nano-objects can be further divided into nanoplates, nanofibres, and nanoparticles (ISO/TS 27687:2008). Their small size arouses a variety of nano-specific effects depending on the material's nature. Gold nanoparticles are the major focus of the present study. Thus, properties and applications of gold nanoparticles are reviewed within the next section.

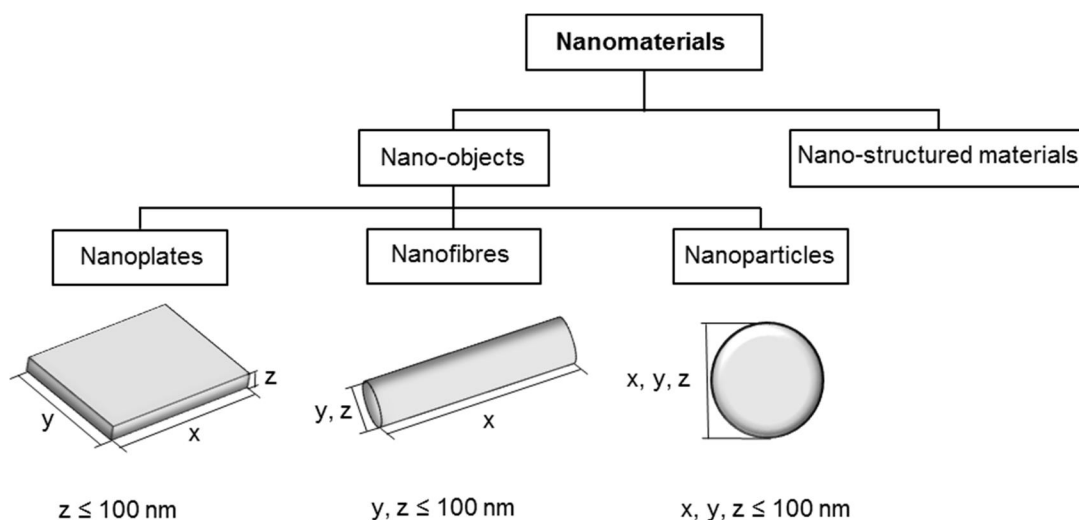


Figure 1: Classification of nanomaterials.

Nanomaterials can be divided into nano-objects and nano-structured material (ISO/TS 80004-1:2010). Nano-objects have at least one dimension in the nanometer range (1 - 100 nm) and can be further divided into nanoplates, nanofibres, and nanoparticles (ISO/TS 27687:2008). Figure was adapted from Krug and Wick 2011 and modified.

1.1.2 Gold nanoparticles

1.1.2.1 Optical properties and applications

One of the first known applications of gold nanoparticles goes back to the fifth century, when Romans used colloidal metal particles for the coloring of ceramics or glass works. A well-known example is the famous Lycurgus cup, which exhibits a green color under reflected light. However, under transmitted light its color turns into red. This optical phenomenon is caused by small silver and gold particles, which were incorporated into the glass during its manufacture (Freestone *et al.*, 2007; Hashim 2012). Nowadays, the usage of gold nanoparticles is still based on their special optical properties, which were first described by Mie (Mie 1908). In brief, an interaction of metal nanoparticles with light causes a collective oscillation of free electrons on the particle surface. This electron gas is called surface plasmon and its resonant oscillation is known as surface plasmon resonance (SPR) (Jain *et al.*, 2007). The SPR depends on the physicochemical properties of the particles. For gold nanoparticles, SPR was observed for frequencies within the range of visible light (Daniel and Astruc 2004). The SPR is accompanied by light absorption and scattering at the SPR frequency and is influenced by particle size and shape. Thus, light absorption and scattering properties of gold nanoparticles are highly tunable by particle size, making them a valuable tool for a wide range of optical applications. Small and non-aggregated gold nanoparticles absorb light in the blue-green range whereas red light is reflected. With increasing particle diameter or due to particle aggregation, the SPR shifts and particles appear more violet due to an increased reflection of blue light (Figure 2). For particle diameters below 3 nm, the SPR decreases dramatically, which is due to the quantum size effect. The quantum size effect describes the alteration of electronic properties of solids with great reduction in particle size (Halperin 1986). Thus, the SPR is lacking for particles with a core diameter less than 2 nm (Daniel and Astruc 2004).

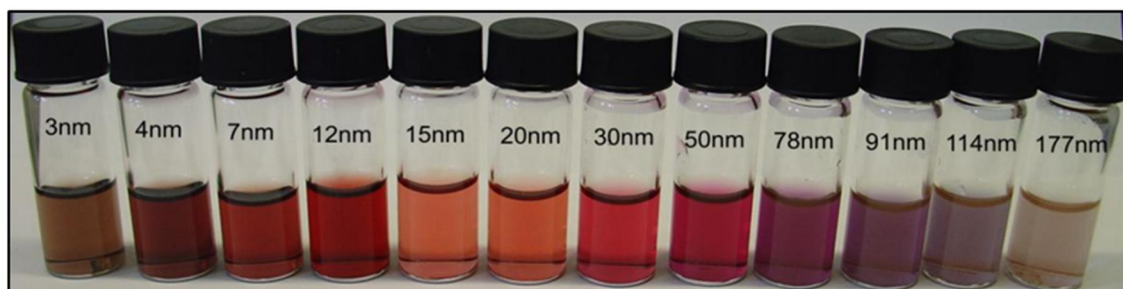


Figure 2: Dispersions of gold nanoparticles under visible light.

Gold nanoparticles are able to absorb light in the visible range. With increasing particle diameter (4 - 114 nm), the SPR and in consequence the absorption peak shifts to longer wavelengths. For 3 nm and 177 nm gold particles, a SPR is lacking (Image provided by Dr. C. Cavellius).

The optical properties of gold nanoparticles are highly valuable for a wide range of sensor applications (Sperling *et al.*, 2008). Although some of them are still under investigation or of theoretical nature, a few sensor systems basing on gold nanoparticles are commercially available by now. One example is a home pregnancy test (First Response®, Church & Dwight Co., Inc.), which uses the light absorption properties of gold nanoparticles to indicate a pregnancy. In detail, the urine of pregnant women has a significant excess of human gonadotropin hormone (hCG). This hormone is detected by a mixture of hCG-antibody-coated microspheres (~1 μm) and hCG-antibody-coated gold particles (40 nm), which appear red under visible light. The presence of hCG in urine samples causes an agglomeration of both particles, yielding red clumps. A filter retains and concentrates the clumps

resulting in a red colored filter. For negative urine, no particle agglomeration occurs, the gold nanoparticles pass through the filter, and no reddish color develops (Bangs 1996).

Other potential sensor applications of gold nanoparticle are e.g. the detection of arsenic in groundwater (Kalluri *et al.*, 2009) or the monitoring of glutathione, which is needed in toxicity studies to describe and quantify oxidative cell stress (Li *et al.*, 2010). Furthermore, fluorescence quenching properties of gold nanoparticles can be used for monitoring applications. Gold nanoparticles are able to quench fluorescence, if their absorption spectrum overlaps with the emission spectrum of the fluorophore. Fluorescence or Förster resonance energy transfer (FRET) between two fluorophores is well-known and leads to a quenching of the donor fluorescence. However, FRET between two fluorescent molecules is typically limited by the required donor-acceptor distances of less than 5 - 8 nm (Förster 1948). In contrast, gold nanoparticles are efficient quenchers also for long distances between donor and acceptor (Anger *et al.*, 2006). These properties are also highly valuable for sensor applications such as sandwich immunoassays (Mayilo *et al.*, 2009). Scattering of gold nanoparticles can be used for spectroscopic techniques like surface enhanced Raman scattering (SERS). In brief, this technique enhances the Raman scattering of molecules adsorbed on rough metal surfaces or metal nanoparticles and enables the detection of scattering signals from a small amount of molecules. Recently, gold nanoparticles were tested as potential sensors for SERS detection of explosives (Herrera *et al.*, 2013).

Further applications of gold nanoparticles can be found in the imaging and biomedical sectors. Upon light absorption, the excited surface plasmon thermally relaxes, causing a heating of gold nanoparticles. These unique properties can be used for photothermal or photoacoustic imaging techniques (Boyer 2002; Mallidi *et al.*, 2007). The heating properties can also be employed for photothermal cancer therapy. Within this approach, gold nanoparticles are linked to antibodies that recognize cancer cell specific markers. In this manner, the nanoparticles are directed to the cancerous tissue. Afterwards the cells are irradiated, which leads to a heating of the particles. The generated heat is transferred to the surrounding cells or tissue causing cell death and finally a breakdown of cancerous tissue. Still, this application has not entered clinical routine yet (Cai *et al.*, 2008; Li and Gu 2010).

The absorption and scattering properties of gold nanoparticles allow for microscopic applications, e.g. as labeling agents. The scattered light of gold nanoparticles can be detected by dark-field microscopy and differential image interference contrast. Both strategies have been used to track gold particle labeled peptides (Tkachenko *et al.*, 2003) and viruses (Souza 2006) inside cells. Besides an interaction with visible light, gold nanoparticles interact with electrons as well. The high atomic number of gold and therefore the high electron density is used in electron microscopy for the generation of image contrast. Traditionally, gold nanoparticles have been used as antibody labels enabling the visualization of cellular structures or organelles, which are typically composed of low atomic number elements (Faulk and Taylor 1971). The molecular interaction of antibodies with cellular structures turns the target structure into an electron dense material that can be imaged by electron microscopy. A further microscopy-based application of gold nanoparticles lies in the multiphoton-absorption-induced luminescence. The absorption of multiple photons from near infrared ultrafast lasers can lead to luminescence of noble-metal nanostructures (Farrer *et al.*, 2005). Recently, this approach has been applied for imaging of gold nanoparticle penetration into reconstructed human skin (Labouta *et al.*, 2012).

1.1.2.2 Chemical properties and applications

Chemical properties of gold nanoparticles arise mainly from their catalytic activity and their high functionalization potential. Gold nanoparticles are catalysts that work even under mild conditions, e.g. at room temperature (Thompson 2007). An example for their catalytic activity is the production of gluconic acid, which to date is exclusively realized by biotechnological fermentation. The use of gold nanoparticles enables a direct conversion of glucose to gluconic acid with a long-term stability of the nanoparticle catalyst (Thielecke and Prüße 2007). The Südzucker AG filed a patent covering the use of gold nanoparticles in selective carbohydrate oxidation (Südzucker Aktiengesellschaft Mannheim/Ochsenfurt EP1631537 B1).

Besides catalytic activity, gold nanoparticles show a high functionalization potential. The gold surface provides excellent linking capabilities by anchoring thiol linkers onto the gold surface. Initially, a functionalization with thiol ligands was used to stabilize gold nanoparticles and to prevent them from aggregation (Brust *et al.*, 1995). More than that, the gold-thiol bond allows for a functionalization of gold nanoparticles with a large array of molecules leading to a variety of applications. The coupling properties of gold nanoparticles allow for delivery applications, e.g. of genes and drugs. For gene delivery, DNA is coupled to the particle surface *via* thiol linkers and cells can be transfected by introducing DNA-loaded nanoparticles into cells (Lévy *et al.*, 2010; Chang *et al.*, 2008). Gold nanoparticles show also a great potential for the delivery of drugs (Cai *et al.*, 2008). Nanoparticle-based drug delivery has two major goals: I) a better targeting and release of the drug, and II) the minimization of side-effects (Jong and Borm 2008). Aurimmune (or CYT-6091) is a potential drug candidate employing drug delivery *via* gold nanoparticles. The drug contains tumor necrosis factor- α (TNF- α), which is anti-carcinogenic but causes systemic toxicity, which limits its application in cancer therapy. To circumvent a systemic toxicity, TNF- α is linked to 30 nm polyethylene glycol (PEG)-coated gold particles. The functionalization with PEG reduces the drug from clearance by the reticulo endothelial system and TNF- α can be transported *via* the bloodstream with a reduced immune detection and hence permanently minimized toxic side-effects. Furthermore, the nanoparticle based construct exits the blood circulation only *via* leaky vasculature at tumor sites. This strategy prevents an uptake of the drug by healthy tissue and allows for targeted drug delivery (Paciotti *et al.*, 2004). Currently, Aurimmune has completed phase I clinical trial. A phase II clinical program for treatment of pancreatic cancer, melanoma, soft tissue sarcoma, ovarian, and breast cancer patients is in preparation (Jelveh and Chithrani 2011).

1.1.2.3 Toxicity of gold nanoparticles

The high biomedical potential of gold nanoparticles, e.g. for photothermal cancer therapy or drug delivery, requires detailed analyses of nanoparticle safety. Bulk gold is a very inert material and is generally regarded as biocompatible. However, nanotoxicity can arise due to the small size of nanoparticles and their unique properties. Besides concentration and exposure time, nanoparticle toxicity is a function of primary particle size (Nel 2006), particle coating (Clift *et al.*, 2008), particle surface charge (Ruizendaal *et al.*, 2009), potential contaminants like endotoxins (Vallhov *et al.*, 2006), the used cell system (Clift *et al.*, 2008), and the method that is used to describe toxicity (Monteiro-Riviere *et al.*, 2009). Hence, nanoparticles have to be well-characterized prior to their use in toxicity studies (Warheit 2008).

Table 1 overviews reported data concerning gold nanoparticle toxicity, including data of the used cell system, the particle size, the test system, and the nanoparticle concentration. Goodman *et al.* reported a toxicity of 2 nm gold particles, whereas positively charged gold particles had a higher cytotoxic potential than negatively charged ones (Goodman *et al.*, 2004). A study by Pan *et al.*

suggested a size-dependent gold nanoparticle toxicity. Gold particles of 1 - 2 nm were shown to be more toxic than larger particles with a size of 15 nm (Pan *et al.*, 2007). Furthermore, gold nanoparticles affected A549 cells, a human alveolar cell line, to a higher extent than cell lines derived from kidney or liver (Patra *et al.*, 2007). However, some of the studies did not determine a cytotoxic potential of gold nanoparticles at relevant concentrations (Connor *et al.*, 2005; Freese *et al.*, 2012).

For *in vitro* studies, different methods for cytotoxicity testing are available and not all of them are suitable to assess nanoparticle toxicity. Misinterpretation of nanotoxicity testing can occur due to nanoparticle-dye interactions (Monteiro-Riviere *et al.*, 2009; Wörle-Knirsch *et al.*, 2006). Absorption-based assays for determination of cellular viability, like the MTT (3-(4,5-dimethylthiazol-2-yl)-2,5-diphenyltetrazolium bromide) or the WST-1 (water soluble tetrazolium) assay, are widely used (Table 1). However, especially for the evaluation of gold nanoparticle toxicity, optical properties have to be considered. As mentioned previously, gold nanoparticles absorb light within the visible range and therefore can interfere with colorimetric enzyme-based cell assays, like the MTT or the WST-1 assay. An absorption of gold nanoparticles at the measurement wavelength of toxicity assays can lead to an underestimation of cell viability.

Besides cytotoxicity, nanoparticles can also trigger genotoxicity (Singh *et al.*, 2009; Donaldson *et al.*, 2010). Genotoxicity can be caused by nanoparticles that interact with the DNA directly, or *via* reactive oxygen species (ROS), which can be generated on nanoparticle surfaces (Nel 2006). Interactions of nanoparticles or nanoparticle-derived ROS with DNA are assumed to cause DNA damage (Tkachenko *et al.*, 2003). Several studies suggest a genotoxic potential of gold nanoparticles. Surface-modified 3.7 nm gold particles were able to penetrate the nucleus of HeLa cells and caused little impact on the cell viability (Gu *et al.*, 2009). Li *et al.* showed that 20 nm gold particles inhibited cell proliferation by a downregulation of cell cycle genes and by affecting genes associated with genomic stability and DNA repair (Li *et al.*, 2010). Hence, both the cytotoxic and the genotoxic potential of gold nanoparticles have to be taken into account during studies of nanoparticle-cell interactions.

Table 1: Reported toxicity of gold nanoparticles on different human cells and cell lines.
The table was adapted from Zhang *et al.* (Zhang *et al.*, 2009) and modified.

Author	Cells or cell line	Primary particle size [nm]	Assay	Impact on cell viability	Mass or molar concentration
Goodman <i>et al.</i> , 2004	Cos-1	2	MTT	Yes	1,000 nM
Connor <i>et al.</i> , 2005	K562	18	MTT	No	250,000 nM
Pernodet <i>et al.</i> , 2006	CF-31	13	Cell number	Yes	100 - 800 µg ml ⁻¹
Pan <i>et al.</i> , 2007	HeLa	0.8	MTT	Yes	250,000 nM
		1.2		Yes	140,000 nM
		1.4		Yes	46,000 nM
		1.8		Yes	230,000 nM
		15		No	6,300,000 nM
Patra <i>et al.</i> , 2007	A549	33	MTT	Yes	10 - 120 nM
Li <i>et al.</i> , 2008	MRC-5	20	Cell number	Yes	0.5 - 1 nM
Gu <i>et al.</i> , 2009	HeLa	3.7	MTT	Yes	80 - 10,000 nM
Zhang <i>et al.</i> , 2009	K562	15	CellTitre-Glo	Yes	18.75 - 600 µg ml
Kumar <i>et al.</i> , 2007	HeLa	2	MTT	No	0.831 nM
		10		Yes	
		25		Yes	
Freese <i>et al.</i> , 2012	Endothelial cells	18	MTS	No	10 - 250 µg ml ⁻¹
		35			
		65			
Paino <i>et al.</i> , 2012	HepG2	11	MTT	Yes	10 - 50,000 nM
		18		Yes	

1.2 The human lung

1.2.1 Structure and function

Nanoparticles can enter the lung by inhalation. The hierarchical structure of the lung offers a huge surface area for nanoparticles to interact with. 2.5 m² of the total lung surface area are provided by the conducting airways, comprising trachea, bronchi, and bronchioles. In contrast, the alveolar region, where gas exchange takes place, has an average surface area of about 100 - 120 m² (Patton 1996; Schmitz and Müller 1991). Hence, alveoli play an important role regarding nanoparticle uptake *via* inhalation. Alveolar epithelial cells and macrophages represent the cell types of the alveolar surface (*Figure 3*), whereby about 95 % of the alveolar surface is covered by type I alveolar epithelial cells (Schmitz and Müller 1991). These flat cells contain just a few organelles and are unable to divide. Their main role is a barrier function between air and blood, thereby mediating gas exchange (Schmitz and Müller 1991; Andreeva *et al.*, 2007). Type I alveolar epithelial cells act as signaling

partners for type II alveolar epithelial cells, the second type of cells organizing the alveolar epithelium. These cuboidal cells have numerous functions. In addition to alveolar macrophages, they participate in particle clearance and protect the lung from inhaled particles by altering the amount of surfactant (George and Hook 1984) and releasing chemotaxins that attract alveolar macrophages (Barlow *et al.*, 2005). Furthermore, alveolar epithelial cells type II are able to differentiate into type I cells if necessary. Type II alveolar epithelial cells possess repair functions as they are able to migrate to damaged epithelium and to proliferate. However, the basic function of type II cells is the production and excretion of lung surfactant by exocytosis of lamellar bodies (LB) (Haller *et al.*, 1998). The surfactant is part of the alveolar lining fluid that consists of an aqueous hypophase and a lipid epiphase. The surfactant layer decreases the surface tension of alveoli resulting in a stabilized air-liquid-interface. This enables the lung to expand during inspiration and prevents the lung from collapsing during expiration (Haagsman and van Golde 1991). Additionally, the lung surfactant provides a barrier protecting the alveolar epithelium from microorganisms or inhaled particles. The surfactant proteins (SP) SP-A and SP-D play an important role in defense mechanisms by binding and clearing inhaled microorganism from the lung (Khubchandani 2001; Kingma and Whitsett 2006). Besides 10 % of proteins, the surfactant layer is composed of 80 % phospholipids and 10 % cholesterol (Andreeva *et al.*, 2007). Its production is a very dynamic process and seems to be highly regulated by SP (Hawgood and Clements 1990; Schmitz and Müller 1991).

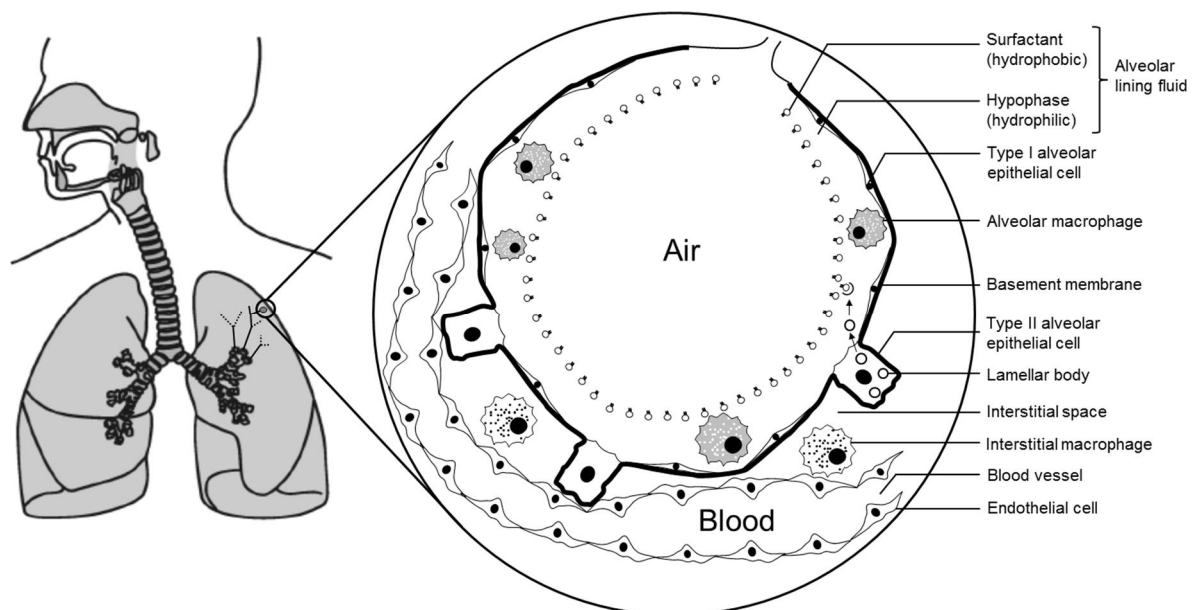


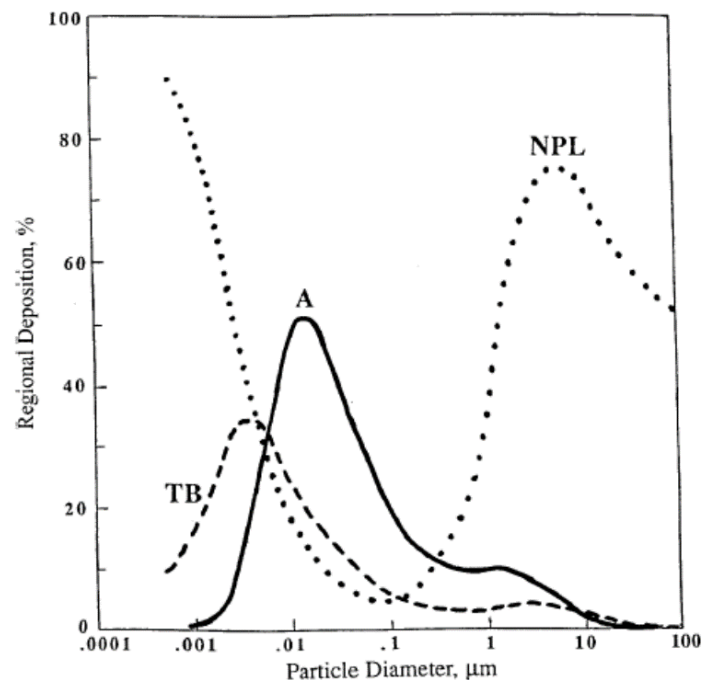
Figure 3: The human lung and alveoli.

A cross-section of an alveolus showing alveolar cells and connected blood vessels. The barrier between air and blood is very thin in this deeper lung region. The figure was adapted from Andreeva *et al.*, 2007 and Hawgood and Clements 1990 and modified.

In the alveolar region, the air-blood tissue barrier has a thickness of about 2.2 μm and a harmonic mean thickness, the relevant thickness for diffusion, of 0.62 μm (Gehr *et al.*, 1978). This thin barrier enables a fast gas exchange. Inhaled oxygen is transported *via* the alveolar epithelium into blood vessels, carbon dioxide is transported in the opposite direction and is exhaled. Inhaled particles, which interact with alveolar epithelial cells can theoretically be transferred to the surrounding blood vessels as already shown in animal studies (Geiser *et al.*, 2005). An entrance of particles into the circulation can lead to a particle deposition in secondary organs (Kreyling *et al.*, 2002).

1.2.2 Particle-lung interactions and particle-induced lung inflammation

In general, particulate matter (PM) can be divided into respirable PM₁₀, particles equal to or less than 10 µm, fine PM_{2.5}, particles equal to or less than 2.5 µm, and ultrafine particles (UFP) or PM_{0.1}, particles with diameters less than 0.1 µm. Previous studies provided evidence that pulmonary particle deposition and particle-induced lung injury are a function of particle size. Rats either exposed to fine (~250 nm) or ultrafine (~20 nm) TiO₂ and Al₂O₃ particles showed a higher pulmonary uptake of UFP, presumably due to the higher particle number of UFP (Ferin *et al.*, 1991). However, an accumulation of UFP inside the lung was shown to provoke inflammation (Oberdörster *et al.*, 1994). Upon nanoparticle exposure alveolar macrophages express and release pro-inflammatory signaling factors and alveolar epithelial cells start to release cytokines and chemotaxins to attract macrophages (Unfried *et al.*, 2007). This inflammatory potential of UFP was related to the higher specific surface area, the greater interstitial access, and an altered biopersistence of UFP compared to fine particles. Furthermore, a pulmonary deposition of UFP can result in a translocation of particles to single cells, e.g. epithelial cells. Once the particles are internalized they can potentially cause inflammation, oxidative stress, activation of signaling pathways, or genotoxicity (Oberdörster 2010). An inhalation of engineered nanoparticles is expected to cause similar responses, too. Particle inhalation and pulmonary deposition are predicted to be highly size-dependent (Figure 4). Particles with diameters above 10 µm are not deposited inside the trachea-bronchial or alveolar region of the lung. They are rather retained in the nose, pharynx, or larynx. Particles of 10 - 100 nm show a high deposition in the alveolar region, whereas particles of 1 - 10 nm are deposited mainly in the trachea-bronchial region. Hence, the major target of inhaled nanoparticles are alveoli, comprising the alveolar lining fluid, alveolar epithelial cells, and alveolar macrophages.



Fractional Deposition Nose Breathing

A = Alveolar; TB = Tracheo-bronchial; NPL = Nasal, Pharynx, Larynx

Figure 4: Model of particle deposition in different parts of the respiratory tract.

Inhaled particles above 10 µm are deposited in the nose, pharynx, or larynx and do not reach the bronchial or alveolar region. An alveolar deposition is highest for particles between 10 and 100 nm. A trachea-bronchial deposition occurs mainly for particles sized 1 - 10 nm. The figure was taken from Oberdörster 2001.

Several lung diseases are related to an extensive inhalation of PM. It is well known that a high exposure to airborne particles can cause aggravated asthma (Koenig 1999), chronic lung diseases like chronic obstructive pulmonary disease (COPD) (Neuberger *et al.*, 2004), and a decreased lung function (El-Fadel and Massoud 2000). Increasing evidence suggests that inhaled airborne particles can affect secondary organs and evoke cardiovascular diseases including an increased risk of myocardial infarction (Brook *et al.*, 2010). Furthermore, PM exposure was also shown to be detrimental to the liver and could be related to steatohepatitis (Conklin 2013).

1.2.3 Nanoparticle-lung interactions

Interactions of manufactured nanoparticles with different components of the bronchial and alveolar region are of great interest due to their high deposition potential and the inflammatory potential of airborne particles in the nanometer range. Kirch *et al.* showed that nanoparticles adhere to the pulmonary mucus, the lung lining fluid of the conducting airways, and might be trapped inside its porous structure (Kirch *et al.*, 2012). Furthermore, nanoparticles interacting with SP undergo an increased clearance by macrophages (Ruge *et al.*, 2012). Both studies revealed a protecting barrier function of the lung surfactant. However, once this barrier is overcome by nanoparticles, interactions with alveolar cells can occur. Alveolar macrophages typically remove inhaled particles within the micrometer range (Geiser 2002). However, nanoparticles were also shown to be taken up by alveolar macrophages and to amplify their inflammatory response (Diesel *et al.*, 2013). A clearance of particles in the nanometer range by macrophages is suggested to be less efficient than for particles of larger dimensions (Geiser and Kreyling 2010). An insufficient phagocytosis of nanoparticles by macrophages can cause interactions of inhaled nanoparticles with alveolar epithelial cells. *In vivo* and *in vitro*, endocytosis was determined as major mode of nanoparticle uptake. Inhaled gold nanoparticles were found in membrane-bound vesicles of alveolar epithelial cells type I in rat lungs (Takenaka *et al.*, 2006). Similar results were observed *in vitro*, for the uptake of gold nanoparticles by A549 cells, a model for type II alveolar epithelial cells. The particles were observed inside vesicles of different sizes (Brandenberger *et al.*, 2010). TiO₂ nanoparticles were even detected inside multivesicular bodies (MVB) and LB of A549 cells (Stearns *et al.*, 2001; Singh *et al.*, 2007).

Within the present study, nanoparticle-lung interactions were studied *in vitro*. The A549 cell line was chosen as a model for human type II alveolar epithelial cells. The cells were initiated from a human alveolar cell carcinoma (Lieber *et al.*, 1976) and are widely used to study pulmonary drug delivery (Foster *et al.*, 1998) or nanoparticle-lung interactions (Lanone *et al.*, 2009). Gold nanoparticles were chosen as particle system because of their optical properties, which allow for a wide range of microscopy analyses concerning nanoparticle-cell interactions. Furthermore, gold nanoparticles of different sizes can be synthesized very precisely and a size-dependency of cellular nanoparticle uptake and toxicity can be easily studied. The chemical properties of gold nanoparticles permit surface modifications, which are usually needed to stabilize nanoparticles in biological environment.

1.2.4 Nanoparticle exposure to human lung cells

1.2.4.1 Particle dosage

Nanoparticle dosage is important with regard to real exposure scenarios. The alveolar deposition of nanoparticles is limited due to aerosol-physical limitations. From calculations it was assumed that a maximum of 2×10^{13} nanoparticles can be inhaled within one day by an adult human (Bangs 1996). Regarding the deposition within the alveolar epithelium, maximally 120 nanoparticles encounter

alveolar epithelial surface cells per hour (Bangs 1996). Hence, care should be taken to avoid overload conditions of human lung cells if a realistic environmental particle exposure is in focus of the study (Donaldson and Poland 2012).

Interactions of nanoparticles and human lung cells occur *via* inhalation. The cells are in contact with inhaled air from the apical side, and with the blood circulation from the basolateral side. However, the exposure of cell cultures to nanoparticle aerosols is hard to mimic due to technical demands and safety issues. Furthermore, the establishment of cell systems that grow at the air-liquid interface is challenging. For these reasons, submerged cell systems are used. Under submerged conditions, the cells are totally covered with cell culture medium. Nanoparticles are diluted in cell culture medium and applied as dispersions. Although this approach does not mimic real exposure scenarios, it is widely used due to its feasibility. There are some approaches that aim to simulate real exposure scenarios. Brandenberger *et al.* studied the uptake of gold nanoparticles by human lung cells at the air-liquid interface (Brandenberger *et al.*, 2010). The particles were deposited using the ALICE (air-liquid interface cell exposure) system, which generates a dense cloud of droplets from nanoparticle dispersions and allows for a dose-controlled particle exposure (Lenz *et al.*, 2009). A recent comparison of submerged and air-liquid interface conditions indicated that toxicity testing with conventional submerged systems may cause more false negatives than the air-liquid interface systems (Lenz *et al.*, 2013).

1.2.4.2 Particle stability and protein corona

The exposure of nanoparticles to human lung cells requires special attention regarding particle stability. *In vivo* and *in vitro*, nanoparticles have to withstand physiological conditions, such as an isotonic environment, a pH of 7.4, and the presence of proteins (Schulze *et al.*, 2008). The high free surface energy of nanoparticles contributes to a low stability under the aforementioned conditions (Pomogailo and Kestelman 2005) and can lead to particle agglomeration or precipitate fallout. Hence, nanosized particles require a proper stabilization to avoid agglomeration in cell experiments. Nanoparticles can be prevented from agglomeration by steric or electrostatic stabilization. Electrostatic stabilization is achieved by modifying the particle surface charge, which is indicated by the zeta potential. Nanoparticles with zeta potentials below or above ± 30 mV are regarded as stable (Mohanraj and Chen 2006). A second way to achieve nanoparticle stabilization comprises the use of stabilizer molecules. When nanoparticles are functionalized, e.g. with polymers, they are prevented from aggregation due to steric hindrance and electrostatic repulsion (Pomogailo and Kestelman 2005). There are several protocols available describing the use of polymers for nanoparticle stabilization as well as for particle functionalization (Lin *et al.*, 2008; Alexandridis 2011; Sperling and Parak 2010). However, both, the particle surface charge and the stability of the stabilizer molecules, are influenced by environmental conditions. When nanoparticles are dispersed in biological fluids, a protein corona is formed (Nel *et al.*, 2009). This protein layer, which is built-up around the nanoparticle, influences particle surface properties but also particle agglomeration. Gebauer *et al.* demonstrated that a protein corona formed by human serum albumin stabilizes nanoparticles against agglomeration (Gebauer *et al.*, 2012). By altering nanoparticle characteristics, the protein corona influences also the biocompatibility as well as uptake and intracellular fate of nanoparticles (Lesniak *et al.*, 2012).

1.3 Intracellular transport

1.3.1 Endo- and exocytic transport

Endocytosis is generally regarded as the predominant uptake route of nanoparticles into cells (Mühlfeld *et al.*, 2008; Zhao *et al.*, 2011). The small size of nanoparticles is similar to that of biogenic cargo, e.g. proteins, and might induce cellular uptake. Depending on the nature of the cargo and the cell type, different forms of endocytosis can occur, comprising phagocytosis, macropinocytosis, clathrin- or caveolin-mediated endocytosis, and an entry independent of either clathrin or caveolin (Conner and Schmid 2003; Doherty and McMahon 2009). Just a few cells are capable of phagocytosis, e.g. macrophages, and only larger particles or nanoparticle agglomerates (< 0.5 μm) are taken up by this pathway (Aderem and Underhill 1999).

Clathrin- or caveolin-mediated endocytosis is initiated by a close contact of cargo and cell membrane. (Figure 5). Once the cell membrane fuses with the cargo, it is invaginated and pinched off (Mukherjee *et al.*, 1997). Material, which has been taken up, is packed into vesicles. Typically, endocytic vesicles have sizes of 60 - 120 nm, depending on the uptake route (Conner and Schmid 2003). Macropinocytosis is a rather unspecific uptake and is introduced by membrane ruffling and blebbing (Mercer and Helenius 2009). Macropinosomes that were formed *via* macropinocytosis are much larger compared to endocytic vesicles and can have sizes up to 10 μm (Mercer and Helenius 2009). Internalized endocytic vesicles fuse with each other and form another endocytic compartment, the early endosome (Huotari and Helenius 2011). Early endosomes act as a sorting station within the endocytic pathway. From early endosomes, cargo, e.g. internalized receptors, can be recycled back to the cell surface. Small vesicles with recycling molecules pinch off and are returned to the cell membrane; molecules that are designated for a lysosomal degradation are retained in the early endosome (Dunn *et al.*, 1989). With progress of the endocytic pathway, early endosomes mature to late endosomes. It is hypothesized that maturation from early to late endosome occurs *via* MVB, which migrate slowly along microtubules towards the perinuclear region of the cell (Huotari and Helenius 2011). MVB contain large amounts of invaginated membranes and internal vesicles (Hanson and Cashikar 2012). These internal vesicles capture molecules, which are intended to undergo lysosomal degradation (Piper and Katzmann 2007). From MVB, late endosomes are generated. In contrast to early endosomes, late endosomes no longer recycle vesicles to the cell membrane and exhibit a lower pH. Within the endocytic pathway, the pH drops from 6.5 - 6.0 in early endosomes, to 5.5 - 4.5 in late endosomes and lysosomes (Sorkin and Zastrow 2002). Late endosomes communicate with the *trans*-Golgi and receive protein-filled vesicles, which trigger the conversion into lysosomes (Alberts and Wilson 2008). However, also other concepts of lysosome formation are found in literature. The kiss-and-run concept proposes that late endosomes and lysosomes can fuse partly (kiss), allowing for the exchange of components, before detaching again (run) (Luzio *et al.*, 2007). Lysosomes are cell organelles filled with acidic hydrolases, which are responsible for the catabolic capacity of the lysosome and degrade previously endocytosed material (Saftig and Klumperman 2009). Macropinosomes also undergo lysosomal degradation by fusing with late endosomes (Kerr and Teasdale 2009).

The exocytic pathway governs the transport of vesicles from the cell interior to the cell membrane and to the extracellular space (Figure 5). By this, lipids and proteins required for the maintenance of the cell membrane are provided and molecules can be secreted into the extracellular matrix. The packaging of proteins, which are intended to leave the cell *via* secretory vesicles, is processed in the *trans*-Golgi network (Alberts and Wilson 2008). Hence, nanoparticles that reach the Golgi complex

can undergo exocytosis. Exocytosis of peptide functionalized gold nanoparticles from endothelial cells has been recently published (Bartczak *et al.*, 2012). However, the mechanism of exocytosis remained unclear. From A549 cells, nanoparticle exocytosis can also occur *via* LB. Schumann *et al.* found silica nanoparticles associated with LB (Schumann *et al.*, 2012). LB, which are responsible for surfactant release (see 1.2.1), are known to interact with MVB (Weaver *et al.*, 2002). By this, endocytosed nanoparticles would gain access to the exocytic transport route of surfactant release.

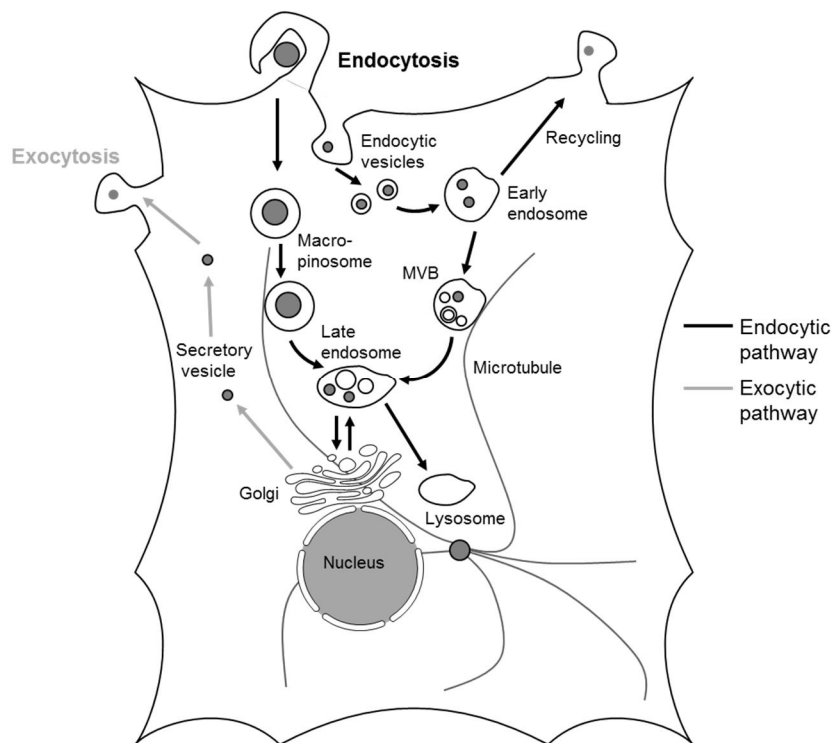


Figure 5: Intracellular transport along the endo- and exocytic pathway.

Cargo is taken up and transported into the cell via the endocytic pathway (black arrows). The exocytic pathway (gray arrows) transports cargo from the cell interior to the cell membrane. Figure was adapted from Alberts and Wilson 2008 and modified.

1.3.2 Microtubules - Structure and function

As mentioned in the previous section, microtubules facilitate the transport of internalized cargo. Microtubule-mediated transport is essential during cell division when replicated chromosomes are distributed between two dividing cells (Alberts and Wilson 2008). Microtubules transport also endocytosed nanoparticles. Microtubules represent dynamic filaments, which are spread out throughout the whole cell. Together with actin and intermediate filaments they form the cytoskeleton, which controls cell shape and cell mechanics (Fletcher and Mullins 2010). Microtubules are cylindrical-like structures with 25 nm in diameter and are assembled of tubulin. The tubulin protein is a dimer consisting of α - and β -tubulin subunits. Tubulin dimers polymerize to protofilaments *via* the hydrolysis of guanosine triphosphate (GTP) to guanosine diphosphate (GDP). Finally, 13 protofilaments are assembled to one microtubule (Figure 6) (Valiron *et al.*, 2001).

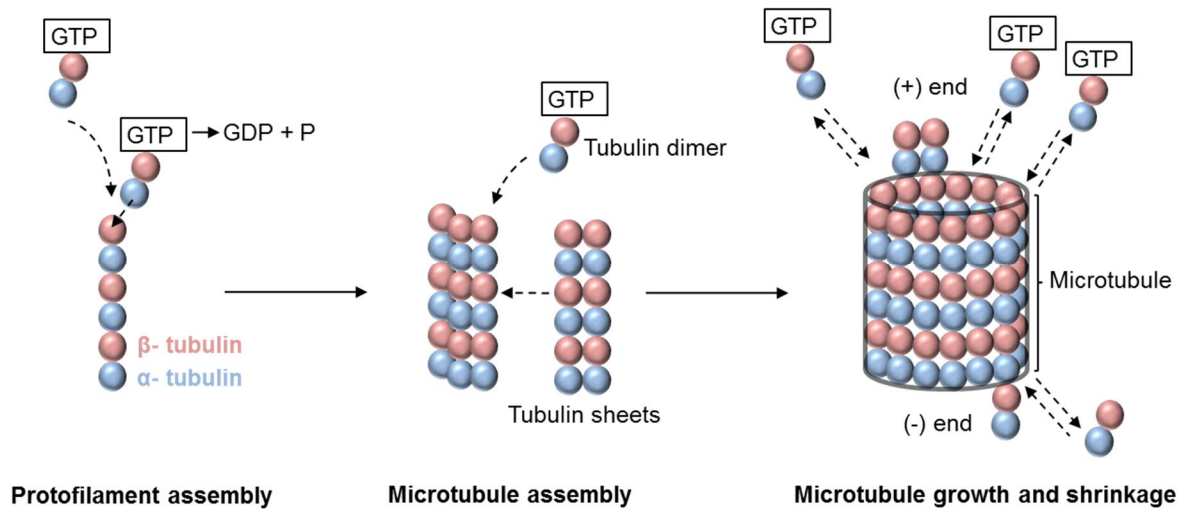


Figure 6: Assembly and growth of microtubules.

Microtubules are assembled of dimeric subunits consisting of α - and β - tubulin by the conversion of GTP to GDP. Protofilaments are built up from these subunits and are assembled to one microtubule. At the microtubule (+)-end, the addition of tubulin dimers is favored due to the presence of a GTP cap. Figure was adapted from Lodish 2008 and modified.

Microtubules are polar structures with a fast-growing (+)-end and a slow-growing (-)-end. This dynamic instability is essential for a rapid rearrangement of the microtubule system, e.g. within the cell cycle (Gelfand 1991) and can be modulated in part by microtubule-associated proteins (MAPs). MAPs cross-link single tubulin filaments and in consequence stabilize the microtubule network when a more stable microtubule network is needed. The polarity of microtubules is also crucial for intracellular transport. The (-)-ends point towards the microtubule organizing center (MTOC), which is located close to the cell nucleus. The (+)-ends are directed to the cell periphery. Microtubule-based transport is mediated by special motor proteins, which move along the filaments. Kinesins transport cargo from (-)-ends to (+)-end and dyneins move towards (-)-ends. The transported cargo can be of different nature. Both, endocytosed vesicles as well as cell organelles are transported by kinesins and dyneins and can be kept at one location, if needed (Alberts and Wilson 2008).

1.3.3 Interactions of nanoparticles with microtubules

An evidence of microtubule-mediated nanoparticle transport has been given by a study of Nan *et al.* who observed individual steps of kinesins and dyneins in living cells by following endocytosed quantum dots (Nan *et al.*, 2005). Similar results were obtained by Ruan *et al.*, who reported an active transport of vesicle-bound quantum dots along microtubules with a destination to the MTOC (Ruan *et al.*, 2007). For silica nanoparticles, an active intracellular transport was suggested as well (Schumann *et al.*, 2012). However, detailed data concerning a microtubule-based transport of nanoparticles are lacking. Furthermore, the impact of nanoparticles on the microtubule structure and function is not well-studied. Titanium dioxide nanoparticles were shown to interact with isolated microtubules and to inhibit microtubule polymerization (Gheshlaghi *et al.*, 2008). The exposure of cells to iron oxide nanoparticles induced a remodeling of the microtubule cytoskeleton (Apopa *et al.*, 2009; Soenen *et al.*, 2010). These few studies show the potential of nanoparticles to affect microtubule structure and function and to be transported along microtubules.

1.4 Imaging at the nanoscale level

1.4.1 Fluorescence microscopy and its limitations

The term light microscopy comprises a variety of different techniques using light for image generation, such as phase contrast microscopy, differential interference contrast microscopy, bright field or dark field microscopy. Fluorescence microscopy has several advantages over these transmitted light methods, e.g. a specific staining of proteins and cellular structures, a linearity between labeling density and fluorescence signal, and the ability for multiplex imaging. Thus, it is a versatile tool for studying the interaction of nanoparticles and cells. Fluorescence is the emission of light by a system that has previously been excited by the absorption of photons (Figure 7). Due to the large array of fluorescent probes, which cover the whole spectrum of visible light, fluorescence microscopy allows for simultaneous imaging of different cellular, subcellular, or molecular components (Lichtman and Conchello 2005). Furthermore, the invention of the confocal microscope enabled 3D imaging of fluorescent probes, like fluorescently labeled cells (Amos and White 2003). The discovery of fluorescent proteins further extended the use of fluorescence microscopy towards living cells (Chudakov *et al.*, 2010). These properties make fluorescence microscopy a valuable tool to elucidate nanoparticle-cell interactions (Wang *et al.*, 2012). A prerequisite for applying fluorescence microscopy in terms of nanoparticle-cell interactions is the availability of fluorescent nanoparticles. Quantum dots exhibit intrinsic fluorescence properties (Alivisatos *et al.*, 2005). However, most nanoparticles have to be labeled with dyes to be available for fluorescence microscopy. The dye can either be incorporated into the particle itself (e.g. silica or polymer nanoparticles) (Ruedas-Rama *et al.*, 2012) or attached *via* linker molecules to the particle surface (Kumar 2007).

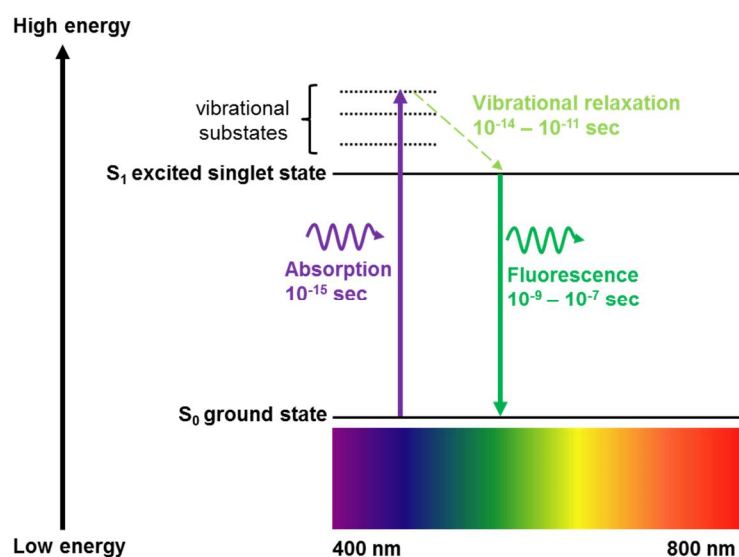


Figure 7: Jablonski diagram of fluorescence.

A fluorophore that has absorbed light of a certain wavelength transits to a higher electronically excited state. During vibrational relaxation the fluorophore loses part of its absorbed energy and subsequently falls back to the electronically ground state. The transition from s_1 to s_0 is accompanied by the emission light, which is called fluorescence. Due to the energy loss during vibrational relaxation, the emitted light has a longer wavelength compared to the initially absorbed photons. Figure was adapted from Müller *et al.*, 2012 and modified.

The main drawback of all light microscopic techniques is the restricted resolution due to the diffraction of light. Resolution in light microscopy defines the minimal distance between two objects that still allows for a separated detection of the two entities (Pawley 2010). In lateral and axial dimension, resolution is described by the Rayleigh criterion (*Equation 1.1*):

$$d_{xy} = 0.61 \frac{\lambda}{n \sin \alpha} = 0.61 \frac{\lambda}{NA} \quad (1.1)$$

The criterion is satisfied when the central maximum in the diffraction pattern of one object coincides with the first minimum of the diffraction pattern of the other object (*Figure 8*).

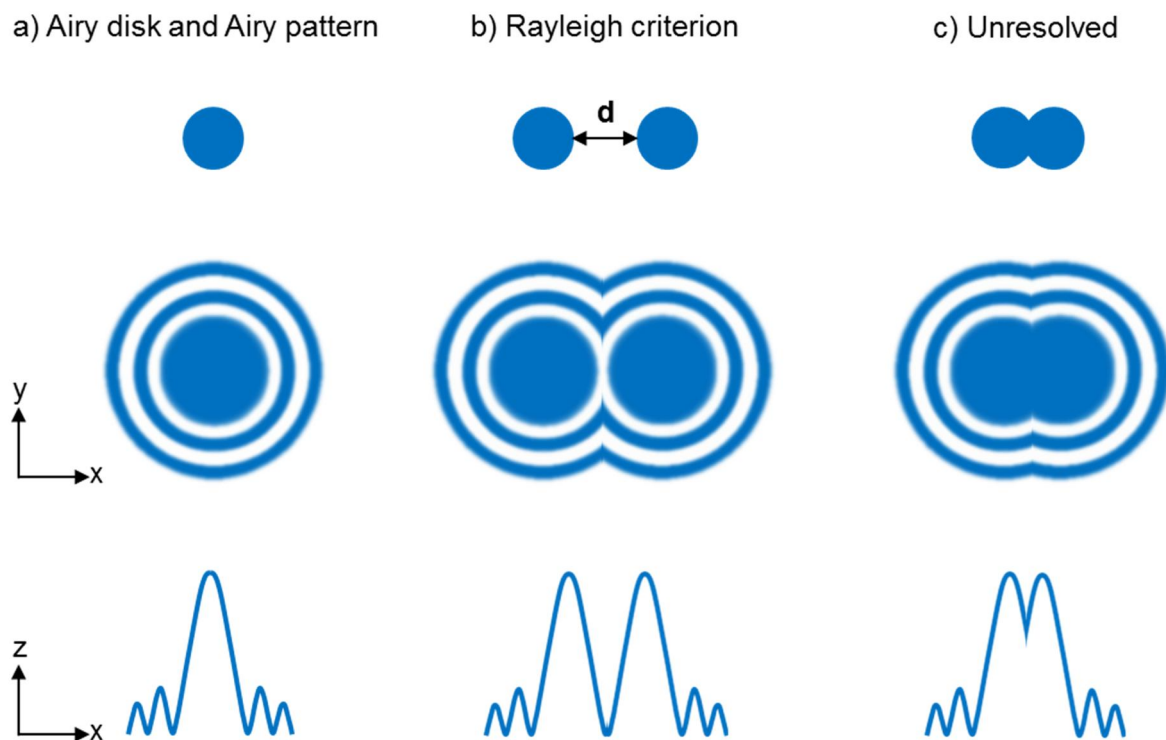


Figure 8: Resolution according to the Rayleigh criterion.

a) The lateral and axial profile of a pointlike emitter. The microscopic image is characterized by the Airy disk (bright region in the center) and the Airy pattern (concentric rings around the Airy disk). b) The resolution limit of two objects according to the Rayleigh criterion. c) Two unresolved objects. The Rayleigh criterion is not satisfied. Figure was adopted from Ishikawa-Ankerhold *et al.*, 2012 and modified.

According to the Rayleigh criterion, resolution in light microscopy is determined by the wavelength λ , the refractive index n between the focal plane and the objective lens, and the half angular aperture α of the used objective lens. The product of n and $\sin \alpha$ is described as numerical aperture (NA) and is a quality parameter of objectives. For oil objectives, the NA is usually around 1.4. Typical wavelengths applied in light microscopy are 400 - 600 nm. According to *Equation 1.1*, the lateral resolution is limited to ~ 200 nm. The axial resolution (z) is restricted to 500 - 700 nm (Schermelleh *et al.*, 2010). Thus, a spatial resolution of nanoparticles with diameters of 1 - 100 nm cannot be achieved by the use of conventional light microscopy methods.

$$d_{xy} = \frac{0.61 \cdot 400 \text{ nm}}{1.4} = \underline{174 \text{ nm}}$$

$$d_{xy} = \frac{0.61 \cdot 600 \text{ nm}}{1.4} = \underline{261 \text{ nm}}$$

1.4.2 Stimulated emission depletion (STED) microscopy

Super-resolution light microscopy techniques aim to compensate the pitfall of restricted resolution in light microscopy (Schermelleh *et al.*, 2010). Stimulated emission depletion (STED) microscopy is one of these techniques (Hell and Wichmann 1994). STED microscopy enables fluorescence microscopy with an improved lateral resolution. Its concept is based on a depletion of excited fluorophores in the s_1 state by stimulated emission. This process is induced by a second photon matching the energy gap between the s_1 and s_0 state. Excited electrons in the s_1 state that absorb such a photon relax to the s_0 state whereby the emission is stimulated. The wavelength of this stimulated emission is the same wavelength, which was used for de-excitation (Müller *et al.*, 2012). This fluorescence-free depopulation of the s_1 state is used to selectively switch off fluorophores in STED microscopy, thereby increasing the resolution by decreasing the focal spot size (Huang *et al.*, 2009). Photons of the longer STED wavelength, which are generated within the STED process, can be disregarded as they can be separated from the fluorescence signal (Figure 9).

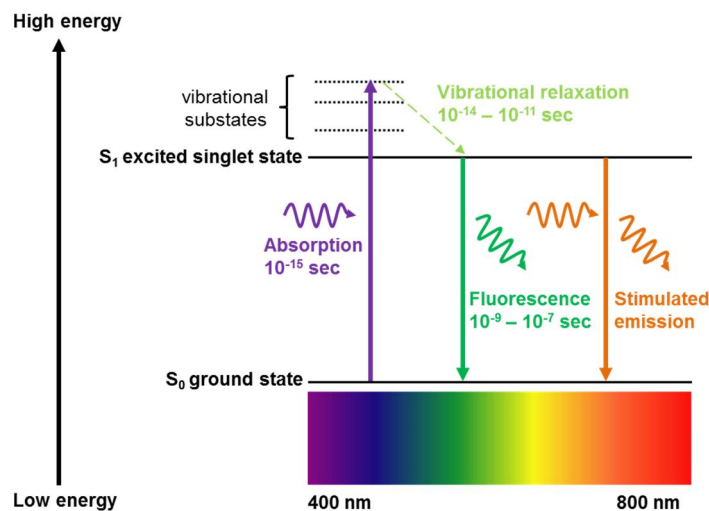


Figure 9: Jablonski diagram of spontaneous fluorescence and stimulated emission.

Fluorophores can absorb light, which forces electrons to their first excited state s_1 . The transition back to the electronic ground state occurs by energy loss due to the emission of fluorescence. A depopulation of the s_1 state by stimulated emission prevents the fluorophore from fluorescence emission. Figure was adapted from Müller *et al.*, 2012 and modified.

In the present study, a Leica TCS SP5 STED system (Leica, Germany) was used. In this setup, the STED module is implemented in a conventional confocal microscope. Two different technical systems are generally used. The continuous wave (CW) STED system is based on a continuous excitation and depletion of fluorophores (Willig *et al.*, 2007). Within this study, a STED microscope with pulsed excitation and depletion has been used. The STED process is realized by two lasers, i.e. an excitation and a depletion laser (Figure 10). The excitation beam is overlaid by a doughnut-shaped depletion beam, the STED beam, with a central intensity of zero. This overlay is realized by a phase plate creating a doughnut-shaped beam profile. Fluorophores in outer parts of the excitation focus are hit by the depletion beam (Müller *et al.*, 2012). Fluorophores in the center of the beam focus relax *via* spontaneous emission. The result is a sub-diffraction fluorescence spot with an improved lateral resolution. The whole specimen can be scanned using the STED mechanism resulting in a superior lateral resolution.

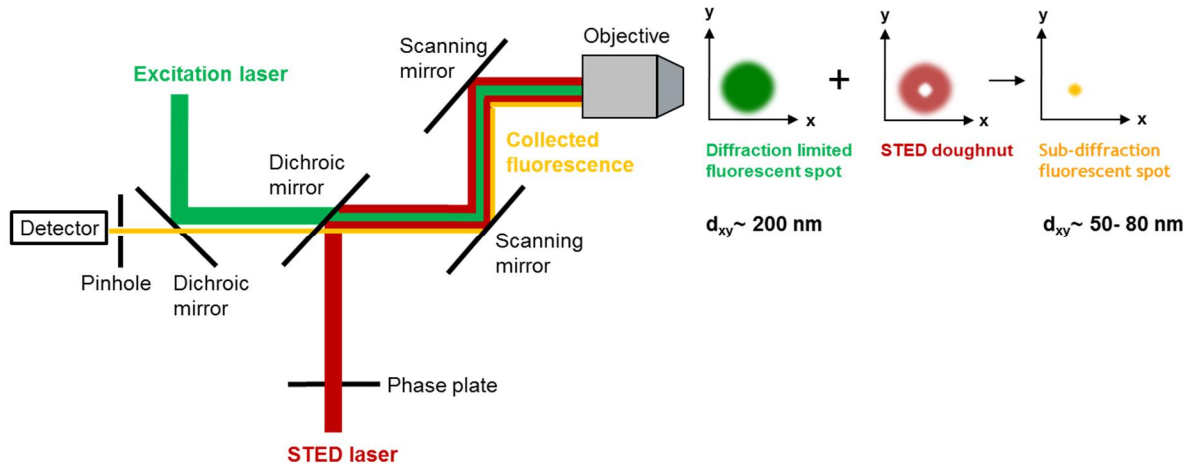


Figure 10: Beam path inside the STED microscope.

The excitation laser is overlaid by the STED laser beam, with a central intensity of zero. Thereby, a fluorescent spot with sub-diffraction lateral dimensions is generated. Commercial STED systems reach a lateral resolution of 50 - 80 nm. Figure was adapted from Müller *et al.*, 2012 and modified.

Equation 1.2 describes the resolution in STED microscopy and is an extension of the Abbe formula:

$$d_{xy} = \frac{\lambda}{2n \sin \alpha \sqrt{1 + \frac{I}{I_{sat}}}} = \frac{\lambda}{2NA \sqrt{1 + \frac{I}{I_{sat}}}} \quad (1.2)$$

Besides the wavelength λ and the NA, the lateral resolution in STED microscopy depends on the intensity I of the depletion beam and the saturation intensity I_{sat} , which describes the laser intensity needed to suppress the fluorescence to half of the original signal. I_{sat} depends on the used wavelength and also on the dye properties (Westphal and Hell 2005). Theoretically, an increase in the intensity of the depletion beam results in an infinitely enhanced lateral resolution. Special STED setups in combination with special probes have already shown a resolution down to 6 nm (Rittweger *et al.*, 2009). However, on fixed or living cell samples the xy-resolution has been shown to be 20 - 70 nm (Donnert 2006; Berning *et al.*, 2012). This limitation is due to the limited photostability of available fluorophores. High intensities of the STED beam can cause photobleaching (Dyba and Hell 2003), a chemical destruction of fluorophores upon excitation and thus a loss of fluorescence ability (Song *et al.*, 1995). Concepts to avoid photobleaching in STED microscopy have been described in the literature. They comprise the addition of chemical reagents, which shorten the lifetime of triplet states (Vogelsang *et al.*, 2008; Kasper *et al.*, 2010) or a change in the STED regime (Donnert 2006). Dyes suitable for STED microscopy exhibit a negligible $s_1 \rightarrow s_n$ absorption at the STED wavelength to avoid generation of higher excited states (Hotta *et al.*, 2010). Furthermore, the STED laser line should not overlap with the excitation spectrum of the dye to avoid a re-excitation of the fluorophores. This is given for Atto 647N, the dye used within the present study (Figure 11). Atto 647N is excitable at 635 nm and can be properly de-excited for STED purposes at 750 nm.

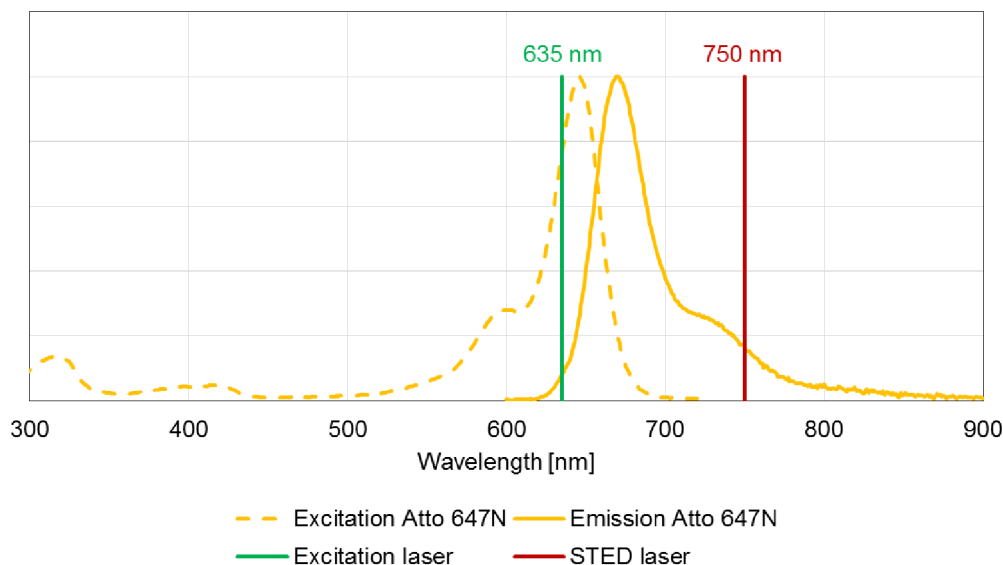


Figure 11: Excitation and emission of the STED-suitable dye Atto 647N.

Within this work, the fluorescent dye Atto 647N (Atto-Tec, Germany) was used for STED microscopy. The dye is excitable with a pulsed 635 nm laser and has its maximum emission at 647 nm. A de-excitation of the dye can be achieved with a pulsed 750 nm laser. Data sheets for excitation and emission spectra of Atto 647N were obtained from www.atto-tec.com and graphs were reproduced from these data.

STED microscopy comprises advantages from light microscopy, such as multiplex imaging, a highly specific staining, or live cell imaging, and additionally offers a superior resolution compared to conventional light microscopy methods. Thus, the application of STED microscopy exhibits a high potential for observing nanoparticle-cell interactions. Recent studies demonstrated the application of STED microscopy for the imaging of 32 nm and 83 nm silicon dioxide nanoparticles (Schübbe *et al.*, 2012) and nanoparticle agglomerates (Schübbe *et al.*, 2010) inside cells. However, the imaging of very small nanoparticles (< 20 nm) still needs to be realized by electron microscopy if resolution of single particles is needed.

1.4.3 Electron microscopy

In contrast to light microscopy, electron microscopy uses electrons for image generation and thus offers a much higher resolution. The superior resolution is attributed to the short wavelength of electrons that can be calculated from the de Broglie formula (Equation 1.3). Besides the constant factor h , the Planck constant, the wavelength λ is determined by v , the velocity of electrons, and m , the electrons mass. The mass of electrons is a function of their acceleration. Hence, highly accelerated electrons generate shorter wavelengths and finally increase the resolution in electron microscopy (Lickfeld 1979).

$$\lambda = \frac{h}{mv} \quad (1.3)$$

Basically, an electron microscope consists of an electron source, which generates electrons that are used for image formation (Aescht *et al.* 2010). The emitted, negatively charged electrons are accelerated by positively charged electrodes and form an electron beam, which is focused onto the sample by electromagnetic lenses. The resolution of electron microscopy can be below 1 nm, which is almost 1000-fold higher compared to light microscopy. Therefore, the use of electron microscopy

techniques can contribute to a more detailed visualization of nanoparticle-cell interactions (Schrand *et al.*, 2010; Nativo *et al.*, 2008).

Imaging by electron microscopy requires special sample preparations especially for biological specimen. Usually, imaging is carried out under vacuum conditions to avoid interactions of electrons with atoms of the atmosphere, which are usually present under environmental conditions (Aescht *et al.* 2010). Water evaporates at low vapor pressures, which introduces artefacts or even causes a destruction of non-dehydrated biological specimen. This circumstance requires a dehydration of biological specimen before imaging by electron microscopy. Usually, water is removed by critical point- or freeze-drying (Smith and Finke 1972; Gilkey and Staehelin 1986), or by air drying after treatment of the sample with fluids of low surface tension (Reville and Cotter 1991), e.g. hexamethyldisilazane (Braet *et al.*, 1997).

Electron microscopy has two major branches. In transmission electron microscopy (TEM), the electron beam penetrates the sample similarly to a light beam in an optical microscope. For biological specimen, an image is formed mainly due to absorption and scattering of the incident electrons by the sample. Thick parts of the sample as well as sample areas composed of elements with high atomic number absorb and scatter electrons to a higher extent than thinner parts or sample areas composed of elements of lower atomic number, and thus, they appear darker in the recorded image (mass thickness contrast) (Aescht *et al.* 2010). A prerequisite for TEM imaging is a sample, which is penetrable for the electron beam. Therefore, biological samples like cells are usually cut into sections, which involves an extensive sample preparation (Allen 2008). In scanning electron microscopy (SEM), the electron beam is scanned over the specimen surface and penetrates only a few μm into the sample. Interactions of the electron beam with the sample cause various signals that provide information concerning surface topography (secondary electrons) or chemical composition (backscattered electrons, characteristic X-rays) (Vernon-Parry 2000) (*Figure 12*). For investigating nanoparticle-cell interactions, secondary electrons can provide information concerning the cell surface or cell topography, whereas X-ray microanalyses allows an identification, localization, and quantification of elements (Allen 2008), such as cell-associated nanoparticles.

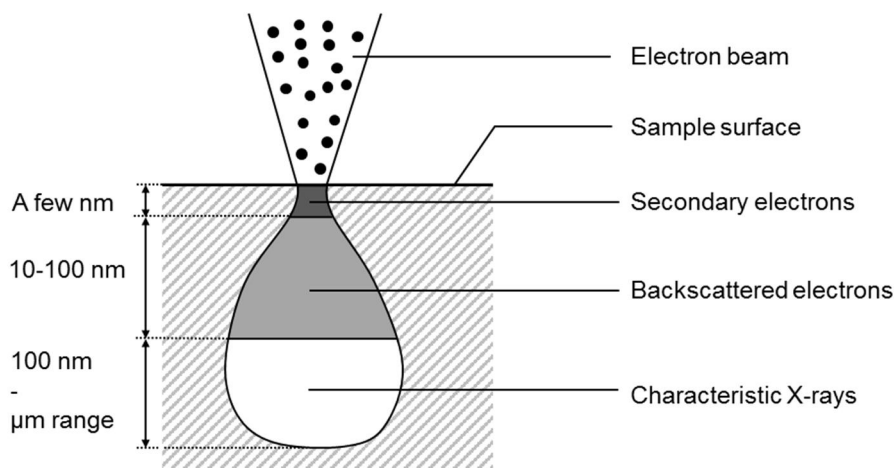


Figure 12: Interactions of the electron beam in SEM with the specimen surface.

Secondary electrons are generated within a few nm of the specimen surface and therefore can be used for describing the surface topography of a sample. Backscattered electrons derive from up to 100 nm below the specimen surface and indicate the sample composition. Characteristic X-rays derive from down to μm range below the scanned surface and can be used for precisely determining the chemical composition. Figure was adapted from Vernon-Parry 2000 and modified.

1.5 Objective of the thesis

The present study investigated the uptake, the intracellular location, and the transport of nanoparticles in human lung cells. Humans are exposed to nanoparticles in an increasing manner, which may lead to a nanoparticle uptake *via* inhalation. Therefore, impacts of nanoparticles on human lung cells are of great importance. Particles with sizes of 1 - 100 nm are mainly deposited in the alveolar region of the lung. Hence, the A549 cell line, a model for type II human lung alveolar epithelial cells, was chosen to study nanoparticle uptake and intracellular localization. Gold nanoparticles were used as particle system for different reasons. Firstly, gold nanoparticles allow for a wide range of detection techniques, such as electron microscopy. Secondly, gold particles are widely used within the biomedical sector, which requires special knowledge concerning cellular uptake and toxicity. Furthermore, gold nanoparticles can be chemically modified to guarantee particle stabilization and simultaneously allowing for a proper functionalization. In the present work, 3 nm, 8 nm, and 15 nm gold particles bearing a similar polymer shell were synthesized and labeled with Atto 647N, a fluorescent and STED-compatible dye. A549 cells were exposed to the different nanoparticles at concentrations close to real exposure scenarios and analyzed by confocal, STED, and electron microscopy. During these studies, the focus was on an active nanoparticle transport, which occurs along microtubules. In addition, the nanoparticle localization inside different cellular compartments, like the Golgi complex and the cell nucleus, was investigated. The cell morphology was analyzed to evaluate influences of nanoparticle exposure on human alveolar cells. Besides an extensive analysis by microscopy, the potential of the differently sized gold nanoparticles to affect cellular viability and cell proliferation was studied.

The second part of the work paid attention to a blebbing of A549 cells as a response to nanoparticle exposure. Live cell imaging was applied to visualize and characterize this cellular process. For this purpose, A549 pAcGFP1Mem cells, a stable cell line expressing a GFP-labeled membrane protein, was established.

The last part of the work comprised the application of correlative light and electron microscopy in nanoparticle studies. Confocal microscopy and TEM were used simultaneously to detect gold nanoparticles inside A549 cells. This approach allowed for a correlation of nanoparticle fluorescence observed by confocal microscopy and the number of gold nanoparticles detected by TEM.

1.6 References

- Aderem, A.; Underhill, D. M. (1999): Mechanisms of phagocytosis in macrophages. In *Annu. Rev. Immunol.* 17 (1), pp. 593–623.
- Aescht, E.; Büchl-Zimmermann, S.; Burmester, A.; Dänhardt-Pfeiffer, S.; Desel, C.; Hamers, C.; Jach, G.; Kässens, M.; Makovitzky, J.; Mulisch, M. (2010): Romeis Mikroskopische Technik [Elektronische Ressource]. 18th ed. Edited by Maria Mulisch, Erna Aescht, Benno Romeis, Barbara Nixdorf-Bergweiler, Detlef Pütz, Bernd Riedelsheimer *et al.* Heidelberg: Spektrum Akademischer Verlag.
- Alberts, Bruce; Wilson, John H. (2008): Molecular biology of the cell. 5th ed. New York: Garland Science.
- Alexandridis, P. (2011): Gold Nanoparticle Synthesis, Morphology Control, and Stabilization Facilitated by Functional Polymers. In *Chem. Eng. Technol.* 34 (1), pp. 15–28.
- Alivisatos, A. P.; Gu, W.; Larabell, C. (2005): Quantum dots as cellular probes. In *Annu. Rev. Biomed. Eng.* 7 (1), pp. 55–76.
- Allen, Terence D. (Ed.) (2008): Introduction to Electron Microscopy for Biologists: Elsevier (Methods Cell Biol.).
- Amos, W.; White, J. (2003): How the Confocal Laser Scanning Microscope entered Biological Research. In *Biol. Cell* 95 (6), pp. 335–342.
- Andreeva, A. V.; Kutuzov, M. A.; Voyno-Yasenetskaya, T. A. (2007): Regulation of surfactant secretion in alveolar type II cells. In *Am. J. Physiol. Lung Cell Mol. Physiol.* 293 (2), pp. L259.
- Anger, P.; Bharadwaj, P.; Novotny, L. (2006): Enhancement and Quenching of Single-Molecule Fluorescence. In *Phys. Rev. Lett.* 96 (11).
- Apopa, P. L.; Qian, Y.; Shao, R.; Guo, N. L.; Schwegler-Berry, D.; Pacurari, M.; Porter, D.; Shi, X.; Vallyathan, V.; Castranova, V.; Flynn, D. C. (2009): Iron oxide nanoparticles induce human microvascular endothelial cell permeability through reactive oxygen species production and microtubule remodeling. In *Part. Fibre Toxicol.* 6 (1), p. 1.
- Bangs, L. B. (1996): New developments in particle-based immunoassays: introduction. In *Pure & Appl. Chem.* 68 (10), pp. 1873–1879.
- Barlow, P. G.; Clouter-Baker, A.; Donaldson, K.; MacCallum, J.; Stone, V. (2005): Carbon black nanoparticles induce type II epithelial cells to release chemotaxins for alveolar macrophages. In *Part. Fibre Toxicol.* 2 (1), p. 11.
- Bartczak, D.; Nitti, S.; Millar, T. M.; Kanaras, A. G. (2012): Exocytosis of peptide functionalized gold nanoparticles in endothelial cells. In *Nanoscale* 4 (15), p. 4470.
- Berndt, H.; Haji, B. A.; Kowalczyk, J.; Pitsch, I.; Prüsse, U.: Method for selective carbohydrate oxidation using supported gold catalysts. Applied for by Südzucker Aktiengesellschaft Mannheim/Ochsenfurt. App. no. EP20040730988. Patent no. EP1631537 B1.
- Berning, S.; Willig, K. I.; Steffens, H.; Dibaj, P.; Hell, S. W. (2012): Nanoscopy in a Living Mouse Brain. In *Science* 335 (6068), p. 551.
- Boyer, D. (2002): Photothermal Imaging of Nanometer-Sized Metal Particles Among Scatterers. In *Science* 297 (5584), pp. 1160–1163.
- Braet, F.; Zanger, R. de; Wisse, E. (1997): Drying cells for SEM, AFM and TEM by hexamethyldisilazane: a study on hepatic endothelial cells. In *J. Microsc.* 186 (Pt 1), pp. 84–87.
- Brandenberger, C.; Mühlfeld, C.; Ali, Z.; Lenz, A.-G.; Schmid, O.; Parak, W. J.; Gehr, P.; Rothen-Rutishauser, B. (2010): Quantitative Evaluation of Cellular Uptake and Trafficking of Plain and Polyethylene Glycol-Coated Gold Nanoparticles. In *Small* 6 (15), pp. 1669–1678.
- Brook, R. D.; Rajagopalan, S.; Pope, C. A.; Brook, J. R.; Bhatnagar, A.; Diez-Roux, A. V.; Holguin, F.; Hong, Y.; Luepker, R. V.; Mittleman, M. A.; Peters, A.; Siscovick, D.; Smith, S. C.; Whitsel, L.; Kaufman, J. D. (2010): Particulate Matter Air Pollution and Cardiovascular Disease: An Update to the Scientific Statement From the American Heart Association. In *Circulation* 121 (21), pp. 2331–2378.
- Brust, M.; Fink, J.; Bethell, D.; Schiffrin, D. J.; Kiely, C. (1995): Synthesis and reactions of functionalised gold nanoparticles. In *J. Chem. Soc., Chem. Commun.* (16), p. 1655.
- Cai, W.; Gao, T.; Hong, H.; Sun, J. (2008): Applications of gold nanoparticles in cancer nanotechnology. In *Nanotechnol. Sci. Appl.* (1), pp. 17–32.
- Chang, M.-L.; Chen, J.-C.; Yeh, C.-T.; Chang, M.-Y.; Liang, C.-K.; Chiu, C.-T.; Lin, D.-Y.; Liaw, Y.-F. (2008): Gene Gun Bombardment with DNA-Coated Gold Particles Is a Potential Alternative to Hydrodynamics-Based Transfection for Delivering Genes into Superficial Hepatocytes. In *Hum. Gene Ther.* 19 (4), pp. 391–395.

- Chudakov, D. M.; Matz, M. V.; Lukyanov, S.; Lukyanov, K. A. (2010): Fluorescent Proteins and Their Applications in Imaging Living Cells and Tissues. In *Phy. Rev.* 90 (3), pp. 1103–1163.
- Clift, M. J.; Rothen-Rutishauser, B.; Brown, D. M.; Duffin, R.; Donaldson, K.; Proudfoot, L.; Guy, K.; Stone, V. (2008): The impact of different nanoparticle surface chemistry and size on uptake and toxicity in a murine macrophage cell line. In *Toxicol. Appl. Pharmacol.* 232 (3), pp. 418–427.
- Conklin, D. J. (2013): From lung to liver: How does airborne particulate matter trigger NASH and systemic insulin resistance? In *J. Hepatol.* 58 (1), pp. 8–10.
- Conner, S. D.; Schmid, S. L. (2003): Regulated portals of entry into the cell. In *Nature Nanotech.* 422.
- Connor, E. E.; Mwamuka, J.; Gole, A.; Murphy, C. J.; Wyatt, M. D. (2005): Gold Nanoparticles Are Taken Up by Human Cells but Do Not Cause Acute Cytotoxicity. In *Small* 1 (3), pp. 325–327.
- Daniel, M.-C.; Astruc, D. (2004): Gold Nanoparticles: Assembly, Supramolecular Chemistry, Quantum-Size-Related Properties, and Applications toward Biology, Catalysis, and Nanotechnology. In *Chem. Rev.* 104 (1), pp. 293–346.
- Dekkers, S.; Krystek, P.; Peters, R. J. B.; Lankveld, D. P. K.; Bokkers, B. G. H.; van Hoeven-Arentzen, P. H.; Bouwmeester, H.; Oomen, A. G. (2011): Presence and risks of nanosilica in food products. In *Nanotoxicology* 5 (3), pp. 393–405.
- Diesel, B.; Hoppstädter, J.; Hachenthal, N.; Zarbock, R.; Cavalius, C.; Wahl, B.; Thewes, N.; Jacobs, K.; Kraegeloh, A.; Kiemer, A. K. (2013): Activation of Rac1 GTPase by nanoparticulate structures in human macrophages. In *Eur. J. Pharmaceut. Biopharmaceut.* 84 (2), pp. 315–324.
- Doherty, G. J.; McMahon, H. T. (2009): Mechanisms of Endocytosis. In *Annu. Rev. Biochem.* 78 (1), pp. 857–902.
- Donaldson, K.; Poland, C. A. (2012): Inhaled nanoparticles and lung cancer - what we can learn from conventional particle toxicology. In *Swiss Med. Wkly.*
- Donaldson, K.; Poland, C. A.; Schins, R. P. F. (2010): Possible genotoxic mechanisms of nanoparticles: Criteria for improved test strategies. In *Nanotoxicology* 4 (4), pp. 414–420.
- Donnert, G. (2006): Macromolecular-scale resolution in biological fluorescence microscopy. In *Proc. Natl. Acad. Sci. USA* 103 (31), pp. 11440–11445.
- Dunn, K. W.; McGraw, T. E.; Maxfield, F. R. (1989): Iterative fractionation of recycling receptors from lysosomally destined ligands in an early sorting endosome. In *J. Cell Biol.* 109 (6), pp. 3303–3314.
- Dyba, M.; Hell, S. W. (2003): Photostability of a Fluorescent Marker Under Pulsed Excited-State Depletion through Stimulated Emission. In *Appl. Opt.* 42 (25), p. 5123.
- El-Fadel, M.; Massoud, M. (2000): Particulate matter in urban areas: health-based economic assessment. In *Sci. Total Environ.* 257 (133-146).
- European Union (20/10/2011): Commission recommendation of 18 October 2011 on the definition of nanomaterial. In *Official Journal of the European Union* (L 275), pp. 38–40.
- Farrer, R. A.; Butterfield, F. L.; Chen, V. W.; Fourkas, J. T. (2005): Highly Efficient Multiphoton-Absorption-Induced Luminescence from Gold Nanoparticles. In *Nano Lett.* 5 (6), pp. 1139–1142.
- Faulk, P. W.; Taylor, M. G. (1971): An immunocolloid method for the electron microscope. In *Immunochemistr.* 8, pp. 1081–1108.
- Ferin, J.; Oberdörster, G.; Soderholm, S. C.; Gelein, R. (1991): Pulmonary Tissue Access of Ultrafine Particles. In *J. Aerosol. Med.* 4 (1), pp. 57–68.
- Fletcher, D. A.; Mullins, R. D. (2010): Cell mechanics and the cytoskeleton. In *Nature* 463 (7280), pp. 485–492.
- Förster, T. (1948): Zwischenmolekulare Energiewanderung und Fluoreszenz. In *Ann. Phys.* 437 (1-2), pp. 55–75.
- Foster, K. A.; Oster, C. G.; Mayer, M. M.; Avery, M. L.; Audus, K. L. (1998): Characterization of the A549 Cell Line as a Type II Pulmonary Epithelial Cell Model for Drug Metabolism. In *Exp. Cell Res.* 243, pp. 359–366.
- Freese, C.; Gibson, M. I.; Klok, H.-A.; Unger, R. E.; Kirkpatrick, C. J. (2012): Size- and Coating-Dependent Uptake of Polymer-Coated Gold Nanoparticles in Primary Human Dermal Microvascular Endothelial Cells. In *Biomacromolecules* 13 (5), pp. 1533–1543.
- Freestone, I.; Meeks, N.; Sax, M.; Higgitt, C. (2007): The Lycurgus Cup – A Roman Nanotechnology. In *Gold Bulletin* 40 (4), pp. 270–277.
- Gebauer, J. S.; Malissek, M.; Simon, S.; Knauer, S. K.; Maskos, M.; Stauber, R. H.; Peukert, W.; Treuel, L. (2012): Impact of the Nanoparticle-Protein Corona on Colloidal Stability and Protein Structure. In *Langmuir* 28 (25), pp. 9673–9679.
- Gehr, P.; Bachofen, M.; Weibel, E. R. (1978): The Normal Human Lung: Ultrastructure and Morphometric Estimation of Diffusion Capacity. In *Resp. Physiol.* 32, pp. 121–140.

- Geiser, M. (2002): Morphological aspects of particle uptake by lung phagocytes. In *Microsc. Res. Tech.* 57 (6), pp. 512–522.
- Geiser, M.; Kreyling, W. G. (2010): Deposition and biokinetics of inhaled nanoparticles. In *Part. Fibre Toxicol.* 7 (1), p. 2.
- Geiser, M.; Rothen-Rutishauser, B.; Kapp, N.; Schürch, S.; Kreyling, W.; Schulz, H.; Semmler, M.; Im Hof, V.; Heyder, J.; Gehr, P. (2005): Ultrafine Particles Cross Cellular Membranes by Nonphagocytic Mechanisms in Lungs and in Cultured Cells. In *Environ. Health Perspect.* 113 (11), pp. 1555–1560.
- Gelfand, V. I. (1991): Microtubule dynamics: mechanism, regulation, and function. In *Annu. Rev. Cell Biol.* 7, pp. 93–116.
- George, G.; Hook, G. E. R. (1984): The Pulmonary Extracellular Lining. In *Environ. Health Perspect.* 55, pp. 227–237.
- Gheshlaghi, Z. N.; Riazi, G. H.; Ahmadian, S.; Ghafari, M.; Mahinpour, R. (2008): Toxicity and interaction of titanium dioxide nanoparticles with microtubule protein. In *Acta Bioch. Bioph. Sin.* 40 (9).
- Gilkey, J. C.; Staehelin, L. A. (1986): Advances in ultrarapid freezing for the preservation of cellular ultrastructure. In *J. Elec. Microsc. Tech.* 3 (2), pp. 177–210.
- Goodman, C. M.; McCusker, C. D.; Yilmaz, T.; Rotello, V. M. (2004): Toxicity of Gold Nanoparticles Functionalized with Cationic and Anionic Side Chains. In *Bioconjugate Chem.* 15 (4), pp. 897–900.
- Gu, Y.-J.; Cheng, J.; Lin, C.-C.; Lam, Y. W.; Cheng, S. H.; Wong, W.-T. (2009): Nuclear penetration of surface functionalized gold nanoparticles. In *Toxicol. Appl. Pharm.* 237 (2), pp. 196–204.
- Haagsman, H. P.; van Golde, L. M. G. (1991): Synthesis and Assembly of Lung Surfactant. In *Annu. Rev. Physiol.* 53 (1), pp. 441–464.
- Haller, T.; Ortmayr, J.; Friedrich, F.; Völkl, H.; Dietl, P. (1998): Dynamics of surfactant release in alveolar type II cells. In *Proc. Natl. Acad. Sci. USA* 95, pp. 1579–1584.
- Halperin, W. (1986): Quantum size effects in metal particles. In *Rev. Mod. Phys.* 58 (3), pp. 533–606.
- Hanson, P. I.; Cashikar, A. (2012): Multivesicular Body Morphogenesis. In *Annu. Rev. Cell Dev. Biol.* 28 (1), pp. 337–362.
- Hashim, Abbas A. (Ed.) (2012): The Delivery of Nanoparticles. Nanoparticles in Ancient Materials: The Metallic Lustre Decorations of Medieval Ceramics. With assistance of Philippe Sciau.
- Hawgood, S.; Clements, J. A. (1990): Pulmonary Surfactant and Its Apoproteins. In *J. Clin. Invest.* 86, pp. 1–6.
- Hell, S. W.; Wichmann, J. (1994): Breaking the diffraction resolution limit by stimulated emission: stimulated-emission-depletion fluorescence microscopy. In *Opt. Lett.* 19 (11), p. 780.
- Herrera, G.; Padilla, A.; Hernandez-Rivera, S. (2013): Surface Enhanced Raman Scattering (SERS) Studies of Gold and Silver Nanoparticles Prepared by Laser Ablation. In *Nanomaterials* 3 (1), pp. 158–172.
- Hotta, J.; Fron, E.; Dedecker, P.; Janssen, K. P. F.; Li, C.; Müllen, K.; Harke, B.; Bückers, J.; Hell, S. W.; Hofkens, J. (2010): Spectroscopic Rationale for Efficient Stimulated-Emission Depletion Microscopy Fluorophores. In *J. Am. Chem. Soc.* 132 (14), pp. 5021–5023.
- Huang, B.; Bates, M.; Zhuang, X. (2009): Super-Resolution Fluorescence Microscopy. In *Annu. Rev. Biochem.* 78 (1), pp. 993–1016.
- Huotari, J.; Helenius, A. (2011): Endosome maturation. In *EMBO J.* 30 (17), pp. 3481–3500.
- ISO/TS 27687:2008: Nanotechnologies -- Terminology and definitions for nano-objects -- Nanoparticle, nanofibre and nanoplate.
- ISO/TS 80004-1:2010: Nanotechnologies -- Vocabulary -- Part 1: Core terms.
- ISO/TS 80004-4:2011: Nanotechnologies -- Vocabulary -- Part 4: Nanostructured materials.
- Ishikawa-Ankerhold, H. C.; Ankerhold, R.; Drummen, G. P. C. (2012): Advanced Fluorescence Microscopy Techniques—FRAP, FLIP, FLAP, FRET and FLIM. In *Molecules* 17 (12), pp. 4047–4132.
- Jain, P. K.; Huang, X.; El-Sayed, I. H.; El-Sayed, M. A. (2007): Review of Some Interesting Surface Plasmon Resonance-enhanced Properties of Noble Metal Nanoparticles and Their Applications to Biosystems. In *Plasmonics* 2 (3), pp. 107–118.
- Jelveh, S.; Chithrani, D. B. (2011): Gold Nanostructures as a Platform for Combinational Therapy in Future Cancer Therapeutics. In *Cancers* 3 (4), pp. 1081–1110.
- Jong, W. H. de; Borm, P. J. A. (2008): Drug delivery and nanoparticles: Applications and hazards. In *Int. J. Nanomedicine* 3 (2), pp. 133–149.
- Kalluri, J. R.; Arbneshi, T.; Afrin Khan, S.; Neely, A.; Candice, P.; Varisli, B.; Washington, M.; McAfee, S.; Robinson, B.; Banerjee, S.; Singh, A. K.; Senapati, D.; Ray, P. C. (2009): Use of Gold Nanoparticles in a Simple Colorimetric and Ultrasensitive Dynamic Light Scattering Assay: Selective Detection of Arsenic in Groundwater. In *Angew. Chem.* 121 (51), pp. 9848–9851.

- Kasper, R.; Harke, B.; Forthmann, C.; Tinnefeld, P.; Hell, S. W.; Sauer, M. (2010): Single-Molecule STED Microscopy with Photostable Organic Fluorophores. In *Small* 6 (13), pp. 1379–1384.
- Kerr, M. C.; Teasdale, R. D. (2009): Defining Macropinocytosis. In *Traffic* 10 (4), pp. 364–371.
- Khubchandani, K. R. (2001): Surfactant protein A (SP-A): the alveolus and beyond. In *FASEB J.* 15 (1), pp. 59–69.
- Kingma, P. S.; Whitsett, J. A. (2006): In defense of the lung: surfactant protein A and surfactant protein D. In *Curr. Opin. Pharmacol.* 6 (3), pp. 277–283.
- Kirch, J.; Schneider, A.; Abou, B.; Hopf, A.; Schaefer, U. F.; Schneider, M.; Schall, C.; Wagner, C.; Lehr, C.-M. (2012): Optical tweezers reveal relationship between microstructure and nanoparticle penetration of pulmonary mucus. In *Proc. Natl. Acad. Sci. USA* 109 (45), pp. 18355–18360.
- Koenig, J. Q. (1999): Air pollution and asthma. In *J. Allergy Clin. Immunol.* 104, pp. 717–722.
- Kreyling, W. G.; Semmler, M.; Erbe, F.; Mayer, P.; Takenaka, S.; Schulz, H.; Oberdörster, G.; Ziesenis, A. (2002): Translocation of ultrafine insoluble iridium particles from lung epithelium to extrapulmonary organs is size dependent but very low. In *J. Toxicol. Environ. Health, Part A* 65 (20), pp. 1513–1530.
- Krug, H. F.; Wick, P. (2011): Nanotoxikologie - eine interdisziplinäre Herausforderung. In *Angew. Chem.* 123 (6), pp. 1294–1314.
- Kumar, Challa S. S. R. (2007): Biofunctionalization of nanomaterials. 1st ed. Weinheim: WILEY-VCH (Nanotechnologies for the life sciences, 1).
- Kumar, S.; Harrison, N.; Richards-Kortum, R.; Sokolov, K. (2007): Plasmonic Nanosensors for Imaging Intracellular Biomarkers in Live Cells. In *Nano Lett.* 7 (5), pp. 1338–1343.
- Labouta, H. I.; Hampel, M.; Thude, S.; Reutlinger, K.; Kostka, K.-H.; Schneider, M. (2012): Depth profiling of gold nanoparticles and characterization of point spread functions in reconstructed and human skin using multiphoton microscopy. In *J. Biophoton.* 5 (1), pp. 85–96.
- Lanone, S.; Rogerieux, F.; Geys, J.; Dupont, A.; Maillot-Marechal, E.; Boczkowski, J.; Lacroix, G.; Hoet, P. (2009): Comparative toxicity of 24 manufactured nanoparticles in human alveolar epithelial and macrophage cell lines. In *Part. Fibre Toxicol.* 6 (1), p. 14.
- Lenz, A.-G.; Karg, E.; Brendel, E.; Hinze-Heyn, H.; Maier, K. L.; Eickelberg, O.; Stoeger, T.; Schmid, O. (2013): Inflammatory and Oxidative Stress Responses of an Alveolar Epithelial Cell Line to Airborne Zinc Oxide Nanoparticles at the Air-Liquid Interface: A Comparison with Conventional, Submerged Cell-Culture Conditions. In *Biomed Res. Int.* 2013 (4), pp. 1–12.
- Lenz, A.; Karg, E.; Lentner, B.; Dittrich, V.; Brandenberger, C.; Rothen-Rutishauser, B.; Schulz, H.; Ferron, G. A.; Schmid, O. (2009): A dose-controlled system for air-liquid interface cell exposure and application to zinc oxide nanoparticles. In *Part. Fibre Toxicol.* 6 (1), p. 32.
- Lesniak, A.; Fenaroli, F.; Monopoli, M. P.; Åberg, C.; Dawson, K. A.; Salvati, A. (2012): Effects of the Presence or Absence of a Protein Corona on Silica Nanoparticle Uptake and Impact on Cells. In *ACS Nano* 6 (7), pp. 5845–5857.
- Lévy, R.; Shaheen, U.; Cesbron, Y.; Sée, V. (2010): Gold nanoparticles delivery in mammalian live cells: a critical review. In *Nano Rev.* 1 (0).
- Lichtman, J. W.; Conchello, J.-A. (2005): Fluorescence microscopy. In *Nat. Meth.* 2 (12), pp. 910–919.
- Lickfeld, Karl Gerhard (1979): Elektronenmikroskopie. Eine Einführung in die Grundlagen der Durchstrahlungs-Elektronenmikroskopie und ihrer Präparationstechniken. Stuttgart: Ulmer (Uni-Taschenbücher Biologie, Medizin, Physik, 965).
- Lieber, M.; Smith, B.; Szakal, A.; Nelson-Rees, W.; Todaro, G. (1976): A continuous tumor-cell line from a human lung carcinoma with properties of type II alveolar epithelial cells. In *Int. J. Cancer* 17 (1), pp. 62–70.
- Li, J. J.; Zou, L.; Hartono, D.; Ong, C.-N.; Bay, B.-H.; Lanry Yung, L.-Y. (2008): Gold Nanoparticles Induce Oxidative Damage in Lung Fibroblasts In Vitro. In *Adv. Mater.* 20 (1), pp. 138–142.
- Li, J.-L.; Gu, M. (2010): Gold-Nanoparticle-Enhanced Cancer Photothermal Therapy. In *IEEE J. Select. Topics Quantum Electron.* 16 (4), pp. 989–996.
- Lin, C.-A. J.; Sperling, R. A.; Li, J. K.; Yang, T.-Y.; Li, P.-Y.; Zanella, M.; Chang, W. H.; Parak, W. J. (2008): Design of an Amphiphilic Polymer for Nanoparticle Coating and Functionalization. In *Small* 4 (3), pp. 334–341.
- Li, Y.; Wu, P.; Xu, H.; Zhang, H.; Zhong, X. (2010): Anti-aggregation of gold nanoparticle-based colorimetric sensor for glutathione with excellent selectivity and sensitivity. In *Analyst* 136 (1), p. 196.
- Lodish, Harvey F. (2008): Molecular cell biology. 6th ed. New York, NY: Freeman.
- Luzio, J. P.; Pryor, P. R.; Bright, N. A. (2007): Lysosomes: fusion and function. In *Nat. Rev. Mol. Cell Biol.* 8 (8), pp. 622–632.

- Mallidi, S.; Larson, T.; Aaron, J.; Sokolov, K.; Emelianov, S. (2007): Molecular specific optoacoustic imaging with plasmonic nanoparticles. In *Opt. Express* 15 (11), pp. 6583–6588.
- Mayilo, S.; Kloster, M. A.; Wunderlich, M.; Lutich, A.; Klar, T. A.; Nichtl, A.; Kürzinger, K.; Stefani, F. D.; Feldmann, J. (2009): Long-Range Fluorescence Quenching by Gold Nanoparticles in a Sandwich Immunoassay for Cardiac Troponin T. In *Nano Lett.* 9 (12), pp. 4558–4563.
- Mercer, J.; Helenius, A. (2009): Virus entry by macropinocytosis. In *Nat. Cell Biol.* 11 (5), pp. 510–520.
- Mie, G. (1908): Beiträge zur Optik trüber Medien, speziell kolloidaler Metallösungen. In *Ann. Phys.* 330 (3), pp. 377–445.
- Mohanraj, V.; Chen, Y. (2006): Nanoparticles - A Review. In *Trop. J. Pharm. Res.* 5 (1), pp. 561–573.
- Monteiro-Riviere, N.; Inman, A.; Zhang, L. (2009): Limitations and relative utility of screening assays to assess engineered nanoparticle toxicity in a human cell line. In *Toxicol. Appl. Pharm.* 234 (2), pp. 222–235.
- Mühlfeld, C.; Gehr, P.; Rothen-Rutishauser, B. (2008): Translocation and cellular entering mechanisms of nanoparticles in the respiratory tract. In *Swiss Med. Wkly.* 138 (27-28), pp. 387–391.
- Mukherjee, S.; Ghosh, R. N.; Maxfield, F. R. (1997): Endocytosis. In *Physiol. Rev.* 77 (3), pp. 759–803.
- Müller, T.; Schumann, C.; Kraegeloh, A. (2012): STED Microscopy and its Applications: New Insights into Cellular Processes on the Nanoscale. In *ChemPhysChem* 13 (8), pp. 1986–2000.
- Nan, X.; Sims, P. A.; Chen, P.; Xie, X. S. (2005): Observation of Individual Microtubule Motor Steps in Living Cells with Endocytosed Quantum Dots. In *J. Phys. Chem. B* 109 (51), pp. 24220–24224.
- Nativo, P.; Prior, I. A.; Brust, M. (2008): Uptake and Intracellular Fate of Surface-Modified Gold Nanoparticles. In *ACS Nano* 2 (8), pp. 1639–1644.
- Nel, A. (2006): Toxic Potential of Materials at the Nanolevel. In *Science* 311 (5761), pp. 622–627.
- Nel, A. E.; Mädler, L.; Velegol, D.; Xia, T.; Hoek, E. M. V.; Somasundaran, P.; Klaessig, F.; Castranova, V.; Thompson, M. (2009): Understanding biophysicochemical interactions at the nano–bio interface. In *Trop. J. Pharm. Res.* 8 (7), pp. 543–557.
- Neuberger, M.; Schimek, M. G.; Horak, F.; Moshhammer, H.; Kundi, M.; Frischer, T.; Gomiscek, B.; Puxbaum, H.; Hauck, H. (2004): Acute effects of particulate matter on respiratory diseases, symptoms and functions. In *Atmos. Environ.* 38 (24), pp. 3971–3981.
- Oberdörster, G. (2001): Pulmonary effects of inhaled ultrafine particles. In *Int. Arch. Occup. Environ. Health* 74 (1), pp. 1–8.
- Oberdörster, G. (2010): Safety assessment for nanotechnology and nanomedicine: concepts of nanotoxicology. In *J. Intern. Med.* 267 (1), pp. 89–105.
- Oberdörster, G.; Ferin, J.; Lehnert, B. E. (1994): Correlation between Particle Size, In Vivo Particle Persistence, and Lung Injury. In *Environ. Health Perspect.* 102 (5).
- Paciotti, G. F.; Myer, L.; Weinreich, D.; Goia, D.; Pavel, N.; McLaughlin, R. E.; Tamarkin, L. (2004): Colloidal Gold: A Novel Nanoparticle Vector for Tumor Directed Drug Delivery. In *Drug Deliv.* 11 (3), pp. 169–183.
- Paino, I. M. M.; Marangoni, V. S.; Oliveira, R. C. S. de; Antunes, L. M. G.; Zucolotto, V. (2012): Cyto and genotoxicity of gold nanoparticles in human hepatocellular carcinoma and peripheral blood mononuclear cells. In *Toxicol. Lett.* 215 (2), pp. 119–125.
- Pan, Y.; Neuss, S.; Leifert, A.; Fischler, M.; Wen, F.; Simon, U.; Schmid, G.; Brandau, W.; Jahnen-Dechent, W. (2007): Size-Dependent Cytotoxicity of Gold Nanoparticles. In *Small* 3 (11), pp. 1941–1949.
- Patra, H. K.; Banerjee, S.; Chaudhuri, U.; Lahiri, P.; Dasgupta, A. K. (2007): Cell selective response to gold nanoparticles. In *Nanomed. Nanotech. Biol. Med.* 3 (2), pp. 111–119.
- Patton, J. S. (1996): Mechanisms of macromolecule absorption by the lungs. In *Adv. Drug Deliver. Rev.* 19, pp. 3–36.
- Pawley, James (2010): Handbook of Biological Confocal Microscopy. 3rd ed.: Springer-Verlag.
- Pernodet, N.; Fang, X.; Sun, Y.; Bakhtina, A.; Ramakrishnan, A.; Sokolov, J.; Ulman, A.; Rafailovich, M. (2006): Adverse Effects of Citrate/Gold Nanoparticles on Human Dermal Fibroblasts. In *Small* 2 (6), pp. 766–773.
- Piper, R. C.; Katzmann, D. J. (2007): Biogenesis and Function of Multivesicular Bodies. In *Annu. Rev. Cell Dev. Biol.* 23 (1), pp. 519–547.
- Pomogailo, Anatolii D.; Kestelman, Vladimir N. (2005): Metallopolymer Nanocomposites. Berlin, Heidelberg: Springer Berlin Heidelberg (Springer Series in Materials Science, 81).
- Reville, W. J.; Cotter, M. P. (1991): An Evaluation of the Usefulness of Air-Drying Biological Samples from Tetramethylsilane in Preparation for Scanning Electron Microscopy. In *J. Electron Microsc.* 40 (198-202).

- Rittweger, E.; Han, K. Y.; Irvine, S. E.; Eggeling, C.; Hell, S. W. (2009): STED microscopy reveals crystal colour centres with nanometric resolution. In *Nature Photon.* 3 (3), pp. 144–147.
- Ruan, G.; Agrawal, A.; Marcus, A. I.; Nie, S. (2007): Imaging and Tracking of Tat Peptide-Conjugated Quantum Dots in Living Cells: New Insights into Nanoparticle Uptake, Intracellular Transport, and Vesicle Shedding. In *J. Am. Chem. Soc.* 129 (47), pp. 14759–14766.
- Ruedas-Rama, M. J.; Walters, J. D.; Orte, A.; Hall, E. A. (2012): Fluorescent nanoparticles for intracellular sensing: A review. In *Anal. Chim. Acta* 751, pp. 1–23.
- Ruge, C. A.; Schaefer, U. F.; Herrmann, J.; Kirch, J.; Cañadas, O.; Echaide, M.; Pérez-Gil, J.; Casals, C.; Müller, R.; Lehr, C.-M.; Prow, T. W. (2012): The Interplay of Lung Surfactant Proteins and Lipids Assimilates the Macrophage Clearance of Nanoparticles. In *PLoS ONE* 7 (7), pp. e40775.
- Ruizendaal, L.; Bhattacharjee, S.; Pournazari, K.; Rosso-Vasic, M.; Haan, L. H. J. de; Alink, G. M.; Marcelis, A. T. M.; Zuilhof, H. (2009): Synthesis and cytotoxicity of silicon nanoparticles with covalently attached organic monolayers. In *Nanotoxicology* 3 (4), pp. 339–347.
- Saftig, P.; Klumperman, J. (2009): Lysosome biogenesis and lysosomal membrane proteins: trafficking meets function. In *Nat. Rev. Mol. Cell Biol.* 10 (9), pp. 623–635.
- Schermelleh, L.; Heintzmann, R.; Leonhardt, H. (2010): A guide to super-resolution fluorescence microscopy. In *J. Cell Biol.* 190 (2), pp. 165–175.
- Schmitz, G.; Müller, G. (1991): Structure and function of lamellar bodies, lipid-protein complexes involved in storage and secretion of cellular lipids. In *J. Lipid Res.* 32, pp. 1539–1570.
- Schrand, A. M.; Schlager, J. J.; Dai, L.; Hussain, S. M. (2010): Preparation of cells for assessing ultrastructural localization of nanoparticles with transmission electron microscopy. In *Nat. Protoc.* 5 (4), pp. 744–757.
- Schübbe, S.; Cavelius, C.; Schumann, C.; Koch, M.; Kraegeloh, A. (2010): STED Microscopy to Monitor Agglomeration of Silica Particles Inside A549 Cells. In *Adv. Eng. Mater.* 12 (5), pp. 417–422.
- Schübbe, S.; Schumann, C.; Cavelius, C.; Koch, M.; Müller, T.; Kraegeloh, A. (2012): Size-Dependent Localization and Quantitative Evaluation of the Intracellular Migration of Silica Nanoparticles in Caco-2 Cells. In *Chem. Mater.* 24 (5), pp. 914–923.
- Schulze, C.; Kroll, A.; Lehr, C.-M.; Schäfer, U. F.; Becker, K.; Schneidenburger, J.; Schulze Isfort, C.; Landsiedel, R.; Wohlleben, W. (2008): Not ready to use – overcoming pitfalls when dispersing nanoparticles in physiological media. In *Nanotoxicology* 2 (2), pp. 51–61.
- Schumann, C.; Schübbe, S.; Cavelius, C.; Kraegeloh, A. (2012): A correlative approach at characterizing nanoparticle mobility and interactions after cellular uptake. In *J. Biophoton.* 5 (2), pp. 117–127.
- Singh, N.; Manshian, B.; Jenkins, G. J.; Griffiths, S. M.; Williams, P. M.; Maffei, T. G.; Wright, C. J.; Doak, S. H. (2009): NanoGenotoxicology: The DNA damaging potential of engineered nanomaterials. In *Biomaterials* 30 (23-24), pp. 3891–3914.
- Singh, S.; Shi, T.; Duffin, R.; Albrecht, C.; Vanberlo, D.; Hohr, D.; Fubini, B.; Martra, G.; Fenogli, I.; Borm, P. (2007): Endocytosis, oxidative stress and IL-8 expression in human lung epithelial cells upon treatment with fine and ultrafine TiO₂: Role of the specific surface area and of surface methylation of the particles. In *Toxicol. Appl. Pharm.* 222 (2), pp. 141–151.
- Smijs, T.; Pavel (2011): Titanium dioxide and zinc oxide nanoparticles in sunscreens: focus on their safety and effectiveness. In *Nanotechnol. Sci. Appl.*, p. 95.
- Smith, M. E.; Finke, E. H. (1972): Critical point drying of soft biological material for the scanning electron microscope. In *Invest. Ophthalmol.* 11 (3), pp. 127–132.
- Soenen, S. J. H.; Nuytten, N.; Meyer, S. F. de; Smedt, S. C. de; Cuyper, M. de (2010): High Intracellular Iron Oxide Nanoparticle Concentrations Affect Cellular Cytoskeleton and Focal Adhesion Kinase-Mediated Signaling. In *Small* 6 (7), pp. 832–842.
- Song, L.; Hennink, E. J.; Young, I. T.; Tanke, H. J. (1995): Photobleaching kinetics of fluorescein in quantitative fluorescence microscopy. In *Biophys. J.* 68 (6), pp. 2588–2600.
- Sorkin, A.; Zastrow, M. von (2002): Signal transduction and endocytosis: close encounters of many kinds. In *Nat. Rev. Mol. Cell Biol.* 3 (8), pp. 600–614.
- Souza, G. R. (2006): Networks of gold nanoparticles and bacteriophage as biological sensors and cell-targeting agents. In *Proc. Natl. Acad. Sci. USA* 103 (5), pp. 1215–1220.
- Sperling, R. A.; Parak, W. J. (2010): Surface modification, functionalization and bioconjugation of colloidal inorganic nanoparticles. In *Phil. Trans. R. Soc. A* 368 (1915), pp. 1333–1383.

- Sperling, R. A.; Rivera Gil, P.; Zhang, F.; Zanella, M.; Parak, W. J. (2008): Biological applications of gold nanoparticles. In *Chem. Soc. Rev.* 37 (9), p. 1896.
- Stearns, R. C.; Paulauskis, J. D.; Godleski, J. J. (2001): Endocytosis of ultrafine particles by A549 cells. In *Am. J. Respir. Cell Mol. Biol.* 24 (2), pp. 108–115.
- Takenaka, S.; Karg, E.; Kreyling, W. G.; Lentner, B.; Möller, W.; Behnke-Semmler, M.; Jennen, L.; Walch, A.; Michalke, B.; Schramel, P.; Heyder, J.; Schulz, H. (2006): Distribution Pattern of Inhaled Ultrafine Gold Particles in the Rat Lung. In *Inhal. Toxicol.* 18 (10), pp. 733–740.
- Thielecke, N.; Prüße, U. (2007): Selektive Oxidation von Kohlenhydraten mit Goldkatalysatoren im kontinuierlichen Rührkessel. In *Chem-Ing-Tech* 79 (9), pp. 1456–1457.
- Thompson, D. T. (2007): Using gold nanoparticles for catalysis. In *Nano Today* 2 (4), pp. 40–43.
- Tkachenko, A. G.; Xie, H.; Coleman, D.; Glomm, W.; Ryan, J.; Anderson, M. F.; Franzen, S.; Feldheim, D. L. (2003): Multifunctional Gold Nanoparticle–Peptide Complexes for Nuclear Targeting. In *J. Am. Chem. Soc.* 125 (16), pp. 4700–4701.
- Unfried, K.; Albrecht, C.; Klotz, L.-O.; Mikecz, A. von; Grether-Beck, S.; Schins, R. P. (2007): Cellular responses to nanoparticles: Target structures and mechanisms. In *Nanotoxicology* 1 (1), pp. 52–71.
- Valiron, O.; Caudron, N.; Job, D. (2001): Microtubule dynamics. In *Cell. Mol. Life Sci.* 58, pp. 2069–2084.
- Vallhov, H.; Qin, J.; Johansson, S. M.; Ahlborg, N.; Muhammed, M. A.; Scheynius, A.; Gabrielsson, S. (2006): The Importance of an Endotoxin-Free Environment during the Production of Nanoparticles Used in Medical Applications. In *Nano Lett.* 6 (8), pp. 1682–1686.
- Vernon-Parry, K. (2000): Scanning electron microscopy: an introduction. In *III-Vs Review* 13 (4), pp. 40–44.
- Vogelsang, J.; Kasper, R.; Steinhauer, C.; Person, B.; Heilemann, M.; Sauer, M.; Tinnefeld, P. (2008): Ein System aus Reduktions- und Oxidationsmittel verringert Photobleichen und Blinken von Fluoreszenzfarbstoffen. In *Angew. Chem.* 120 (29), pp. 5545–5550.
- Wang, T.; Bai, J.; Jiang, X.; Nienhaus, G. U. (2012): Cellular Uptake of Nanoparticles by Membrane Penetration: A Study Combining Confocal Microscopy with FTIR Spectroelectrochemistry. In *ACS Nano* 6 (2), pp. 1251–1259.
- Warheit, D. B. (2008): How Meaningful are the Results of Nanotoxicity Studies in the Absence of Adequate Material Characterization? In *Toxicol. Sci.* 101 (2), pp. 183–185.
- Weaver, T. E.; Na, C.-L.; Stahlman, M. (2002): Biogenesis of lamellar bodies, lysosome-related organelles involved in storage and secretion of pulmonary surfactant. In *Semin. Cell Dev. Biol.* 13 (4), pp. 263–270.
- Westphal, V.; Hell, S. (2005): Nanoscale Resolution in the Focal Plane of an Optical Microscope. In *Phys. Rev. Lett.* 94 (14).
- Wijnhoven, S. W.; Peijnenburg, W. J.; Herberths, C. A.; Hagens, W. I.; Oomen, A. G.; Heugens, E. H.; Roszek, B.; Bisschops, J.; Gosens, I.; van de Meent, D.; Dekkers, S.; Jong, W. H. de; van Zijverden, M.; Sips, A. J.; Geertsma, R. E. (2009): Nano-silver – a review of available data and knowledge gaps in human and environmental risk assessment. In *Nanotoxicology* 3 (2), pp. 109–138.
- Willig, K. I.; Harke, B.; Medda, R.; Hell, S. W. (2007): STED microscopy with continuous wave beams. In *Nat. Meth.* 4 (11), pp. 915–918.
- Wörle-Knirsch, J. M.; Pulskamp, K.; Krug, H. F. (2006): Oops They Did It Again! Carbon Nanotubes Hoax Scientists in Viability Assays. In *Nano Lett.* 6 (6), pp. 1261–1268.
- Zhang, X.-D.; Guo, M.-L.; Wu, H.-Y.; Sun, Y.-M.; Ding, Y.-Q.; Feng, X.; Zhang, L.-A. (2009): Irradiation stability and cytotoxicity of gold nanoparticles for radiotherapy. In *Int. J. Nanomedicine* 4, pp. 165–173.
- Zhao, F.; Zhao, Y.; Liu, Y.; Chang, X.; Chen, C.; Zhao, Y. (2011): Cellular Uptake, Intracellular Trafficking, and Cytotoxicity of Nanomaterials. In *Small* 7 (10), pp. 1322–1337.

2. Interactions of 3 nm, 8 nm, and 15 nm gold particles with A549 cells

2.1 Introduction

The increasing exposure of humans to nanoparticles (1 - 100 nm) requires a detailed understanding of interactions of nanoparticles with potential target organs, tissues, and cells. Different routes for nanoparticle uptake into the human body have been described. Nanoparticles are capable to enter the human body *via* the lungs, the intestinal tract, the skin, and the olfactory nerve (Krug and Wick 2011). An uptake *via* inhalation is of special importance. The exposure of rats to fine (~250 nm) and ultrafine (~20 nm) TiO₂ and Al₂O₃ particles *via* inhalation to investigate a size-dependent effect of airborne particles on pulmonary uptake and lung injury, suggested a higher pulmonary uptake of UFP (Ferin *et al.*, 1991). Within follow-up studies, an accumulation of UFP inside the lung was shown to provoke inflammation (Oberdörster *et al.*, 1994). This was related to the high specific surface area, the greater interstitial access, and the altered biopersistence of UFP. Similar responses are expected to be also relevant for other types of engineered nanoparticles. Furthermore, a respiratory nanoparticle uptake is critical as the air-blood barrier in the alveolar region is very thin, i.e. 0.1 - 0.3 µm (Patton 1996). Nanoparticles, which are deposited in the alveoli might cross this barrier and enter the blood circulation. Once nanoparticles enter the vasculature, a transport to secondary organs can occur. *In vivo* experiments showed that after inhalation small fractions of inhaled UFP could be detected inside the liver (Brown *et al.*, 2002; Kreyling *et al.*, 2002), the spleen and heart (Kreyling *et al.*, 2002), or even in the nervous system (Oberdörster *et al.*, 2004; Oberdörster *et al.*, 2005). The translocation and accumulation of particles within secondary organs is assumed to cause side-effects, e.g. steatohepatitis (Conklin 2013). However, nanoparticles first have to reach the alveolar region of the lung. Based on a mathematic model it has been predicted that high amounts of small particles in a size range of 10 - 30 nm are deposited in the alveolar region (Oberdörster 2001). This is critical as for particles below a diameter of 20 - 30 nm non-bulk properties start to get prominent, influencing their chemical reactivity and intrinsic properties (Auffan *et al.*, 2009). Therefore, the potential deposition of particles <20 nm calls for a detailed analysis regarding the interactions of nanoparticles with cells from the alveolar region. Important aspects are uptake and accumulation of nanoparticles by these cells and a potential cytotoxic effect.

Many studies with a large array of nanoparticles and different types of alveolar cells have been conducted up to now (Park *et al.*, 2007; Lanone *et al.*, 2009). However, often these studies are not in accordance with real life exposure scenarios as very high nanoparticle concentrations are used. An alveolar deposition of nanoparticles is always restricted due to aerosol-physical limitations. From calculations it was assumed that maximally 2×10^{13} nanoparticles can be inhaled within one day by an adult human (Geiser and Kreyling 2010). Regarding the deposition within the alveolar epithelium, maximally 120 nanoparticles encounter alveolar epithelial surface cells per hour (Geiser and Kreyling 2010). Moreover, in literature reports nanoparticles have been used that are known to release toxic ions, like ZnO (Vandebriel and Jong 2012). Furthermore, nanoparticle stabilization agents or coatings can mediate cytotoxicity (Suresh *et al.*, 2012). Within the present study, differently sized gold nanoparticles are used at a realistic dose to investigate a potential effect on A549 cells, a model for type II human lung epithelial cells. Gold nanoparticles are an ideal system for studying size-dependent effects of nanoparticles on human cells. Firstly, "bulk gold" is generally regarded as non-toxic and biocompatible. Secondly, gold nanoparticles of different sizes can be synthesized with a

very high precision (Daniel and Astruc 2004). Furthermore, they can easily be stabilized by adsorption or chemical binding of ligands, for example thiols (Daniel and Astruc 2004; Sperling *et al.*, 2008), and functionalized, e.g. for imaging applications (Robinson and Vandr e 1997). Moreover, gold nanoparticles are promising agents for biomedical applications, such as photothermal cancer therapy (Cai *et al.*, 2008) or drug delivery (Jelveh and Chithrani 2011; Pissuwan *et al.*, 2011). Therefore, the impact of gold nanoparticles on human cells is of great importance with regard to safe therapy approaches that occasionally require higher particle doses than present in environmental exposure scenarios. *In vitro* studies have already shown that cells derived from the alveolar region are able to take up gold nanoparticles of different sizes and various stabilization agents (Brandenberger *et al.*, 2010). After uptake, gold nanoparticles were shown to be present inside vesicles (Chithrani *et al.*, 2006; Chithrani *et al.*, 2009), MVB (Jiang *et al.*, 2008), and lysosomes (Chithrani *et al.*, 2009). Accordingly, well-defined routes of endocytosis and endocytic transport seem to mediate nanoparticle uptake and intracellular transport (Zhao *et al.*, 2011). Intracellular transport of organelles or other cellular structures is mediated by the action of motor proteins along microtubules (Howard and Hyman 2003). Microtubules are involved in the transport of MVB and carrier vesicles to the perinuclear region, enabling fusion with late endosomes and lysosomes (Griffiths 1996; Clague 1998). However, only a few studies address the involvement of microtubules in the transport of inorganic nanoparticles (Nan *et al.*, 2005; Schumann *et al.*, 2012). Additionally, only little is known about a nanoparticle impact on the microtubule structure and function. Iron oxide nanoparticles were reported to induce a remodeling of microtubules in endothelial cells (Apopa *et al.*, 2009; Soenen *et al.*, 2010). TiO₂ nanoparticles were shown to interact with isolated microtubules and to inhibit microtubule polymerization (Gheslaghi *et al.*, 2008). To increase the knowledge of nanoparticle-microtubule interactions, this study aims to clarify a potential gold nanoparticle transport along microtubules and further focuses on the impact of nanoparticles on the microtubule structure and the cell viability. For this purpose, fluorescently labeled gold nanoparticles with sizes less than 20 nm were used as this value is generally seen as a threshold below which non-bulk properties occur ("nano-effects"). Gold nanoparticles of varying sizes were synthesized according to two different protocols. The particles were polymer-coated to allow for a comparison of the different particle sizes in cell experiments. Furthermore, to mimic exposure scenarios that are almost realistic for alveolar cells, less overload doses were used in comparison to examples from the literature. The uptake of 0.02 µg ml⁻¹ 3 nm (7.3 x 10¹⁰ particles), 8 nm (3.9 x 10⁹ particles), and 15 nm (5.9 x 10⁸ particles) gold particles by A549 cells was studied using super-resolution light microscopy and electron microscopy. STED microscopy was applied, which is known to overcome the diffraction limit of light microscopy (Hell and Wichmann 1994) and was shown to be applicable for the imaging of fluorescent nanoparticles inside cells (Sch ubbe *et al.*, 2010). The focus of the light microscopy analysis was on the intracellular distribution of the differently sized gold nanoparticles in relation to the tubulin cytoskeleton as well as on an impact of the particles on the morphology of A549 cells, especially on the microtubule structure and function. By using electron microscopy, an association of gold nanoparticles and microtubules was investigated with regard to a microtubule-mediated nanoparticle transport. Cell-based assays were carried out to evaluate nanoparticle toxicity as a function of particle size.

2.2 Experimental section

2.2.1 Gold nanoparticle synthesis

Gold particle synthesis was carried out by Dr. C. Cavelius. All chemicals were purchased from Sigma-Aldrich in the highest purity available. The fluorescent dye Atto 647N-NH₂ was purchased from Atto-Tec (Germany) and stored at -20°C prior to use. Ultrapure water with a resistivity of >18 MΩ cm⁻¹ was used for all preparation and purification steps.

3 nm gold particles were prepared according to the method described by Zheng *et al.* (Zheng *et al.*, 2006). Briefly, 0.2 g (0.4 mmol) AuPPh₃Cl were dissolved in 10 ml of chloroform, followed by the addition of 237 μl (1 mmol) dodecanthiol. Particle formation was induced by adding 0.34 g (3.91 mmol) tert-butylamino-borane complex under stirring. The mixture was stirred at room temperature overnight resulting in a red-orange dispersion of 3 nm gold particles.

8 nm gold particles were prepared according to the method described by Zheng (Zheng *et al.*, 2006). In brief, 0.31 g (0.63 mmol) AuPPh₃Cl and 313 μl (1.31 mmol) dodecanthiol were dissolved in 50 ml of toluene. After heating to 55°C, 0.54 g (6.25 mmol) tert-butylamine-borane were added under stirring. The mixture was reacted at 55°C for 60 min resulting in a dispersion of 8 nm gold particles.

The obtained 3 nm and 8 nm gold particles were precipitated with ethanol followed by centrifugation and dispersion in 10 ml cyclohexane. Hydrophilic gold nanoparticles were prepared using a modified phase transfer protocol described by Pellegrino *et al.* (Pellegrino *et al.*, 2004). For this purpose, 100 mg of the amphiphilic polymer poly (maleic anhydride-alt-1-octadecene) (PMAO), modified with mPEG750, were dissolved in 40 ml of water. 2 ml of lipophilic dodecanthiol-capped gold nanoparticles were added under stirring. The mixture was then emulsified for 5 min using an ultrasound disintegrator (Branson, 50% amplitude, 20 W output) and heated to 70°C to evaporate the solvent. Subsequent heating and ultrasonication yielded hydrophilic polymer-coated particles as a wine red transparent dispersion. The particles were purified by centrifugation (20,000 x *g*) and again dispersed in water. Purification was repeated two times to remove non-adsorbed polymer. The obtained dispersion was filtered into sterile falcon tubes using pyrogen-free 0.22 μm hydrophilic cellulose acetate membranes and kept sterile at 4°C. Modification of the polymer coated particles with Atto 647N dye was achieved through activation of carboxylate groups on the particle surface with N-(3-dimethylaminopropyl)-N'-ethylcarbodiimide (EDC) / N-hydroxysuccinimide (NHS) and further reaction with amine-modified Atto 647N-NH₂ (Atto-Tech, Germany). To obtain nanoparticles with sufficient fluorescence for imaging, an excess dye to nanoparticle ratio of 5,000: 1 was chosen. After labeling, the particles were isolated by centrifugation (20,000 x *g*) and dispersed in water. This step was repeated until no dye fluorescence could be detected in the supernatant (3 - 4 cycles).

15 nm sized gold particles were prepared according to the Frens method (Frens 1973). After addition of 2 ml of a 0.12 M trisodium citrate dehydrate solution to a boiling solution of 17 mg (0.05 mmol) HAuCl₄ in 200 ml water, monodisperse 15 nm gold particles were obtained after refluxing for further 30 min under stirring. The obtained nanoparticles were citrate-capped and had to be transferred into the non-polar phase to allow a similar modification of the gold surface with amphiphilic polymer as was achieved for 3 nm and 8 nm gold particles. For this purpose, 5 ml of freshly prepared gold suspensions were added to 5 ml of a 0.02 M octadecylamine solution under vigorous stirring according to a protocol described by Wang *et al.* (Wang *et al.*, 2010b). After 30 sec, 3 ml of cyclohexane were added to transfer the octadecylamine-capped gold particles into the non-polar phase. The aqueous phase was discarded and the nanoparticles were precipitated upon addition of ethanol and centrifugation (3,000 *g*, 30 min). The obtained particles are soluble in non-polar solvents

and were phase transferred using a similar protocol as described for the 3 nm and 8 nm gold particles.

2.2.2 Characterization of gold nanoparticles

Gold particle characterization was carried out by Dr. C. Cavalius. Freshly dialyzed and sterile filtered colloidal gold nanoparticle dispersions were used for characterization. The nanoparticle size, size distribution, and morphology were analyzed by TEM, using a Philips CM200 FEG (FEI Company, NL). Samples were prepared by drying the gold nanoparticle dispersions onto TEM grids.

Particle size distributions of TEM images were obtained using the free image analysis software ImageJ (<http://rsb.info.nih.gov/ij/>). In brief, after background subtraction and adjustment of brightness and contrast, the TEM images were converted into 8 bit binary images. Particle size analysis was performed by using the "analyze particle" tool, which counts the number of particles, determines the particle boundaries, and measures the Feret diameter. The gold concentration in aqueous dispersions was determined by inductively coupled plasma- optical emission spectroscopy (ICP-OES) with an Ultima 2 ICP-OES device (Horiba Jobin Yvon, Germany). A Cary 5000 spectrophotometer (Varian Inc., Germany) was used to record UV-Vis spectra of undiluted solutions in the range from 300 to 800 nm. Fluorescence spectra of diluted particle suspension in MilliQ water (1:100) at an excitation wavelength of 647 nm were recorded using a Spex FluoroMax-3 (HORIBA Scientific, Germany). To determine the hydrodynamic diameter of the particles in aqueous suspension by dynamic light scattering, a Dyna Pro Titan instrument (Wyatt Technology, Wyatt Technology Europe GmbH, Germany) with a laser wavelength of 831 nm was used. Prior to measurements, the gold nanoparticle suspensions were filtered through a sterile 0.22 μm cellulose acetate membrane and adjusted to a nanoparticle concentration of 0.1 nM. Zeta-potential measurements of the same suspensions were recorded using a Malvern Zetasizer Nano (Malvern, Germany).

2.2.3 Cell culture

The human lung carcinoma cell line A549 (ACC 107), a model for type II alveolar epithelial cells (Lieber *et al.*, 1976), was used within this study. The cells were obtained from the German Collection of Microorganisms and Cell Culture (DSMZ, Braunschweig, Germany). A549 cells were grown in Dulbecco's modified Eagle's medium (DMEM) (Gibco, Life Technologies, USA) supplemented with 10 % (v/v) fetal bovine serum (FBS) (PAN biotech, Germany). The cells were incubated in a humidified incubator (Binder, Germany) at 37 °C and under 9 % CO₂ atmosphere. Culture medium was replaced every two days. After reaching 80 % confluence, cell cultures were split using 0.05 % trypsin containing 0.02 % EDTA (PAN biotech, Germany). Trypsinized cells were separated by centrifugation (Centrifuge 5810 R, Eppendorf, Germany) at 200 x *g* and the cell concentration was determined using the CASY TT system (Innovatis, Roche, Germany). 3 x 10⁵ or 1 x 10⁶ cells were transferred into T25 flasks or T75 flasks, respectively. For experiments, cells from passage 6 - 30 were used.

2.2.4 Exposure of cells to gold nanoparticles and polymer

For microscopy analyses of gold nanoparticle and polymer uptake, A549 cells were grown on coverslips (#1.5, Menzel, ThermoFisher). Sterilized coverslips (20 min, 121°C) were placed into 12-well plates filled with 1 ml cell culture medium per well. DMEM without phenol red (PAN biotech, Germany) was used to avoid an excitation of residual phenol red during microscopy. 5 x 10⁴ cells were seeded into each well (3.9 cm²) and were allowed to attach for 20-24 h under cell culture

conditions before exposure to gold nanoparticles or the polymer. Dispersions of 3 nm, 8 nm, and 15 nm gold particles, each containing $0.02 \mu\text{g gold ml}^{-1}$, were prepared freshly prior to each experiment by diluting the nanoparticle stock dispersions in cell culture medium. A solution of the fluorescent polymer was prepared in the same way and a concentration of 7.31 mg ml^{-1} was adjusted. The preparations were mixed using a vortex mixer and 1 ml dispersion per well was added. The cells were exposed to gold nanoparticles and polymer for 5 h, 24 h, and 48 h under cell culture conditions and were subsequently stained for the respective cell structure.

2.2.5 Nocodazole treatment

To study microtubule-mediated nanoparticle transport, A549 cells were exposed to 8 nm gold particles as described in the section before. After 24 h, $10 \mu\text{M}$ nocodazole (Sigma) in dimethyl sulfoxide (DMSO) (PAN biotech, Germany) was added (adapted from Ying *et al.*, 2010). Cells were cultivated in the presence of nocodazole for 30 min and were subsequently stained for α -tubulin and the cell nucleus. In an additional experiment, nocodazole was removed after 30 min of incubation. For this purpose, cells were rinsed and further cultivated in cell culture medium for another hour to allow reformation of microtubules and thus a potential rearrangement of the internalized nanoparticles. As a control, A549 cells were exposed to 0.03 % (v/v) DMSO for 24 h to exclude an effect of the solvent itself onto the microtubule structure. After immunostaining, the intracellular distribution of the 8 nm gold particles was investigated by confocal microscopy.

2.2.6 Sample preparation for STED and confocal microscopy

2.2.6.1 Preparation of gold nanoparticles

3 nm, 8 nm, and 15 nm gold particles were imaged by confocal and STED microscopy to investigate their suitability for microscopy studies. For this purpose, coverslips with a thickness of 0.17 mm (#1.5, Menzel, ThermoFisher) were cleaned in oxygen plasma for 3 - 5 min. Subsequently, the coverslips were covered with $10 \mu\text{l}$ of 0.1 mg ml^{-1} poly-L-lysine hydrobromide (Sigma). After 15 min, the residual poly-L-lysine was aspirated. Nanoparticles were diluted in water (1:1,000 - 1:100,000) to adjust an appropriate density for microscopy. $10 \mu\text{l}$ of the nanoparticle dispersion were added onto the coverslips. After drying, the nanoparticles were mounted in Mowiol 4-88 (Roth, Germany), containing 2.5 % of the anti-bleaching reagent 1,4-Diazabicyclo[2.2.2]octane (DABCO) (Roth, Germany). Mowiol-DABCO was prepared according to the manufacturer's instructions and stored at $-20 \text{ }^\circ\text{C}$.

2.2.6.2 Preparation of A549 cells

A549 cells were stained with fluorescent dyes and antibodies to allow analyses by STED and confocal microscopy (*Table 2*). In brief, cells were rinsed with PBS and subsequently fixed using 4 % paraformaldehyde (PFA) or formaldehyde. Cells were permeabilized and prior to antibody labeling, blocking of unspecific antibody binding sites was carried out using bovine serum albumin (BSA). Microtubules and the Golgi complex were immunostained (*Table 3*). The nucleus was counterstained using Hoechst 33342 (Invitrogen, Life Technologies, USA), a DNA specific dye. Labeled cells were mounted in Mowiol 4-88 (Roth, Germany), containing 2.5 % anti-bleaching reagent DABCO (Roth, Germany), or in FluorSave (Calbiochem, Merck Millipore, Germany).

A stock solution of 40 % PFA (Roth, Germany) was prepared and stored up to six months at $-20 \text{ }^\circ\text{C}$. Ampoules of a 16 % formaldehyde solution (Electron microscopy science, UK) were stored at $4 \text{ }^\circ\text{C}$ and

were used for up to one week after opening. Stock solutions of primary antibodies were stored at -20 °C. The secondary antibody stock solution was stored at 4 °C. A Hoechst stock solution in H₂O (10 µg ml⁻¹) was prepared and stored at 4 °C. Labeling solutions were prepared freshly prior to use.

Table 2: Workflow for the staining of A549 cells for fluorescence microscopy.

Step	Treatment	Composition
1. Washing	3 x rinse, RT	137 mM NaCl (Roth, Germany) 2.7 mM KCl (Roth, Germany) 10 mM Na ₂ HPO ₄ (Roth, Germany) 1.8 mM KH ₂ PO ₄ (Merck, Germany) pH 7.4
2. Fixation	30 min, RT	4 % (v/v) Formaldehyde or 4 % (w/v) PFA in PBS
3. Washing	3 x rinse, RT	PBS
4. Permeabilization	15 min, RT	0.2 % (v/v) Triton X-100 (Roth, Germany) in PBS
5. Washing	3 x rinse, RT	PBS
6. Blocking	30 min, RT	5 % (w/v) BSA (AppliChem, Germany) in PBS
7. Primary antibody	1 h, RT or 4 °C overnight	Primary antibody (<i>Table 3</i>) 1 % (w/v) BSA in PBS
8. Blocking	4 x rinse, RT	1 % (w/v) BSA (AppliChem, Germany) in PBS
9. Secondary antibody	1 h, RT	Secondary antibody (<i>Table 4</i>) 1 % (w/v) BSA (AppliChem, Germany) in PBS
10. Washing	3 x rinse, RT	PBS
11. DNA stain	15 min, RT	500 ng ml ⁻¹ Hoechst 33342 1 % BSA (AppliChem, Germany) in PBS
12. Washing	3 x rinse, RT	PBS

Table 3: Primary antibodies.

Antibody	Target	Working concentration
Mouse anti- α -tubulin IgG (Invitrogen, Life Technologies, USA).	α -tubulin	1 µg ml ⁻¹
Mouse anti-GM 130 antibody (BD Transduction Laboratories, USA)	Golgi <i>cis</i> -compartment	1.25 µg ml ⁻¹

Table 4: Secondary antibodies.

Antibody	λ_{Ex} [nm]	λ_{Em} [nm]	Working concentration
Goat anti-mouse IgG Alexa 488 (Invitrogen, Life Technologies, USA)	495	519	3 µg ml ⁻¹

2.2.7 STED and confocal microscopy

2.2.7.1 Imaging of gold nanoparticles

Confocal and STED images of labeled gold nanoparticles were recorded using the Leica TCS SP5 STED system (Leica, Germany) with a 100 x / 1.4 oil immersion objective (HCX PL APO, Leica, Germany). The setup is based on a conventional confocal microscope complemented with the STED module. Confocal imaging of Atto 647N-labeled gold nanoparticles was performed using a 633 nm CW HeNe laser. For STED imaging, a pulsed 635 nm diode laser (PicoQuant, Germany) was used for excitation and a pulsed TiSa laser (Spectraphysics, USA) was used for depletion at 750 nm. A highly sensitive avalanche photodiode (APD) was used to detect the fluorescence of Atto 647N. For this purpose, a reflection short pass filter (RSP 630) was chosen from the x1-port settings to allow detection of light with wavelengths longer than 630 nm by the external APD. 8 bit images were recorded with a format of 512², a scan speed of 400 Hz, and an 8-fold frame average. The scans were performed in unidirectional mode. The pinhole diameter was set to 1 airy unit (AU). STED imaging was performed using pixel sizes of ~30 nm². Confocal images were recorded using the same pixel size. Intensity measurements of the recorded nanoparticles were performed in Fiji by plotting the intensity line profile of the nanoparticles (Schindelin *et al.*, 2012). For a better graphical visualization, the plot values were taken from Fiji and were further fitted in Origin using a Gauss fit for confocal and a Lorentz fit for STED measurements. The full width at half maximum (FWHM) values were calculated from the applied fits.

2.2.7.2 Imaging of A549 cells

To monitor the intracellular distribution of 3 nm, 8 nm, and 15 nm gold particles within A549 cells, z-stacks and images of representative cells were recorded using the aforementioned Leica TCS SP5 STED system. Excitation and fluorescence detection of the labeled gold nanoparticles was carried out as described in the previous section. Alexa 488-labeled structures were imaged using an argon laser line with an excitation wavelength of 488 nm. The emitted fluorescence was detected by a photomultiplier tube (PMT). The detection range was set from 500 nm to 600 nm and the pinhole diameter was set to 1 AU. For the imaging of Hoechst 33342 the pulsed 750 nm TiSa laser was used in multiphoton mode. A wavelength of 780 nm was adjusted to allow a two-photon excitation of the nucleus stain. For image acquisition the pinhole was opened completely. The emission light was detected by using a PMT and setting the detection range from 400 - 478 nm. All images and z-stacks were recorded sequentially. For confocal imaging, a z-step size of 130 nm and pixel sizes of 50 - 70 nm² were chosen, according to the Nyquist sampling theorem (Pawley 2010). 8 bit images were taken, with a format of 1024² or 2048², a scan speed of 200 Hz, and a frame average of 3 - 4. All scans were performed in unidirectional mode.

2.2.8 Widefield microscopy

The quantification of bleb formation and mitosis was carried out in widefield mode on a Leica TCS SP2 system (Leica, Mannheim, Germany) equipped with a mercury arc-lamp and a camera (ProgRes[®] C3, Jenoptik). Images were taken using a 10 x or 20 x dry objective. Cell numbers were counted manually by using the point tool and the ROI manager in Fiji.

2.2.9 Image processing and image analysis

Confocal and STED z-stacks were deconvolved by Huygens professional software (SVI, Netherlands) using the classic maximum likelihood estimation algorithm. Experimentally determined point spread functions (PSFs) were used for deconvolution. Confocal PSFs were recorded using 0.1 μm TetraSpeck microspheres (Invitrogen, Life Technologies, USA). For the generation of STED PSFs, FluoSpheres carboxylate-modified microspheres, 0.04 μm , dark red fluorescent (Invitrogen, Life Technologies, USA), were used. Recorded z-stacks of microspheres were processed in Huygens PSF distiller and the distilled PSF was used for deconvolution.

Fluorescence signals from gold nanoparticles and polymer, which were located inside the nucleus of A549 cells, were counted from recorded z-stacks by using the 3D objects counter plugin from the Fiji software package (Schindelin *et al.*, 2012). 3D volumes from z-stacks were reconstructed using Fiji's 3D volume viewer plugin. Orthogonal views and maximum intensity projections of z-stacks were prepared in Fiji. For illustration, the contrast of the images shown was enhanced.

2.2.10 Preparation of A549 cells for SEM and TEM

For SEM analyses, A549 cells were grown on silicon wafers. Silicon wafers exhibit a higher conductivity than glass coverslips and therefore were used for SEM imaging. Prior to use, a silicon wafer was cut into pieces fitting into wells of a 12-well plate. The prepared pieces were rinsed with water and sterilized at 180 °C for 3 h. For TEM imaging, A549 cells were directly grown on 300 mesh copper TEM grids covered with a carbon film (Electron microscopy science, UK). Prior to use, the TEM grids were disinfected by exposure to UV light for 30 min. The treated silicon wafers and TEM grids were placed into wells of a 12-well plate with a growth area of 3.9 cm^2 , filled with 1 ml culture medium, and were populated with 5×10^4 cells. The cells were allowed to attach for 20 - 24 h under cell culture conditions before exposure to gold nanoparticles. For SEM imaging, A549 cells were exposed to $2 \mu\text{g ml}^{-1}$ of non-fluorescent 8 nm gold particles for 4 h. For TEM, A549 cells were exposed to $50 \mu\text{g ml}^{-1}$ of non-fluorescent 8 nm gold particles for 24 h. A higher concentration of gold nanoparticles was applied due to the smaller field of view, which is given in SEM and TEM.

After exposure to nanoparticles, cytoskeleton whole mounts were prepared according to a modified protocol by Bell *et al.* (Bell *et al.*, 1987) to allow the visualization of the cytoskeleton of non-sectioned A549 cells. In brief, the cells were rinsed with PBS-A, lacking Ca^{2+} and Mg^{2+} , were treated with the detergent to extract detergent-soluble components and fixed according to the scheme stated in Table 5. All steps were carried out in a 12-well plate and a reaction volume of 1 ml.

Table 5: Workflow for the preparation of cytoskeletons whole mounts.

Step	Treatment	Solution	Composition
1.	3 x rinse, RT	PBS-A	137 mM NaCl (Roth, Germany) 3 mM KCl (Roth, Germany) 0.5 mM Na ₂ HPO ₄ (Roth, Germany) 1.5 mM KH ₂ PO ₄ (Merck, Germany) pH 7.4
2.	10 min, RT	TSB	0.5 % (v/v) Triton X-100 (Roth, Germany) in SB (composition see Table 6)
3.	2 x 5 min, RT	TSB	
4.	10 min, RT	ThSB	0.5 % (v/v) Triton X-100 (Roth, Germany) 250 mM [NH ₄] ₂ SO ₄ (Merck, Germany) in SB (composition see Table 7)
5.	2 x 5 min, RT	ThSB	
6.	15 min, RT	Fixative 1	4 % (v/v) Paraformaldehyde (Electron microscopy science, UK) in PBS-A
7.	2 x 5 min, RT	Glycine-PBS-A	0.1 M Glycine (Fluka) in PBS-A
8.	2 x 5 min, RT	PBS-A	
9.	30 min, RT	Fixative 2	2.5 % (v/v) Glutaraldehyde (Electron microscopy science, UK)
10.	Overnight, 4 °C		in wash buffer
11.	3 x rinse, RT	Wash buffer	0.1 M Sucrose (Roth, Germany) 0.1 M Sodium cacodylate trihydrate (Sigma) pH 7.2

Table 6: Composition of salt buffer.

Compound	Concentration
EDTA (Roth, Germany)	1 mM
PEG 2000 (Fluka)	2 %
HEPES (Roth, Germany)	100 mM
	pH 6.9

To compare whole mounts with non-treated cells, A549 cells grown on coverslips were rinsed with PBS, and fixed for 30 min at RT using 4 % (v/v) PFA in PBS.

Dehydration of the cells was carried out using an ethanol series with increasing concentration of ethanol, followed by a substitution with hexamethyldisilazane (HMDS) (Roth, Germany) (Nation 1983). The procedure is listed below. All steps were carried out in a 12-well plate at RT using a reaction volume of 1 ml.

- 30 % EtOH	10 min
- 50 % EtOH	10 min
- 70 % EtOH	10 min
- 80 % EtOH	10 min
- 90 % EtOH	10 min
- 96 % EtOH	10 min
- 99 % EtOH	2 x 15 min
- 99 % EtOH and HMDS, 1:1	15 min
- 100 % HMDS	2 x 15 min

After the complete evaporation of HMDS (approx. 1 h), the cells were transferred to a desiccator and stored until imaging.

2.2.11 SEM and TEM imaging of A549 cells

For SEM imaging of A549 cells exposed to gold nanoparticles an FEI Quanta 400 ESEM FEG (FEI Company, USA) was used. The silicon wafers were mounted on double sided carbon tape attached to aluminum stubs, fixed on a SEM sample holder, and investigated without any conductive coating under high vacuum conditions. The dried samples were analyzed at 293 K using secondary and back scattered electrons at different accelerating voltages. Conditions and detections modes used for imaging are indicated in the respective figure legends.

TEM imaging was carried out on a Philips CM200 FEG (FEI Company, NL) equipped with a MultiScan camera (Model 794, Gatan, USA) and an energy dispersive X-ray (EDX) spectrometer (EDAX DX-4/Phönix, Ametek, Germany) at 200 kV acceleration voltage. The TEM tilt angle series was recorded by tilting the sample holder from +30° to -28° in steps of 2°.

2.2.12 Cytotoxicity and cell proliferation assays

2.2.12.1 Cell seeding and exposure to nanoparticles

The WST-1 assay and the BrdU assay were applied to assess the influence of 3 nm, 8 nm, and 15 nm gold particles on A549 cells. For this purpose, 5×10^4 cells per well were seeded into 96-well plates. For the WST-1 assay transparent 96-well plates (Greiner Bio-One, Germany) were used. The BrdU assay was carried out in white 96-well plates with clear bottom (Greiner Bio-One, Germany). Each well was filled with 100 μ l culture medium (DMEM + 10 % FBS). DMEM without phenol red was used to avoid an influence of residual phenol red during the assay readout. The cells were allowed to attach for 20 - 24 h before exposure to gold nanoparticles. Gold nanoparticles were diluted in culture medium and dispersions of 0.02 μ g ml⁻¹, 0.2 μ g ml⁻¹, 2 μ g ml⁻¹ and 20 μ g ml⁻¹ were prepared. 100 μ l of dispersion were added to the respective wells and A549 cells were incubated in the presence of gold nanoparticles for 5 h, 24 h, and 48 h. After nanoparticle exposure, the cells were investigated by light microscopy (Axiovert 25, Carl Zeiss, Germany) and subsequently prepared for the respective assay.

2.2.12.2 WST-1 assay

For the evaluation of cellular viability, the cell metabolism reagent WST-1 (Roche, Germany) was used. The principle of this colorimetric assay is based on the conversion of the water soluble tetrazolium WST-1 by enzymes of the cellular respiratory chain. The resulting formazan can be detected by light absorption at 450 nm. The WST-1 assay was carried out according to the manufacturer's instruction. 10 µl of the WST-1 reagent were added to each well and the cells were incubated for 1 h. The absorption of the generated formazan was measured in a microplate reader (Spectramax 190, Molecular Devices). As a reference, the absorption at 750 nm was determined and subtracted from the absorption at 450 nm. Before addition of the WST-1 reagent, the background absorption of each plate was determined and subtracted from the values after WST-1 conversion. Thereby, a contribution of the gold nanoparticle absorption to the signal was prevented.

2.2.12.3 BrdU assay

To evaluate a potential inhibition of the cell proliferation due to nanoparticle exposure, the cell proliferation ELISA BrdU (Roche, Germany) was used. This assay is based on the incorporation of the thymidine analogue BrdU (5-bromo-2'-deoxyuridine) into the cell DNA during the cell cycle. The incorporated BrdU can be detected by antibodies conjugated with peroxidase. The peroxidase reaction with luminol results in a chemiluminescent signal that is proportional to the amount of BrdU incorporated and can be quantified by luminescence measurement. The BrdU assay was carried out according to the manufacturer's instruction. In brief, the cells were allowed to incorporate the BrdU reagent for 2 h. The subsequent antibody reaction was carried out for 2 h. After adding the substrate solution, the generated luminescence was determined using the Infinite M200 PRO plate reader (Tecan, Switzerland).

2.2.13 Assay data analysis

Data analysis of cell-based assays was performed in MS Office Excel using Student's *t*-test. An unpaired two-sample *t*-test was used for the determination of statistical significances of the data derived from the WST-1 and BrdU assay. All graphs were created using the KyPlot software or Origin.

2.3 Results

2.3.1 Characterization of fluorescently labeled gold nanoparticles

Gold nanoparticles of different sizes were synthesized by Dr. C. Cavellius according to two different protocols. The resulting particles were functionalized with a polymer to I) allow a comparison of gold nanoparticles from different synthesis routes regarding nanoparticle-cell interactions, II) to disperse the particles in a polar environment, such as cell culture medium, and III) to enable modifications needed for nanoparticle stability and dye coupling. In brief, dodecanthiol-capped gold nanoparticles or octadecylamine-capped gold particles were modified with the amphiphilic polymer poly (maleic anhydride-alt-1-octadecene) (PMAO) (Figure 13). The hydrophobic part of the polymer, the octadecen, interacted with the alkyl chains of alkylthiols or alkylamines, which were bound to the gold particle surface *via* van-der-Waals forces. Thereby, a covalent-like coupling of nanoparticles and polymer was achieved and the particles were phase transferred from nonpolar into polar environment. The PMAO was modified with mPEG750 to obtain a steric nanoparticle stabilization. Free carboxy groups of the polymer contributed to an electrostatic stabilization and were used for the labeling with the fluorescent dye Atto 647N. Hence, the gold nanoparticles became available for fluorescence microscopy.

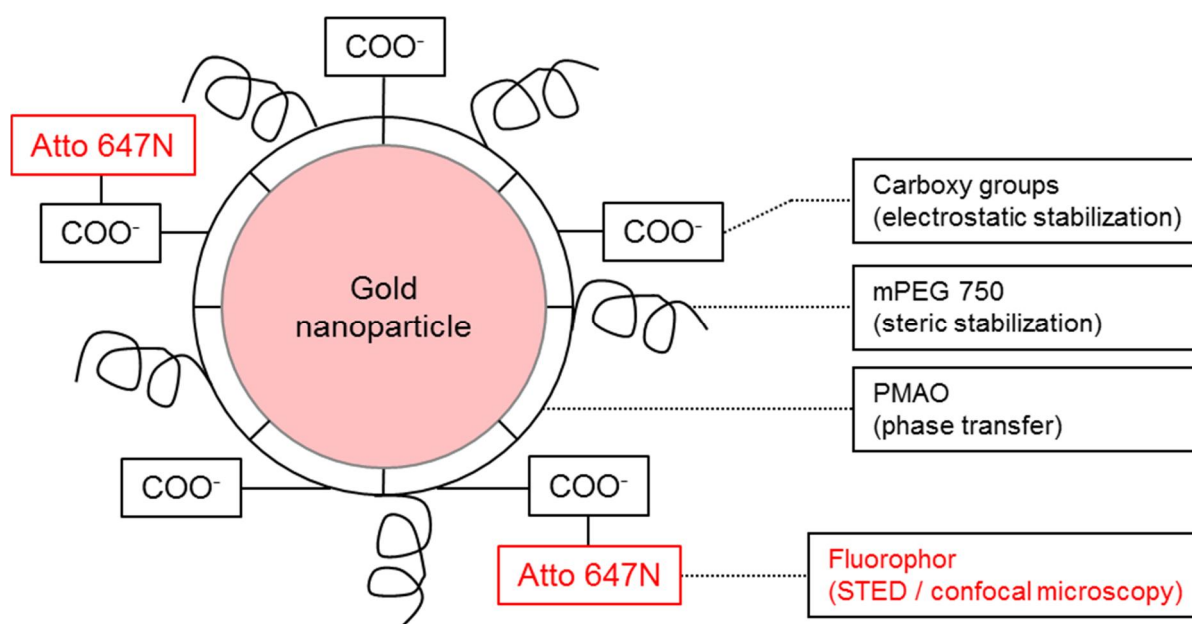


Figure 13: Structure of fluorescently labeled gold nanoparticles.

The hydrophobic residues of poly (maleic anhydride-alt-1-octadecene) (PMAO) were attached to the gold particle surface *via* alkylthiols or alkylamine linkers. The hydrophilic parts of PMAO pointed outwards and enabled a phase transfer from non-polar into polar medium. PMAO was modified with mPEG 750 to permit a sterical stabilization of the nanoparticles. Free carboxy groups on the polymer were used for coupling of the fluorescent dye Atto 647N *via* a peptide bond. Carboxy groups that remained after functionalization with Atto 647N provided an additional electrostatic stabilization of the gold nanoparticles.

TEM was used to monitor the morphology and size of the fluorescently labeled gold nanoparticles (Figure 14). The particles were roughly spherical with diameters of 3 nm, 8 nm, and 15 nm. Since the particles were separated and no significant agglomeration was observed, we conclude that the particles were well-stabilized.

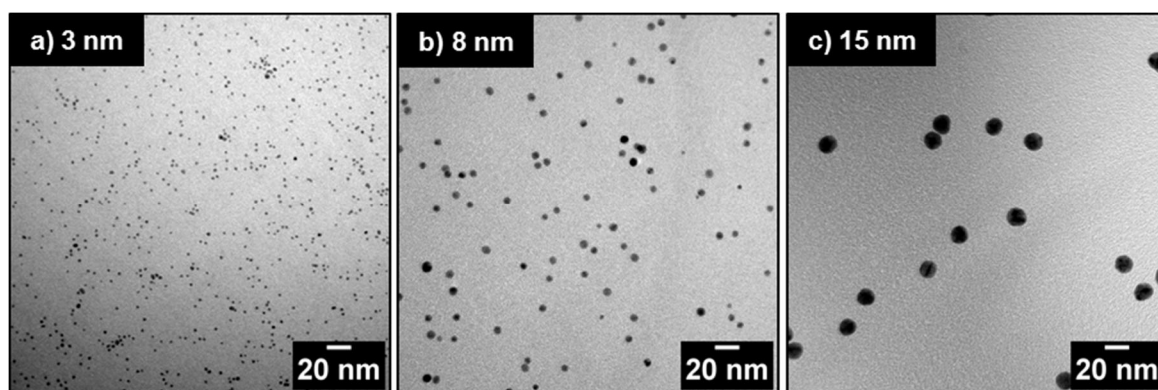


Figure 14: TEM images of fluorescently labeled gold nanoparticles with diameters of 3 nm, 8 nm, and 15 nm. a) 3 nm gold particles, b) 8 nm gold particles and c) 15 nm gold particles were dispersed in water and analyzed for their morphology by TEM. The particles exhibited a roughly spherical morphology. Images were recorded by Dr. Marcus Koch.

The physicochemical properties as well as the spectroscopic characteristics of the gold nanoparticles are stated in *Table 7*. Different batches of non-labeled and fluorescently labeled gold nanoparticles were used within the present study. Every parameter was determined at least once for each nanoparticle size. Fluorescently labeled gold nanoparticles were synthesized based on the respective batch of non-labeled particles. Using TEM analyses, the diameter of the gold cores was obtained. The data revealed nanoparticle sizes of 3 nm, 8 nm, and 15 nm with a narrow size distribution. The hydrodynamic diameter was determined from nanoparticles dispersed in water. The respective dynamic light scattering (DLS) measurements revealed a hydrodynamic diameter of 12 nm for the 3 nm and 8 nm gold particles. A hydrodynamic diameter of 40 nm was determined for the 15 nm gold particles. These higher values for the diameter were caused by the polymer that was used for nanoparticle stabilization and fluorescence labeling. The negative zeta potential reflected the surface functionalization of the nanoparticles that was used for particle stabilization. In general, colloidal systems are regarded as stable above and below a value of ± 30 mV (Mohanraj and Chen 2006). Hence, all three types of nanoparticles can be regarded as stable in water after phase transfer. From the nanoparticle mass concentration, determined by inductively coupled plasma optical emission spectrometry (ICP-OES) and the TEM diameter, the molar particle concentration was calculated. Additionally, absorption spectra of the gold nanoparticles were measured. The 3 nm, 8 nm, and 15 nm gold particles exhibited absorption maxima at 512 nm, 520 nm, and 523 nm, respectively. These can be attributed to the surface plasmon resonance of gold nanoparticles, which is highly dependent on the nanoparticle diameter (Daniel and Astruc 2004). The absorption maxima did not significantly shift after dispersion of the particles in cell culture medium, indicating particle stability under these conditions. The fluorescently labeled particle batches additionally showed an absorption at 647 nm, the extinction maximum of Atto 647N, the dye coupled to the nanoparticles surface. The emission maximum of the dye was determined at 660 - 665 nm.

Table 7: Physico-chemical and spectroscopic properties of 3 nm, 8 nm, and 15 nm gold particles.

Different batches of nanoparticles were indicated by 1 and 2. L indicates the fluorescently labeled batches. ND: not determined. All parameters were determined in H₂O by Dr. C. Cavelius.

Batch	d _{TEM} [nm]	d _{hyd} [nm]	Zeta potential [mV]	Gold concentration [μg ml ⁻¹]	Particle concentration [nM]	Particle concentration [particles ml ⁻¹]	Abs _{max} [nm]	λ _{Ex} [nm]	λ _{Em} [nm]
3 nm-1	2.7 ± 0.7	12.8 ± 2.0	-58.2	249.1	2,077	1.3 × 10 ¹⁵	512	-	-
3 nm-1 L	2.5 ± 0.8	12.2 ± 1.8	-30.8	150.8	1,584	9.5 × 10 ¹⁴	512	647	661
3 nm-2	2.9 ± 0.2	ND	ND	170.6	1,148	6.9 × 10 ¹⁴	512	-	-
3 nm-2 L	2.6 ± 0.5	ND	ND	136.0	1,270	7.7 × 10 ¹⁴	512	647	662
8 nm-1	8.0	12.8 ± 1.6	-55.9	215.0	69	4.2 × 10 ¹³	519	-	-
8 nm-1 L	7.6 ± 1.5	ND	ND	215.0	80	4.8 × 10 ¹³		647	665
8 nm-2	8.1 ± 0.7	ND	ND	2,902.0	896	5.4 × 10 ¹⁴	520	-	-
8 nm-2 L	8.4 ± 0.5	13.2 ± 4.8	-49.7	963.0	267	1.6 × 10 ¹⁴	520	647	663
15 nm-1	15.0 ± 1.9	41.0 ± 7.0	-42.2	22.0	1	6.4 × 10 ¹¹	525	-	-
15 nm-1 L	ND	40.2 ± 5.0	-59.5	29.5	ND			647	660
15 nm-2	ND	44.2 ± 5.2	-43.1	234.1	ND		523	-	-
15 nm-2 L	12.7 ± 1.3	ND	ND	407.0	33	2 × 10 ¹³	522	647	661

Recorded fluorescence spectra indicated a different Atto 647N labeling density of 3 nm, 8 nm, and 15 nm gold particles (Table 8). For 3 nm gold particles a value of 8.06×10^{-8} fluorescence counts per particle was calculated. This was 3.4 times less than the value calculated for 8 nm gold particles (2.73×10^{-7} counts per particle), and 2.1 times less fluorescence per particle compared to the 15 nm gold particles (1.69×10^{-7} counts per particle). The calculated values were similar between different batches of labeled gold nanoparticles.

Table 8: Fluorescence labeling density of 3 nm, 8 nm, and 15 nm gold particles.

The measured fluorescence of Atto 647N was divided by the number of particles. The resulting fluorescence per particle indicated a different labeling density of the gold nanoparticles.

Batch	Fluorescence intensity [counts ml ⁻¹]	Number of particles [ml ⁻¹]	Fluorescence per particle [counts particle ⁻¹]
3 nm-2 L	4×10^5	4.96×10^{12}	8.06×10^{-8}
8 nm-2 L	5×10^5	1.83×10^{12}	2.73×10^{-7}
15 nm-2 L	2×10^4	1.18×10^{11}	1.69×10^{-7}

2.3.2 Confocal and STED microscopy of fluorescently labeled gold nanoparticles

Three batches of fluorescently labeled gold nanoparticles (3 nm-2 L, 8 nm-2 L, 15 nm-2 L) were analyzed by confocal and STED microscopy to ensure their suitability for fluorescence microscopy. The 8 nm gold particles, which exhibited the highest labeling density of Atto 647N, were successfully analyzed by confocal and STED microscopy (Figure 15). The confocal (Figure 15a) and the STED image (Figure 15b) revealed the same pattern of fluorescence signals. However, the STED image was recorded initially and apparently, some fluorescence signals suffered from bleaching and were not detectable anymore in the subsequently recorded confocal image. One spot was chosen from the recorded image and illustrated with increased magnification (Figure 15c, d). Intensity profiles of this spot were derived from STED and confocal images (Figure 15e, f). A FWHM of 380 nm was calculated from the confocal image. This FWHM_{conf} value was larger than the theoretical optical lateral resolution of confocal microscopy that can be calculated for the given conditions according to the Rayleigh criterion (Pawley 2010), whereas λ is the excitation wavelength of the used fluorophore (Atto 647N) and NA the numerical aperture of the objective that was used (100 x / 1.4):

$$R_{conf} = \frac{0.61 * \lambda}{NA} = \frac{0.61 * 635 \text{ nm}}{1.4} = 277 \text{ nm}$$

The larger FWHM value potentially indicates that the nanoparticles formed particle agglomerates during preparation for microscopy. Presumably, the detected fluorescence spot consisted of numerous single nanoparticles. Nevertheless, a STED effect could be demonstrated as illustrated in Figure 15f. The measured FWHM_{STED} of 150 nm was significantly below the FWHM_{conf} of 380 nm. But also in this case, the resolution was lower than the one that has been achieved using latex beads (Schübbe *et al.*, 2010). For the used Leica TiSa STED microscope a lateral resolution of ~ 90 nm was determined. A small portion of the imaged gold nanoparticles, potentially single particles or nanoparticles carrying less fluorophores, suffered from bleaching. A calculation of the FWHM of these weaker fluorescent spots was not possible due to the insufficient signal-to-noise ratio. Thus, the particle labeling might hampers a better resolution. However, 8 nm gold particles turned out to be suited for confocal and STED microscopy.

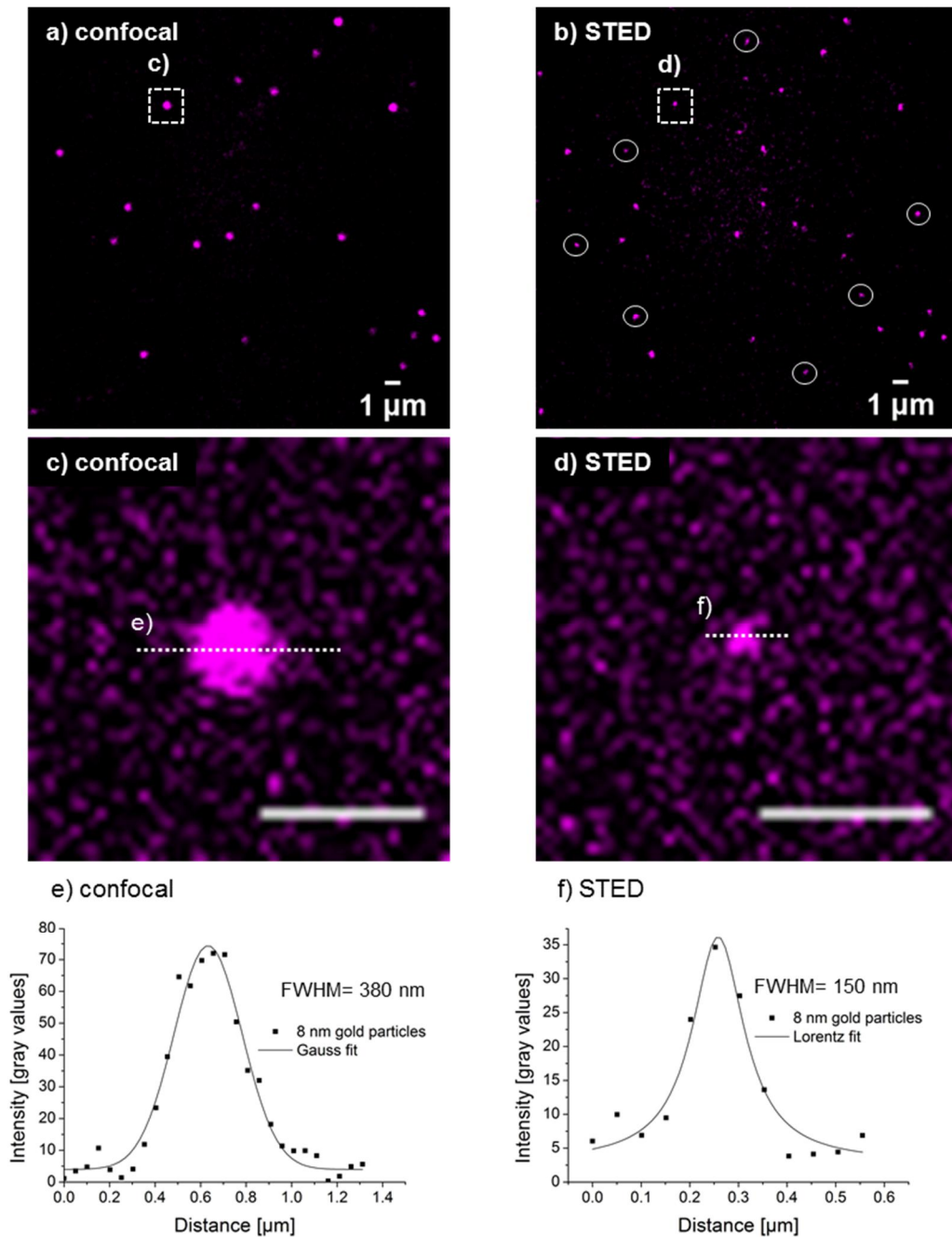


Figure 15: Confocal and STED microscopy of fluorescently labeled 8 nm gold particles.

a) Confocal and b) STED image of 8 nm gold particles (8 nm-2L). The synthesized nanoparticles were STED-compatible, although some detected fluorescence signals suffered from bleaching and were not present in the confocal image anymore (see circles). The STED image was recorded firstly. c) Magnified image of one fluorescence spot imaged in confocal mode (see rectangle). d) Magnified image of the same fluorescence spot imaged in STED mode (see rectangle). Scale bar: 1 μm . e)

Intensity profile of the fluorescence spot shown in c). An FWHM of 380 nm was calculated. f) Intensity profile of the fluorescence spot shown in d). An FWHM of 150 nm was calculated. Figure a) and b) were smoothed and background was removed. Figure c) and d) are raw data. The contrast of the images was enhanced.

15 nm gold particles were also analyzed by confocal and STED microscopy (Figure 16). The recorded confocal (Figure 16a) and STED image (Figure 16b) showed less and much dimmer fluorescence spots compared to the 8 nm gold particles sample. This can be related to a lower number of nanoparticles in the sample and the weaker fluorescence per nanoparticle, which was calculated for 15 nm gold particles (Table 8). From the recorded image, a bright fluorescence signal was chosen and illustrated with increased magnification (Figure 16c, d). Intensity measurements on this spot were carried out in

STED and confocal mode (*Figure 16e, f*). An FWHM of 370 nm was calculated from the confocal measurement, which is in accordance with the FWHM of 380 nm determined for the 8 nm gold particles imaged in confocal mode. However, the theoretical optical lateral resolution of 277 nm, which was determined on the basis of the Rayleigh criterion, was also not achieved. The imaged fluorescent spot consisted of more than one nanoparticle and therefore does not allow for further resolution. Nevertheless, by the use of STED microscopy, an increased lateral resolution of the fluorescence signal was achieved as shown in the recorded image (*Figure 16d*) and the respective intensity profile (*Figure 16f*). From the applied Lorentz fit an FWHM of 170 nm was determined, which was in accordance with the FWHM of 150 nm, calculated for the 8 nm gold particles imaged in STED mode. A comparison of the intensity line profiles of the 8 nm gold particles (*Figure 15e, f*) and the 15 nm gold particles (*Figure 16e, f*) revealed lower maximum peak intensities for the 15 nm gold particles. This can be attributed to less Atto 647N dye on the particle surface (*Table 8*). In the course of fluorescence measurements, 8 nm gold particles gave 2.73×10^{-7} counts per particle, whereas for 15 nm gold particles a value of 1.69×10^{-7} counts per particle was determined. Even an agglomeration of 8 nm and 15 nm gold particles, as observed by confocal and STED microscopy, might cause different intensities of the fluorescence spots. Due to the lower labeling density of the 15 nm gold particles, the signal-to-noise ratio was lower and the applied Gauss and Lorentz fit did not matched perfectly.

A comparison of confocal and STED imaging of 3 nm gold particles was not reliably conductible under the applied conditions. With 8.06×10^{-8} counts per particle, the fluorescence signal was weak and therefore single nanoparticles were hardly detectable and distinguishable from noise. For the 8 nm gold particles 2.73×10^{-7} counts per particle were determined, which is approx. three times higher. Therefore, it was not possible to apply STED microscopy on 3 nm gold particles.

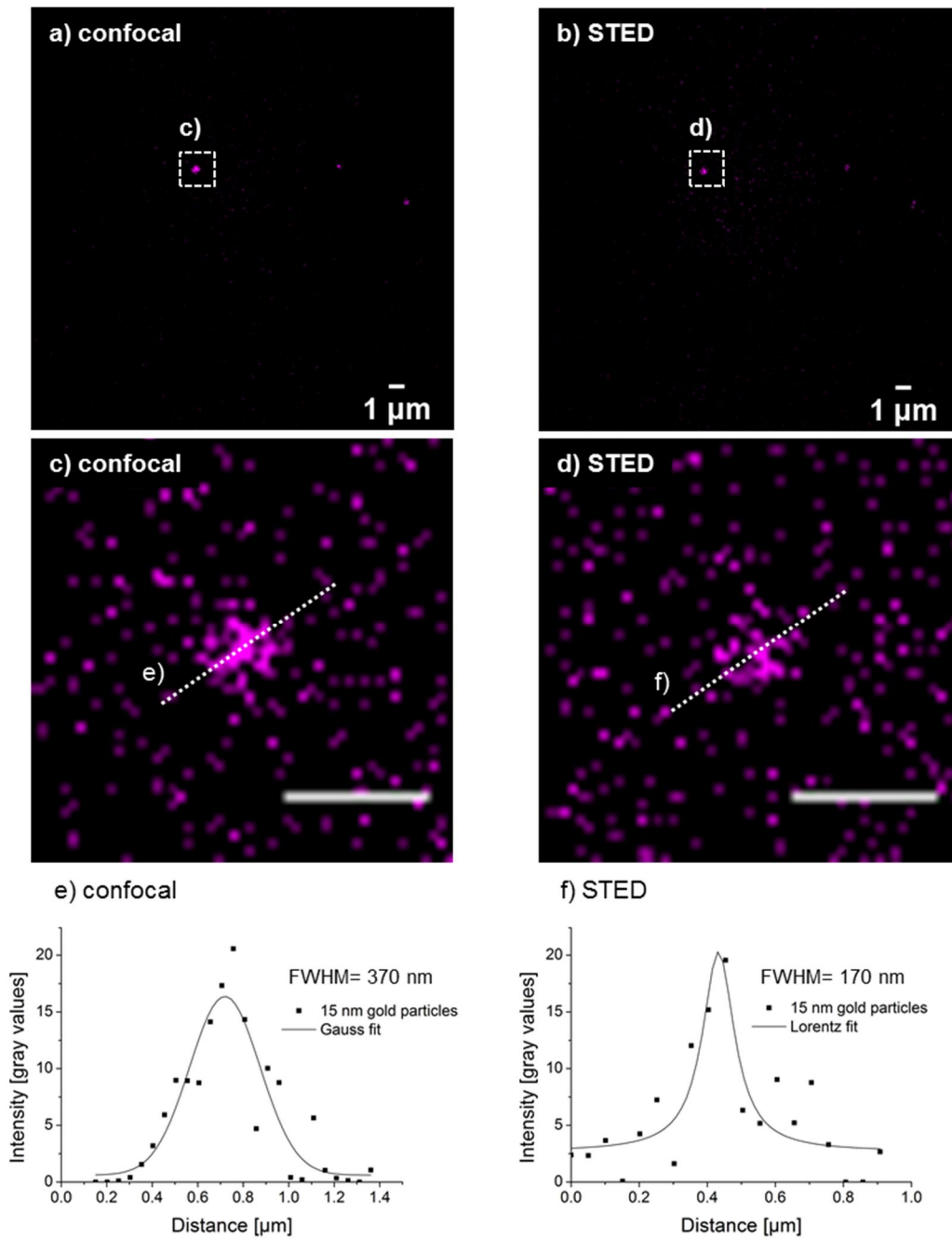


Figure 16: Confocal and STED microscopy of fluorescently labeled 15 nm gold particles.
 a) Confocal and b) STED image of 15 nm gold particles (15 nm-2 L). The synthesized nanoparticles were STED compatible, although the fluorescence signals were very dim. c) Magnified image of one fluorescence spot imaged in confocal mode (see rectangle). d) Magnified image of the same fluorescence spot imaged in STED mode (see rectangle). Scale bar: 1 μm . e) Intensity profile of the fluorescence spot shown in c). An FWHM of 370 nm was calculated. f) Intensity profile of the fluorescence spot shown in d). An FWHM of 170 nm was calculated. Figure a) and b) were smoothed and background was removed. Figure c) and d) are raw data. The contrast of the images was enhanced.

2.3.3 The intracellular distribution of gold particles in relation to the tubulin cytoskeleton

The intracellular distribution of 3 nm, 8 nm, and 15 nm gold particles was studied by exposing A549 cells to $0.02 \mu\text{g ml}^{-1}$ of each nanoparticle size. The fluorescence of Atto 647N, which was coupled to the particle surface *via* the polymer, was used for the detection of cell-associated and internalized gold nanoparticles. Additionally, the intracellular distribution of the fluorescent polymer was investigated by exposing A549 cells to $7.13 \mu\text{g ml}^{-1}$ of the polymer itself. If a maximal polymer labeling in the range of the gold mass concentration is assumed, $7.13 \mu\text{g ml}^{-1}$ is 350 times more polymer than we would expect for $0.02 \mu\text{g ml}^{-1}$ gold nanoparticles. However, the applied concentration turned out to be suitable for microscopy studies.

After 5 h of exposure, all sizes of gold nanoparticles as well as the polymer were detected inside A549 cells as shown by orthogonal views of the recorded z-stacks (*Figure 17*). For studying the intracellular particle and polymer distribution, the recorded z-stacks were depicted further as maximum intensity projections (*Figure 18*). After 5 h, 3 nm gold particles (*Figure 18a*), 8 nm gold particles (*Figure 18d*), 15 nm gold particles (*Figure 18g*), and the polymer (*Figure 18j*) could be found in the center of the cell, close to the nucleus. After 24 h, this perinuclear accumulation increased further, as can be seen for 3 nm gold particles (*Figure 18b*), 8 nm gold particles (*Figure 18e*), 15 nm gold particles (*Figure 18h*), and the polymer (*Figure 18k*). Although no stain for the microtubule organization center (MTOC) was applied, a particle accumulation close to it was assumed from the data (see arrows in *Figure 18*). However, the accumulation was less prominent in A549 cells, which were exposed to 3 nm gold particles. In this case, the particles tend to a more random intracellular distribution, which was confirmed by the microscopy data recorded after 48 h exposure (*Figure 18c*). With increasing exposure times, the perinuclear presence of 3 nm gold particles disappeared and the particles were found throughout the whole cell. In contrast to that, an increasing exposure time showed no further changes in the intracellular pattern of 8 nm gold particles (*Figure 18f*), 15 nm gold particles (*Figure 18i*), and the polymer (*Figure 18l*). Therefore, uptake and intracellular transport of 8 nm and 15 nm gold particles might be driven partly by the polymer surrounding the nanoparticles. Additionally, the perinuclear accumulation patterns suggested an intracellular transport of 8 nm and 15 nm gold particles, which potentially occurred along the endocytic pathway. In cells, the endocytic pathway governs the uptake of biogenic cargo (Alberts and Wilson 2008). The endpoint of this transport route are lysosomes, which are also located in the perinuclear region. Hence, a nanoparticle transport by endocytic transport routes can be assumed from the recorded data. In contrast, 3 nm gold particles lost their perinuclear accumulation indicating a different transport and targeting mechanisms of 3 nm gold particles compared to 8 nm and 15 nm gold particles.

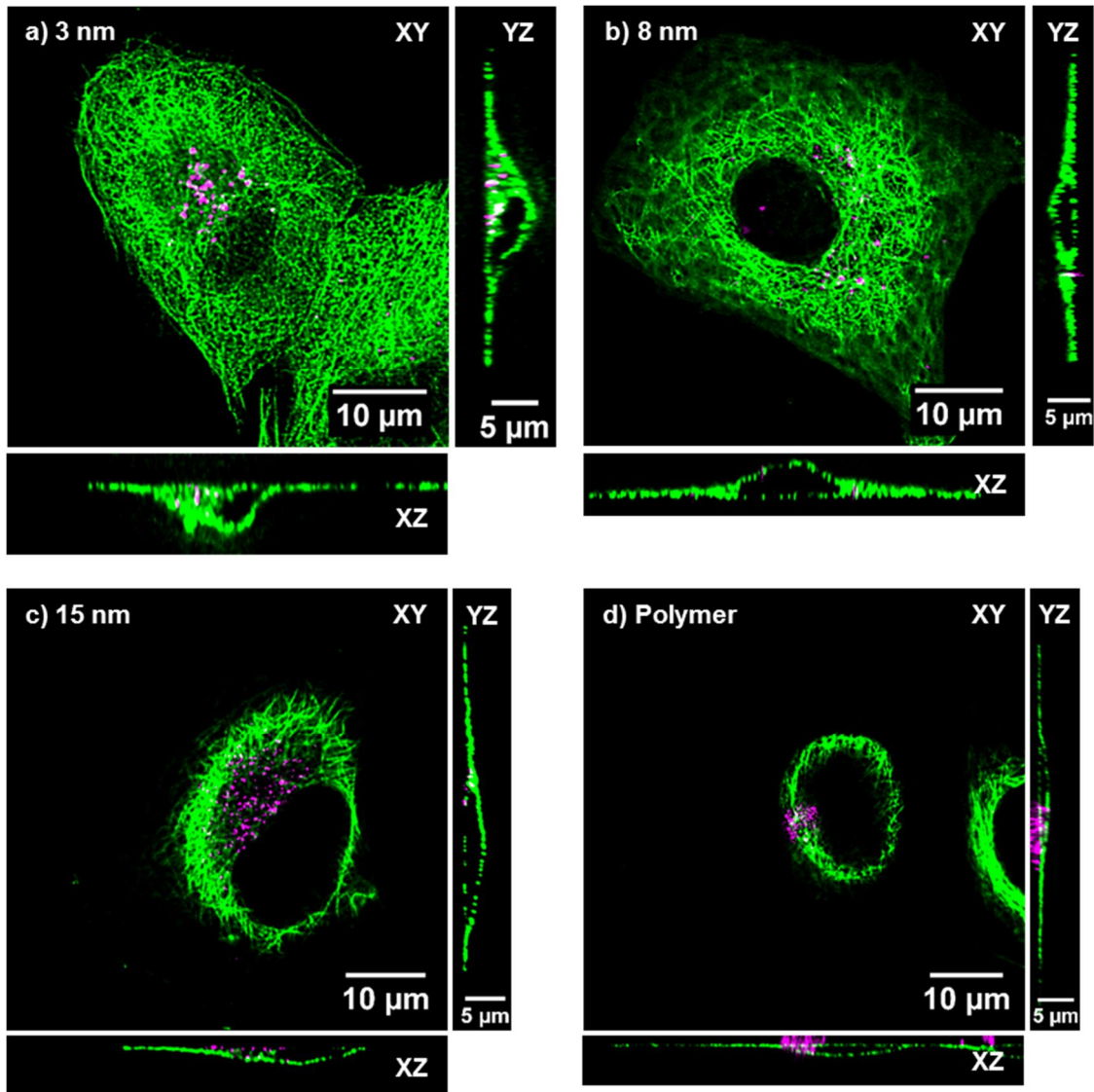


Figure 17: Localization of gold nanoparticles and the polymer inside A549 cells.

A549 cells were exposed for 5 h to $0.02 \mu\text{g ml}^{-1}$ of a) 3 nm, b) 8 nm, and c) 15 nm gold particles (magenta) as well as to d) $7.13 \mu\text{g ml}^{-1}$ of the polymer (magenta) and stained for α -tubulin (green). The gold nanoparticles and the polymer were found inside A549 cells as indicated by orthogonal views of the recorded z-stacks. Z-stacks were deconvolved and the contrast of the images was enhanced. $n = 2$ (biological replicates) with 2 technical replicates.

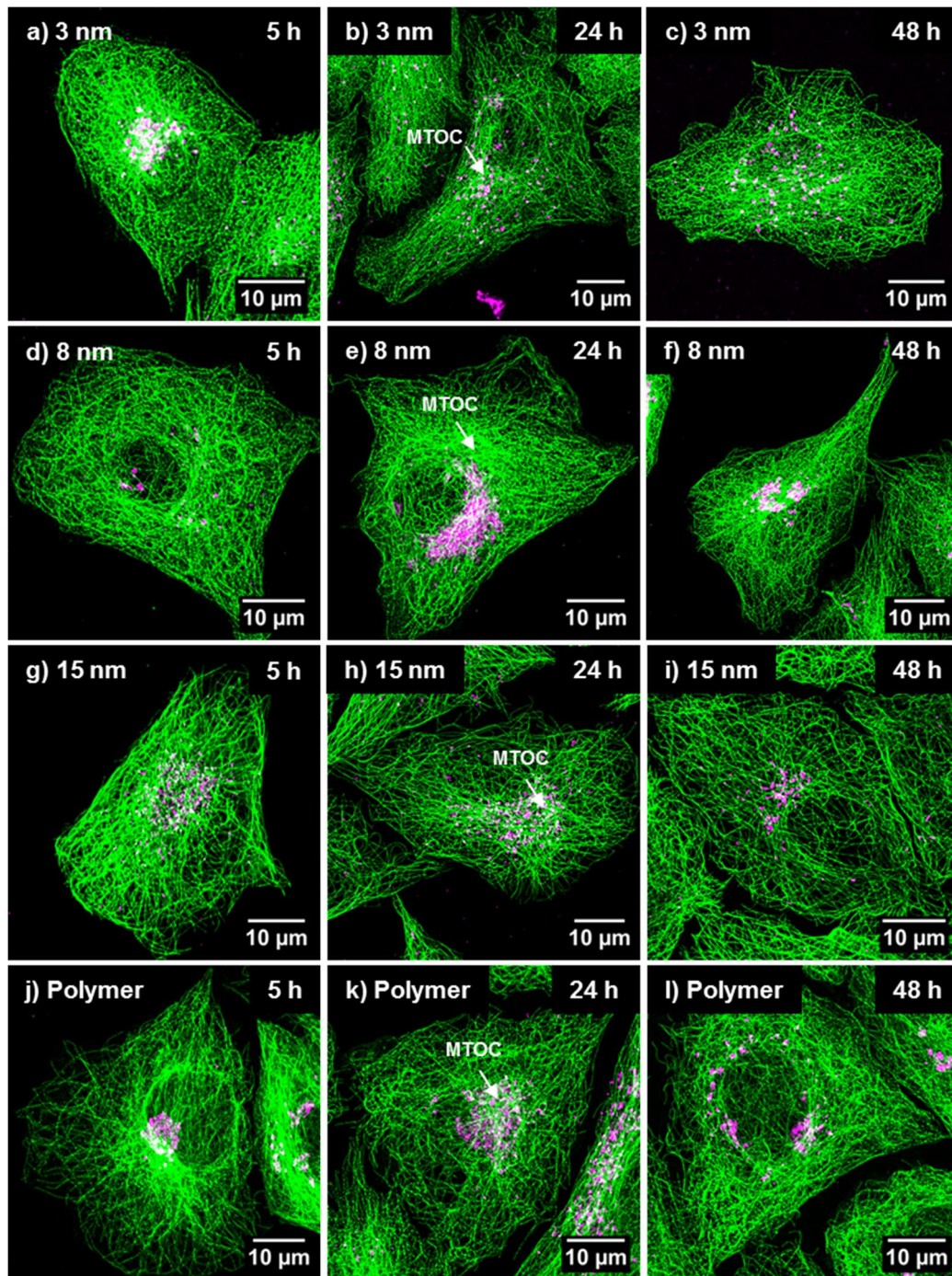


Figure 18: Intracellular distribution of 3 nm, 8 nm, and 15 nm gold particles and the polymer in relation to the tubulin cytoskeleton.

A549 cells were exposed to $0.02 \mu\text{g ml}^{-1}$ of 3 nm, 8 nm, and 15 nm gold particles (magenta) and $7.13 \mu\text{g ml}^{-1}$ of the polymer (magenta) and stained for α -tubulin (green). First row: Exposure of A549 cells to 3 nm gold particles. Second row: Exposure of A549 cells to 8 nm gold particles. Third row: Exposure of A549 cells to 15 nm gold particles. Fourth row: Exposure of A549 cells to the polymer. The location of the MTOC was estimated from the α -tubulin stain and is indicated by arrows. 8 nm and 15 nm gold particles as well as the fluorescent polymer were imaged by STED microscopy. α -tubulin and 3 nm gold particles were imaged by confocal microscopy. Z-stacks were deconvolved and the contrast of the maximum intensity projections was enhanced. $n = 2$ with 2 technical replicates.

2.3.4 The intracellular distribution of gold nanoparticles in relation to the Golgi

The intracellular distribution of 3 nm, 8 nm, and 15 nm gold particles after 24 h of exposure suggested a potential association of the nanoparticles with the Golgi complex, which is also located close to the nucleus. The Golgi is an essential part of the exocytic pathway, which governs the transport of vesicles from the cell interior to the cell membrane and the extracellular space (Alberts and Wilson 2008). An interaction of nanoparticles with the Golgi complex would strengthen the assumption of an active nanoparticle transport back to the cell membrane. However, gold nanoparticles reaching the Golgi can also stay in this compartment or, depending on the vesicle modification, transported to other destinations inside the cell. For studying a translocation of internalized nanoparticles to the Golgi complex, A549 cells were exposed to 3 nm and 8 nm gold particles for 24 h and analyzed concerning a nanoparticle accumulation at the *cis*-Golgi complex. Confocal images were recorded to overview the nanoparticle distribution in relation to the Golgi. For 3 nm (Figure 19a) and 8 nm gold particles (Figure 19b) a particle accumulation at the side of the nucleus facing the *cis*-Golgi was observed. For a more detailed analysis, confocal z-stacks of single cells were recorded and depicted as maximum intensity projections. 3 nm gold particles were predominately found at the side of the nucleus facing the *cis*-Golgi (Figure 19c). 8 nm gold particles accumulated also at the Golgi complex as illustrated by the maximum intensity projection (Figure 19d). An interaction of 3 nm and 8 nm gold particles with the Golgi could be assumed from the microscopy data. Orthogonal views of the recorded z-stacks revealed an association of 3 nm (Figure 20a) and 8 nm gold particles (Figure 20b) with the *cis*-Golgi complex.

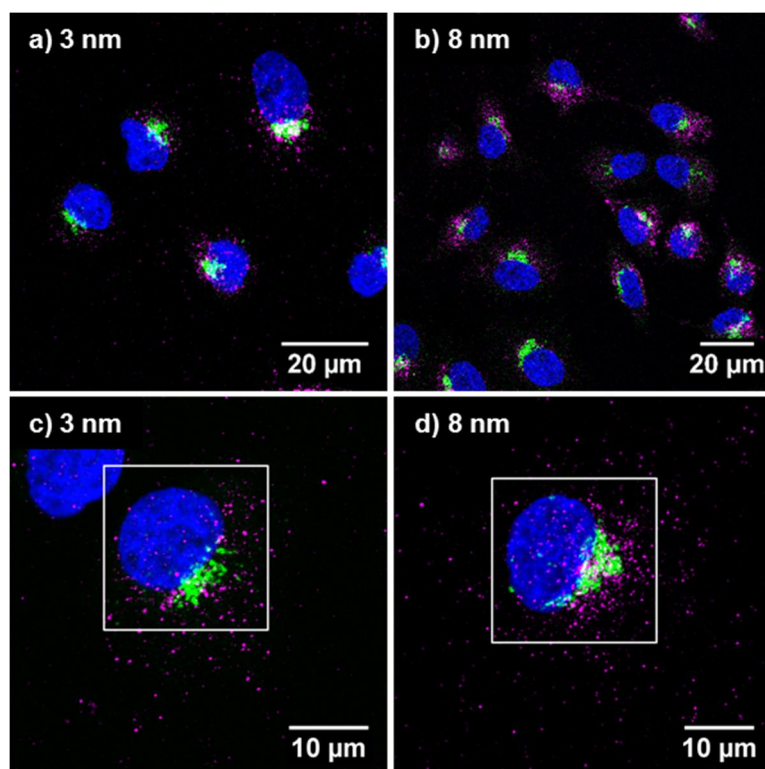


Figure 19: Intracellular distribution of 3 nm and 8 nm gold particles in relation to the Golgi complex.

A549 cells were exposed to $0.02 \mu\text{g ml}^{-1}$ gold nanoparticles (magenta) for 24 h and stained for the *cis*-Golgi complex by labeling the *cis*-Golgi matrix protein GM130 (green) and the cell nucleus (blue). Confocal images of A549 cells exposed to a) 3 nm gold particles and b) 8 nm gold particles. Maximum intensity projection of recorded confocal z-stacks of A549 cells exposed to c) 3 nm gold particles and d) 8 nm gold particles. Orthogonal views of the indicated regions (white squares) are presented in Figure 20. Confocal images and z-stacks were smoothed and background was subtracted. The contrast of all images was enhanced. n = 1 with 3 technical replicates.

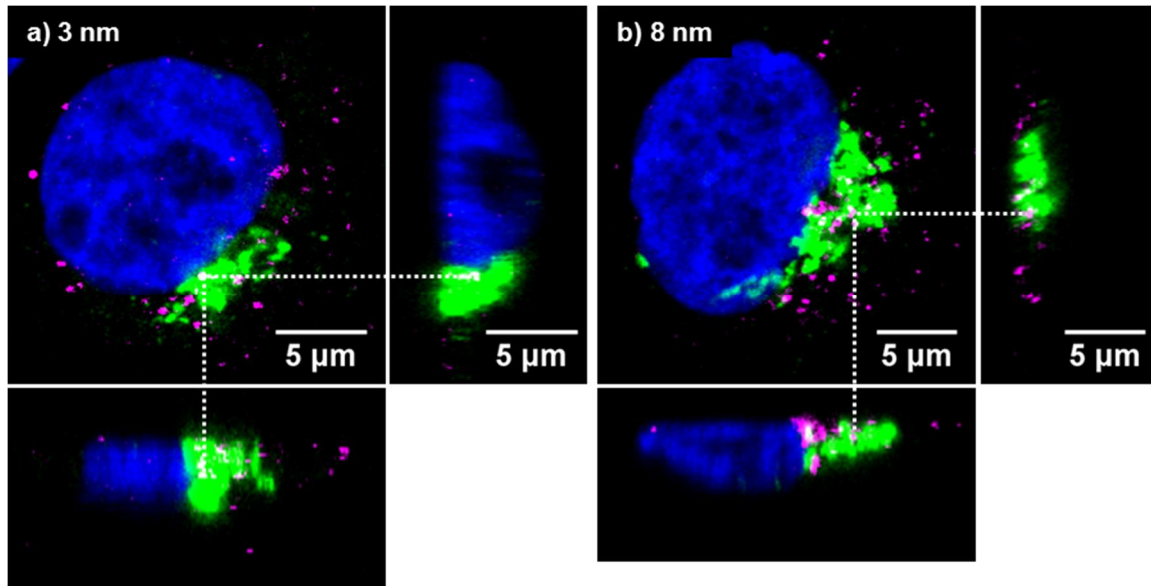


Figure 20: Association of 3 nm and 8 nm gold particles with the Golgi complex

The region of interest of the z-stacks, shown as maximum intensity projection in *Figure 19c* and *d* (see square), was analyzed by orthogonal views concerning an association of gold nanoparticles and the Golgi. A549 cells were exposed to a) 3 nm and b) 8 nm gold particles.

2.3.5 Localization of gold nanoparticles inside the nucleus of A549 cells

The small size of the gold nanoparticles used within this study would allow a translocation of the particles inside the cell nucleus of A549 cells. The central transport channel of nuclear pores in mammalian cells is approximately 40 nm in diameter (Duarte-Rey *et al.*, 2012) and macromolecules with 39 nm in size are able to translocate from the cytoplasm into the nucleus (Pante 2002). For studying a nuclear penetration of the used nanoparticles, A549 cells were exposed to $0.02 \mu\text{g ml}^{-1}$ of 3 nm and 8 nm gold particles and the nucleus was stained with Hoechst. The Hoechst stain labels the DNA inside the cell nucleus, but not the nuclear lamina. Hence, only a rough estimation of the nuclear boundaries can be concluded. The fluorescence of 3 nm gold particles was observed inside the nucleus of A549 cells after 5 h (*Figure 21a*), 24 h (*Figure 21b*), and 48 h (*Figure 21c*) of exposure. Atto 647N signals of 8 nm gold particles were detected inside the nucleus of A549 cells after exposure times of 5 h (*Figure 22a*), 24 h (*Figure 22b*), and 48 h (*Figure 22c*) as well. For both particle sizes a penetration into the nucleus was observed even after a short nanoparticle exposure of 5 h. The fluorescent polymer was also observed inside the cell nucleus (*Figure 23*). However, most particle and polymer fluorescence was found outside of the cell nucleus and only a small amount could be detected inside the nucleus. A quantification showed that most fluorescence signals were detected inside the nucleus for 8 nm gold particles (*Figure 24*). After 5 h, 24 h, and 48 h of exposure an average of 23, 25, and 26 fluorescence spots were located inside the nucleus of three analyzed datasets (*Table S1*). The number of 8 nm gold particles inside the cell nucleus appeared to be constant over time. However, the high standard deviations revealed a non-homogenous uptake into the nucleus of different cells. In contrast to these results, the nuclear translocation of 3 nm gold particles was less pronounced and seemed to decrease over time. Interestingly, only small amounts of the fluorescently labeled polymer (< 6 fluorescence signals) were detected inside the cell nucleus of both analyzed cells indicating a higher nuclear translocation of gold nanoparticles. Nanoparticle- and polymer-derived fluorescence was observed in all nuclei of analyzed cells. However, as already mentioned, the amount of the signal differed.

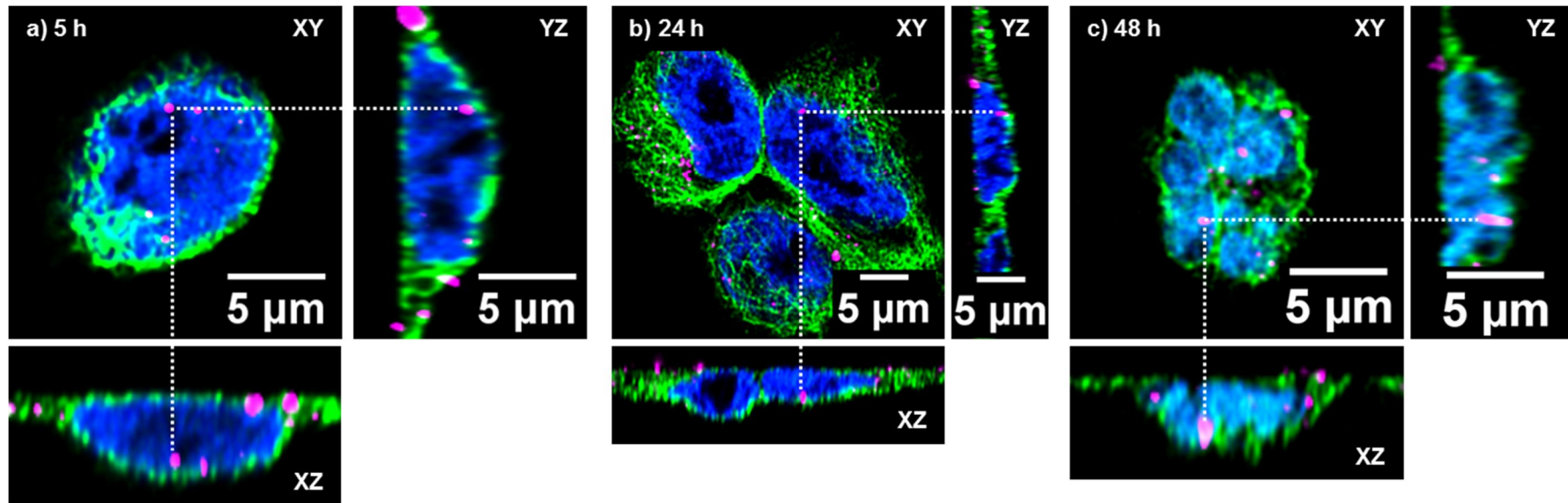


Figure 21: Localization of 3 nm gold particles inside the nucleus of A549 cells.

A549 cells were exposed to $0.02 \mu\text{g ml}^{-1}$ 3 nm gold particles (magenta) and stained for α -tubulin (green) and the cell nucleus (blue). Confocal z-stacks of cells were recorded and analyzed by orthogonal views. 3 nm gold particles were found inside the nucleus after a) 5 h, b) 24 h, and c) 48 h of nanoparticle exposure. Orthogonal sections of recorded z-stacks are shown. The z-stacks were deconvolved and the contrast of the images was enhanced. $n = 2$ with 2 technical replicates.

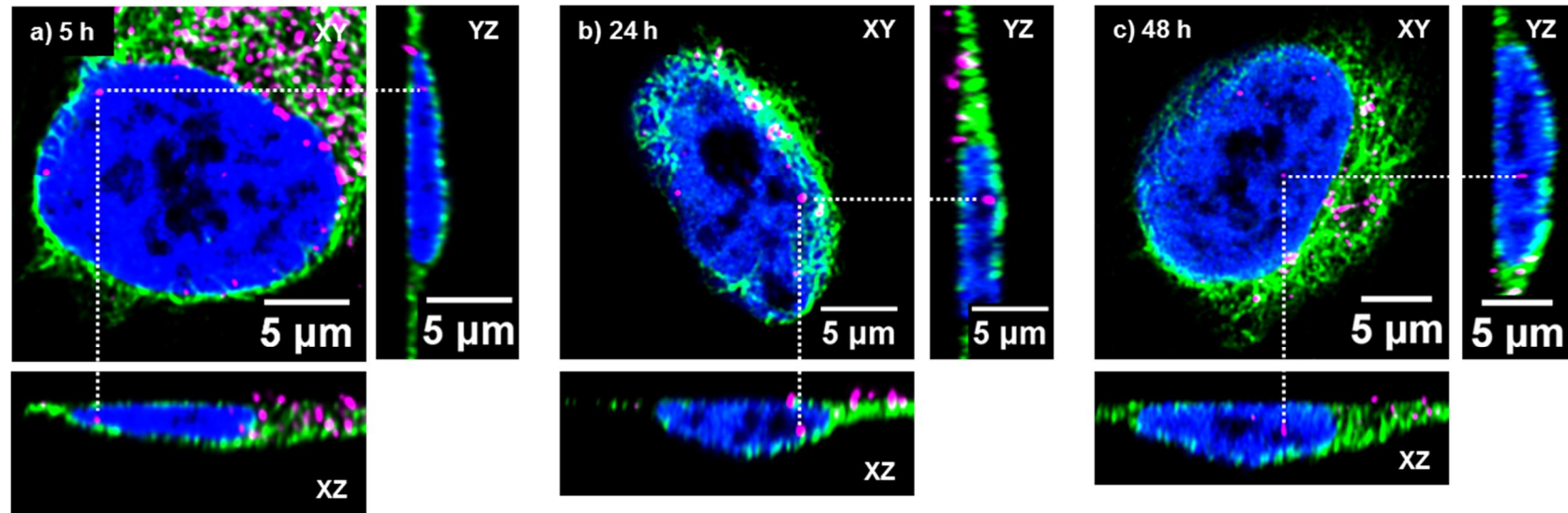


Figure 22: Localization of 8 nm gold particles inside the nucleus of A549 cells.

A549 cells were exposed to $0.02 \mu\text{g ml}^{-1}$ 8 nm gold particles (magenta) and stained for α -tubulin (green) and the cell nucleus (blue). Confocal z-stacks of cells were recorded and analyzed by orthogonal views. 8 nm gold particles were found inside the nucleus after a) 5 h, b) 24 h, and c) 48 h of nanoparticle exposure. Orthogonal sections of recorded z-stacks are shown. The z-stacks were deconvolved and the contrast of the images was enhanced. The results are representative for two independent experiments with different cell passage numbers. $n = 2$ with 2 technical replicates.

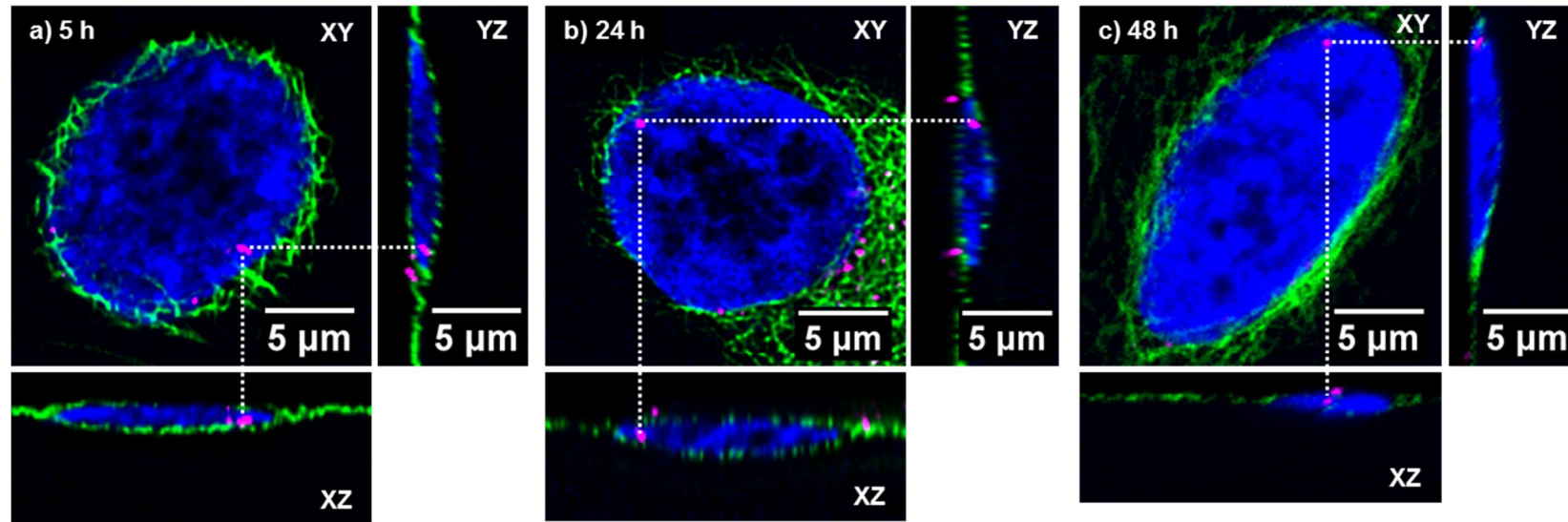


Figure 23: Localization of the fluorescent polymer inside the nucleus of A549 cells.

A549 cells were exposed to $7.13 \mu\text{g ml}^{-1}$ of the fluorescent polymer (magenta) and stained for α -tubulin (green) and the cell nucleus (blue). Confocal z-stacks of cells were recorded and analyzed by orthogonal views. The polymer was found inside the nucleus after a) 5 h, b) 24 h, and c) 48 h of exposure. Orthogonal sections of recorded z-stacks are shown. The z-stacks were deconvolved and the contrast of the images was enhanced. $n = 1$ with 2 technical replicates.

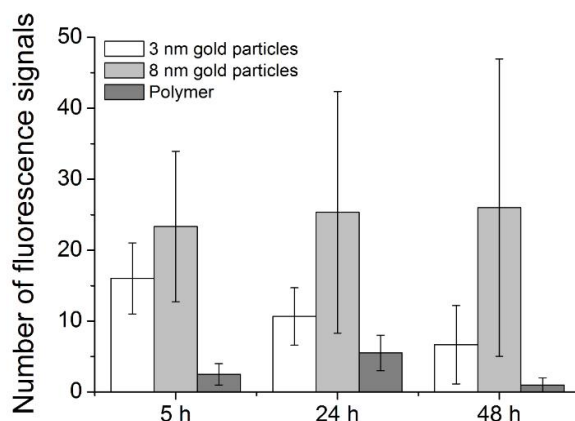


Figure 24: Quantification of fluorescence signals inside the nucleus of A549 cells.

From confocal z-stacks fluorescence spots of 3 nm and 8 nm gold particles and the polymer inside the cell nucleus were counted. For the respective numbers of counted fluorescence spots see Table S1. Polymer: $n = 1$ with 2 technical replicates. Gold nanoparticles: $n = 2$ and with 2 technical replicates. Error bars represent SD.

2.3.6 Changes in the morphology of nuclei of A549 cells after exposure to gold nanoparticles

Within the previous section the potential of 3 nm and 8 nm gold particles to penetrate the cell nucleus was shown. This observation raised the question of a potential influence of the particles on the nuclear morphology. A549 cells were exposed to $0.02 \mu\text{g ml}^{-1}$ of 3 nm gold particles and analyzed concerning the structure of the nucleus by staining the DNA. The exposure of A549 cells to 3 nm gold particles was accompanied by diverse changes in the structure of the cell nucleus (Figure 25). Similar effects were not triggered by 8 nm gold particles. Firstly, apoptotic cells were observed as indicated by the fragmented DNA and the round cellular morphology (Figure 25a), and the condensed DNA (Figure 25c). Apoptosis occurred even after a short nanoparticle exposure of 5 h but was observed also within longer exposure times. To quantify the cytotoxic potential of 3 nm gold particles further cell-based assays were carried out (see section 2.3.8).

Besides apoptosis, the formation of micronuclei occurred (Figure 25b). Micronuclei are indicators for genotoxicity and are formed due to chromosome fragmentation (Bhatia and Kumar 2013).

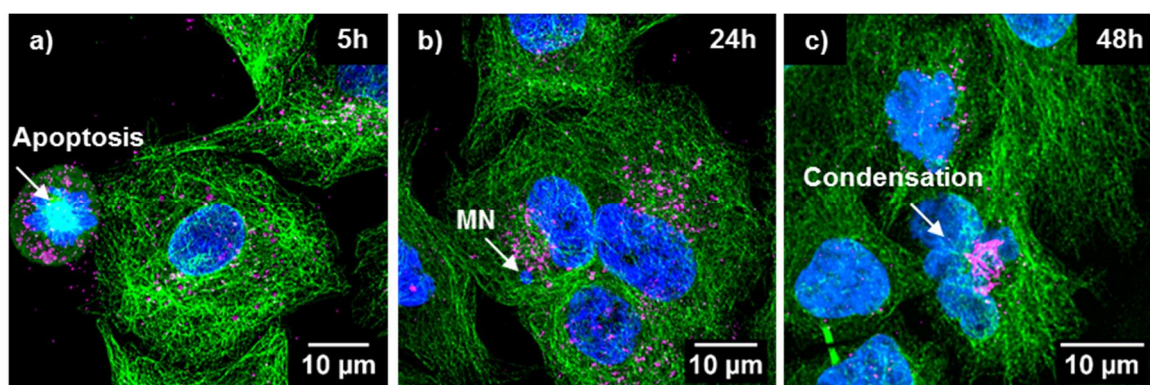


Figure 25: The impact of 3 nm gold nanoparticles on the morphology of the cell nucleus of A549 cells. A549 cells were exposed to $0.02 \mu\text{g ml}^{-1}$ of 3 nm gold particles (magenta) and stained for α -tubulin (green) and the cell nucleus (blue). Maximum intensity projections of confocal z-stacks from Figure 21 are presented. a) After 5 h of nanoparticle exposure, small DNA fragments and a round cellular morphology indicated apoptosis. b) After 24 h of nanoparticle exposure, the formation of a micronucleus (MN) was observed. c) After 48 h of nanoparticle exposure, condensation of DNA was observed, also an indicator for apoptosis. Z-stacks were deconvolved and the contrast of the depicted maximum intensity projections was enhanced. $n = 1$ with 3 technical replicates.

2.3.7 Effects of gold nanoparticles on the microtubule structure

The tubulin antibody stain revealed changes in the microtubule structure of A549 cells after gold nanoparticle exposure. These changes were predominately triggered by 3 nm gold particles. After 5 h of nanoparticle exposure, a dense tubulin network in the outer cell region and a round cellular morphology was observed (*Figure 26a*). Both observations were indicators for apoptosis and were in consistence with the apoptotic events observed due to changes in the morphology of the cell nucleus. Additionally, mitosis seemed to be disturbed by 3 nm gold particles. After nanoparticle exposure, an incorrect cell division was observed for some cells (*Figure 26b*). The daughter cells seemed not to be separated correctly during the cytokinesis phase of mitosis. The contractile ring, consisting of actin, myosin, and tubulin (Conrad *et al.*, 1992), is clearly visible by the applied tubulin stain. Another observation was the formation of blebs (*Figure 26c, d*) that exhibited sizes of up to 10 - 15 μm . The blebs were detected even after short nanoparticle exposure (3 h) but also with increasing exposure times (24 h). For all observed cells only one or two blebs per cell were determined.

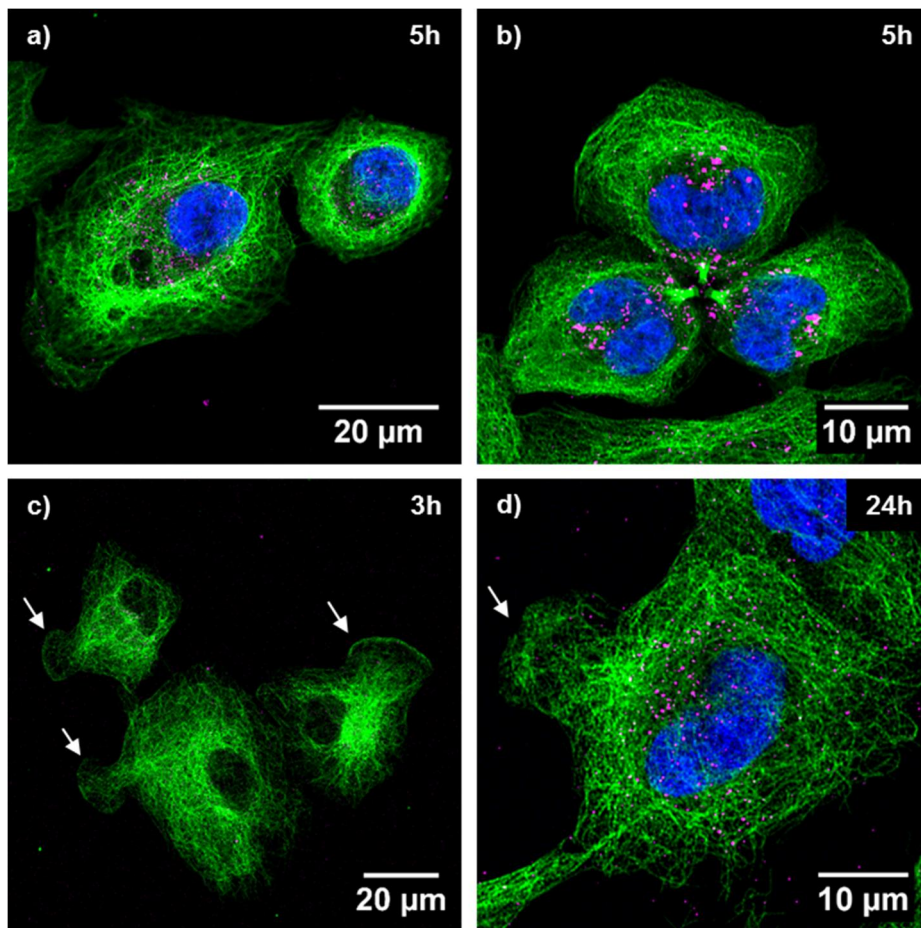


Figure 26: Changes in the microtubule structure of A549 cells induced by 3 nm gold particles. A549 cells were exposed to $0.02 \mu\text{g ml}^{-1}$ of 3 nm gold particles (magenta) for 3 h, 5 h, and 24 h and stained for α -tubulin (green) and the cell nucleus (blue). a) The round morphology of the cell and the dense tubulin network in the outer cell region indicated apoptosis. b) Incorrect mitosis was observed with a failure in cytokinesis. c) Bleb formation of tubulin filaments was observed as a reaction on the exposure of cells to 3 nm gold particles for short and d) long exposure times.

n = 1 with 3 technical replicates.

The formation of blebs was not exclusively observed for A549 cells exposed to 3 nm gold particles. Quantification by microscopy (*Figure S1* and *Table S2*) demonstrated that a bleb formation did not solely depend on nanoparticle exposure (*Figure 27a*). Control cells without nanoparticle treatment showed some blebs, too. In comparison, for A549 cells exposed to 3 nm, 8 nm, and 15 nm gold particles more blebs were counted. The nanoparticle mass concentration was kept equal. However, the applied particle number differed and indicated a dependency of the bleb formation on the applied nanoparticle number (*Figure 27b*).

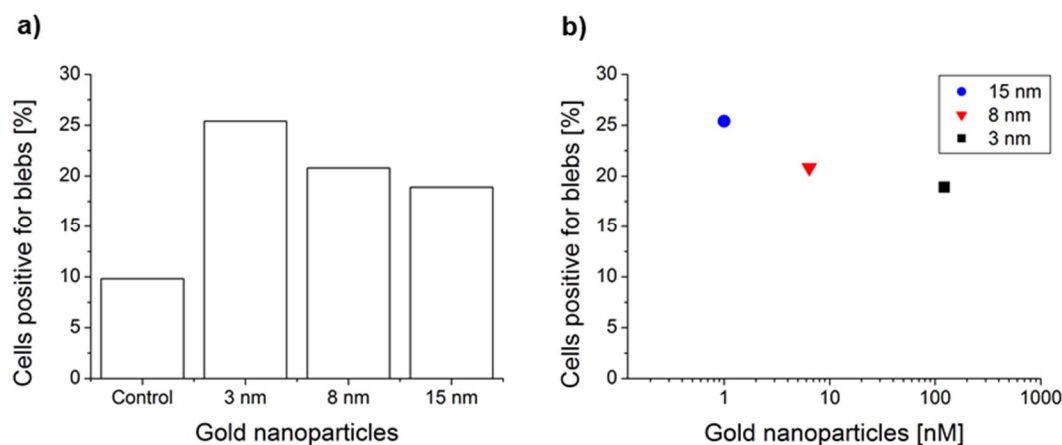


Figure 27: Quantification of bleb formation.

A549 cells were exposed to $0.02 \mu\text{g ml}^{-1}$ of 3 nm (122 nM), 8 nm (6.4 nM), and 15 nm (1 nM) gold particles for 24 h. a) Cells positive for blebs were quantified by widefield microscopy (*Figure S1* and *Table S2*). Control cells exhibited a less pronounced potential of bleb formation compared to cells exposed to gold nanoparticles. With decreasing particle diameter and increasing particle number, the formation of blebs increased. $n = 1$. b) The bleb formation was plotted against the molar particle concentration (logarithmic scale). An increasing number of nanoparticles caused the formation of blebs to a higher extent.

A similar quantification was carried out for mitotic cells. An impact of 3 nm gold particles on cell division was observed (*Figure 26b*). Quantification by microscopy (*Figure S2* and *Table S3*) demonstrated that only minor differences in the number of mitotic events were observed. For control cells, 6.3 % of mitotic events were calculated (*Figure 28a*). All cells exposed to gold nanoparticles showed less mitosis. After treatment with 3 nm gold particles, only 4.9 % mitotic events were counted. An exposure to 8 nm and 15 nm gold particles resulted in 5.4 % and 5.5 % of mitotic events, respectively. With increasing molar particle concentration less mitosis was observed (*Figure 28b*). However, the quantification revealed only slight differences.

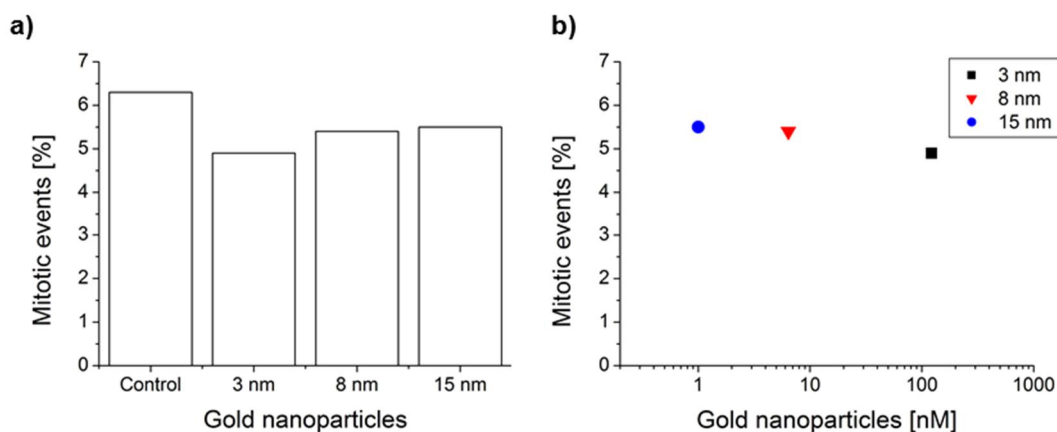


Figure 28: Quantification of mitosis.

A549 cells were exposed to $0.02 \mu\text{g ml}^{-1}$ of 3 nm (122 nM), 8 nm (6.4 nM), and 15 nm (1 nM) gold particles for 24 h. a) Mitosis was quantified by widefield microscopy (Figure S2 and Table S3). For control cells more mitotic events were observed compared to cells exposed to gold nanoparticles. b) The percentage of mitotic events was plotted against the molar particle concentration (logarithmic scale). Mitosis slightly decreased with increasing particle number. $n = 1$.

2.3.8 Cytotoxicity testing of gold nanoparticles

2.3.8.1 WST-1 assay

Within the previous sections, the intracellular distribution of 3 nm, 8 nm, and 15 nm gold particles in A549 cells was observed by STED and confocal microscopy. Thereby, especially the 3 nm gold particles induced morphological changes, like the formation of blebs, a micronuclei formation, or a nuclear penetration of the particles. To evaluate nanoparticle toxicity, an enzyme-based cell assay was applied. For toxicity testing, concentrations ranging from $0.02 \mu\text{g ml}^{-1}$, the concentration used for the microscopy analyses, up to $20 \mu\text{g ml}^{-1}$ gold nanoparticles were tested.

The WST-1 assay was applied to monitor the impact of the differently sized gold nanoparticles on the cellular viability of A549 cells. For this purpose, the enzymatic activity of mitochondrial dehydrogenases was measured. The conversion of the water soluble tetrazolium (WST-1) by these dehydrogenases results in the formation of formazan, which can be detected by absorption measurements at 450 nm. The interference of nanoparticles with different cell based assays is well known and has been studied extensively (Monteiro-Riviere *et al.*, 2009). Also for gold nanoparticles assay interferences have been described (Keene *et al.*, 2011). To exclude an interference of the WST-1 assay and the optical properties of the gold nanoparticles, measurements without cells were carried out initially. For this purpose, different concentrations of non-fluorescent 8 nm gold particles were diluted in cell culture medium (DMEM) and an absorption spectrum from 400 nm to 800 nm was recorded (Figure 29a). With increasing nanoparticle concentration, the absorption increased slightly over the whole spectrum compared to the medium. Concentrations of $0.2 \mu\text{g ml}^{-1}$ and $2 \mu\text{g ml}^{-1}$ of 8 nm gold particles showed only a slight influence on the absorption of 0.025 and 0.05 units, respectively. In contrast, the highest concentration of $20 \mu\text{g ml}^{-1}$ of 8 nm gold particles revealed a significant increase in the absorption of about 0.1 units. Furthermore, the plasmon resonance of the nanoparticles at 520 nm was clearly visible. To demonstrate the influence of the gold nanoparticle concentration on the measurement wavelength of the WST-1 assay, the absorption values at 450 nm were plotted against the respective nanoparticle concentrations (Figure 29b). From these data, a clear dependency of the absorption at 450 nm from the gold nanoparticle concentration was demonstrated. To avoid the generation of absorption values that might

erroneously be related to a high cell viability, the gold nanoparticle absorption at 450 nm was measured before reagent addition and subtracted from the finally measured absorption at 450 nm in the respective well.

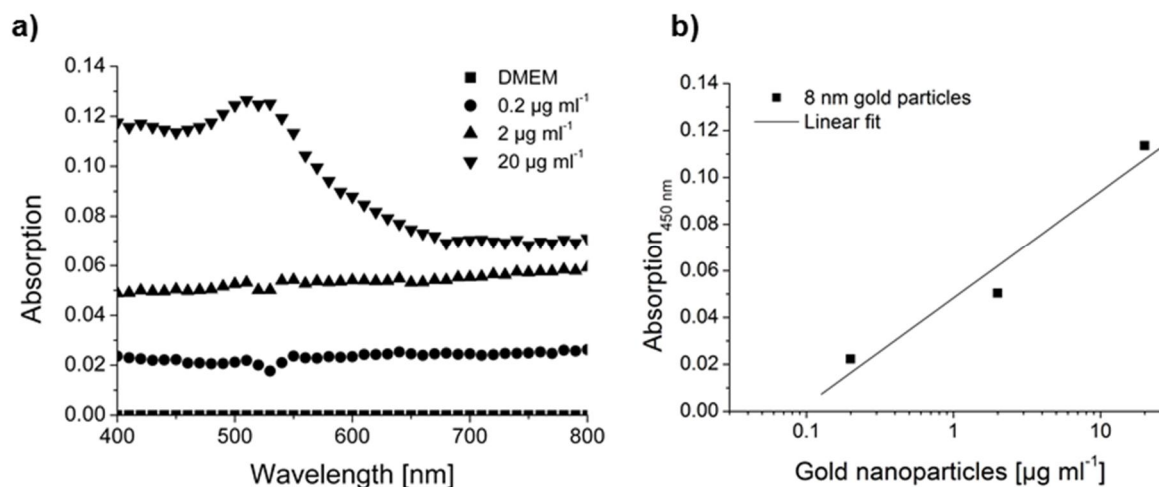


Figure 29: The interference of gold nanoparticles with the WST-1 assay.

The absorption of 8 nm gold particle dispersions was measured from 400 - 800 nm. a) Increasing concentrations of gold nanoparticles ranging from 0 - 20 µg ml⁻¹ amplified the absorption over the whole recorded spectrum. b) At 450 nm, the measurement wavelength of the WST-1 assay, the absorption increased linearly as a function of the gold nanoparticle concentration. The higher absorption values were related to the SPR of the particles. The x-axis is displayed in logarithmic scale.

3 nm gold particles had no effect on the viability of A549 cells at concentrations of 0.02 µg ml⁻¹, 0.2 µg ml⁻¹, and 2 µg ml⁻¹ (Figure 30a). Even varying exposure times of 5 h, 24 h, and 48 h caused no significant changes in the cellular viability. For the highest tested concentration of 20 µg ml⁻¹, 3 nm gold particles showed a significant decrease in cell viability after 48 h of exposure. In comparison to control cells, the viability decreased to 90 %. 8 nm gold particles exhibited no significant impact on A549 cells at all tested concentrations (Figure 30b). 15 nm gold particles affected the viability of A549 cells only at a concentration of 20 µg ml⁻¹ and after a minimal exposure time of 24 h. After 48 h of nanoparticle exposure, almost no cellular viability was detectable anymore (Figure 30c). To exclude an impact of the gold nanoparticle coating on the viability of A549 cells, cells were exposed to varying concentrations of the polymer. The WST-1 assay revealed no impairment of the cell viability due to the polymer up to a concentration of 713 µg ml⁻¹ (Figure 30d). Neither an increasing concentration of the polymer nor increasing exposure times affected the viability of A549 cells. These results strongly indicated that the measured cytotoxicity of gold nanoparticles could be related to the gold cores and not to the particle coating.

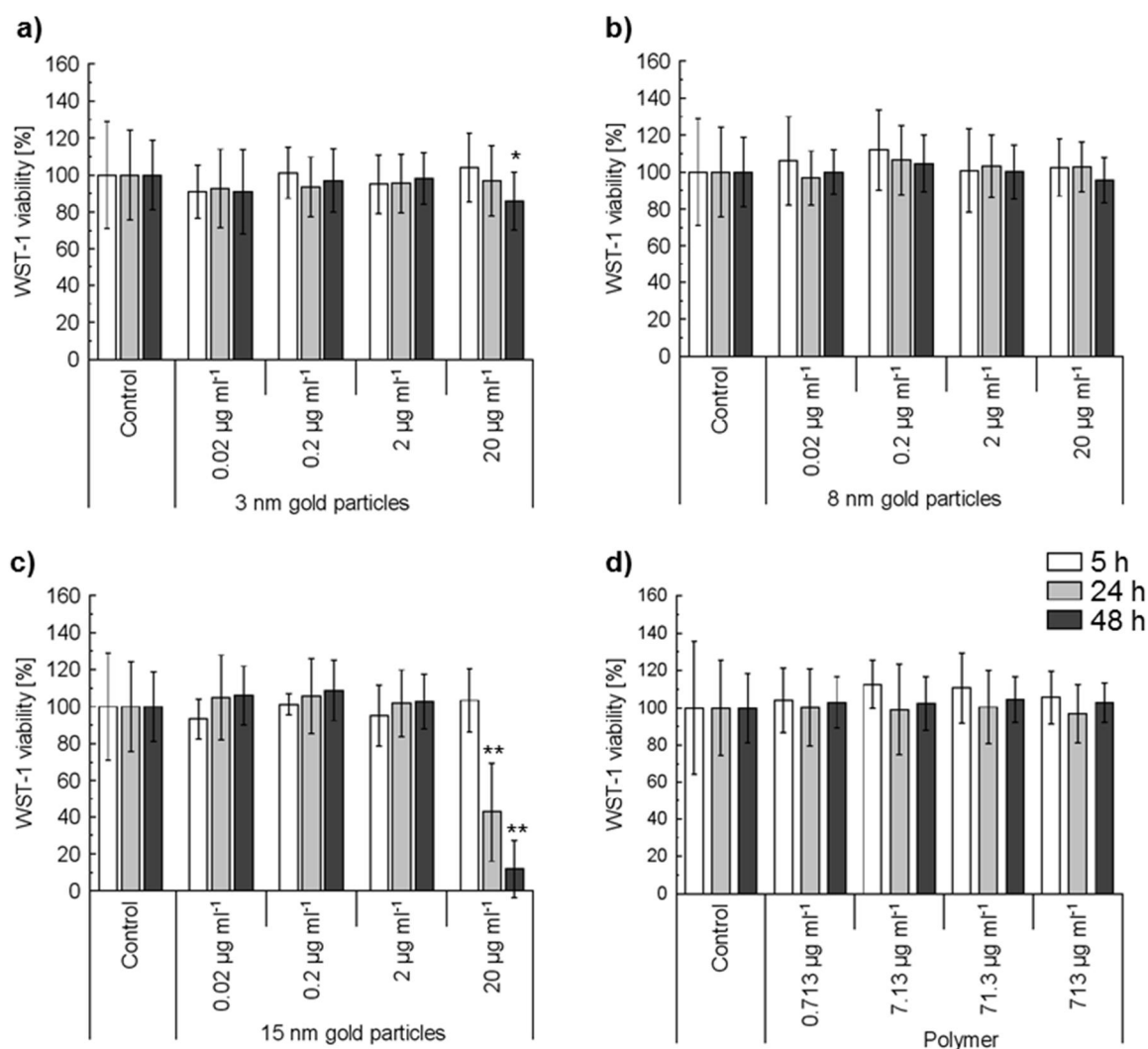


Figure 30: WST-1 assay of A549 cells exposed to gold nanoparticles and the nanoparticle coating.

The WST-1 assay was used to determine the cell viability of A549 cells after exposure to a) 3 nm, b) 8 nm, c) 15 nm gold particles, and d) the polymer. The control signal, cells without nanoparticle treatment, was assumed as 100 % cell viability and compared with viabilities of nanoparticle treated cells. Error bars represent SD. * $p < 0.1$, ** $p < 0.05$ compared to control. $n = 3$ with 4 technical replicates.

2.3.8.2 BrdU assay

From the microscopy data, an impaired cell division of A549 cells after gold nanoparticle exposure was suggested (Figure 28). Therefore, the BrdU assay was used to describe the cell proliferation of A549 cells in the presence of gold nanoparticles. The amount of incorporated BrdU was determined by an antibody reaction and is a measurement for cell proliferation. Within the present study, a chemiluminescent reaction was used for BrdU quantification. By this means, an interference of the gold nanoparticle plasmon resonance with the measurement wavelength in absorption-based assays, such as seen in the WST-1 assay, was avoided. A549 cells were exposed to nanoparticles in the same way as described previously for the WST-1 assay.

After 5 h of nanoparticle exposure, no inhibition of the proliferation of A549 cells was observed. Also actinomycin D, which is known to inhibit proliferation, did not show any significant impact on the cells. 3 nm gold particles caused a significant decrease in cell proliferation with increasing exposure time (Figure 31a). This effect was present for all tested concentrations, even for the lowest concentration of $0.02 \mu\text{g ml}^{-1}$. The observed decrease in cell proliferation was dependent on

concentration. The exposure of A549 cells to 8 nm gold particles caused no significant impact on the cell proliferation for concentrations from 0.02 to 2 $\mu\text{g ml}^{-1}$ (Figure 31b). The highest tested concentration of 20 $\mu\text{g ml}^{-1}$ affected the cell proliferation significantly after 48 h of exposure. The exposure of A549 cells to 15 nm gold particles caused no impact on the cell proliferation for concentrations from 0.02 to 2 $\mu\text{g ml}^{-1}$ (Figure 31c). However, a concentration of 20 $\mu\text{g ml}^{-1}$ significantly affected the cell proliferation. After 48 h nanoparticle exposure, no cell proliferation activity was detectable anymore. In comparison to the WST-1 assay, the BrdU assay showed a higher sensitivity regarding the determination of nanoparticle induced cytotoxicity.

To examine the gold nanoparticle toxicity as a function of particle number, the molar particle concentrations were calculated. The BrdU proliferation of A549 cells, which was measured after 48 h of nanoparticle treatment was plotted against the respective molar particle concentrations (Figure 32). For 3 nm (Figure 32a), 8 nm (Figure 32b), and 15 nm gold particles (Figure 32c) the cell proliferation decreased with increasing molarity. A comparison of the three different particle sizes demonstrated a higher cytotoxic potential of 15 nm gold particles (Figure 32d). A particle number of 1 nM caused a decrease of the cell viability to 10 %. In contrast, 1 nM of 3 nm and 8 nm gold particles reduced the viability of A549 cells only slightly, to a value of 80-90 %.

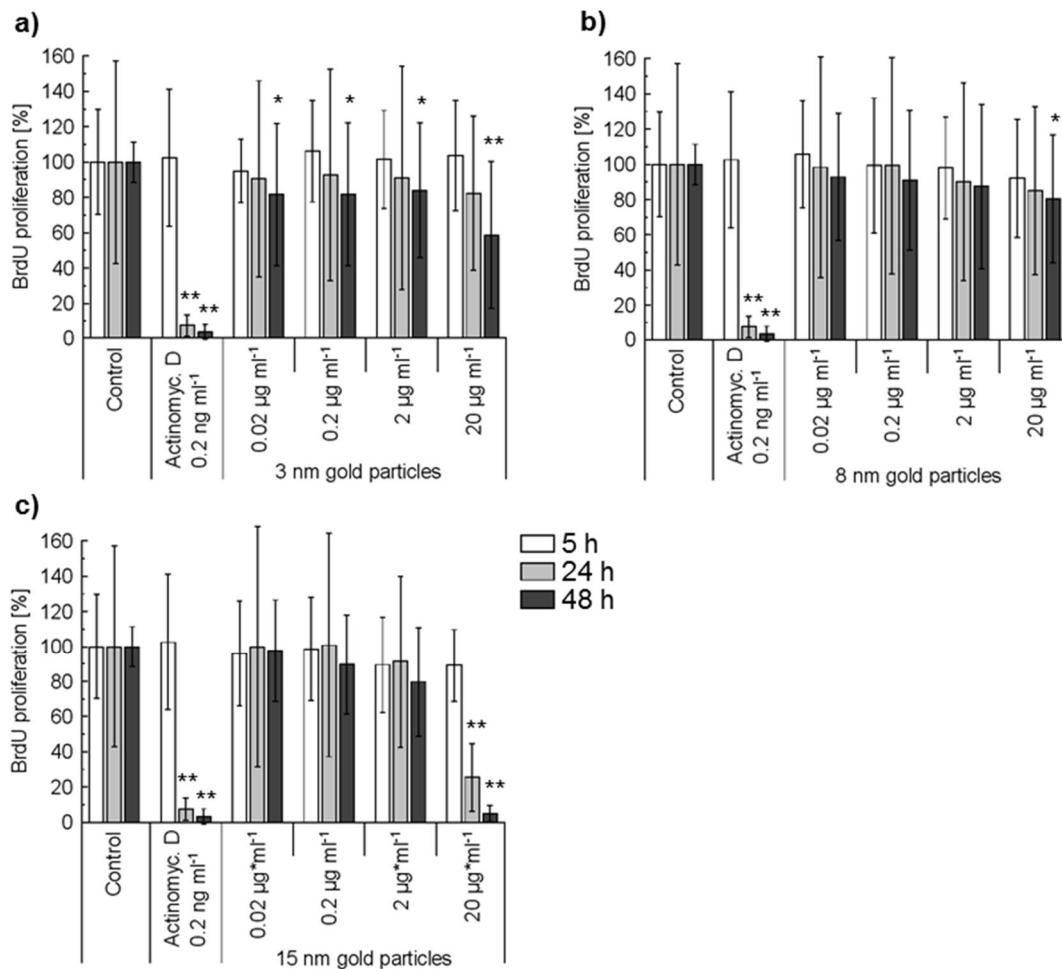


Figure 31: BrdU assay of A549 cells exposed to gold nanoparticles.

The BrdU assay was used to determine the proliferation of A549 cells after exposure to a) 3 nm, b) 8 nm, and c) 15 nm gold particles. Actinomycin D was used as a positive control for the inhibition of cell proliferation. The control signal, cells without nanoparticle treatment, was assumed as 100 % cell proliferation and compared with the proliferation of actinomycin D and nanoparticle treated cells. Error bars represent SD. *p < 0.1, **p < 0.05 compared to control. n = 3 with 4 technical replicates.

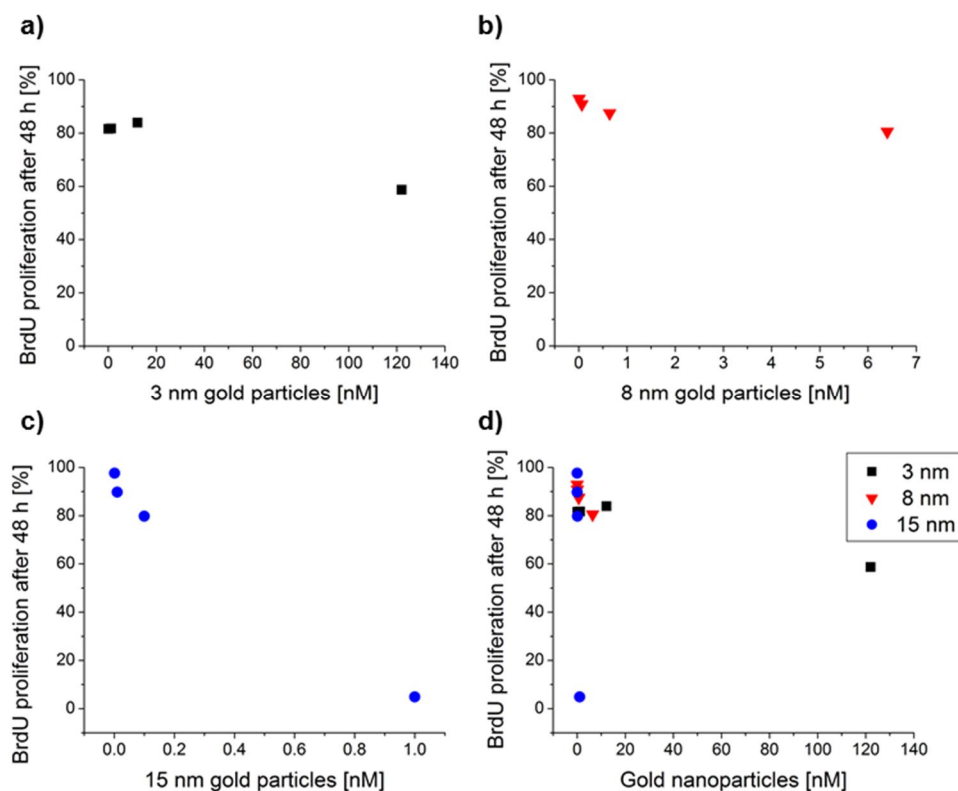


Figure 32: Gold nanoparticle toxicity as a function of molar particle concentration. The BrdU proliferation after 48 h of nanoparticle exposure was plotted against the molar particle concentrations corresponding to 0.02 - 20 $\mu\text{g ml}^{-1}$ gold nanoparticles.

2.3.8.3 Cellular morphology

In addition to the applied assays, the cellular morphology as an indicator for cell viability was controlled by light microscopy (Figure 33). After 48 h, control cells without any treatment showed a confluent cell layer (Figure 33a). In contrast, the exposure of A549 cells to 20 $\mu\text{g ml}^{-1}$ of 3 nm gold particles resulted in a less confluent layer. Additionally, a few apoptotic or dead cells were observed (Figure 33b). A similar result was obtained for cells exposed to 20 $\mu\text{g ml}^{-1}$ of 8 nm gold particles. In contrast to an exposure to 3 nm gold particles, less apoptotic or dead cells were detected (Figure 33c). These observations confirmed the data generated by the WST-1 and BrdU assay. An exposure to 20 $\mu\text{g ml}^{-1}$ of 15 nm gold particles was shown to dramatically decrease the proliferation and viability of A549 cells. After 48 h of nanoparticle exposure, only a few cells were detectable and most of them were apparently not viable anymore (Figure 33d). The polymer did not cause any decrease in cell proliferation and viability. Even at high concentrations the image revealed a confluent cell layer of A549 cells (Figure 33e). In conclusion, the images recorded by light microscopy were in good accordance with the assay outcome.

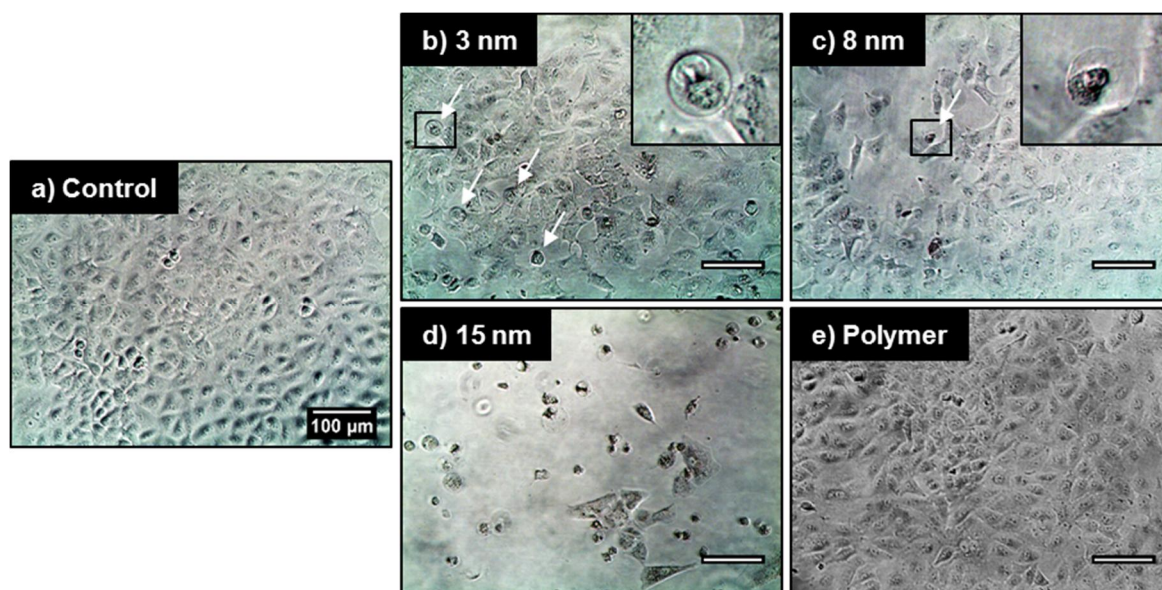


Figure 33: The cell morphology of A549 cells after exposure to cytotoxic nanoparticle concentrations. A549 cells were analyzed by light microscopy during the cytotoxicity testing. Control cells are shown in a). On the other images, cells after 48 h exposure to b) $20 \mu\text{g ml}^{-1}$ of 3 nm gold particles, c) $20 \mu\text{g ml}^{-1}$ of 8 nm gold particles, d) $20 \mu\text{g ml}^{-1}$ of 15 nm gold particles, and e) $713 \mu\text{g ml}^{-1}$ of polymer are shown. Dead or apoptotic cells are indicated by arrows. Magnifications of apoptotic or dead cells are shown in the upper right. The results are representative for three independent experiments with different cell passage numbers.

2.3.9 Inhibition of microtubule-mediated transport by nocodazole treatment

STED and confocal microscopy revealed an internalization of 3 nm, 8 nm, and 15 nm gold particles in A549 cells. The accumulation pattern of the 8 nm gold particles in particular indicated an active nanoparticle transport to the perinuclear region according to well-defined routes of endocytic transport. Within the present section, a potential microtubule-mediated transport of internalized gold nanoparticles was investigated. For this purpose, A549 cells were exposed to 8 nm gold particles for 24 h. This led to the aforementioned perinuclear accumulation of the nanoparticles (*Figure 34a*). To inhibit microtubule-mediated transport, the microtubule depolymerization agent nocodazole was added to the cells. Nocodazole caused a depolymerization of the tubulin cytoskeleton and only a few tubulin filaments were still visible (*Figure 34b*). Furthermore, the perinuclear accumulation of the 8 nm gold particles after 24 h exposure was affected. When nocodazole was removed and the cells were incubated for another hour in cell culture medium, the tubulin network and the gold nanoparticles started to organize again (*Figure 34c*). DMSO, the nocodazole solvent, did not cause any microtubule depolymerization (*Figure 34d*).

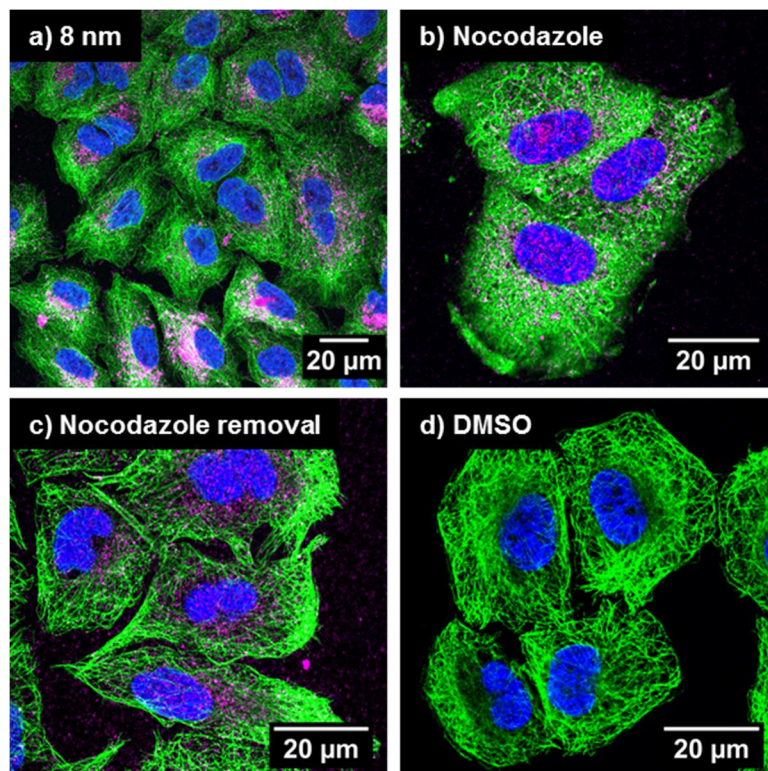


Figure 34: Images of A549 cells after nocodazole treatment.

Confocal images of gold nanoparticles (magenta), α -tubulin (green), and the cell nucleus (blue) were recorded. a) A549 cells exposed to 8 nm gold particles for 24 h. A perinuclear nanoparticle accumulation was observed. b) A549 cells treated with 10 μ M nocodazole for 30 min after a 24 h exposure to 8 nm gold particles. The perinuclear nanoparticle accumulation disappeared after 30 min nocodazole treatment and the microtubule network was disrupted. c) A549 cells treated with 10 μ M nocodazole for 30 min after a 24 h exposure to 8 nm gold particles and a subsequent incubation in DMEM + 10 % FBS for 1 h. After removal of nocodazole, microtubules polymerized again and the gold nanoparticles were re-organized at the perinuclear region. d) A549 cells incubated with 0.03 % DMSO. The nocodazole solvent had no influence on the microtubule structure as seen for nocodazole. The background of the images was removed and the contrast was enhanced. n = 1 with 3 technical replicates.

For a better visualization of the intracellular nanoparticle distribution after nocodazole treatment, confocal z-stacks of single A549 cells were recorded (Figure 35). The corresponding maximum intensity projections illustrated the random distribution of 8 nm gold particles after 24 h exposure and nocodazole treatment (Figure 35a). After nocodazole washout and a re-incubation of the cells in cell culture medium for 1 h, the gold nanoparticles accumulated again at the perinuclear region (Figure 35b). A549 cells exposed to 8 nm gold particles and not treated with nocodazole showed a perinuclear accumulation of the 8 nm gold particles as well (Figure 35c). This observation demonstrated a strong dependency of the intracellular gold nanoparticle transport and the gold nanoparticle accumulation on the integrity of the microtubule network.

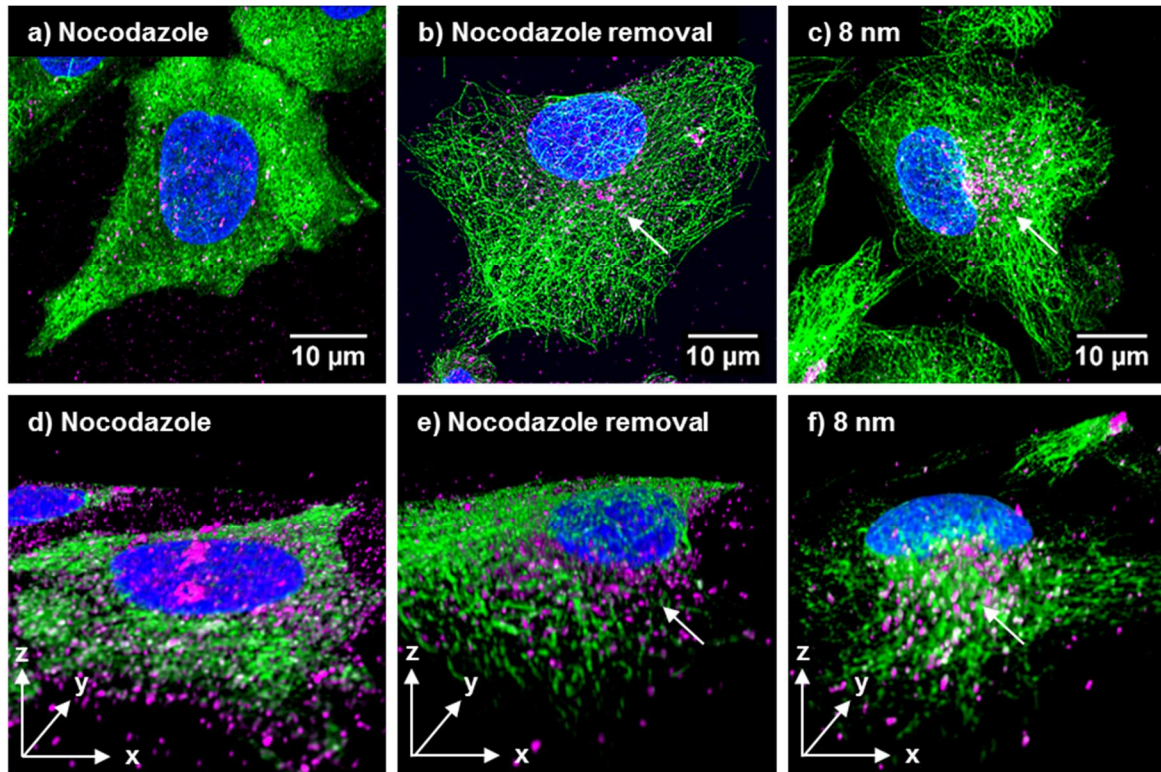


Figure 35: Maximum intensity projections and 3D volumes of A549 cells after nocodazole treatment. Confocal z-stacks of gold nanoparticles (magenta), α -tubulin (green), and the cell nucleus (blue) were recorded and plotted as maximum intensity projections or 3D volumes. a) Maximum intensity projection and d) 3D volume of a cell treated with 10 μ M nocodazole for 30 min after a 24 h exposure to 8 nm gold particles. Microtubules were depolymerized and the nanoparticles were randomly distributed throughout the whole cells. b) Maximum intensity projection and e) 3D volume of a cell treated with 10 μ M nocodazole for 30 min after a 24 h exposure to 8 nm gold particles and a subsequent incubation in DMEM + 10 % FBS for 1 h. After nocodazole wash-out and a re-incubation of the cells, microtubules re-polymerized and once again the nanoparticles started to organize at the perinuclear region of the cell (see arrows). c) Maximum intensity projection and f) 3D volume of a control cell exposed to 8 nm gold particles, without nocodazole treatment. The nanoparticles accumulated at the perinuclear region of the cell. Z-stacks were deconvolved and the contrast of the images was enhanced. n = 1 with 3 technical replicates.

2.3.10 Electron microscopy of gold nanoparticles and cytoskeletons of A549 cells

2.3.10.1 SEM analyses

The intracellular distribution of gold nanoparticles in relation to the tubulin cytoskeleton and a transport of gold nanoparticles along microtubules was studied by fluorescence microscopy as described in the previous sections. However, the high atomic number of gold provided a sufficient contrast to the biological specimen and allowed for a detection of cell-associated gold nanoparticles by electron microscopy techniques as well (Robinson and Vandr  1997). Within this study, whole cell samples of A549 cells were prepared for electron microscopy. For visualization of the tubulin cytoskeleton, detergent-soluble components of A549 cells, like the cell membrane, were removed according to a protocol presented by Bell *et al.* (Bell *et al.*, 1987). Cells treated using this procedure were compared with untreated cells (Figure 36). For untreated A549 cells, the convex cell nuclei were clearly visible and the cells were covered by their cell membrane (Figure 36a, c). After the extraction procedure, intracellular filamentous structures became visible, indicating a removal of the cytoplasmic membrane (Figure 36b, d). The cell nuclei appeared to be surrounded by a dense filamentous network. Former cell boundaries still can be recognized. The applied method resulted in

a preparation of the whole cytoskeleton, including actin filaments and microtubules, but did not allow for a discrimination of different types of cytoskeletal filaments.

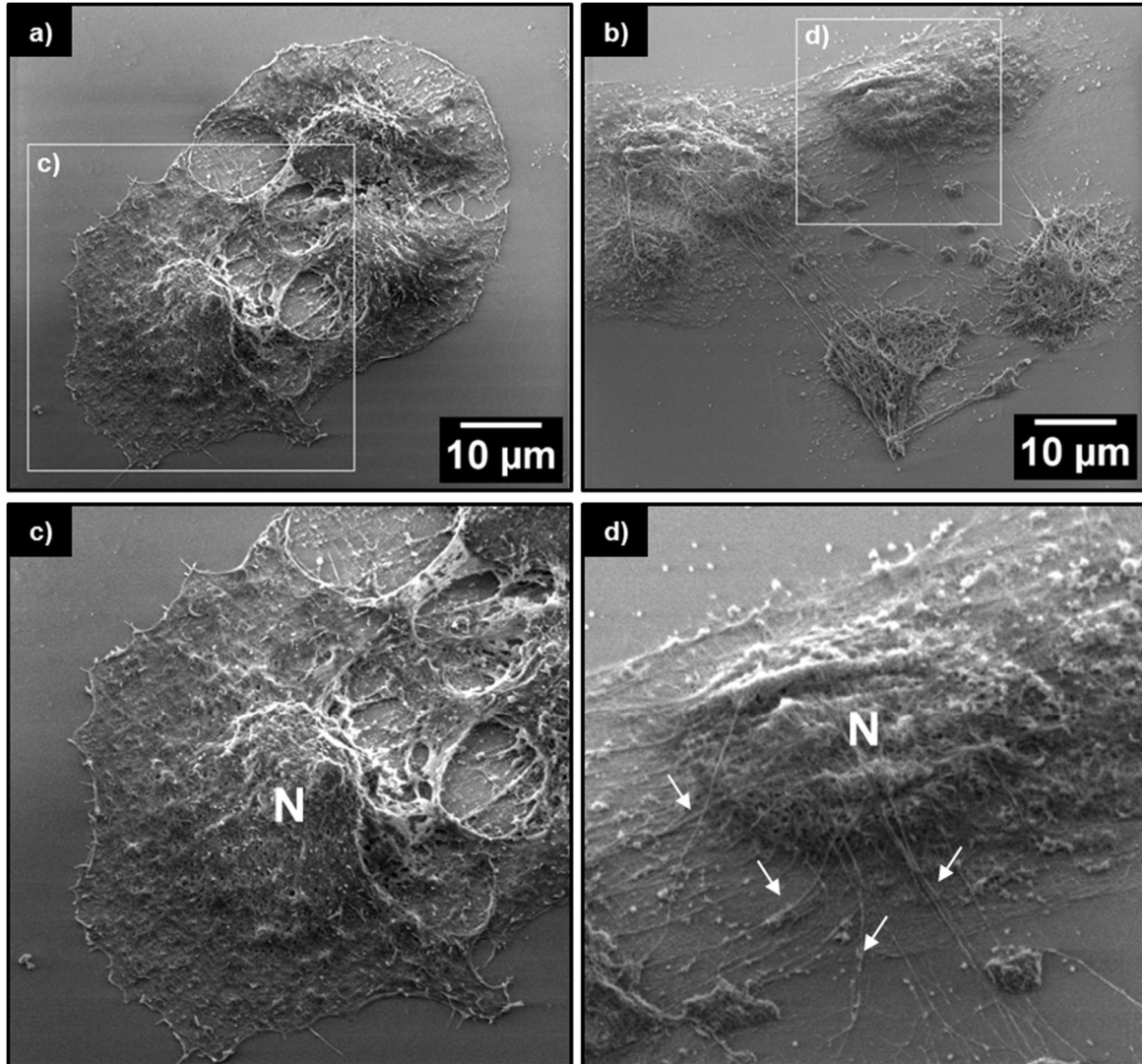


Figure 36: SEM images of untreated A549 cells and cells after the preparation of the cytoskeleton. A549 cells were fixed and imaged by SEM. a) A549 cells without any detergent treatment. b) A549 cells after detergent treatment and removal of detergent-soluble components; according to Bell *et al.* (Bell *et al.*, 1987). c) An untreated cell was depicted with higher magnification (see rectangle). The convex nucleus (N) was visible. The cell showed clear boundaries and was covered with the cell membrane. No cytoskeletal filaments were observed. d) A treated cell was depicted with higher magnification (see rectangle). The cell nucleus was visible as well. However, no clear cell boundaries were left indicating a loss of the cell membrane. In addition, cytoskeletal filaments could be recognized from the image (see arrows). Secondary electrons were detected and used for image generation. Images were recorded under high vacuum conditions by using an acceleration voltage of 2 keV. n = 1. Images were taken by Dr. M. Koch.

The applied protocol was regarded to be suitable for the imaging of the complete cytoskeleton from A549 cells. Therefore, A549 cells were exposed to $2 \mu\text{g ml}^{-1}$ of 8 nm gold particles for 4 h and were subsequently prepared to investigate a potential association of nanoparticles and cytoskeletal filaments. Secondary electrons were detected to describe the cell morphology (Figure 37a-c) whereas backscattered electrons were used for the imaging of the gold nanoparticles (Figure 37d-f). By secondary electrons, the cytoskeletal network of the imaged cell was visible indicating a proper extraction of detergent-soluble components, such as the cell membrane (Figure 37a-c). By increasing the magnification, single cytoskeletal filaments became visible. Size measurements of the filaments

revealed diameters from 9 nm to 27 nm (*Figure 37c*). These results were in accordance with diameters for actin filaments (5 - 9 nm) and microtubules (25 nm) (Alberts and Wilson 2008). Backscattered electrons indicated the presence of gold nanoparticles, which appeared as bright spots due to their high atomic number (*Figure 37d-f*). Single gold nanoparticles were found to be associated with filaments, as indicated by arrows (*Figure 37f*). Furthermore, the gold nanoparticles accumulated, which resulted in a high gold signal that was represented by the bright spot in *Figure 37f*. The corresponding secondary electron image (*Figure 37c*) indicated a vesicular structure, by which the particles potentially were transported throughout the cell. The recorded image exhibited analogy to an electron micrograph of a single microtubule, associated with two vesicles from the literature (Schnapp *et al.*, 1985) (*Figure 38a*). Hence, a vesicular structure associated with cytoskeletal filaments can be assumed from the recorded data (*Figure 38b*). Additionally, backscattered electrons revealed the accumulation of 8 nm gold particles inside the potential vesicle (*Figure 38c*). For the single microtubule filament shown in *Figure 38a*, which derived from freeze-dried squid giant axon, diameters of 22 - 27 nm were measured (Schnapp *et al.*, 1985). The filament from *Figure 38b*, to which the vesicle seemed to be attached, exhibited a diameter of 55 nm. This value is above 25 nm, which is generally regarded as the diameter of a single microtubule filament (Alberts and Wilson 2008). Therefore, the measured filament potentially consisted of two single microtubules, which cannot be recognized as separated filaments from the data.

The SEM images indicated two different populations of gold nanoparticles. One fraction was found to accumulate inside vesicular structures whereas another portion was detected as single particles associated with cytoskeletal filaments. The removal of detergent-soluble membrane components, as carried out during sample preparation, might affect the intracellular gold nanoparticle pattern due to the invasion of membrane-associated particles that were released from the cell membrane after detergent treatment. However, the images recorded by SEM strengthened the assumption of a partial active nanoparticle transport by vesicles along filaments of the cytoskeleton.

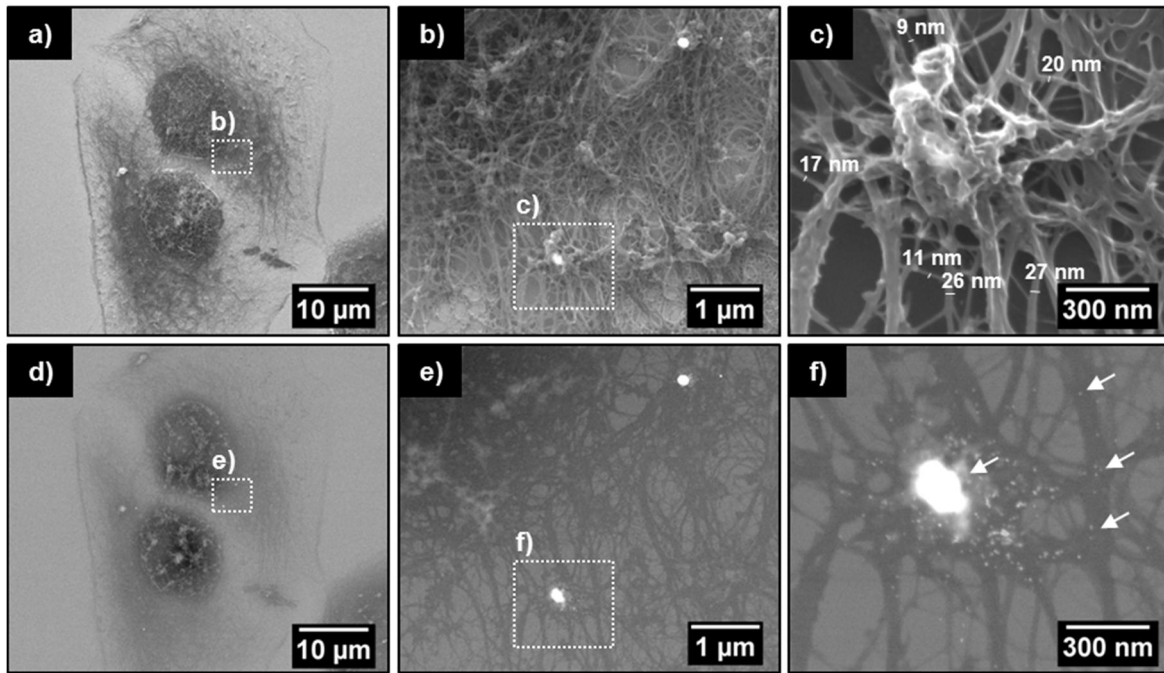


Figure 37: SEM images of A549 cells after exposure to 8 nm gold particles and the preparation of whole cytoskeletons.

A549 cells were exposed to $2 \mu\text{g ml}^{-1}$ of 8 nm gold particles for 4 h and subsequently prepared for the cytoskeleton according to Bell *et al.* (Bell *et al.*, 1987) a) - c) Secondary electron images showed the cell topography and the prepared cytoskeleton. By increasing the magnification, the filament network became visible and finally single filaments were detected. Diameters of selected filaments were measured. The obtained values were in accordance with the dimensions of actin filaments and microtubules. d) - f) Backscattered electron images from the same positions revealed the presence of gold nanoparticles (bright spots). Single gold nanoparticles were attached to filaments (see arrows) whereas others accumulated resulting in a high gold signal that is represented by the very bright spot (see arrowhead). For image acquisition, an acceleration voltage of 20 keV was applied. $n = 1$ with 2 technical replicates. Images were taken by Dr. M. Koch.

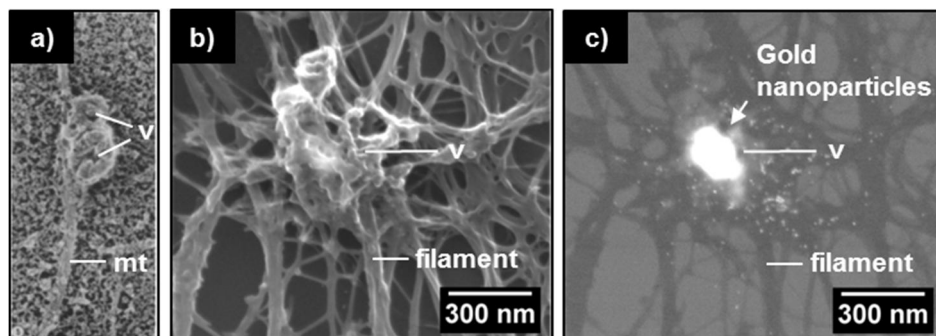


Figure 38: Comparison of the recorded SEM images with electron micrographs of a microtubule and associated vesicular structures from the literature (Schnapp *et al.*, 1985).

a) Single tubulin filaments were prepared from squid giant axon, rapid-frozen, freeze-dried, and subsequently imaged by TEM. One microtubule (mt) was imaged by TEM, which was associated with two vesicular structures (v). Magnification 220,000 x. b) The secondary electron image from Figure 37c showed a similar structure including a vesicle (v) attached to a cytoskeletal filament. Magnification 200,000 x. c) The backscattered electron image revealed the accumulation of 8 nm gold particles inside the vesicular structure. Magnification 200,000 x.

2.3.10.2 TEM analyses

In order to confirm the results obtained from the SEM analyses, TEM imaging was carried out. In comparison to SEM, TEM allows an even higher resolution that can be used to resolve single gold nanoparticles inside a cell. However, a prerequisite for TEM is a rather thin sample, which is completely penetrable for the electron beam. Thick samples or sample areas composed of elements with high atomic number absorb and scatter the electron beam to a higher extent and therefore appear black in the final image. To minimize scattering effects of the cell substrate, A549 cells were grown directly on the carbon film of TEM grids. The carbon film, with a thickness of 30 - 50 nm and low atomic number, can be penetrated by the electron beam and allows for imaging of cells grown on top. Thereby, the thickness of the cell (usually 5 - 10 μm) contributes to the contrast formation (mass-thickness contrast). A549 cells grown on TEM grids were exposed to 50 $\mu\text{g ml}^{-1}$ of 8 nm gold particles for 24 h. From the cytotoxicity assays, this concentration is expected to be toxic. Still, the small field of view in TEM hampered the detection of cell-associated gold nanoparticles at low concentrations. Therefore a higher concentration of gold nanoparticles was chosen to facilitate TEM imaging. The cells were treated according to Bell *et al.* (Bell *et al.*, 1987), as described previously. An overview of the imaged cell showed the cell nucleus as a black spot in the center of the cell (*Figure 39a*). The strong signal of the nucleus was attributed to the mass-thickness contrast. The surrounding cell body was thinner and in consequence more transparent for the electron beam. An area in the outer cell region was imaged with increasing steps of magnification (*Figure 39b-f*). Due to their high atomic number gold nanoparticles appeared as black dots in the TEM. Within the highest magnification single gold nanoparticles that seemed to be associated with cytoskeletal filaments were resolved (*Figure 39f*). Size measurements of the imaged gold nanoparticles were in accordance with the initial TEM diameter of the gold particles (8 nm). Thus, an association of gold nanoparticles and cytoskeletal filaments was implied. However, from the images taken only 2D information were obtained. Three-dimensional imaging was used to confirm an association of nanoparticles and filaments. To gain 3D information, the TEM sample holder was tilted and a tilt angle series of cytoskeletal filaments and gold nanoparticles was recorded from another part of the cell (*Figure 40*). Tilt angles from +30° to -28° were applied in steps of 2°. Images for tilt angles of +30°, +20°, +10°, 0°, -10° and -20° are presented in *Figure 40a-f*. Four single nanoparticles (number 1 - 4), which were potentially associated with cytoskeletal filaments were chosen and followed throughout the tilt angle series. Nanoparticles 1 - 3 stayed attached to the filaments during the tilting process. Thereby, an association of filaments and gold nanoparticles was confirmed. Nanoparticle 4, which appeared to be associated to a filament, lost its connection to the filament by increasing the tilt angle of the TEM sample holder. In contrast to the SEM images (*Figure 37*), no vesicular structures could be observed by TEM. The imaged areas only contained single nanoparticles and did not showed a particle accumulation inside vesicles as observed previously. This fact demonstrated the presence of two different nanoparticle populations. Accumulated gold nanoparticles were found to associate with the cytoskeleton *via* vesicles whereas single particles seemed to directly interact with cytoskeletal filaments.

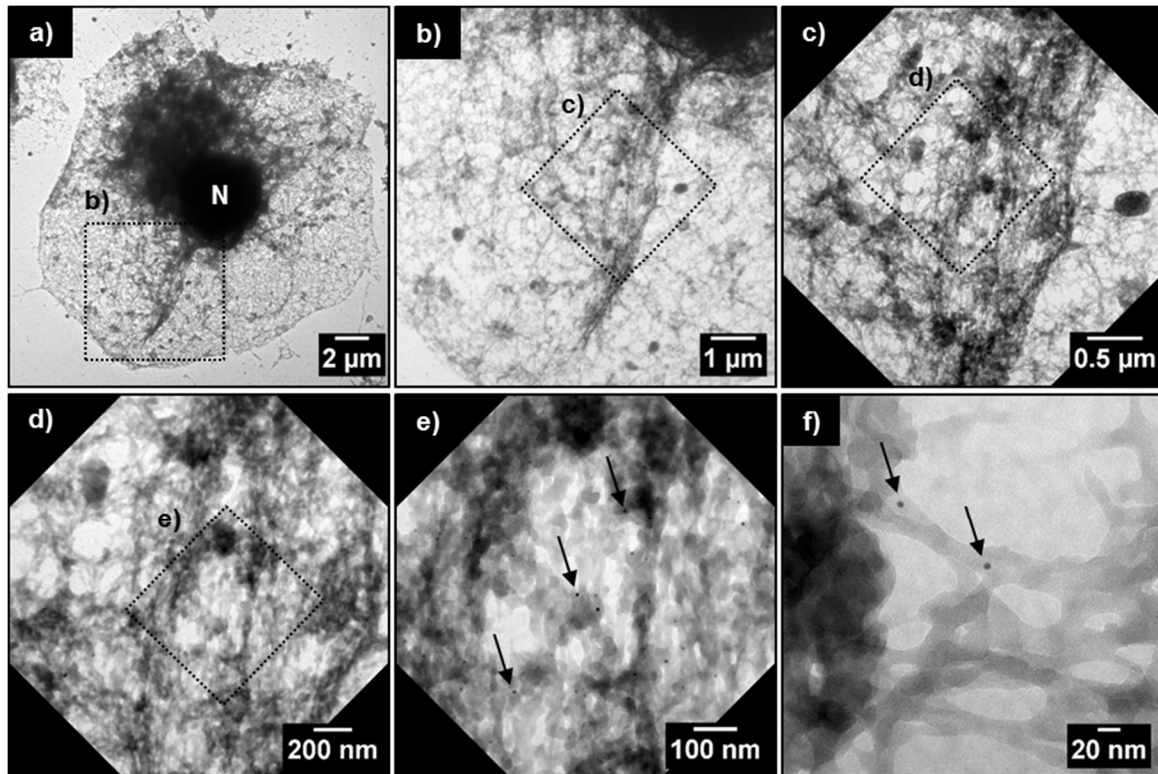


Figure 39: Imaging of A549 cells and 8 nm gold particles by TEM after cytoskeleton preparation.

A549 cells were exposed to $50 \mu\text{g ml}^{-1}$ of 8 nm gold particles for 24 h and subsequently prepared for the imaging of the cytoskeleton. a) - e) By increasing the magnification, cytoskeletal filaments and internalized gold nanoparticles, partially indicated by arrows, became visible. The rectangle specifies the magnified part of the cell. The nucleus (N) was indicated by the black spot in the center of the cell. f) 8 nm gold particles were shown to associate with filaments of the cytoskeleton. Images c) - e) were rotated for a better correlation. $n = 1$ with 2 technical replicates. Images were taken by Dr. M. Koch.

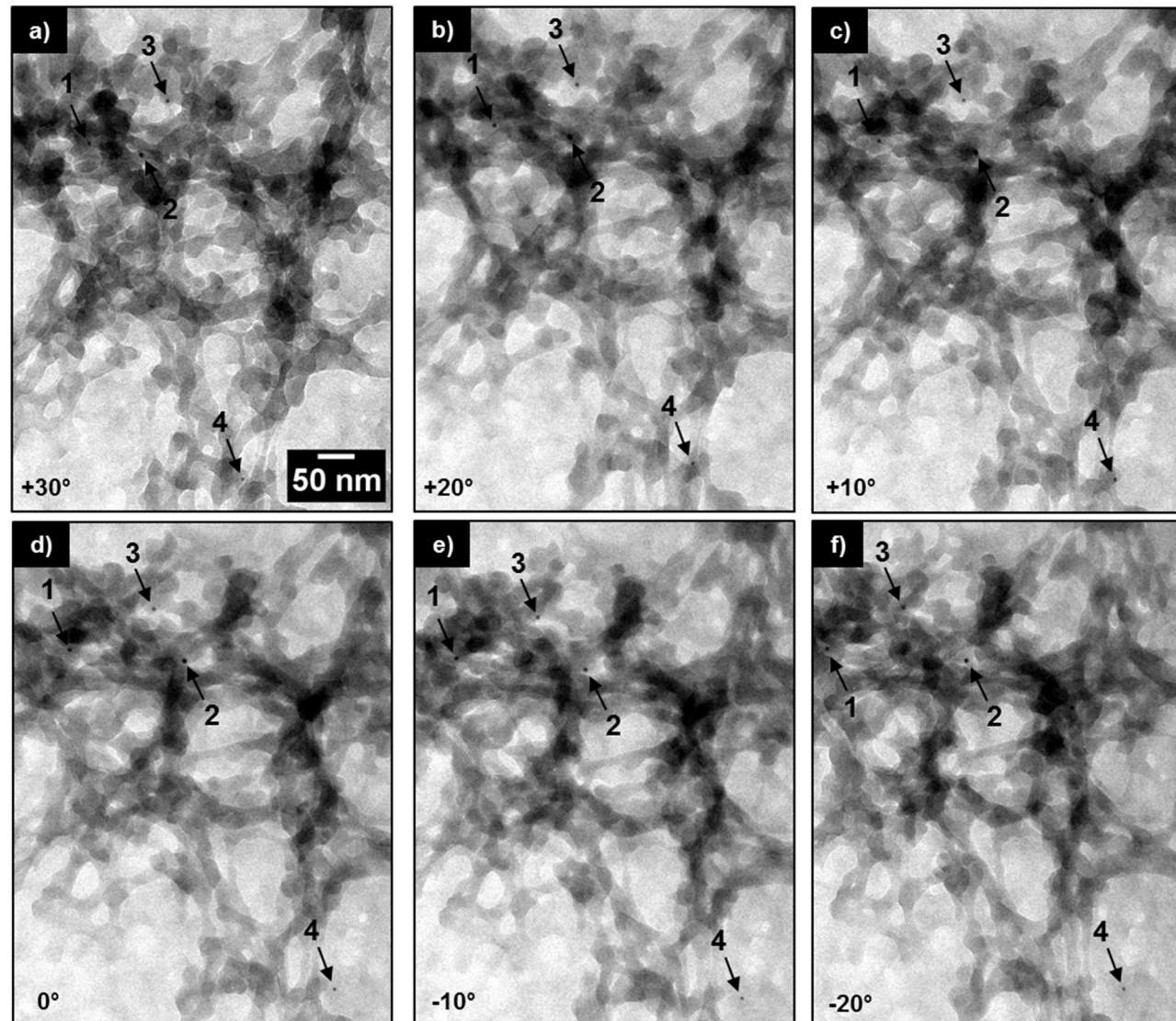


Figure 40: TEM tilt angle series of A549 cells after 24 h exposure to 8 nm gold particles and preparation of the cytoskeleton. Four nanoparticles (1-4) were followed within the tilting process and the association of nanoparticles and filaments was investigated. The tilt angles are stated in the lower left of each image.

2.4 Discussion

2.4.1 The intracellular distribution of gold nanoparticles in A549 cells

2.4.1.1 Gold nanoparticle distribution in relation to the tubulin cytoskeleton

Endocytosis is generally regarded as the predominant uptake mechanism of nanoparticles that enter the lung (Mühlfeld *et al.*, 2008), or *in vitro*, when nanoparticles interact with cells (Zhao *et al.*, 2011). Gold nanoparticles have already been found inside different compartments of the endocytic pathway, such as endosomes (Chithrani *et al.*, 2006; Chithrani *et al.*, 2009), MVB (Jiang *et al.*, 2008), and lysosomes (Chithrani *et al.*, 2009; Coradeghini *et al.*, 2013), indicating an active intracellular gold nanoparticle transport. In the present study, fluorescently labeled gold nanoparticles with sizes of 3 nm, 8 nm, and 15 nm were taken up by A549 cells, which were used as a model for type II alveolar epithelial cells. For A549 cells, an uptake of inorganic nanoparticles by endocytosis has already been demonstrated (Stearns *et al.*, 2001; Brandenberger *et al.*, 2010). In the present study, nanoparticle internalization *via* endocytosis was confirmed by the perinuclear accumulation pattern of the internalized gold particles. Such a pattern is typical for cargo, which has been endocytosed and transported to late endosomes or lysosomes (Alberts and Wilson 2008). In addition, the nanoparticles accumulated close to the MTOC, where microtubule (-) ends are located. The transport of endocytic compartments is mediated by dyneins. These enzymes move along microtubules from (+) to (-) ends (Aniento 1993). Hence, an accumulation of nanoparticles at the MTOC can be related to a microtubule-mediated transport of internalized gold nanoparticles. A similar behavior was shown for virus capsids, which accumulated at the MTOC of Vero cells after dynein-mediated transport (Sodeik 1997), and for silica nanoparticles, which were grouped around the MTOC of human alveolar macrophages after particle uptake (Diesel *et al.*, 2013).

The intracellular accumulation pattern of 8 nm and 15 nm did not change by increasing the exposure time to 48 h. In comparison to that, 3 nm gold particles were distributed randomly throughout A549 cells after 48 h of exposure. No accumulation close to the nucleus was observed. The different behavior of these particles can be explained by a possible endosomal escape. It is known that under certain conditions nanoparticles (Vasir and Labhasetwar 2007), and also gold nanoparticles (Nativo *et al.*, 2008), are able to escape from distinct uptake and transport routes and thus might end up inside the cytoplasm or inside cellular components, which are usually not linked to the intracellular transport machinery. Virus capsids use an endosomal escape to reach the cell nucleus. After endosomal escape, they bind to cytosolic import receptors *via* nuclear localization signals (NLS), which allow a translocation into the cell nucleus (Smith 2004). Import receptors are located in the cytoplasm (Alberts and Wilson 2008) and in principle are also able to bind to escaped nanoparticles as well as other proteins forming the protein corona. An endosomal escape of nanoparticles can be increased by surface functionalization, e.g. with cell penetrating peptides or cationic polymers (Varkouhi *et al.*, 2011).

Besides the nanoparticle distribution, the intracellular distribution of the fluorescently labeled polymer surrounding the gold particles was studied. Interestingly, a similar accumulation pattern as seen for the gold nanoparticles was observed. This fact indicates that the intracellular gold nanoparticle transport was mediated at least in part by the polymer shell that was used for particle stabilization and fluorescence labeling. The polymer that was used for particle stabilization was functionalized with mPEG750 and was strongly negatively charged due to free carboxy groups. Within recent studies, nanoparticle uptake and intracellular transport was shown to be dependent

on the nanoparticle coating. For iron oxide nanoparticles, which were functionalized with either PEG, glucose, or galactose a different uptake in Vero cells was shown (Moros *et al.*, 2012). Iron oxide nanoparticles with a high density of PEG were not taken up by the cells. In comparison to the PEG-coated gold nanoparticles used within the present studies, these particles exhibited a zeta potential close to zero. The surface charge, which is reflected by the zeta potential, influences cellular nanoparticle uptake and trafficking (Fröhlich 2012) and explains the different outcome of the present study compared to the work done by Moros *et al.* The glucose-functionalized nanoparticles were found throughout the cell whereas galactose-functionalized iron oxide nanoparticles remained in the cell periphery or stayed attached to the cell membrane (Moros *et al.*, 2012). For gold nanoparticles, differences between the cellular uptake of PEG-coated and citrate-stabilized nanoparticles have been reported (Brandenberger *et al.*, 2010). 15 nm PEG-coated gold particles entered A549 cells *via* caveolin- and/or clathrin-mediated endocytosis. In comparison, 15 nm citrate-stabilized gold particles were predominately taken up by macropinocytosis. The different uptake mechanisms influenced the subsequent intracellular trafficking of the particles. However, the preferred intracellular targets of both types of nanoparticles were vesicles of different sizes. In addition, the limited stability of citrate-stabilized nanoparticles should be considered. Citrate-capped gold nanoparticles are susceptible to aggregation (Giljohann *et al.*, 2010) and the observed differences in cell entry might also arise from a decreased nanoparticle stability.

Besides the composition of the stabilizing agent, nanoparticle uptake is also dependent on surface charge. The used gold nanoparticles were strongly negatively charged and internalized by A549 cells. Generally, charged nanoparticles are taken up better than uncharged ones, whereas positively charged particles are taken up to a higher extent than negatively charged particles (Fröhlich 2012). Additionally, positively charged nanoparticles cause a greater cytotoxicity compared to nanoparticles with a negative surface charge, presumably due to cell membrane polarization and an increased calcium influx (Arvizo *et al.*, 2010). Differences in the intracellular fate of positive and negative polylactic acid (PLA) nanoparticles, functionalized with PEG, have been studied in polarized epithelial kidney cells (MDCK cells). PLA nanoparticles bearing a negative charge were internalized *via* endocytosis and underwent lysosomal degradation. Positively charged PLA particles were also taken up *via* endocytosis but stayed within endosomes or transcytosed to the basolateral membrane, thereby avoiding a transport to lysosomes (Harush-Frenkel *et al.*, 2008). Accordingly, the perinuclear accumulation, which was observed for gold nanoparticles internalized by A549 cells, could be attributed also to the negative particle surface charge.

2.4.1.2 Gold nanoparticle distribution in relation to the Golgi

The perinuclear accumulation pattern of 3 nm, 8 nm, and 15 nm gold particles indicated a localization of the nanoparticles inside or in close proximity to the Golgi. The Golgi complex is responsible for transport and modification of secretory proteins. It is part of the exocytic pathway that governs the transport of cargo from the cell to the cell membrane and is also located near the nucleus. Within the exocytic pathway, the Golgi functions as a sorting and packing station for secretory vesicles (Mellman *et al.*, 1986). Nanoparticles that reach the Golgi complex are able to potentially undergo an active nanoparticle export *via* exocytosis. The applied antibody stain of the Golgi *cis*-compartment revealed an accumulation of 3 nm and 8 nm gold particles at the side of the nucleus facing the *cis*-Golgi and an association of Golgi and gold nanoparticles was confirmed by the microscopy data. This observation was in accordance with studies on poly(lactic-co-glycolic acid) (PLGA) nanoparticles that colocalized with the Golgi in OK and HBE cells. For short times after nanoparticle exposure (1 - 4 h), only little colocalization of nanoparticles and the Golgi was present.

This colocalization increased with increasing exposure time and was highest after 24 h of nanoparticle exposure (Cartiera *et al.*, 2009). In contrast, Coradeghini *et al.* could not detect 5 nm and 15 nm gold particles inside the Golgi of mouse fibroblasts by TEM (Coradeghini *et al.*, 2013). Similar results were obtained by Brandenberger *et al.*, who did not detect any gold nanoparticles within the Golgi complex of A549 cells, although different nanoparticle coatings (PEG and citrate) were used (Brandenberger *et al.*, 2010). However, both studies used TEM analysis for gold nanoparticle quantification within the Golgi. The extended sample preparation of cells, which is required for TEM imaging, can also induce a disruption of cellular compartments leading to a loss of cell-associated nanoparticles. Apparently, the interaction of nanoparticles and the Golgi complex differs depending on the nanoparticle properties and the cell type that was investigated. However, exocytosis of nanoparticles has been reported, e.g. for silica nanoparticles (Slowing *et al.*, 2011). A study by Chen *et al.* demonstrated exocytosis of positively charged gold nanoparticles from HT-29 cells (Chen *et al.*, 2010).

2.4.1.3 Gold nanoparticle distribution in relation to the cell nucleus

The translocation of 3 nm and 8 nm gold particles into the nucleus of A549 cells was revealed by confocal microscopy and subsequently quantified by image analyses. Fluorescence signals of both nanoparticle sizes were found inside the nucleus. Compared to the total applied particle number only a small fraction entered the nucleus. The highest nuclear uptake was observed for 8 nm gold particles, but the number of nanoparticles inside the nucleus differed between the three analyzed datasets, which were used for quantification. It is known that cellular nanoparticle uptake is influenced by the cell cycle (Kim *et al.*, 2011). Cells in G2 phase and mitosis internalize a higher amount of nanoparticles than cells in S phase or G0 / G1 phase. Potentially, also the amount of gold nanoparticles inside the nucleus depends on the cell cycle phase. Compared to the 8 nm gold particles, less fluorescence signals deriving from 3 nm gold particles were found inside the nucleus. The 3D objects counter plugin from the Fiji software that was used for quantification required a certain threshold. To guarantee equal conditions the same threshold value was applied to all quantifications carried out. As the 3 nm gold particles exhibited a lower fluorescence labeling than the 8 nm ones, an imperfect detection of the fluorescence spots cannot be excluded and possibly contributed to the lower amount that was quantified. The quantification procedure was further restricted by the optical resolution in confocal microscopy, which does not allow for a detection of single nanoparticles. Hence, only fluorescence of particle aggregates was detected and the real nanoparticle number remained unknown. Additionally, the applied Hoechst stain only allowed an estimation of the nuclear boundaries. The nuclear lamina defines the nucleoplasm and is composed of lamins (intermediate filaments) (Aebi *et al.*, 1986) and is consequently not stained by a DNA specific dye. Signals coming from outside the DNA stain were not considered during the quantification. Despite these drawbacks, the quantification revealed only little fluorescence of the labeled polymer inside the nucleus. Thus, the nuclear penetration of gold nanoparticles seemed to be more efficient compared to the uptake of the particle shell alone. One explanation is based on the polymer structure that has been visualized by SEM (*Figure S3*). In water, the polymer was assembled as a particle-like structure, presumably due to its amphiphilic character. The observed particles had sizes of 30 - 40 nm after drying on a TEM grid. A diameter of 39 nm is generally seen as a threshold for the nuclear penetration of macromolecules (Pante 2002). Hence, only a small fraction of the polymer was able to translocate into the cell nucleus. Though, the drying of the polymer onto the TEM grid is expected to cause a conformation change leading to larger polymeric particles. A different size distribution of the polymer in solution is assumed but hardly measurable. This fact

limits a reliable statement concerning a hampered nuclear translocation of the polymer coating due to the nuclear pore sizes.

Nanoparticles can reach the nucleus by escaping from distinct uptake and transport routes, e.g. by an endosomal escape, which has already been discussed in the previous section. An endosomal escape usually requires the functionalization of nanoparticles, e.g. with cell penetrating peptides or cationic polymers (Varkouhi *et al.*, 2011). Gu *et al.* demonstrated a nuclear uptake of surface-modified gold nanoparticles with sizes of 3 - 5 nm. This uptake was primarily related to the surface modification. However, a size effect was also discussed as nanoparticles of such a small size could diffuse more efficiently through nuclear pores (Gu *et al.*, 2009). A nuclear penetration of surface-functionalized 13 nm gold particles was demonstrated as well (Nativo *et al.*, 2008). However, for gold nanoparticles without any coating of cell penetrating peptides or cationic polymers, like the ones used in the present study, no nuclear penetration was observed (Brandenberger *et al.*, 2010).

2.4.2 Genotoxicity of gold nanoparticles

Nanoparticles are capable to induce DNA damage, which is also known as genotoxicity. Direct genotoxicity is triggered by an interaction of nanoparticles with the cell nucleus (Donaldson *et al.*, 2010). DNA can either physically interact with nanoparticles, or with ROS that can be generated on nanoparticle surfaces (Nel 2006). An indirect genotoxicity is caused by the release of endogenous ROS due to mitochondrial damage by nanoparticles, an increased NADPH oxidase activity, or due to the depletion of antioxidants, such as glutathione (Donaldson *et al.*, 2010; Singh *et al.*, 2009). Increasing ROS levels and / or the depletion of antioxidants, which usually counteract free radicals like ROS, can lead to oxidative stress resulting in DNA damage. An indicator for genotoxicity is the formation of micronuclei, small nuclei in the cytoplasm that are formed whenever a chromosome or its fragment is not incorporated into one of the daughter cell nuclei during cell division (Bhatia and Kumar 2013). In the present study, micronuclei were observed in A549 cells that were treated with 3 nm gold particles. However, micronuclei formation was not quantified, which limits an evaluation of genotoxicity. Besides micronuclei formation, 3 nm and 8 nm gold particles were detected inside the nucleus of A549 cells, potentially followed by an interaction of nanoparticles and DNA causing a direct genotoxicity. A study by Pan *et al.* revealed the genotoxic potential of 1.4 nm gold particles, which caused oxidative stress and mitochondrial damage. The ROS formation was related to the high surface/volume ratio of the particles (Pan *et al.*, 2009). In addition, Li *et al.* demonstrated the downregulation of DNA repair genes in lung fibroblasts after gold nanoparticle exposure (Li *et al.*, 2008). Taken together, the results from the present study and the results known from the literature suggest a genotoxic potential of gold nanoparticles, which, however, requires further investigations.

2.4.3 Cytotoxicity of gold nanoparticles

The WST-1 assay and the BrdU assay were conducted to assess the impact of 3 nm, 8 nm, and 15 nm gold particles on viability and proliferation of A549 cells. Two different types of assays were applied to measure cytotoxicity and cell proliferation. Generally, the outcome of cell-based assays can be influenced by interactions of nanoparticles and the assay. Misinterpretation of toxicity testing can occur due to nanoparticle-dye interactions (Monteiro-Riviere *et al.*, 2009; Wörle-Knirsch *et al.*, 2006). In the present work, an interaction of the nanoparticles with the cell-based assays was experimentally excluded. The results revealed a cytotoxic potential of gold nanoparticles depended on the gold mass concentration. At the highest concentration tested ($20 \mu\text{g ml}^{-1}$), an impact on cell viability and cell proliferation was observed for all particle sizes. However, cell viability and

proliferation was impaired to a different extent ($15\text{ nm} > 3\text{ nm} > 8\text{ nm}$). This different cytotoxic potential could not be related to the applied particle number. However, it is possible that a higher amount of 15 nm gold particles was taken up by A549 cells. It is well-known that gold nanoparticle uptake into cells depends on the particle size. Chithrani *et al.* investigated the internalization of 14 - 100 nm gold particles and demonstrated that the uptake was highest for particles with a diameter of 50 nm (Chithrani *et al.*, 2006). A higher amount of internalized gold nanoparticles might affect the cell viability to a higher extent. However, no quantification of cell-associated gold nanoparticles was carried out. Coradeghini *et al.* quantified the amount of cell-associated 5 nm and 15 nm gold particles by ICP-MS after uptake into mouse fibroblasts. 5 nm gold particles affected the viability of mouse fibroblasts to a higher extent than 15 nm gold particles at the same molar concentration due to the higher amount of cell-associated 5 nm gold particles (Coradeghini *et al.*, 2013). Although this study has a contrary outcome as it shows a less toxic potential of 15 nm gold particles, it demonstrates the relation between the number of internalized gold nanoparticles and observed cytotoxicity.

A multiplicity studies dealing with gold nanoparticles have been conducted up to now. However, the use of different particle sizes, cell lines, and assays hampers a direct comparison of cytotoxicity. Furthermore, either mass or molar concentrations of particles are used and often only one parameter is given, which does not allow for an easy comparison of the exposure scenario. In *Table 10* examples of past and current studies on gold nanoparticle toxicity are listed and a calculation of both, molar particle concentration and mass concentration, was done to allow for a comparison with the results from the present study. Within the first studies that addressed the toxicity of gold nanoparticles, very high nanoparticle concentrations were used (Goodman *et al.*, 2004; Connor *et al.*, 2005; Pernodet *et al.*, 2006; Pan *et al.*, 2007). The molar concentrations were occasionally 10,000-times higher than the highest molar concentrations used within this work. Whereas Connor and Pan *et al.* reported no toxicity of 15 nm and 18 nm gold particles at molar concentrations of 250 μM up to even 6.3 mM, the present study indicated a massive cytotoxic effect of 15 nm gold particles at a concentration of 1 nM. Zhang *et al.* showed an impact of 15 nm gold particles on erythroleukemia cells at molar concentrations of 7.3 - 29.19 nM, which is more in line with the presented results (Zhang *et al.*, 2009). Patra *et al.* conducted a relevant study regarding the applied nanoparticle concentration and the used cell line. For A549 cells, a toxicity of 33 nm gold particles was demonstrated within a range of 10 - 120 nM (Patra *et al.*, 2007). At the same molarity, toxicity was observed within the present study for 3 nm gold particles. However, other studies revealed no cytotoxic potential of gold nanoparticles even though similar mass and molar concentrations as well as similar particle sizes were used (Cui *et al.*, 2012; Freese *et al.*, 2012). Apparently, gold nanoparticle toxicity is highly dependent on the cell system that is used for toxicity studies even though particles of the same size were used. Besides differences in used cells or cell lines, differences in the applied cytotoxicity measurement have also to be taken into account.

Regarding the scenario of nanoparticle inhalation and a particle deposition in the lung, other concentrations have to be considered. Geiser *et al.* calculated that 2×10^{13} nanoparticles can be inhaled within one day by an adult human, whereof 120 - 2,400 nanoparticles encounter one alveolar epithelial cell per hour (Geiser and Kreyling 2010). Accordingly, a nanoparticle exposure of 5 - 48 h would lead to 6.0×10^2 - 1.2×10^5 particles per cell. The cytotoxicity testing in the present study was carried out with minimal doses of 5.9×10^7 15 nm gold particles, 3.9×10^8 8 nm gold particles, and 7.3×10^9 3 nm gold particles. Considering the initial cell number of 5×10^3 and the liquid column above the cells ($\sim 3\text{ mm}$), each cell residing within the lower 100 μm of this column was exposed to an average of 3.9×10^2 15 nm gold particles, 2.6×10^3 8 nm gold particles, and 4.9×10^4 3 nm gold

particles (Table 9). These values correspond well to 6.0×10^2 - 1.2×10^5 particles per cell, which were calculated based on the study by Geiser *et al.* (Geiser and Kreyling 2010). During microscopy analyses, A549 cells were exposed to a 10-fold higher volume and thus a ten times higher particle number. However, also the initial cell number was one order of magnitude higher and therefore similar particle numbers per cell can be assumed. Based on these calculations, the present study dealt with nanoparticle concentrations in the range of a physiological particle exposure. Contrary, most *in vitro* studies dealing with lung nanoparticle interactions do not state the applied particle number (Park *et al.*, 2007; Lanone *et al.*, 2009). Only a few studies are available where cellular reactions can be correlated with the nanoparticle number. Brandenberger *et al.* reported an increase in the apical plasma membrane surface area of A549 cells after nanoparticle exposure (Brandenberger *et al.*, 2009) and used similar particle numbers according to the present study. Limbach *et al.* demonstrated a nanoparticle-induced formation of ROS in A549 and applied slightly higher particle numbers but also other types of material compared to the present study (Limbach *et al.*, 2007).

Table 9: Determination of nanoparticles per cell with regard to a physiological nanoparticle exposure.

From the gold concentration and the nanoparticle diameter, the number of particles per reaction volume was calculated. This number was divided by the initial cell number of 5×10^3 cells to get the number of particles per cell. Considering that only the first 100 μm of the 3 mm liquid column directly interact with the cells, the number of nanoparticles per cell was recalculated.

Nanoparticle diameter [nm]	Gold concentration [$\mu\text{g ml}^{-1}$]	Number of particles in reaction volume	Number of particles per cell	Number of particles per cell within 100 μm liquid column
3	0.02	7.3×10^9	1.5×10^6	4.9×10^4
8	0.02	3.9×10^8	7.8×10^4	2.6×10^3
15	0.02	5.9×10^7	1.2×10^4	3.9×10^2

The massive impact of $20 \mu\text{g ml}^{-1}$ of 15 nm gold particles was detected by both assays. However, the slight impact of 3 nm gold particles at $0.02 - 2 \mu\text{g ml}^{-1}$ was only determined by the use of the BrdU assay. This observation is based on two different facts. First, the BrdU assay describes the cell proliferation whereas the WST-1 assay displays the cell viability. An inhibition in cell proliferation, e.g. a cell cycle arrest at G_0 / G_1 phase, does not affect metabolic viability immediately. This can be one explanation for the observed decrease in cell proliferation of A549 cells to 3 nm gold particles. An anti-proliferative potential of gold nanoparticles on A549 cells has been described by Choudhury *et al.* (Choudhury *et al.*, 2013). 20 nm, 40 nm, and 60 nm citrate-capped gold particles showed a G_0 / G_1 cell cycle arrest presumably caused by microtubule damage. Second, the different assay principles can lead to different outcomes. The incorporation of BrdU into the DNA of proliferating cells was quantified by an antibody reaction coupled to an enzymatic reaction. In contrast, the WST-1 assay determines the enzymatic conversion of the WST-1 reagent by absorption measurements. The antibody reaction of the BrdU assay was amplified by the subsequent enzymatic reaction and thus might give more accurate values with a higher sensitivity compared to photometric measurements. Furthermore, the BrdU quantification was realized within non-living cells. In contrast, the WST-1 assay was performed on living cells. Viability measurements in living cell systems do not provide an endpoint due to the progress of cellular processes. The limitation of cell-based assays for the evaluation of cell proliferation and viability has been extensively studied. The MTT (3-(4,5-dimethylthiazol-2-yl)-2,5-diphenyltetrazolium bromide) assay produces a water insoluble formazan,

which has to be dissolved in a second step to be accessible for absorption measurement. The MTS (3-(4,5-dimethylthiazol-2-yl)-5-(3-carboxymethoxyphenyl)-2-(4-sulfophenyl)-2H-tetrazolium) assay can be regarded as a one-step MTT assay. Both assays were shown to be not reliable for assessing the cytotoxicity of some substances. Wang *et al.* demonstrated that polyphenols increased the activity of the succinate dehydrogenase of cells or interacted directly with the MTT causing a higher conversion of MTT to formazan (Wang *et al.*, 2010a). For nanomaterials, interactions with the insoluble formazan crystals have been demonstrated causing false positive results (Wörle-Knirsch *et al.*, 2006). The WST-1 assay, which has been used within the present study, is a development of the MTT and MTS assay and uses a water-soluble formazan. No interactions of the dye or the water-soluble formazan product with nanoparticles have been reported yet. But in some cases also the WST-1 assay does reflect metabolic alterations, which not necessarily correlate with the number of viable cells. Medium overconsumption and/or excessive cell density can lead to a strong shutdown of mitochondrial functions. Under such conditions, a WST-1-assay would tend to an underestimation of the number of living cells (Galluzzi *et al.*, 2009).

Neither the WST-1 assay nor the BrdU assay revealed an impact of $0.02 \mu\text{g ml}^{-1}$ gold nanoparticles on A549 cells. Hence, the microscopy studies were carried out at nanoparticle concentrations that apparently not affected the cellular viability and cell proliferation. However, confocal and STED microscopy demonstrated an impact at $0.02 \mu\text{g ml}^{-1}$ of 3 nm gold particles on A549 cells after 5 h of nanoparticle exposure, as indicated by the presence of apoptotic cells. Although the BrdU assay turned out to be suitable for the detection of even low nanoparticle-induced toxicity, an impact of $0.02 \mu\text{g ml}^{-1}$ of 3 nm gold particles on the proliferation of A549 cells was not observed after 5 h of nanoparticle exposure. This observation pointed out that the usage of cell-based assays alone is not satisfactory for describing cytotoxic effects arising from nanoparticles. Especially after short exposure times (e.g. 5 h) the assay outcome cannot be used surely to evaluate impacts on cell viability, presumably due to the small number of proliferating cells. This can be demonstrated on the basis of actinomycin D, the positive control of the BrdU assay that was used to inhibit cell proliferation. A significant decrease in the viability of A549 cells was not detectable after a 5 h exposure to actinomycin D. After 24 h actinomycin D treatment, no proliferation could be measured anymore. Therefore, the assessment of nanoparticle toxicity by the use of cell-based assays should be supported by microscopy data to identify nanoparticle-induced effects.

Table 10: Reported cytotoxicity of gold nanoparticles on different human cells and cell lines.

Gold mass concentrations or molar particle concentrations and particle numbers were recalculated with a $M_{Au} = 196.96 \text{ g mol}^{-1}$ and the respective particle diameter. Underlined concentrations are source data from the publication. ND: not determined (extremely high values without any comparability). The table was partially adapted from Zhang *et al.*, 2009 and modified.

Author	Cells or cell line	Primary particle size [nm]	Impact on cell viability	Gold mass concentration [$\mu\text{g ml}^{-1}$]	Molar particle concentration [nM]	Particle number [particles ml^{-1}]	Assay
Goodman <i>et al.</i> , 2004	Cos-1	2	Yes	49	<u>1,000</u>	6.0×10^{14}	MTT
Connor <i>et al.</i> , 2005	K562	18	No	$8,90 \times 10^6$	<u>250,000</u>	1.5×10^{17}	MTT
Pernodet <i>et al.</i> , 2006	CF-31	13	Yes	<u>100 - 800</u>	7.47 - 59.77	$4.5 \times 10^{12} - 3.6 \times 10^{13}$	Cell number
Pan <i>et al.</i> , 2007	HeLa	0.8	Yes	780	<u>250,000</u>	1.5×10^{17}	MTT
		1.2	Yes	1,470	<u>140,000</u>	8.4×10^{16}	
		1.4	Yes	770	<u>46,000</u>	3.8×10^{16}	
		1.8	Yes	8,180	<u>230,000</u>	1.4×10^{17}	
		15	No	ND	<u>6,300,000</u>	ND	
Patra <i>et al.</i> , 2007	A549	33	Yes	2,190 - 26,280	<u>10 - 120</u>	$6.0 \times 10^{12} - 7.2 \times 10^{13}$	MTT
Li <i>et al.</i> , 2008	MRC-5	20	Yes	24 - 48	<u>0.5 - 1</u>	$3.0 \times 10^{11} - 5.9 \times 10^{11}$	Cell number
Gu <i>et al.</i> , 2009	HeLa	3.7	Yes	25 - 3,100	<u>80 - 10,000</u>	$4.8 \times 10^{13} - 6.0 \times 10^{15}$	MTT
Zhang <i>et al.</i> , 2009	K562	15	Yes	<u>18.75 - 600</u>	0.912 - 29.18	$5.5 \times 10^{11} - 1.8 \times 10^{13}$	CellTitre-Glo
Cui <i>et al.</i> , 2012	HeLa	2	No	0.04	<u>0.831</u>	4.9×10^{11}	MTT
		10	Yes	5			
		25	Yes	79			
Freese <i>et al.</i> , 2012	Endothelial cells	18	No	<u>10 - 250</u>	0.281 - 7.037	$1.7 \times 10^{11} - 4.2 \times 10^{12}$	MTS
		35			0.038 - 0.957	$2.3 \times 10^{10} - 5.8 \times 10^{11}$	
		65			0.006 - 0.150	$3.6 \times 10^9 - 9.0 \times 10^{10}$	
Paino <i>et al.</i> , 2012	HepG2	11	Yes	82 - 40,500	<u>10 - 50,000</u>	$6.1 \times 10^{12} - 3.0 \times 10^{16}$	MTT
		18	Yes	360 - 1,780,000			
Present study	A549	3	Yes	<u>0.02 - 20</u>	0.122 - 122	$7.3 \times 10^{10} - 7.3 \times 10^{13}$	WST-1 BrdU
		8	Yes		0.0064 - 6.4	$3.9 \times 10^9 - 3.9 \times 10^{12}$	
		15	Yes		0,001 - 1	$5.9 \times 10^8 - 5.9 \times 10^{11}$	

2.4.4 The influence of gold nanoparticles on the cellular structure involving microtubules

Only little is known about a nanoparticle influence on the microtubule structure and function and other components of the cytoskeleton, e.g. actin filaments. For iron oxide nanoparticles, a remodeling of microtubules was reported (Apopa *et al.*, 2009; Soenen *et al.*, 2010). A recent study by Diesel *et al.* demonstrated the activation of Rac-1, a small Rho GTPase, after the exposure of macrophages to silica nanoparticles (Diesel *et al.*, 2013). Rac-1 is known as an inducer of actin rearrangement (Ridley 2006), consistently silica nanoparticles induced actin polymerization. TiO₂ nanoparticles were shown to interact with isolated microtubules and to inhibit microtubule polymerization (Gheshlaghi *et al.*, 2008). A very recent study revealed microtubule damage by gold nanoparticles. 20 nm, 40 nm, and 60 nm citrate-capped gold particles inhibited microtubule polymerization and aggregation in a cell-free system (Choudhury *et al.*, 2013). However, a direct interaction of nanoparticles and microtubules, as observed in cell-free experiments, is usually not given inside cells. After endocytosis, internalized nanoparticles were trapped and transported *via* vesicles. Hence, no direct interaction of particles and microtubules occurs. But also inside cells nanoparticles can influence microtubule morphology and function causing different secondary cellular reactions. In A549 cells, gold nanoparticles caused aggregation of microtubules, leading to cell cycle arrest at the G₀ / G₁ phase and apoptosis (Choudhury *et al.*, 2013). Within the present study, the exposure of A549 cells to gold nanoparticles caused changes in the microtubule morphology that were not observed in untreated cells. For some cells a dense tubulin network in the outer cell region as well as a very round cell morphology was observed. Apparently, these cells underwent apoptosis, which is characterized by the bundling of cytoskeletal filaments in the outer cell region (Mills *et al.*, 1999). Furthermore, the present study revealed that cells in the M phase did not separate completely after nanoparticle exposure as observed by confocal microscopy. This failure of complete cell division could be related to an arrest of cytokinesis. The nuclear targeting of gold nanoparticles was shown to selectively disturb the division of cancer cells by cytokinesis arrest (Kang *et al.*, 2010). As 3 nm gold particles were observed inside the cell nucleus, a similar mechanism is imaginable. From this observation and the results derived from literature a close connection of particle induced microtubule dysfunction and genotoxicity can be concluded.

The exposure of A549 cells to gold nanoparticles induced a cell blebbing. In particular, some cells exhibited one or two large blebs filled with tubulin filaments. Due to the huge size of the blebs (10 - 15 µm) and their uneven distribution on the cell surface, the blebs could not be designated as apoptotic blebs. Typically, apoptotic blebs have sizes of 1.3 - 2.7 µm and usually more than one or two blebs were formed on the cell surface (Casciola-Rosen and Anhalt 1994). Therefore, an apoptotic trigger of these blebs can be nearly excluded even though a small portion of untreated cells suffered from blebbing, too. To exclude an apoptotic trigger for the blebbing, an apoptosis assay can be applied in further studies. The observed cell blebs can be explained by a nanoparticle uptake. Macropinocytosis is characterized by an extensive membrane ruffling and can also arouse membrane protrusions in form of blebs (Mercer and Helenius 2009). The involvement of actin filaments in internalization events is well known (Mercer and Helenius 2009; Swanson and Watts 1995). However, only a few studies suggest a role of microtubules in macropinosome formation (Racoosin and Swanson 1992). In conclusion, the formation of the blebs could not be clarified within this study and requires further investigation (Chapter 3).

2.4.5 Gold nanoparticle transport along microtubules

Intracellular transport of organelles or other cellular structures is mediated by the action of motor proteins that move along microtubules (Howard and Hyman 2003). Microtubule motor proteins participate in endocytic transport by moving multivesicular bodies and carrier vesicles to the perinuclear region, where they typically fuse with late endosomes and lysosomes (Clague 1998; Griffiths 1996). The observed perinuclear accumulation of 8 nm and 15 nm gold particles in A549 cells suggested an active endocytic transport of nanoparticles as discussed previously. The disruption of the microtubule network by the microtubule depolymerization drug nocodazole prevented a perinuclear accumulation of 8 nm gold particles. After nocodazole removal and microtubule re-polymerization, the particles started again to accumulate close to the nucleus. This observation showed a dependency of the intracellular nanoparticle transport on the integrity of the microtubule cytoskeleton and confirmed the hypothesis of an active nanoparticle transport *via* the endocytic pathway. The theory of a microtubule-dependent intracellular transport of gold nanoparticles was further strengthened by the association of 8 nm gold particles and cytoskeletal filaments, which was observed by TEM. Furthermore, SEM images indicated a vesicular structure that was filled with gold nanoparticles and was attached to filaments of the cytoskeleton.

Up to now, only a few studies addressed the involvement of microtubules in the transport of inorganic nanoparticles. Schumann *et al.* suggested an active transport of nanoparticles to the perinuclear region in A549 cells, presumably mediated by microtubule motor proteins (Schumann *et al.*, 2012). Single-steps of the microtubule motor protein dynein were visualized by internalized quantum dots in living cells indicating an active transport of inorganic nanoparticles as well (Nan *et al.*, 2005). Johnston *et al.* assumed a colocalization of fluorescently labeled polystyrene nanoparticles with the tubulin cytoskeleton of hepatocytes (Johnston *et al.*, 2010). Taken together, the results from this study reinforce the idea of an intracellular transport of nanoparticles subsequent to an uptake by endocytosis.

2.5 Conclusion

3 nm, 8 nm, and 15 nm gold particles were taken up by endocytosis in A549 cells and followed the endocytic pathway, which was concluded from a perinuclear particle accumulation. The intracellular nanoparticle transport was shown to be mediated by microtubules. Electron micrographs revealed an association of gold nanoparticles with cytoskeletal filaments. Furthermore, the disruption of the microtubule integrity by nocodazole prevented the nanoparticles from a transport towards the cell nucleus and a subsequent perinuclear accumulation. Besides, it was assumed that gold nanoparticles can also undergo exocytosis as they are able to reach the Golgi complex.

3 nm and 8 nm gold particles could be detected within the cell nucleus and indications for genotoxicity were observed after exposure to 3 nm gold particles, presumably due to the high surface-to-volume ratio, but potentially also due to a direct interaction with DNA. In this study, gold nanoparticle toxicity was demonstrated not to be dependent on the applied particle number. In addition to the cell-based assays, confocal microscopy was successfully applied to determine nanoparticle toxicity at low gold concentration ($0.02 \mu\text{g ml}^{-1}$).

The exposure of A549 cells to gold nanoparticles resulted in an increased cell blebbing, which was shown to influence the morphology of the microtubule cytoskeleton. However, the cause of the blebbing could not be clarified within the present study and required further investigation (Chapter 3). Most experiments within this study were carried out with particle numbers that are close to real exposure scenario of nanoparticle inhalation.

2.6 References

- Aebi, U.; Cohn, J.; Buhle, L.; Gerace, L. (1986): The nuclear lamina is a meshwork of intermediate-type filaments. In *Nature* 323 (6088), pp. 560–564.
- Alberts, Bruce; Wilson, John Howard (2008): *Molecular biology of the cell*. 5th ed. New York: Garland Science.
- Aniento, F. (1993): Cytoplasmic dynein-dependent vesicular transport from early to late endosomes [published erratum appears in *J Cell Biol* 1994 Feb;124(3):397]. In *J. Cell Biol.* 123 (6), pp. 1373–1387.
- Apopa, P. L.; Qian, Y.; Shao, R.; Guo, N. L.; Schwegler-Berry, D.; Pacurari, M.; Porter, D.; Shi, X.; Vallyathan, V.; Castranova, V.; Flynn, D. C. (2009): Iron oxide nanoparticles induce human microvascular endothelial cell permeability through reactive oxygen species production and microtubule remodeling. In *Part. Fibre Toxicol.* 6 (1), p. 1.
- Arvizo, R. R.; Miranda, O. R.; Thompson, M. A.; Pabelick, C. M.; Bhattacharya, R.; Robertson, J. D.; Rotello, V. M.; Prakash, Y. S.; Mukherjee, P. (2010): Effect of Nanoparticle Surface Charge at the Plasma Membrane and Beyond. In *Nano Lett.* 10 (7), pp. 2543–2548.
- Auffan, M.; Rose, J.; Bottero, J.-Y.; Lowry, G. V.; Jolivet, J.-P.; Wiesner, M. R. (2009): Towards a definition of inorganic nanoparticles from an environmental, health and safety perspective. In *Nat. Nanotech.* 4 (10), pp. 634–641.
- Bell, J. P. B.; Lindroth, M.; Fredriksson, B. (1987): Use of Sputter Coating to Prepare Whole Mounts of Cytoskeletons for Transmission and High-Resolution Scanning and Scanning Transmission Electron Microscopy. In *J. Electron Microsc.* 7, pp. 149–159.
- Bhatia, A.; Kumar, Y. (2013): Cancer cell micronucleus: an update on clinical and diagnostic applications. In *Acta Path. Micro. Im.* 121 (7), pp. 569–581.
- Brandenberger, C.; Mühlfeld, C.; Ali, Z.; Lenz, A.-G.; Schmid, O.; Parak, W. J.; Gehr, P.; Rothen-Rutishauser, B. (2010): Quantitative Evaluation of Cellular Uptake and Trafficking of Plain and Polyethylene Glycol-Coated Gold Nanoparticles. In *Small* 6 (15), pp. 1669–1678.
- Brandenberger, C.; Rothen-Rutishauser, B.; Blank, F.; Gehr, P.; Mühlfeld, C. (2009): Particles induce apical plasma membrane enlargement in epithelial lung cell line depending on particle surface area dose. In *Respir. Res.* 10 (1), p. 22.
- Brown, J. S.; Zeman, K. L.; Bennett, W. D. (2002): Ultrafine Particle Deposition and Clearance in the Healthy and Obstructed Lung. In *Am. J. Respir. Crit. Care Med.* 166 (9), pp. 1240–1247.
- Cai, W.; Gao, T.; Hong, H. S. J. (2008): Applications of gold nanoparticles in cancer nanotechnology. In *Nanotechnol. Sci. Appl.* 1, pp. 17–32.
- Cartiera, M. S.; Johnson, K. M.; Rajendran, V.; Caplan, M. J.; Saltzman, W. M. (2009): The uptake and intracellular fate of PLGA nanoparticles in epithelial cells. In *Biomaterials* 30 (14), pp. 2790–2798.
- Casciola-Rosen, L. A.; Anhalt, G. R. A. (1994): Autoantigens Targeted in Systemic Lupus Erythematosus Are Clustered in Two Populations of Surface Structures on Apoptotic Keratinocytes. In *J. Exp. Med.* 179.
- Chen, R.; Huang, G.; Ke, P. C. (2010): Calcium-enhanced exocytosis of gold nanoparticles. In *Appl. Phys. Lett.* 97 (9), p. 93706.
- Chithrani, B. D.; Ghazani, A. A.; Chan, W. C. W. (2006): Determining the Size and Shape Dependence of Gold Nanoparticle Uptake into Mammalian Cells. In *Nano Lett.* 6 (4), pp. 662–668.
- Chithrani, B. D.; Stewart, J.; Allen, C.; Jaffray, D. A. (2009): Intracellular uptake, transport, and processing of nanostructures in cancer cells. In *Nanomed. Nanotech. Biol. Med.* 5 (2), pp. 118–127.
- Choudhury, D.; Xavier, P. L.; Chaudhari, K.; John, R.; Dasgupta, A. K.; Thalappil, P.; Chakrabarti, G. (2013): Unprecedented inhibition of tubulin polymerization directed by gold nanoparticles inducing cell cycle arrest and apoptosis. In *Nanoscale* 5, pp. 4476–4489.
- Clague, M. J. (1998): Molecular aspects of the endocytic pathway. In *Biochem. J.* 336, pp. 271–282.
- Conklin, D. J. (2013): From lung to liver: How does airborne particulate matter trigger NASH and systemic insulin resistance? In *J. Hepatol.* 58 (1), pp. 8–10.
- Connor, E. E.; Mwamuka, J.; Gole, A.; Murphy, C. J.; Wyatt, M. D. (2005): Gold Nanoparticles Are Taken Up by Human Cells but Do Not Cause Acute Cytotoxicity. In *Small* 1 (3), pp. 325–327.
- Conrad, A. H.; Paulsen, A. Q.; Conrad, G. W. (1992): The role of microtubules in contractile ring function. In *J. Exp. Zool.* 262 (2), pp. 154–165.
- Coradeghini, R.; Gioria, S.; García, C. P.; Nativo, P.; Franchini, F.; Gilliland, D.; Ponti, J.; Rossi, F. (2013): Size-dependent toxicity and cell interaction mechanisms of gold nanoparticles on mouse fibroblasts. In *Toxicol. Lett.* 217 (3), pp. 205–216.

- Cui, W.; Li, J.; Zhang, Y.; Rong, H.; Lu, W.; Jiang, L. (2012): Effects of aggregation and the surface properties of gold nanoparticles on cytotoxicity and cell growth. In *Nanomed. Nanotech. Biol. Med.* 8 (1), pp. 46–53.
- Daniel, M.-C.; Astruc, D. (2004): Gold Nanoparticles: Assembly, Supramolecular Chemistry, Quantum-Size-Related Properties, and Applications toward Biology, Catalysis, and Nanotechnology. In *Chem. Rev.* 104 (1), pp. 293–346.
- Diesel, B.; Hoppstädter, J.; Hachenthal, N.; Zarbock, R.; Cavalius, C.; Wahl, B.; Thewes, N.; Jacobs, K.; Kraegeloh, A.; Kiemer, A. K. (2013): Activation of Rac1 GTPase by nanoparticulate structures in human macrophages. In *Eur. J. Pharm. Biopharm* 84 (2), pp. 315–324.
- Donaldson, K.; Poland, C. A.; Schins, R. P. F. (2010): Possible genotoxic mechanisms of nanoparticles: Criteria for improved test strategies. In *Nanotoxicology* 4 (4), pp. 414–420.
- Duarte-Rey, C.; Bogdanos, D.; Yang, C.-Y.; Roberts, K.; Leung, P. S.; Anaya, J.-M.; Worman, H. J.; Gershwin, M. E. (2012): Primary biliary cirrhosis and the nuclear pore complex. In *Autoimmun. Rev.* 11 (12), pp. 898–902.
- Ferin, J.; Oberdörster, G.; Soderholm, S. C.; Gelein, R. (1991): Pulmonary Tissue Access of Ultrafine Particles. In *J. Aerosol Med.* 4 (1), pp. 57–68.
- Freese, C.; Gibson, M. I.; Klok, H.-A.; Unger, R. E.; Kirkpatrick, C. J. (2012): Size- and Coating-Dependent Uptake of Polymer-Coated Gold Nanoparticles in Primary Human Dermal Microvascular Endothelial Cells. In *Biomacromolecules* 13 (5), pp. 1533–1543.
- Frens (1973): Controlled Nucleation for the Regulation of the Particle Size in monodisperse Gold Suspensions. In *Nat. Phys. Sci.* 241, pp. 20–22.
- Fröhlich, E. (2012): The role of surface charge in cellular uptake and cytotoxicity of medical nanoparticles. In *IJN*, p. 5577.
- Galluzzi, L.; Aaronson, S. A.; Abrams, J.; Alnemri, E. S.; Andrews, D. W.; Baehrecke, E. H.; Bazan, N. G.; Blagosklonny, M. V.; Blomgren, K.; Borner, C.; Bredesen, D. E.; Brenner, C.; Castedo, M.; Cidlowski, J. A.; Ciechanover, A.; Cohen, G. M.; Laurenzi, V. de; Maria, R. de; Deshmukh, M.; Dynlacht, B. D.; El-Deiry, W. S.; Flavell, R. A.; Fulda, S.; Garrido, C.; Golstein, P.; Gougeon, M.-L.; Green, D. R.; Gronemeyer, H.; Hajnóczky, G.; Hardwick, J. M.; Hengartner, M. O.; Ichijo, H.; Jäättelä, M.; Kepp, O.; Kimchi, A.; Klionsky, D. J.; Knight, R. A.; Kornbluth, S.; Kumar, S.; Levine, B.; Lipton, S. A.; Lugli, E.; Madeo, F.; Malorni, W.; Marine, J.-C.; Martin, S. J.; Medema, J. P.; Mehlen, P.; Melino, G.; Moll, U. M.; Morselli, E.; Nagata, S.; Nicholson, D. W.; Nicotera, P.; Nuñez, G.; Oren, M.; Penninger, J.; Pervaiz, S.; Peter, M. E.; Piacentini, M.; Prehn, J. H. M.; Puthalakath, H.; Rabinovich, G. A.; Rizzuto, R.; Rodrigues, C. M. P.; Rubinsztein, D. C.; Rudel, T.; Scorrano, L.; Simon, H.-U.; Steller, H.; Tschopp, J.; Tsujimoto, Y.; Vandenabeele, P.; Vitale, I.; Vousden, K. H.; Youle, R. J.; Yuan, J.; Zhivotovsky, B.; Kroemer, G. (2009): Guidelines for the use and interpretation of assays for monitoring cell death in higher eukaryotes. In *Cell Death Differ.* 16 (8), pp. 1093–1107.
- Geiser, M.; Kreyling, W. G. (2010): Deposition and biokinetics of inhaled nanoparticles. In *Part. Fibre Toxicol.* 7 (1), p. 2.
- Gheshlaghi, Z. N.; Riazi, G. H.; Ahmadian, S.; Ghafari, M.; Mahinpour, R. (2008): Toxicity and interaction of titanium dioxide nanoparticles with microtubule protein. In *Acta Bioch. Bioph. Sin* 40 (9).
- Giljohann, D. A.; Seferos, D. S.; Daniel, W. L.; Massich, M. D.; Patel, P. C.; Mirkin, C. A. (2010): Gold Nanoparticles for Biology and Medicine. In *Angew. Chem., Int. Ed.* 49 (19), pp. 3280–3294.
- Goodman, C. M.; McCusker, C. D.; Yilmaz, T.; Rotello, V. M. (2004): Toxicity of Gold Nanoparticles Functionalized with Cationic and Anionic Side Chains. In *Bioconjugate Chem.* 15 (4), pp. 897–900.
- Griffiths, G. (1996): On vesicles and membrane compartments. In *Protoplasma* 195, pp. 37–58.
- Gu, Y.-J.; Cheng, J.; Lin, C.-C.; Lam, Y. W.; Cheng, S. H.; Wong, W.-T. (2009): Nuclear penetration of surface functionalized gold nanoparticles. In *Toxicol. Appl. Pharmacol.* 237 (2), pp. 196–204.
- Harush-Frenkel, O.; Rozentur, E.; Benita, S.; Altschuler, Y. (2008): Surface Charge of Nanoparticles Determines Their Endocytic and Transcytotic Pathway in Polarized MDCK Cells. In *Biomacromolecules* 9 (2), pp. 435–443.
- Hell, S. W.; Wichmann, J. (1994): Breaking the diffraction resolution limit by stimulated emission: stimulated-emission-depletion fluorescence microscopy. In *Opt. Lett.* 19 (11).
- Howard, J.; Hyman, A. A. (2003): Dynamics and mechanics of the microtubule plus end. In *Nat. Nanotech.* 422.
- Jelveh, S.; Chithrani, D. B. (2011): Gold Nanostructures as a Platform for Combinational Therapy in Future Cancer Therapeutics. In *Cancers* 3 (4), pp. 1081–1110.
- Jiang, W.; Kim, B. Y. S.; Rutka, J. T.; Chan, W. C. W. (2008): Nanoparticle-mediated cellular response is size-dependent. In *Nat. Nanotech.* 3 (3), pp. 145–150.
- Johnston, H. J.; Semmler-Behnke, M.; Brown, D. M.; Kreyling, W.; Tran, L.; Stone, V. (2010): Evaluating the uptake and intracellular fate of polystyrene nanoparticles by primary and hepatocyte cell lines in vitro. In *Toxicol. Appl. Pharmacol.* 242 (1), pp. 66–78.

- Kang, B.; Mackey, M. A.; El-Sayed, M. A. (2010): Nuclear Targeting of Gold Nanoparticles in Cancer Cells Induces DNA Damage, Causing Cytokinesis Arrest and Apoptosis. In *J. Am. Chem. Soc.* 132 (5), pp. 1517–1519.
- Keene, A. M.; Allaway, R. J.; Sadrieh, N.; Tyner, K. M. (2011): Gold nanoparticle trafficking of typically excluded compounds across the cell membrane in JB6 Cl 41-5a cells causes assay interference. In *Nanotoxicology* 5 (4), pp. 469–478.
- Kim, J. A.; Åberg, C.; Salvati, A.; Dawson, K. A. (2011): Role of cell cycle on the cellular uptake and dilution of nanoparticles in a cell population. In *Nat. Nanotech.* 7 (1), pp. 62–68.
- Kreyling, W. G.; Semmler, M.; Erbe, F.; Mayer, P.; Takenaka, S.; Schulz, H.; Oberdörster, G.; Ziesenis, A. (2002): TRANSLOCATION OF ULTRAFINE INSOLUBLE IRIIDIUM PARTICLES FROM LUNG EPITHELIUM TO EXTRAPULMONARY ORGANS IS SIZE DEPENDENT BUT VERY LOW. In *J. Toxicol. Env. Health* 65 (20), pp. 1513–1530.
- Krug, H. F.; Wick, P. (2011): Nanotoxikologie - eine interdisziplinäre Herausforderung. In *Angew. Chem.* 123 (6), pp. 1294–1314.
- Lanone, S.; Rogerieux, F.; Geys, J.; Dupont, A.; Maillot-Marechal, E.; Boczkowski, J.; Lacroix, G.; Hoet, P. (2009): Comparative toxicity of 24 manufactured nanoparticles in human alveolar epithelial and macrophage cell lines. In *Part. Fibre Toxicol.* 6 (1), p. 14.
- Lieber, M.; Smith, B.; Szakal, A.; Nelson-Rees, W.; Todaro, G. (1976): A continuous tumor-cell line from a human lung carcinoma with properties of type II alveolar epithelial cells. In *Int. J. Cancer* 17 (1), pp. 62–70.
- Li, J. J.; Zou, L.; Hartono, D.; Ong, C.-N.; Bay, B.-H.; Lanry Yung, L.-Y. (2008): Gold Nanoparticles Induce Oxidative Damage in Lung Fibroblasts In Vitro. In *Adv. Mater.* 20 (1), pp. 138–142.
- Limbach, L. K.; Wick, P.; Manser, P.; Grass, R. N.; Bruinink, A.; Stark, W. J. (2007): Exposure of Engineered Nanoparticles to Human Lung Epithelial Cells: Influence of Chemical Composition and Catalytic Activity on Oxidative Stress. In *Environ. Sci. Technol.* 41 (11), pp. 4158–4163.
- Mellman, I.; Fuchs, R.; Helenius, A. (1986): Acidification of the Endocytic and Exocytic Pathways. In *Annu. Rev. Biochem.* 55, pp. 663–700.
- Mercer, J.; Helenius, A. (2009): Virus entry by macropinocytosis. In *Nat. Cell Biol.* 11 (5), pp. 510–520.
- Mills, J. C.; Stone, N. L.; Pittman, R. N. (1999): Extranuclear Apoptosis: The Role of the Cytoplasm in the Execution Phase. In *J. Cell Biol.* 146 (4), pp. 703–707.
- Mohanraj, V.; Chen, Y. (2006): Nanoparticles - A Review. In *Trop. J. Pharm. Res.* 5 (1), pp. 561–573.
- Monteiro-Riviere, N.; Inman, A.; Zhang, L. (2009): Limitations and relative utility of screening assays to assess engineered nanoparticle toxicity in a human cell line. In *Toxicol. Appl. Pharmacol.* 234 (2), pp. 222–235.
- Moros, M.; Hernández, B.; Garet, E.; Dias, J. T.; Sáez, B.; Grazú, V.; González-Fernández, Á.; Alonso, C.; La Fuente, J. M. de (2012): Monosaccharides versus PEG-Functionalized NPs: Influence in the Cellular Uptake. In *ACS Nano* 6 (2), pp. 1565–1577.
- Mühlfeld, C.; Gehr, P.; Rothen-Rutishauser, B. (2008): Translocation and cellular entering mechanisms of nanoparticles in the respiratory tract. In *Swiss Med. Wkly.* 138 (27-28), pp. 387–391.
- Nan, X.; Sims, P. A.; Chen, P.; Xie, X. S. (2005): Observation of Individual Microtubule Motor Steps in Living Cells with Endocytosed Quantum Dots. In *J. Phys. Chem. B* 109 (51), pp. 24220–24224.
- Nation, J. L. (1983): A new method using hexamethyldisilazane for preparation of soft insect tissues for scanning electron microscopy. In *Stain Technol.* 58 (6), pp. 347–351.
- Nativo, P.; Prior, I. A.; Brust, M. (2008): Uptake and Intracellular Fate of Surface-Modified Gold Nanoparticles. In *ACS Nano* 2 (8), pp. 1639–1644.
- Nel, A. (2006): Toxic Potential of Materials at the Nanolevel. In *Science* 311 (5761), pp. 622–627.
- Oberdörster, G. (2001): Pulmonary effects of inhaled ultrafine particles. In *Int. Arch. Occup. Environ. Health* 74 (1), pp. 1–8.
- Oberdörster, G.; Ferin, J.; Lehnert, B. E. (1994): Correlation between Particle Size, In Vivo Particle Persistence, and Lung Injury. In *Environ. Health Perspect.* 102 (5), pp. 173–179.
- Oberdörster, G.; Oberdörster, E.; Oberdörster, J. (2005): Nanotoxicology: an emerging discipline evolving from studies of ultrafine particles. In *Environ. Health Perspect.* 113 (7), pp. 823–839.
- Oberdörster, G.; Sharp, Z.; Atudorei, V.; Elder, A.; Gelein, R.; Kreyling, W.; Cox, C. (2004): Translocation of Inhaled Ultrafine Particles to the Brain. In *Inhalation Toxicol.* 16 (6-7), pp. 437–445.
- Pante, N. (2002): Nuclear Pore Complex Is Able to Transport Macromolecules with Diameters of 39 nm. In *Mol. Biol. Cell* 13 (2), pp. 425–434.

- Pan, Y.; Leifert, A.; Ruau, D.; Neuss, S.; Bornemann, J.; Schmid, G.; Brandau, W.; Simon, U.; Jahn-Dechent, W. (2009): Gold Nanoparticles of Diameter 1.4 nm Trigger Necrosis by Oxidative Stress and Mitochondrial Damage. In *Small* 5 (18), pp. 2067–2076.
- Pan, Y.; Neuss, S.; Leifert, A.; Fischler, M.; Wen, F.; Simon, U.; Schmid, G.; Brandau, W.; Jahn-Dechent, W. (2007): Size-Dependent Cytotoxicity of Gold Nanoparticles. In *Small* 3 (11), pp. 1941–1949.
- Park, S.; Lee, Y. K.; Jung, M.; Kim, K. H.; Chung, N.; Ahn, E.-K.; Lim, Y.; Lee, K.-H. (2007): Cellular Toxicity of Various Inhalable Metal Nanoparticles on Human Alveolar Epithelial Cells. In *Inhalation Toxicol.* 19 (s1), pp. 59–65.
- Patra, H. K.; Banerjee, S.; Chaudhuri, U.; Lahiri, P.; Dasgupta, A. K. (2007): Cell selective response to gold nanoparticles. In *Nanomed. Nanotech. Biol. Med.* 3 (2), pp. 111–119.
- Patton, J. S. (1996): Mechanisms of macromolecule absorption by the lungs. In *Adv. Drug Deliv. Rev.* 19 (1), pp. 3–36.
- Pawley, James (2010): Handbook of Biological Confocal Microscopy. 3rd ed. s.l: Springer-Verlag. Available online at http://ebooks.ciando.com/book/index.cfm/bok_id/330419.
- Pellegrino, T.; Manna, L.; Kudera, S.; Liedl, T.; Koktysh, D.; Rogach, A. L.; Keller, S.; Rädler, J.; Natile, G.; Parak, W. J. (2004): Hydrophobic Nanocrystals Coated with an Amphiphilic Polymer Shell: A General Route to Water Soluble Nanocrystals. In *Nano Lett.* 4 (4), pp. 703–707.
- Pernodet, N.; Fang, X.; Sun, Y.; Bakhtina, A.; Ramakrishnan, A.; Sokolov, J.; Ulman, A.; Rafailovich, M. (2006): Adverse Effects of Citrate/Gold Nanoparticles on Human Dermal Fibroblasts. In *Small* 2 (6), pp. 766–773.
- Pissuwan, D.; Niidome, T.; Cortie, M. B. (2011): The forthcoming applications of gold nanoparticles in drug and gene delivery systems. In *J. Controlled Release* 149 (1), pp. 65–71.
- Racoosin, E. L.; Swanson, J. A. (1992): M-CSF-induced macropinocytosis increases solute endocytosis but not receptor-mediated endocytosis in mouse macrophages. In *J. Cell. Sci.* 102 (Pt 4), pp. 867–880.
- Ridley, A. J. (2006): Rho GTPases and actin dynamics in membrane protrusions and vesicle trafficking. In *Trends Cell Biol.* 16 (10), pp. 522–529.
- Robinson, J. M.; Vandré, D. D. (1997): Efficient immunocytochemical labeling of leukocyte microtubules with FluoroNanogold: an important tool for correlative microscopy. In *J. Histochem. Cytochem.* 45 (5), pp. 631–642.
- Schindelin, J.; Arganda-Carreras, I.; Frise, E.; Kaynig, V.; Longair, M.; Pietzsch, T.; Preibisch, S.; Rueden, C.; Saalfeld, S.; Schmid, B.; Tinevez, J.-Y.; White, D. J.; Hartenstein, V.; Eliceiri, K.; Tomancak, P.; Cardona, A. (2012): Fiji: an open-source platform for biological-image analysis. In *Nat. Meth.* 9 (7), pp. 676–682.
- Schnapp, B. J.; Vale, R. D.; Sheetz, M. P.; Reese, T. S. (1985): Single microtubules from squid axoplasm support bidirectional movement of organelles. In *Cell* 40 (2), pp. 455–462.
- Schübbe, S.; Cavelius, C.; Schumann, C.; Koch, M.; Kraegeloh, A. (2010): STED Microscopy to Monitor Agglomeration of Silica Particles Inside A549 Cells. In *Adv. Eng. Mater.* 12 (5), pp. 417–422.
- Schumann, C.; Schübbe, S.; Cavelius, C.; Kraegeloh, A. (2012): A correlative approach at characterizing nanoparticle mobility and interactions after cellular uptake. In *J. Biophoton.* 5 (2), pp. 117–127.
- Singh, N.; Manshian, B.; Jenkins, G. J.; Griffiths, S. M.; Williams, P. M.; Maffei, T. G.; Wright, C. J.; Doak, S. H. (2009): NanoGenotoxicology: The DNA damaging potential of engineered nanomaterials. In *Biomaterials* 30 (23-24), pp. 3891–3914.
- Slowing, I. I.; Vivero-Escoto, J. L.; Zhao, Y.; Kandel, K.; Peerapatdit, C.; Trewyn, B. G.; Lin, V. S.-Y. (2011): Exocytosis of Mesoporous Silica Nanoparticles from Mammalian Cells: From Asymmetric Cell-to-Cell Transfer to Protein Harvesting. In *Small* 7 (11), pp. 1526–1532.
- Smith, A. E. (2004): How Viruses Enter Animal Cells. In *Science* 304 (5668), pp. 237–242.
- Sodeik, B. (1997): Microtubule-mediated Transport of Incoming Herpes Simplex Virus 1 Capsids to the Nucleus. In *J. Cell Biol.* 136 (5), pp. 1007–1021.
- Soenen, S. J. H.; Nuytten, N.; Meyer, S. F. de; Smedt, S. C. de; Cuyper, M. de (2010): High Intracellular Iron Oxide Nanoparticle Concentrations Affect Cellular Cytoskeleton and Focal Adhesion Kinase-Mediated Signaling. In *Small* 6 (7), pp. 832–842.
- Sperling, R. A.; Rivera Gil, P.; Zhang, F.; Zanella, M.; Parak, W. J. (2008): Biological applications of gold nanoparticles. In *Chem. Soc. Rev.* 37 (9), p. 1896.
- Stearns, R. C.; Paulauskis, J. D.; Godleski, J. J. (2001): Endocytosis of ultrafine particles by A549 cells. In *Am. J. Respir. Cell Mol. Biol.* 24 (2), pp. 108–115.
- Suresh, A. K.; Pelletier, D. A.; Wang, W.; Morrell-Falvey, J. L.; Gu, B.; Doktycz, M. J. (2012): Cytotoxicity Induced by Engineered Silver Nanocrystallites Is Dependent on Surface Coatings and Cell Types. In *Langmuir* 28 (5), pp. 2727–2735.

- Swanson, J. A.; Watts, C. (1995): Macropinocytosis. In *Trends Cell Biol.* 5 (11), pp. 424–428.
- Vandebriel, R.; Jong, W. de (2012): A review of mammalian toxicity of ZnO nanoparticles. In *Nanotechnol. Sci. Appl.*, p. 61.
- Varkouhi, A. K.; Scholte, M.; Storm, G.; Haisma, H. J. (2011): Endosomal escape pathways for delivery of biologicals. In *J. Controlled Release* 151 (3), pp. 220–228.
- Vasir, J. K.; Labhasetwar, V. (2007): Biodegradable nanoparticles for cytosolic delivery of therapeutics. In *Adv. Drug Deliv. Rev.* 59 (8), pp. 718–728.
- Wang, P.; Henning, S. M.; Heber, D.; Deb, S. (2010a): Limitations of MTT and MTS-Based Assays for Measurement of Antiproliferative Activity of Green Tea Polyphenols. In *PLoS ONE* 5 (4), pp. e10202.
- Wang, X.; Xu, S.; Zhou, J.; Xu, W. (2010b): A rapid phase transfer method for nanoparticles using alkylamine stabilizers. In *J. Colloid Interface Sci.* 348 (1), pp. 24–28.
- Wörle-Knirsch, J. M.; Pulskamp, K.; Krug, H. F. (2006): Oops They Did It Again! Carbon Nanotubes Hoax Scientists in Viability Assays. In *Nano Lett.* 6 (6), pp. 1261–1268.
- Ying, H.; Shen, X.; Park, B.; Yue, B. Y. J. T.; Chakravarti, S. (2010): Posttranslational Modifications, Localization, and Protein Interactions of Optineurin, the Product of a Glaucoma Gene. In *PLoS ONE* 5 (2), pp. e9168.
- Zhang, X.-D.; Guo, M.-L.; Wu, H.-Y.; Sun, Y.-M.; Ding, Y.-Q.; Feng, X.; Zhang, L.-A. (2009): Irradiation stability and cytotoxicity of gold nanoparticles for radiotherapy. In *Int. J. Nanomedicine* 4, pp. 165–173.
- Zhao, F.; Zhao, Y.; Liu, Y.; Chang, X.; Chen, C.; Zhao, Y. (2011): Cellular Uptake, Intracellular Trafficking, and Cytotoxicity of Nanomaterials. In *Small* 7 (10), pp. 1322–1337.
- Zheng, N.; Fan, J.; Stucky, G. D. (2006): One-Step One-Phase Synthesis of Monodisperse Noble-Metallic Nanoparticles and Their Colloidal Crystals. In *J. Am. Chem. Soc.* 128 (20), pp. 6550–6551.

Appendix

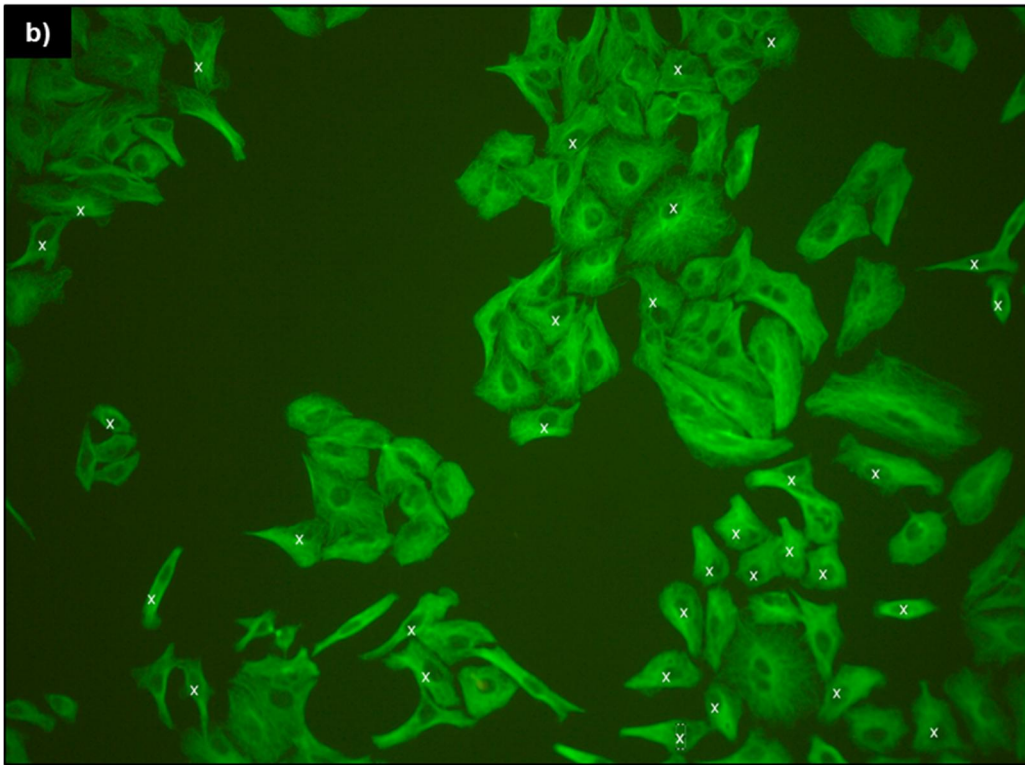
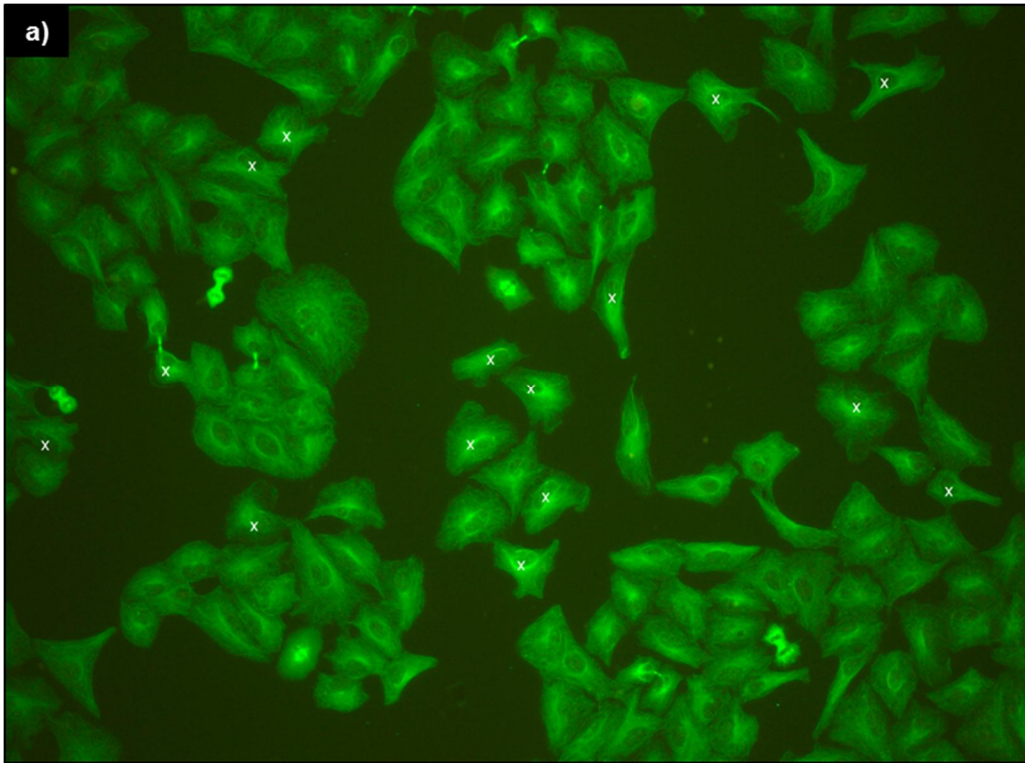
Fluorescence signals inside the cell nucleus of A549 cells were determined by using the 3D objects counter plugin from the Fiji software package. The threshold was set to 60, the size filter set to 10 - 500 voxels for all processed z-stacks. Only fluorescence signals inside the cell nucleus, which was labeled by a Hoechst stain, were taken into account (*Table S1*).

Table S1: Quantification of gold nanoparticles and polymer inside the nucleus of A549 cells.

From confocal z-stacks shown in *Figure 21*, *Figure 22*, and *Figure 23* and two further datasets (data not shown) the fluorescence spots of 3 nm and 8 nm gold particles and the polymer inside the cell nucleus were counted. The mean was calculated and plotted with the respective SD in *Figure 24*.

Exposure time [h]	3 nm	8 nm	Polymer
5	21	33	4
	16	12	1
	11	25	
24	15	24	8
	10	9	3
	7	43	
48	12	31	2
	1	3	0
	3	44	

For quantification of cell blebbing and mitosis, widefield images were analyzed and positive cells were counted manually (*Figure S1* and *S2*). The percentage of blebbing and mitotic cells was calculated by a comparison with control cells (*Table S2* and *S3*).



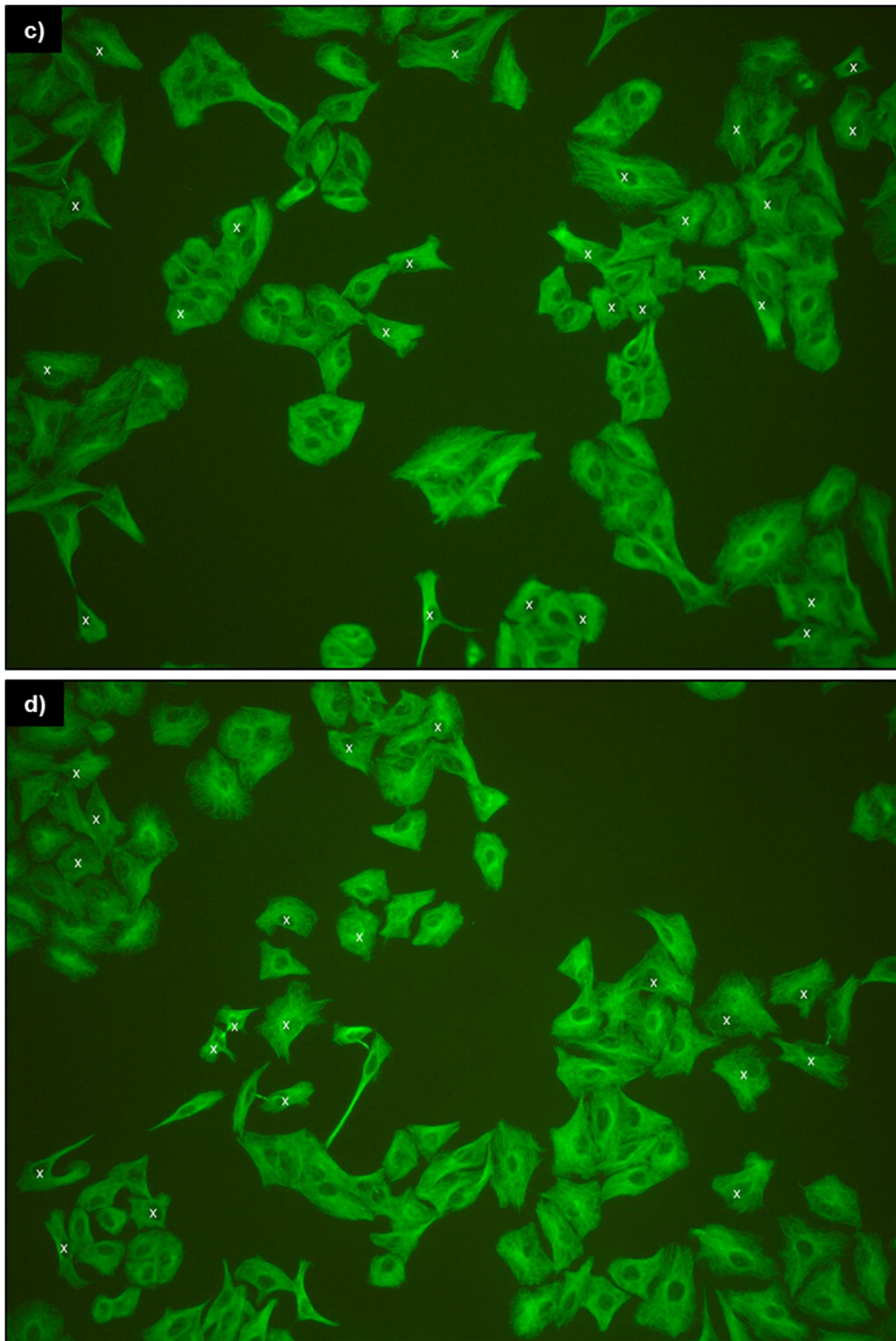
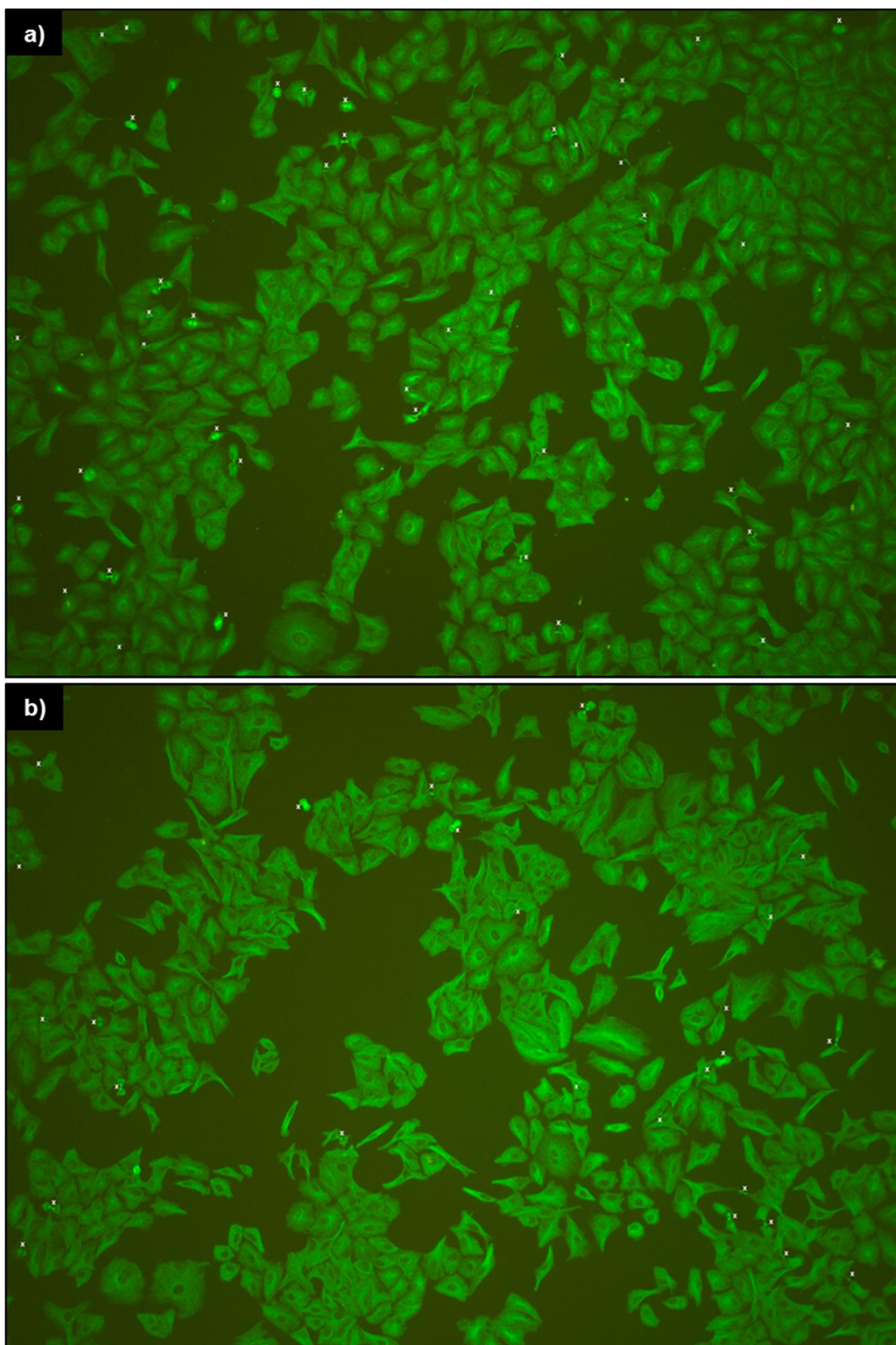


Figure S1: Quantification of cells with blebs.

A549 cells were exposed to $0.02 \mu\text{g ml}^{-1}$ of gold nanoparticles and incubated for 24 h. The tubulin cytoskeleton was stained (green) and the cells were analyzed for the formation of blebs at 20 x magnification in widefield mode. Positive cells were marked (x). a) Untreated cells, b) 3 nm gold particles, c) 8 nm gold particles, and d) 15 nm gold particles. Counted cell numbers are stated in *Table S2*.



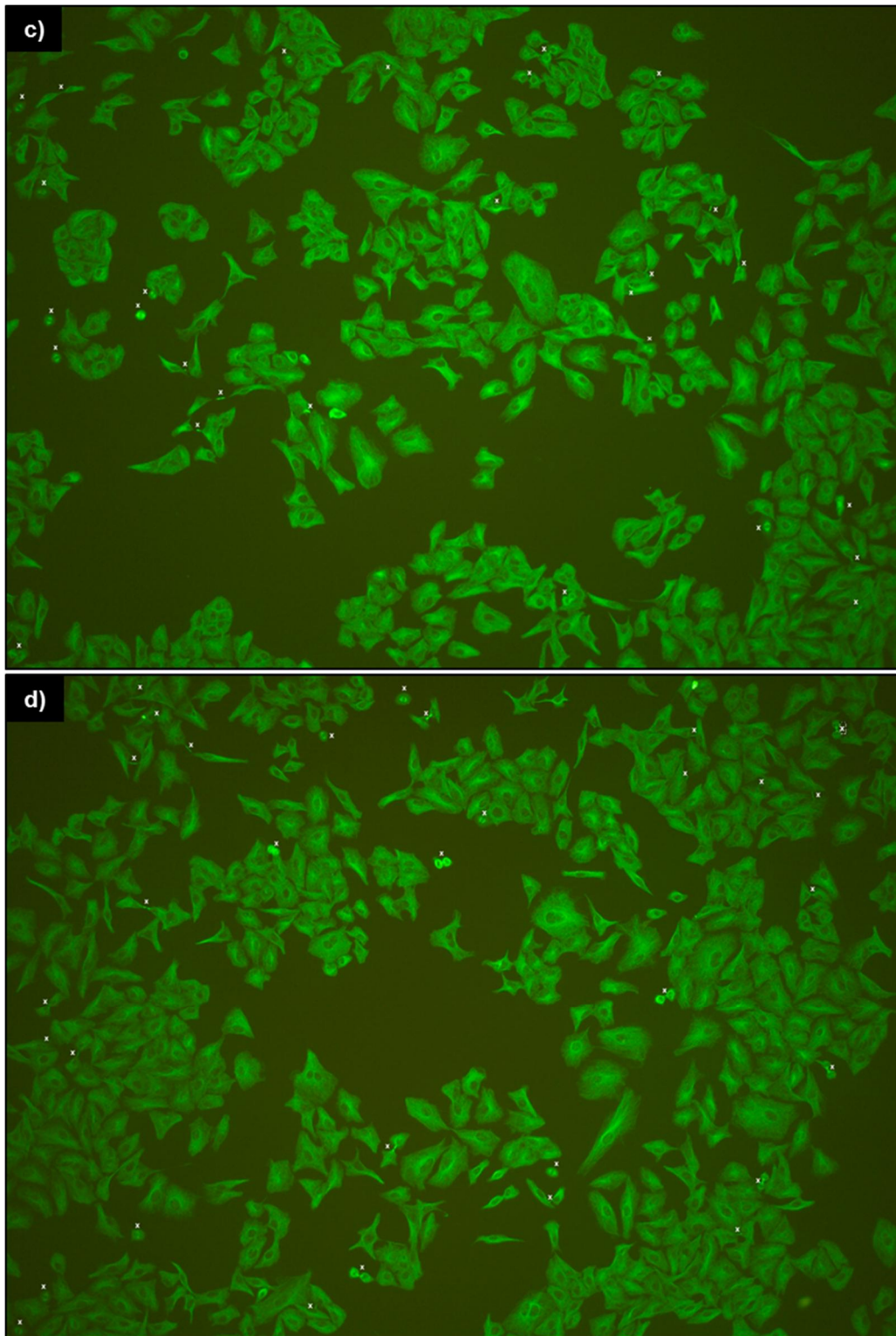


Figure S2: Quantification of mitosis.

A549 cells were exposed to 0.02 $\mu\text{g ml}$ gold nanoparticles and incubated for 24 h. The tubulin cytoskeleton was stained (green) and the cells were analyzed for mitosis at 10 x magnification in widefield mode. Dividing cells are marked (x). a) Untreated cells, b) 3 nm gold particles, c) 8 nm gold particles, and d) 15 nm gold particles. Counted cell numbers are stated in Table S3.

Table S2: Counted cell numbers and calculated percentages blebbing cells.

	Control	3 nm	8 nm	15 nm
Total cells	143	126	120	111
Cells positive for blebs	14	32	25	21
% cells positive for blebs	9.8	25.4	20.8	18.9

Table S3: Counted cell numbers and calculated percentages of mitotic events.

	Control	3 nm	8 nm	15 nm
Total cells	667	575	517	580
Mitotic events	42	28	28	32
% mitosis	6.3	4.9	5.4	5.5

The fluorescent polymer forming the gold nanoparticle shell was analyzed by SEM. Secondary electrons revealed a particle-like conformation with diameters of 30 - 40 nm.

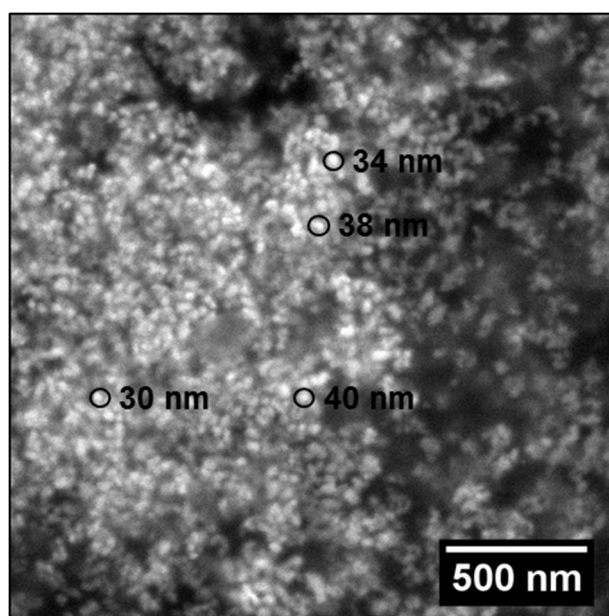


Figure S3: Imaging of the fluorescent polymer by SEM.

1 μ l of the polymer solution ($7130 \mu\text{g ml}^{-1}$) was dried on a TEM grid and imaged at 10 kV by SEM. Secondary electrons revealed a particle-like structure of the polymer with diameters of 30 - 40 nm. Four structures were measured exemplarily and are indicated in the image by circles. The image was taken by Dr. M. Koch.

3. Blebbing of A549 cells caused by nanoparticle exposure

3.1 Introduction

Nanoparticle uptake by cells can induce several effects, such as cytotoxicity (Lewinski *et al.*, 2008), changes in cell signaling (Comfort *et al.*, 2011), or alterations in cell morphology, e.g. caused by apoptosis (Pan *et al.*, 2007). In Chapter 2, the internalization of gold nanoparticles into human lung cells was studied. Within the experiments, one observation was the formation of cell blebs after exposure of A549 cells to gold nanoparticles. The blebs were characterized by an α -tubulin staining. Cell blebs are dynamic cytoskeleton-regulated cell protrusions, which can occur during apoptosis, cytokinesis, cell movement, and macropinocytosis (Fackler and Grosse 2008; Mercer and Helenius 2009).

Apoptosis, a mechanism of programmed cell death (Elmore 2007), is an active and highly controlled process. From a morphological point of view, apoptosis is initiated by cell shrinkage and the release of extracellular matrix attachments (Mills *et al.*, 1999) followed by chromatin condensation and DNA fragmentation (Majno and Joris 1995). With ongoing apoptosis, small protrusions are formed on the cell surface, which later on can pinch-off as vesicles (apoptotic bodies), thereby causing a total collapse of the cell (van Cruchten and van den Broeck 2002; Taylor *et al.*, 2008). Apoptosis controls the normal cell turnover in cell populations. However, it also occurs as a defense mechanism in case of cell damage caused by toxic agents. Some types of nanoparticles have already been shown to be a potential apoptotic trigger, such as gold (Pan *et al.*, 2007; Kang *et al.*, 2010) or TiO₂ nanoparticles (Park *et al.*, 2008). However, as already concluded, size (10 - 15 μm) and number (one bleb per cell) of the observed tubulin blebs are not in line with number (several blebs per cell) and sizes (1.3 - 2.7 μm) known for apoptotic blebs (Casciola-Rosen and Anhalt 1994). Furthermore, the tubulin cytoskeleton is not involved in membrane blebbing during apoptosis. Microtubules are destroyed early in the apoptosis execution phase and are not part of the blebbing process (Mills *et al.*, 1999).

Macropinocytosis is a second mechanism, by which a blebbing of cells can occur. Macropinocytosis is a form of endocytosis and mediates a rather unspecific internalization of fluids and larger particles (Conner and Schmid 2003). It is initiated by an extensive plasma membrane reorganization, by which an external macropinocytic structure is formed, and finally enclosed and internalized. Internalized macropinosomes enter the endosomal - lysosomal pathway and fuse with degradative compartments (Kerr and Teasdale 2009). The mechanism of membrane reorganization, which is also known as membrane ruffling, is an actin-dependent process (Swanson and Watts 1995). Ruffling occurs in different ways, including lamellipodia-like structures, circular ruffles, or blebs (Mercer and Helenius 2009). However, a role of microtubules in membrane blebbing or ruffling has not been demonstrated, yet. Generally, macropinocytosis is regarded as one potential cellular uptake mechanism for nanoparticles (Iversen *et al.*, 2011), also into human lung cells (Mühlfeld *et al.*, 2008). However, only a few studies observed nanoparticle uptake via macropinocytosis (Thurn *et al.*, 2011; Dausend *et al.*, 2008). Meng *et al.* demonstrated that A549 cells were capable to internalize silica nanoparticles by a macropinocytotic mechanism (Meng *et al.*, 2011).

Cell movement is another mechanisms, which can cause cell blebbing. During cell movement, the cell extends a protrusion, which is formed at the leading edge by actin polymerization. This lamellipodium develops new adhesions and the cell body moves towards the new adhesion spots (Ananthkrishnan and Ehrlicher 2007). When the lamellipodium is not attached to the substrate it curls upwards, which appears as membrane ruffling (Small *et al.*, 2002). Although lamellipodia formation is an actin-driven process, the involvement of microtubules in cell migration has been

demonstrated. Ballestrem *et al.* showed that microtubules are essential for the cell body contraction and the release of adhesion contacts (Ballestrem *et al.*, 2000).

The extensive membrane ruffling caused by macropinocytosis as well as the involvement in nanoparticle uptake appeared to be a potential explanation for the increased blebbing, which was observed in A549 cells after exposure to gold nanoparticles, even though an involvement of microtubules is not known. In addition, lamellipodia formation turned out to be a further potential mechanism for the observed cell blebbing. Therefore, gold nanoparticle uptake *via* macropinocytosis and lamellipodia formation were in the focus of this work. For this purpose, A549 cells were transfected with a plasmid encoding for a GFP-tagged plasma membrane peptide. Visualization of membrane ruffling was achieved and compared with the formation of the previously observed cell blebs. Furthermore, the GFP-fusion protein enabled live cell imaging of cell blebbing in the presence of gold nanoparticles. Vesicles pinching off the cell membrane were analyzed concerning a potential nanoparticle uptake and transport.

3.2 Experimental section

3.2.1 Nanoparticle synthesis and characterization

Gold nanoparticles were synthesized as described previously in the experimental section of Chapter 2. Silicon dioxide (SiO₂) nanoparticles were synthesized according to Hartlen *et al.* (Hartlen *et al.*, 2008). Silver (Ag) nanoparticles were synthesized according to Koch *et al.* (Koch *et al.*, 2012). Nanoparticle characterization was described previously for gold nanoparticles in the experimental section of Chapter 2. Dispersions of gold, SiO₂, and Ag nanoparticles were prepared, characterized, and provided by Dr. C. Cavelius.

3.2.2 Expression of a GFP fusion protein in A549 cells for live cell imaging

3.2.2.1 Transformation of *E. coli*

Plasmids encoding fluorescent fusion proteins were purchased from Clontech (Takara Bio, USA). pAcGFP1-Mem was used to label the cell membrane of A549 cells. The plasmid characteristics are shown in Table 11.

Table 11: Characteristics of pAcGFP1-Mem.

Name	Structural protein	Fluorescent protein	Size [kb]	Promoter	Resistance
pAcGFP1Mem	Neuromodulin / GAP 43 (growth associated protein 43)	AcGFP1 (Aequorea coerulescens green fluorescent protein)	4,8	CMV	Neomycin, Kanamycin

The plasmid was propagated in *E. coli*, using the NEB5 α strain (New England Biolabs, USA). Transformation of NEB5 α was done according to the manufacturer's instructions. Positive clones were selected on LB agar (Roth, Germany) supplemented with 30 $\mu\text{g ml}^{-1}$ kanamycin (Roth, Germany).

3.2.2.2 Colony polymerase chain reaction (PCR)

For a detailed analysis of positive *E. coli* clones, the GFP-coding DNA sequence was amplified by PCR. A pair of primers was designed (Table 12) and synthesized by MWG. The resulting PCR product had a length of 765 bp.

Table 12: Primer used for the amplification of the GFP fusion protein from isolated plasmid DNA.
 T_m states the melting temperature of the primer oligonucleotide.

Primer	Direction	Sequence	T_m [°C]	Fragment length [bp]
AcMem-Mem-5'	Forward	ATGCTGTGCTGTATGAGAAG	55.3	765
AcMem-GFP-3'	Reverse	ACAGCTCATCCATGCCGT	56.0	

Positive *E. coli* clones were picked with pipette tips and transferred into the reaction mix, which was used for colony PCR (Table 13). The reaction mix was prepared on ice.

Table 13: Reaction mix used of colony PCR.

Reagent	Company	Volume [μ l]	Final concentration
10 x Taq buffer	Fermentas	5	1 x
dNTP Mix, 2 mM	Fermentas	5	0.2 mM
Forward primer	MWG	0.5	1 mM
Reverse primer	MWG	0.5	1 mM
25 mM MgCl ₂	Fermentas	4	2 mM
Taq DNA polymerase	Fermentas	0.5	2.5 Units
H ₂ O		34.5	
Final volume		50	

The PCR was carried out in a thermocycler (Mastercycler gradient, Eppendorf, Germany). The temperature regime is shown in Table 14.

Table 14: Temperature regime used for colony PCR.

Step	T [$^{\circ}$ C]	t	Number of cycles
Initial denaturation	95	5 min	1
Denaturation	95	30 sec	30
Annealing	50	30 sec	30
Elongation	72	2 min	30
Final elongation	72	10 min	1
	4	∞	

3.2.2.3 Gel electrophoresis

PCR products were analyzed by gel electrophoresis. DNA is a negatively charged molecule. In an electric field, DNA migrates to the plus pole depending on size and conformation. For gel electrophoresis, 1.5 - 2 % agarose (Roth, Germany) were dissolved in 1 x TAE (Tris-acetate-EDTA) (Table 15) and heated in a microwave until the mixture started to boil. The molted gel was placed into an electrophoresis chamber (Fisher Scientific, Germany). After hardening of the agarose, the gel was loaded with DNA samples mixed with loading dye and the GeneRuler 1 kb DNA Ladder (Fermentas, Thermo Fisher Scientific, USA). 1 x TAE was used as running buffer and gels were run at 60 - 80 V for ~1 h. After electrophoresis, agarose gels were transferred into a water bath containing ethidium bromide (Roth, Germany). 50 μ l of a 10 mg ml⁻¹ ethidium bromide were added to 1 l deionized H₂O. Ethidium bromide intercalates into DNA and visualizes dsDNA by the absorption of UV light. Finally, the stained gels were analyzed under UV light by using a bioillumination system (FluorchemQ, Biozym, Germany).

Table 15: 50 x TAE buffer.

Working solution: 1 x.

Compound	Concentration
Tris base	242 g
Acetic acid	57.1 ml
EDTA	100 ml (0.5 M, pH 8.0)

3.2.2.4 Plasmid propagation and isolation

For plasmid propagation, positive clones analyzed by colony PCR were grown in 3 ml LB medium supplemented with $30 \mu\text{g ml}^{-1}$ kanamycin. Cultures were incubated overnight at 37°C and 300 rpm. pAcGFP1-Mem was isolated and purified using the Plasmid Mini Kit (Qiagen, Germany), according to the manufacturer's instructions. Precipitated DNA was dissolved in 30 - 50 μl TE buffer (Tris-EDTA) (Table 16) or in H_2O .

Table 16: TE buffer.

Compound	Concentration
Tris-HCl	10 mM
EDTA	1 mM
pH 8.0	

3.2.2.5 UV spectrophotometric measurements of purified plasmid DNA

DNA absorbs light with a wavelength of 260 nm. Thus, the amount of isolated plasmid DNA was determined by the use of a spectrophotometer (BioPhotometer 6131, Eppendorf, Germany). An absorption value of $A_{260} = 1$ corresponds to a concentration of $50 \mu\text{g ml}^{-1}$ dsDNA, according to Beer-Lambert's law. To guarantee linearity of the spectrophotometric measurement, plasmid DNA was diluted in TE buffer or H_2O to adjust an A_{260} value between 0.1 and 1. The corresponding diluent was used for blank measurements. The absorption at 230 nm, 260 nm, 280 nm, and 320 nm was determined in triplicates. For good DNA quality, the A_{260} / A_{280} ratio should take a value between 1.7 and 2.0; the A_{260} / A_{230} ratio should be greater than 1.5. The absorption at 320 nm was measured to exclude contaminations of the DNA samples. For a high purity, the A_{260} value should be 0.

3.2.2.6 Transfection of A549 cells with pAcGFP1-Mem

1×10^6 A549 cells with low passage number (1 - 3) were seeded into 100 mm petri dishes and were allowed to grow for 20 - 24 h before transfection. The Attractene transfection reagent (Qiagen, Germany) was used to transfer pAcGFP1-Mem into A549 cells according to the manufacturer's instructions. In brief, 4 μg plasmid DNA were dispersed in 300 μl DMEM (without FBS). 15 μl Attractene transfection reagent were added. The solution was mixed using a vortex mixer and incubated for 10 - 15 min at RT. Subsequently, the DNA mixture was added dropwise to the cells while gently moving the petri dish. The cells were incubated at 37°C and 9% CO_2 . Medium containing transfection reagent was removed after 30 h of incubation and cells were split 1 : 10 into new 100 mm petri dishes (Greiner BioOne, Germany) containing selection medium with antibiotic to establish stable cell lines of A549 pAcGFP1-Mem cells.

3.2.2.7 Establishment of stable A549 pAcGFP1-Mem cells

Cells stably expressing pAcGFP1-Mem were selected by adding G418 (Geneticin) (Serva, Germany) to the cell culture medium. A concentration of 400 - 600 $\mu\text{g ml}^{-1}$ turned out to be appropriate for the isolation of A549 cells stably expressing pAcGFP1-Mem. Selection medium was exchanged every 2 - 3 days to remove cell debris as well as to provide fresh G418. After 2 - 3 weeks of selection, fluorescent colonies were picked and transferred into 12 - well plates. The selection was continued for another 1 - 2 weeks. Once GFP positive cells became dominant (~ 80%), cells from one well were transferred into a T-25 flask and were either used for experiments or were prepared for storage in liquid nitrogen.

3.2.3 Cell culture of A549 cells

The human lung carcinoma cell line A549 (ACC 107), a model for type II alveolar epithelial cells (Lieber *et al.*, 1976), was used within this study. The cells were cultivated and maintained as described previously in the experimental section of Chapter 2. Stable cell lines of A549 pAcGFP1-Mem cells were cultivated in DMEM supplemented with 10 % FBS and 200 mg ml⁻¹ of G418.

3.2.4 Sample preparation for confocal microscopy

3.2.4.1 Exposure of cells to nanoparticles

For microscopy analyses of fixed cell samples, A549 pAcGFP1-Mem cells were grown on coverslips (#1.5, Menzel, ThermoFisher, USA). Sterilized coverslips (20 min, 121°C) were placed into 12 - well plates filled with 1 ml cell culture medium per well. DMEM without phenol red (PAN biotech, Germany) was used to avoid an excitation of residual phenol red during microscopy. The cells were cultured in presence of 200 µg ml⁻¹ of G418. 5 x 10⁴ cells were seeded into each well (3.9 cm²) and were allowed to attach for 20 - 24 h under cell culture conditions before nanoparticle exposure. Dispersions of gold, Ag, and SiO₂ nanoparticles were prepared freshly prior to each experiment by diluting the nanoparticle stock dispersions in cell culture medium. The preparations were mixed using a vortex mixer and 1 ml dispersion per well was added. The cells were exposed to nanoparticles for varying times under cell culture conditions and were subsequently stained.

3.2.4.2 Immunostaining

A549 cells were stained with fluorescent dyes and antibodies to allow analyses by confocal microscopy. The whole procedure is described in detail in the experimental section of Chapter 2. In brief, cells were rinsed with PBS and subsequently fixed using 4 % paraformaldehyde (PFA) or formaldehyde. Cells were permeabilized and actin filaments were labeled using phalloidin-Atto 647N (Table 17). The staining was carried out for 20 min at RT. Prior to antibody labeling, blocking of unspecific antibody binding sites was carried out using bovine serum albumin (BSA). Microtubules were immunostained (Table 17 and Table 18). Labeled cells were mounted in Mowiol 4-88 (Roth, Germany), containing 2.5 % anti-bleaching reagent DABCO (Roth, Germany).

Table 17: Primary antibodies and fluorescent dyes.

Primary antibodies and dyes	Target	Working concentration
Phalloidin - Atto 647N (Atto-Tec, Germany)	Actin	0.5 nmol
Mouse anti- α -tubulin IgG (Invitrogen, Life Technologies, USA)	α -tubulin	1 µg ml ⁻¹

Table 18: Secondary antibodies.

Secondary antibody	λ_{Ex} [nm]	λ_{Em} [nm]	Working concentration
Goat anti-mouse IgG Alexa 546 (Invitrogen, Life Technologies, USA)	556	573	4 µg ml ⁻¹

3.2.5 Sample preparation for live cell confocal microscopy

3.2.5.1 Exposure of cells to nanoparticles

For live cell confocal microscopy, A549 pAcGFP1-Mem cells were grown in 35 mm cell culture dishes equipped with a glass bottom (Greiner bio-one, Germany). The dishes were subdivided into four compartments with a growth area of 1.9 cm². 5×10^3 cells were seeded into each compartment 20 - 24 h prior to nanoparticle exposure. A549 pAcGFP1-Mem cells were grown in DMEM without phenol red supplemented with 10 % FBS and 200 $\mu\text{g ml}^{-1}$ of G418. Dispersions of gold nanoparticles were prepared freshly prior to each experiment by diluting the nanoparticle stock dispersions in cell culture medium. The preparations were mixed using a vortex mixer and 500 μl dispersion per compartment were added. The cells were exposed to nanoparticles for varying times under cell culture conditions.

3.2.5.2 Exposure of cells to fluorescent dextran

After 4 h of nanoparticle treatment, a fluorescent dextran was added to the cells to visualize macropinocytosis. A549 pAcGFP1-Mem cells were exposed to 1 mg ml⁻¹ of a 70 kDa Alexa 546-labeled dextran (Invitrogen, Life Technologies, USA) for 5 min.

3.2.6 Confocal microscopy

3.2.6.1 Imaging of fixed cell samples

To monitor the intracellular distribution of 3 nm, 8 nm, and 15 nm gold particles within A549 cells, z-stacks and images of representative cells were recorded using the Leica TCS SP5 STED system and an HCX PL APO 100 x /1.4 oil immersion objective (Leica, Germany). The GFP-labeled cell membrane was excited using an argon laser with an excitation wavelength of 488 nm. The emission light was detected within a detection range of 500 - 560 nm by using a PMT. Alexa 546-labeled α -tubulin was excited using a diode-pumped solid-state (DPSS) laser with an excitation wavelength of 561 nm. The PMT detection range was set from 570 - 620 nm. Imaging of Atto 647N-labeled gold nanoparticles and Atto 647N-labeled actin was performed using a 633 nm HeNe laser. An APD was used to detect gold nanoparticle fluorescence. For this purpose, a reflection short pass filter (RSP 630) was chosen from the x1-port settings to allow detection of light with wavelengths longer than 630 nm by the external APDs. Actin stained with Atto 647N-labeled phalloidin was detected by the use of a PMT. The detection range was set from 640 nm - 720 nm. All images and z-stacks were recorded sequentially. For confocal imaging, a z-step size of 130 nm and pixel sizes of 50 - 70 nm² were chosen, according to the Nyquist sampling theorem (Pawley 2010). 8 bit images were taken, with a format of 1024² or 2048², a scan speed of 200 Hz, and a frame average of 4. All scans were performed in unidirectional mode.

3.2.6.2 Live cell imaging

Prior to live cell imaging, nanoparticle and / or dextran containing culture medium was removed and replaced by 500 μ l DMEM without phenol red supplemented with 10 % FBS and 200 μ g ml⁻¹ of G418. Time series were recorded using a Leica TCS SP5 system with an HCX PL APO CS 63.0 x 1.20 water immersion objective (Leica, Germany). The GFP-labeled cell membrane and Atto 647N-labeled gold nanoparticles were imaged as described in the previous section. Alexa 546-labeled dextran was excited using a diode-pumped solid-state (DPSS) laser with an excitation wavelength of 561 nm. The PMT detection range was set from 570 - 620 nm. For live cell imaging pixel sizes of 130 - 150 nm² were used. 8 bit images were recorded with a format of 512² and a scan speed of 400 Hz. No averaging was applied. The scans were performed in unidirectional mode. The pinhole diameter was set to 1.5 AU. Different frame intervals were used. Specific parameters are stated in the respective figure caption.

3.2.7 Deconvolution and image processing

Deconvolution and image processing was performed with Huygens professional software (SVI, Netherlands) and Fiji (Schindelin *et al.*, 2012). A detailed description on both can be found in the experimental section of Chapter 2.

3.3 Results

3.3.1 Characterization of nanoparticles

Gold nanoparticles were characterized as described in Chapter 2. The batches used within the study of bleb formation are listed in *Table 19*. In addition to gold nanoparticles, non-labeled Ag and SiO₂ nanoparticles were used.

Table 19: Physico-chemical and spectroscopic properties of gold, silver, and SiO₂ nanoparticles. Different types of nanoparticles were used within this study. L indicates fluorescently labeled batches. ND: not determined. All parameters were determined by Dr. C. Cavelius.

Batch	d _{TEM} [nm]	d _{hyd} [nm]	Zeta potential [mV]	Au/ Ag/ SiO ₂ conc. [μg ml ⁻¹]	Particle conc. [nM]	Abs _{max} [nm]	α _{Ex} [nm]	α _{Em} [nm]
Au 3 nm	2.9 ± 0.2	ND	ND	170.6	1,149	512	-	-
Au 3 nm L	2.6 ± 0.5	ND	ND	136.0	1,270	512	647	662
Au 8 nm	7.9 ± 0.1	23.9 ± 7.1	-43.5	495.3	158.8	518	-	-
Au 8 nm L	8.4 ± 0.5	13.2 ± 4.8	-49.7	963.0	267	520	647	663
Au 15 nm	ND	44.2 ± 5.2	-43.1	234.1	ND	523	-	-
Au 15 nm L	12.7 ± 1.3	ND	ND	407.0	33	522	647	663
Ag 10 nm	9.6 ± 0.7	20.0 ± 8.8	-71.9	1,220	417	409	-	-
SiO ₂ 25 nm	24.6 ± 3.4	20.8 ± 2.6	-24.2	2,428	-	-	-	-

3.3.2 Establishment and characterization of A549 pAcGFP1-Mem cells

A549 cells were transfected with the commercially available pAcGFP1-Mem plasmid to label the cell membrane and to allow for live cell imaging of the blebbing. For this purpose, transformation of *E. coli* with pAcGFP1-Mem was carried out. Positive clones were selected, picked, and analyzed by colony PCR. Primer design and colony PCR are described in the experimental section. The resulting PCR products were analyzed by gel electrophoresis (*Figure 41*). The amplified DNA fragments had a size of ~750 bp, which is close to the expected fragment size of 765 bp. Hence, the analyzed *E. coli* clones had incorporated the pAcGFP1-Mem plasmid and were used for plasmid propagation and purification.

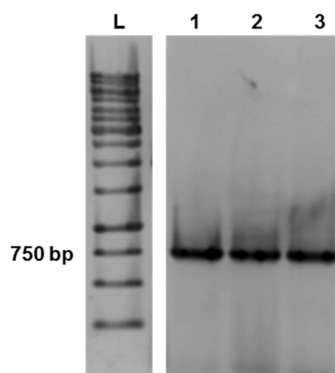


Figure 41: Colony PCR of E. coli transformation with pAcGFP1-Mem. Three clones (1 - 3) were picked and analyzed by colony PCR. The amplified fragment had a size of ~750 bp as indicated by the DNA ladder (L). This was in accordance with the expected fragment size of 765 bp.

Positive *E. coli* clones were used to propagate the plasmid. Plasmid DNA was purified and characterized by UV spectrophotometric measurements (Table 20). DNA purity and concentration were suitable for transfection of A549 cells.

Table 20: Properties of isolated plasmid DNA.
The plasmid pAcGFP1-Mem was propagated in *E. coli*, purified, and analyzed by UV spectrophotometry.

Clone	A ₂₆₀ / A ₂₈₀	A ₂₆₀	dsDNA [$\mu\text{g ml}^{-1}$]
1	1.83	0.406	1,015
2	1.94	0.097	243
3	1.85	0.268	670

Plasmid DNA from clone 1 was used for the transfection of A549 cells. Stable cell lines of A549 pAcGFP1-Mem cells were established and analyzed by confocal microscopy (Figure 42). Most of the isolated cells exhibited a GFP fluorescence although the expression between single cells varied. Besides the cell membrane, several types of vesicles were GFP-labeled. Vesicles that pinch-off the cell membrane are composed of membrane lipids including proteins with membrane anchor and thus also exhibited a GFP fluorescence. The transfected cells seemed to fulfill the requirements as the cell membrane was properly stained and allowed for a detection of single cells.

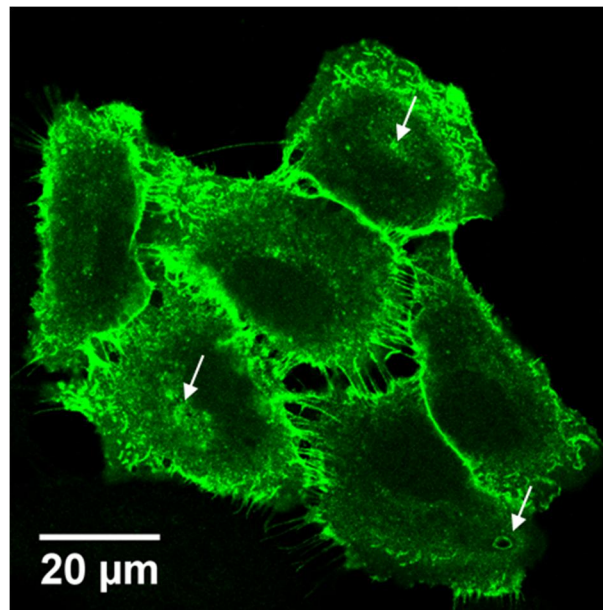


Figure 42: Characterization of A549 pAcGFP1-Mem cells by confocal microscopy.
A549 cells stably expressing pAcGFP1-Mem exhibited green fluorescence of the cell membrane and were suited for investigations by confocal microscopy. Obviously, not only the cell membrane was GFP-labeled. Different kinds of vesicles exhibited a GFP staining as well (indicated by arrows). A representative confocal image is shown. The contrast of the image was enhanced.

3.3.3 Characterization of cell blebbing

3.3.3.1 Cell blebbing caused by gold nanoparticles of different sizes

Results from Chapter 2 demonstrated an increased cell blebbing after exposure of A549 cells to gold nanoparticles. The blebbing was assumed as a function of the applied particle number (see Chapter 2). Therefore, we performed experiments with the same number of 3 nm, 8 nm, and 15 nm gold particles to further characterize this blebbing event. For this purpose, A549 cells transfected with pAcGFP1-Mem as a cell membrane marker, were exposed to 7.3×10^{10} particles ml^{-1} , corresponding to $0.02 \mu\text{g ml}^{-1}$ of 3 nm gold particles, $0.38 \mu\text{g ml}^{-1}$ of 8 nm gold particles, and $2.5 \mu\text{g ml}^{-1}$ of 15 nm gold particles. In addition to the GFP membrane marker, cells were stained for actin and α -tubulin. The staining revealed that morphological changes induced by cell blebbing were not solely observed for microtubules (*Figure 43*). After exposure of A549 cells to 3 nm (*Figure 43a*), 8 nm (*Figure 43b*), and 15 nm gold particles (*Figure 43c*) a re-arrangement of actin filaments and the cell membrane was observed, too. Control cells, which were not treated with nanoparticles, exhibited blebs, too (*Figure 43d*). Generally, the size of the blebs varied. The cell protrusion in *Figure 43c* had a size of 18 μm . In comparison, the bleb in *Figure 43d* exhibited a size of 9 μm .

3.3.3.2 Cell blebbing caused by nanoparticle composition

The bleb formation of A549 cells caused by nanoparticle exposure was further investigated concerning a potential impact of the nanoparticle composition. For this purpose, A549 cells were exposed to 7.3×10^{11} particles ml^{-1} of 3 nm and 8 nm gold particles and the same number of 25 nm SiO_2 and 10 nm Ag particles as well (*Figure 44*). After SiO_2 (*Figure 44a*) and Ag (*Figure 44b*) exposure, A549 cells showed the same blebs as observed after exposure to 3 nm (*Figure 44c*) and 8 nm (*Figure 44d*) gold particles. Hence, a material-dependent trigger could be excluded. As observed previously, the size of the blebs was not consistent and varied between 12 μm (*Figure 44d*) and 18 μm (*Figure 44a*).

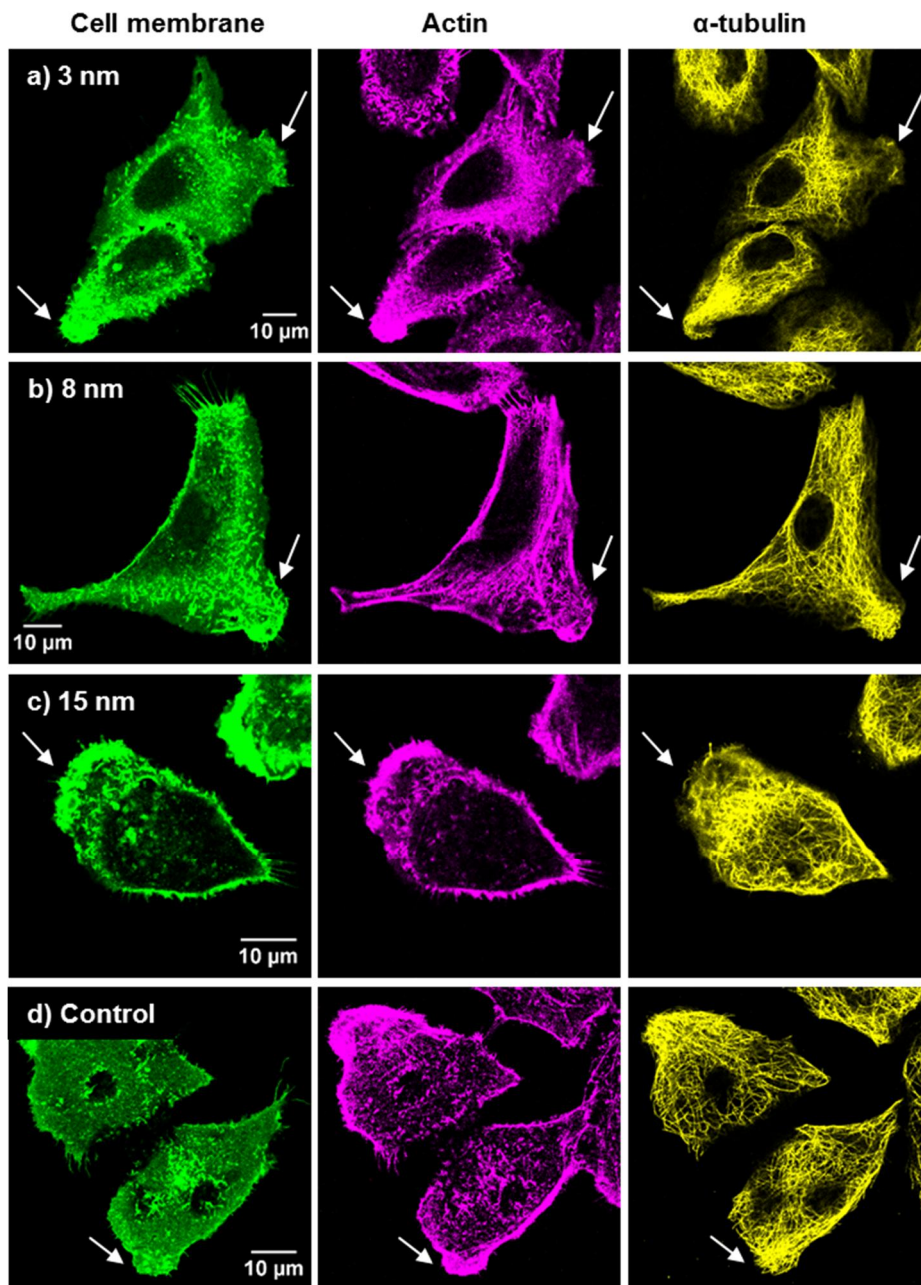


Figure 43: Characterization of bleb formation of A549 cells induced by gold nanoparticles.

Confocal images of A549 pAcGFP1-Mem cells, exposed to gold nanoparticles for 5 h and stained for actin (magenta) and α -tubulin (yellow). The cell membrane was GFP-labeled (green). The cells were exposed to 7.3×10^{10} particles ml^{-1} of a) 3 nm gold particles ($0.02 \mu\text{g ml}^{-1}$), b) 8 nm gold particles ($0.38 \mu\text{g ml}^{-1}$), and c) 15 nm gold particles ($2.5 \mu\text{g ml}^{-1}$). Control cells d) were not treated with nanoparticles. The observed blebbing caused changes in the morphology of the cell membrane, the actin and tubulin cytoskeleton. $n = 1$ with 3 technical replicates.

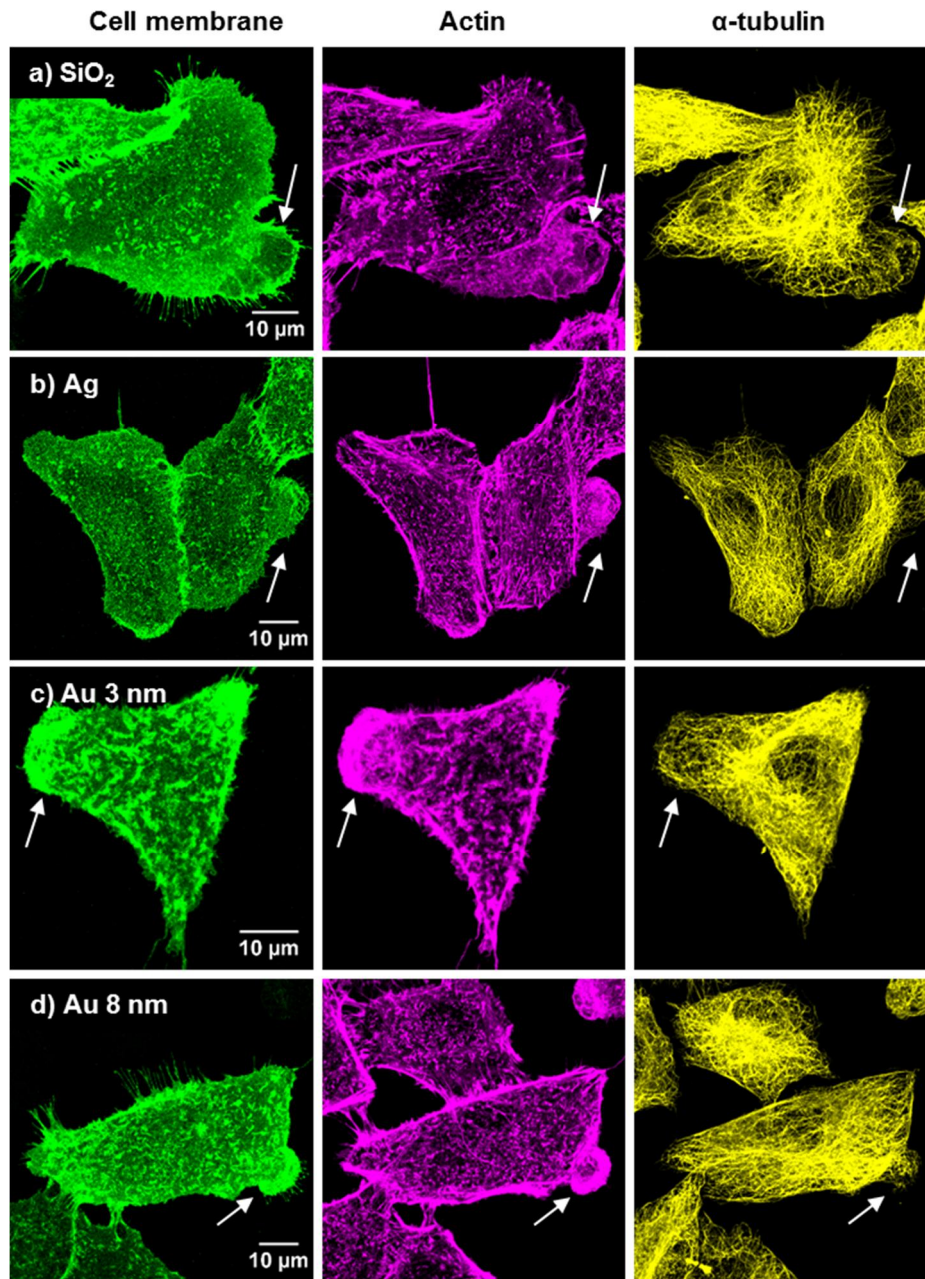


Figure 44: Bleb formation of A549 cells as a function of nanoparticle composition.

A549 pAcGFP1-Mem cells were exposed to nanoparticles for 5 h and stained for actin (magenta) and α -tubulin (yellow). The cell membrane was labeled with GFP (green). The cells were exposed to 7.3×10^{11} particles ml^{-1} of a) 25 nm SiO_2 particles ($10 \mu\text{g ml}^{-1}$), b) 10 nm silver particles ($4 \mu\text{g ml}^{-1}$), c) 3 nm gold particles ($0.2 \mu\text{g ml}^{-1}$), and d) 8 nm gold particles ($3.8 \mu\text{g ml}^{-1}$). The observed blebbing caused changes in the morphology of the cell membrane, the actin and tubulin cytoskeleton, even after an exposure to SiO_2 and Ag nanoparticles. Maximum intensity projection of confocal z-stacks are shown. $n = 1$ with 3 technical replicates.

3.3.4 Cell blebbing and cell movement - formation of lamellipodia

From fixed cell samples, no information regarding the dynamics of bleb formation were obtained. Cell movement is a highly dynamic process and requires imaging of living cells. In order to correlate the cell blebbing with the formation of lamellipodia, live cell imaging was carried out. For this purpose, A549 cells stably transfected with pAcGFP1-Mem, were exposed to $0.2 \mu\text{g ml}^{-1}$ of 3 nm gold particles, which equals 7.3×10^{11} particles ml^{-1} and was shown to promote blebbing of the cell membrane, actin filaments, and microtubules (Figure 44). Although lamellipodia formation is an actin-driven process, the cell protrusion should be visible by a membrane stain, too. After 50 min of

nanoparticle treatment, 3 nm gold particles were already found inside cells and extensive membrane blebbing was observed. A time course of one blebbing cell with frame intervals of 3 sec was recorded. In *Figure 45*, the beginning of the image sequence is shown and blebbing was visible by the strong green membrane signal. Within the first 21 sec of image acquisition, ruffling of the cell membrane occurred and a vesicle was formed inside this region. The diameter of the vesicle was approx. 1.5 μm . Membrane ruffling is typical for an inefficient lamellipodia adhesion (Borm *et al.*, 2005). After 2 min, the vesicle fused with a second vesicle (*Figure 46*). Another 2 min later, the newly formed compartment moved into a region aside from the ruffles (*Figure 47*). The morphology of the compartment changed from elongated to circular. Additionally, the vesicle increased in diameter, up to 3 μm , and did not move further after uptake. It only moved slightly back and forth, but stayed close to the perinuclear region. Frame 191 in *Figure 47* was the last image of the recorded time series. Another two vesicles were generated from the membrane as indicated by the two smaller arrows in that image. Their diameter was 1 μm and slightly below the diameter of the first synthesized vesicle. Frame 191 in *Figure 47* shows further that once vesicles have been internalized membrane blebbing disappeared and the cell showed again a normal morphology without any membrane ruffles or blebs. Some studies provide evidence that besides actin polymerization also polarized endo- and exocytic cycles can cause cell migration (Bretscher 1996a, 1996b) or even macropinocytosis (Gu *et al.*, 2011), which could explain the vesicle formation at the leading edge of the cell. Hence, the live cell data indicated that the observed blebbing potentially could be attributed to lamellipodia formation. The type of the internalized vesicles could not be clarified within this experimental setup. However, the observed vesicle sizes of $> 1 \mu\text{m}$ were similar to sizes known for macropinosomes (Mercer and Helenius 2009). These structures were usually formed at sites of membrane ruffling, e.g. margins of spread cells (Swanson and Watts 1995). Furthermore, type II alveolar epithelial cells, like A549 cells, synthesize LB that also have sizes of 0.1 - 2.4 μm , a circular morphology, and are able to fuse with the cell membrane (Schmitz and Müller 1991).

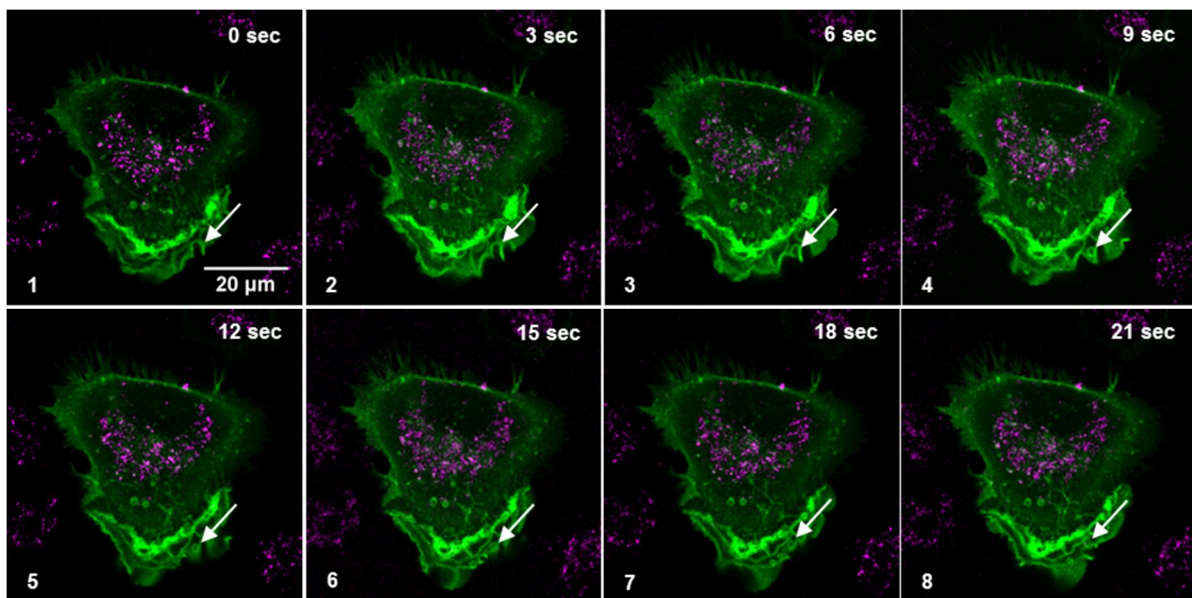


Figure 45: Live cell imaging of blebbing and vesicle formation. A549 cells, transfected with pAcGFP1-Mem, were exposed to $0.2 \mu\text{g ml}^{-1}$ of 3 nm gold particles (7.3×10^{11} particles ml^{-1}) for 50 min and an image sequence with frame intervals of 3 sec was recorded. Single images of the recorded sequence are shown and revealed the formation of a vesicle inside the bleb structure (see arrow). Time is indicated in the top right and frame numbers are stated at the bottom left. The cell membrane is displayed in green, 3 nm gold particles are colored magenta. The smooth function of the Fiji software was used to reduce noise of the images.

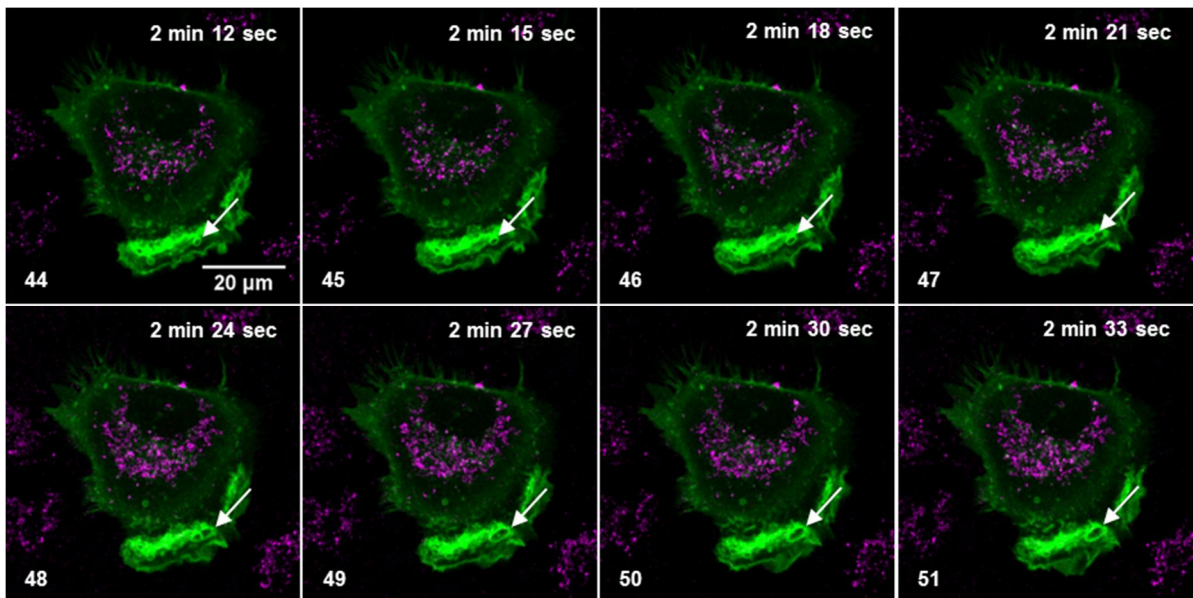


Figure 46: Live cell imaging of blebbing and vesicle fusion.

The generated vesicle (see Figure 45) fused with another vesicle to a much larger compartment. Time is indicated in the top right and frame numbers are stated at the bottom left. The cell membrane is displayed in green, 3 nm gold particles are colored magenta. The smooth function of the Fiji software was used to reduce noise of the images.

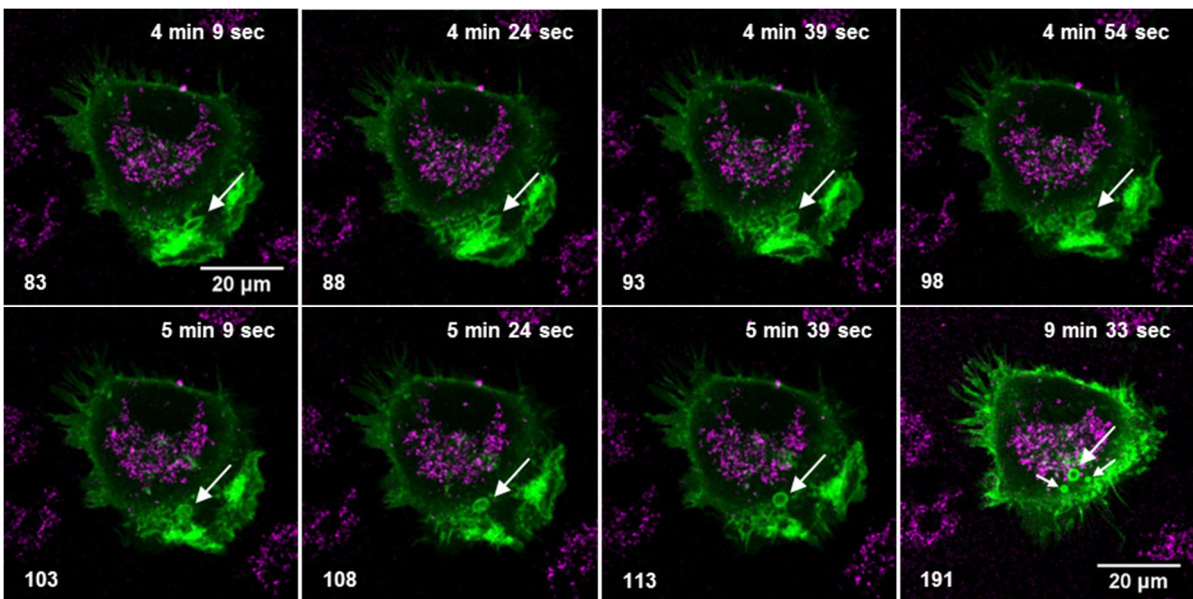


Figure 47: Live cell imaging of blebbing and vesicle movement.

The imaged vesicle moved into a region aside from the ruffles and changed its morphology. Additionally, two smaller vesicles were internalized, as indicated by the smaller arrows in Frame 191. Time is indicated in the top right and frame numbers are stated at the bottom left. The cell membrane is displayed in green, 3 nm gold particles are colored magenta. The smooth function of the Fiji software was used to reduce noise of the images.

3.3.5 Cell blebbing and macropinocytosis

3.3.5.1 The use of labeled dextran to identify macropinosomes

The live cell data demonstrated a relationship between blebbing and vesicle internalization. The generated vesicles had diameters of 1 - 3 μm . Endocytic vesicles that are synthesized during clathrin- or caveolin-mediated endocytosis typically have sizes of 120 nm and 60 nm, respectively. Vesicles that are related to a clathrin- and caveolin-independent endocytosis exhibit diameters of about 90 nm (Conner and Schmid 2003). Vesicles with sizes above 1 μm as observed in the present study can result from macropinocytosis (Conner and Schmid 2003). Macropinosomes exhibit sizes up to 10 μm (Mercer and Helenius 2009) and can result from membrane blebbing (Mercer and Helenius 2009), especially at sites of membrane ruffling (Swanson and Watts 1995). They can be visualized by exposing cells to tracer substances, such as fluorescently-labeled dextran (Falcone *et al.*, 2006). If the observed vesicles were macropinosomes, they should have internalized the fluorescent dextran. To study macropinocytosis in connection with vesicle formation and cell blebbing, A549 cells transfected with pAcGFP1-Mem were exposed to 0.2 $\mu\text{g ml}^{-1}$ of 3 nm gold particles (7.3×10^{11} particles ml^{-1}). After 4 h of nanoparticle exposure, 1 mg ml^{-1} of a 70 kDa Alexa 546-labeled dextran was added for 5 min. Exposure times commonly used for dextran tracers are 0.5 - 30 min (Falcone *et al.*, 2006). To visualize a potential association of internalized dextran and vesicles an image time course was recorded (*Figure 48a*). The imaged cell showed blebbing as indicated by the strong GFP signal. In addition, it exhibited a large vesicle ($\sim 3 \mu\text{m}$), which already had been internalized. However, it did not contain any dextran. Only small amounts of dextran were found attached to the vesicle membrane, as shown in the magnified inlets in the second row. However, the limited resolution in light microscopy, especially during live cell imaging, makes co-localization studies of the dextran and the vesicle membrane difficult. But the common way of intracellular transport of the vesicle and the dextran, as illustrated in *Figure 48a*, demonstrated a co-localization of both structures. During imaging, a second vesicle ($\sim 2 \mu\text{m}$) was internalized (*Figure 48b*). This structure was not filled with dextran. Small amounts of dextran interacted with the vesicle membrane as observed for the previously analyzed vesicle. Hence, the formed vesicles were not surely identified as macropinosomes.

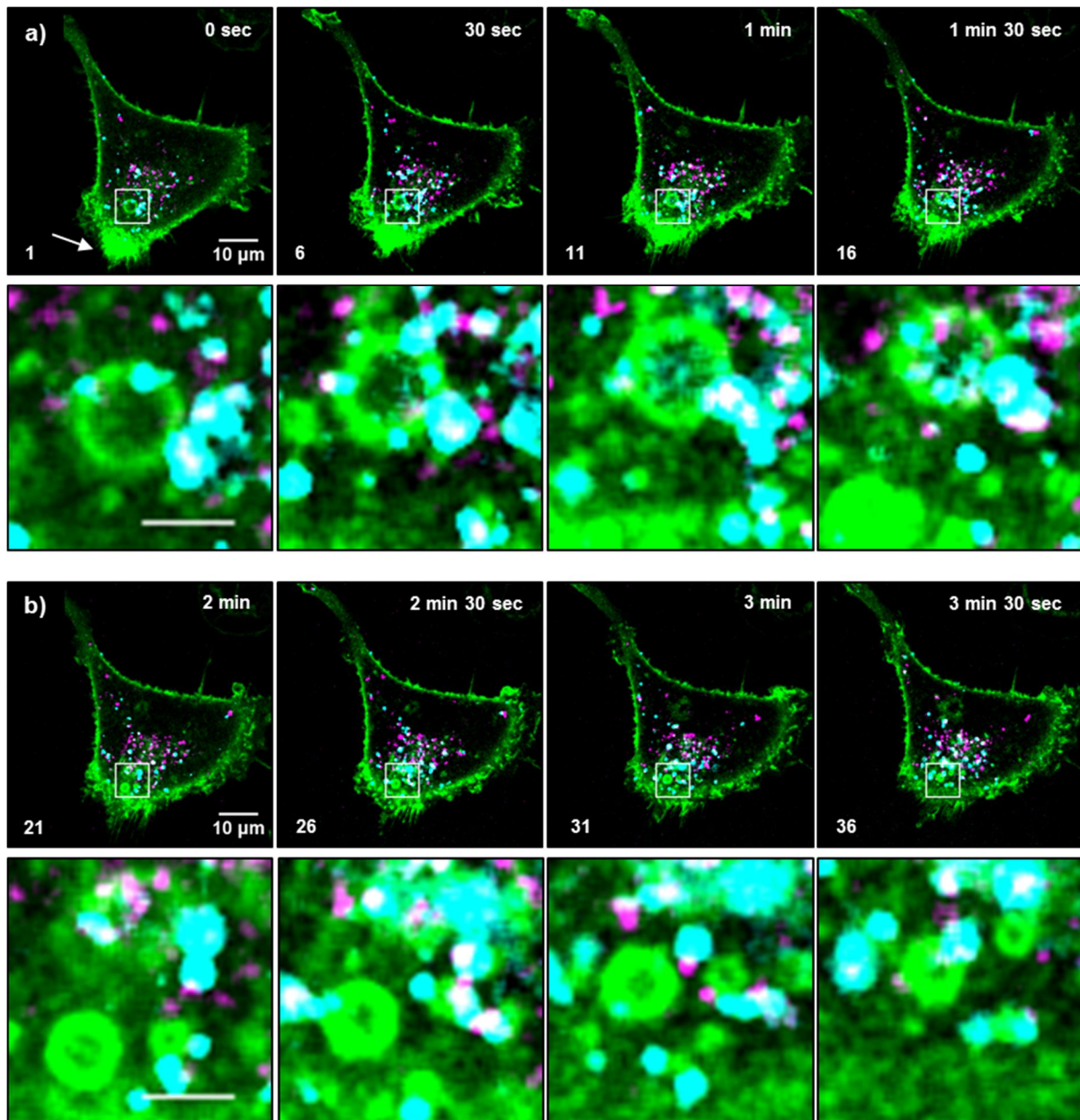


Figure 48: Live cell imaging of macropinocytosis.

A549 pAcGFP1-Mem cells were exposed to $0.2 \mu\text{g ml}^{-1}$ of 3 nm gold particles (7.3×10^{11} particles ml^{-1}) for 4 h. 1 mg ml^{-1} of a 70 kDa Alexa 546-labeled dextran was added to visualize macropinosomes and after 5 min an image sequence with frame intervals of 6 sec was recorded. a) Single images of a blebbing cell (arrow) revealed the presence of a vesicle inside the cell, which was not filled with dextran or nanoparticles (first row). The vesicular structure is displayed magnified in the second row (scale bar: $3 \mu\text{m}$). b) A second vesicle was internalized during imaging. The magnified images in the second row (scale bar: $3 \mu\text{m}$) indicated that the vesicle was also not filled with dextran or nanoparticles. Time is indicated in the top right and frame numbers are stated at the bottom left. The GFP-labeled cell membrane is displayed in green, 3 nm gold particles are colored magenta, and dextran is shown in cyan. The contrast of the images was enhanced. $n = 1$ with 3 technical replicates.

3.3.5.2 Gold nanoparticle transport via macropinosomes

Besides the large vesicles ($> 1 \mu\text{m}$) plenty of smaller vesicles ($\sim 1 \mu\text{m}$) were found inside the cell presented in Figure 48. The real size of the vesicles could not be measured due to restricted resolution in light microscopy. These smaller vesicles were filled with the labeled dextran. Macropinosomes are very inhomogeneous in size (Mercer and Helenius 2009). Since the vesicles above $1 \mu\text{m}$ rather showed an interaction of the vesicle membrane with the dextran and therefore were not surely identified as macropinosomes, the smaller vesicle fraction might represent macropinosomes. The recorded time course revealed that some gold nanoparticles seemed to be

associated with the dextran and moved throughout the cell while staying attached to each other (Figure 49). The simultaneous transport of gold nanoparticles and dextran by vesicles of $\sim 1 \mu\text{m}$ suggested a nanoparticle transport *via* macropinosomes. To really ensure that the observed vesicles pinched off the cell membrane, the last frame shown in Figure 49 was split into single channels and the GFP fluorescence of vesicles was observed (Figure 50). The GFP signal was very dim and did not show a clear vesicle membrane. This might indicate that the macropinosome already entered the endosomal - lysosomal pathway, which causes changes in the vesicle membrane composition and therefore a decrease in the GFP signal. Additionally, vesicle fusion weakens the GFP signal of membrane derived vesicles further. Another explanation for a lacking GFP signal is that the dextran and the gold nanoparticles were not inside vesicles that pinched off the cell membrane and thus not carried a GFP label.

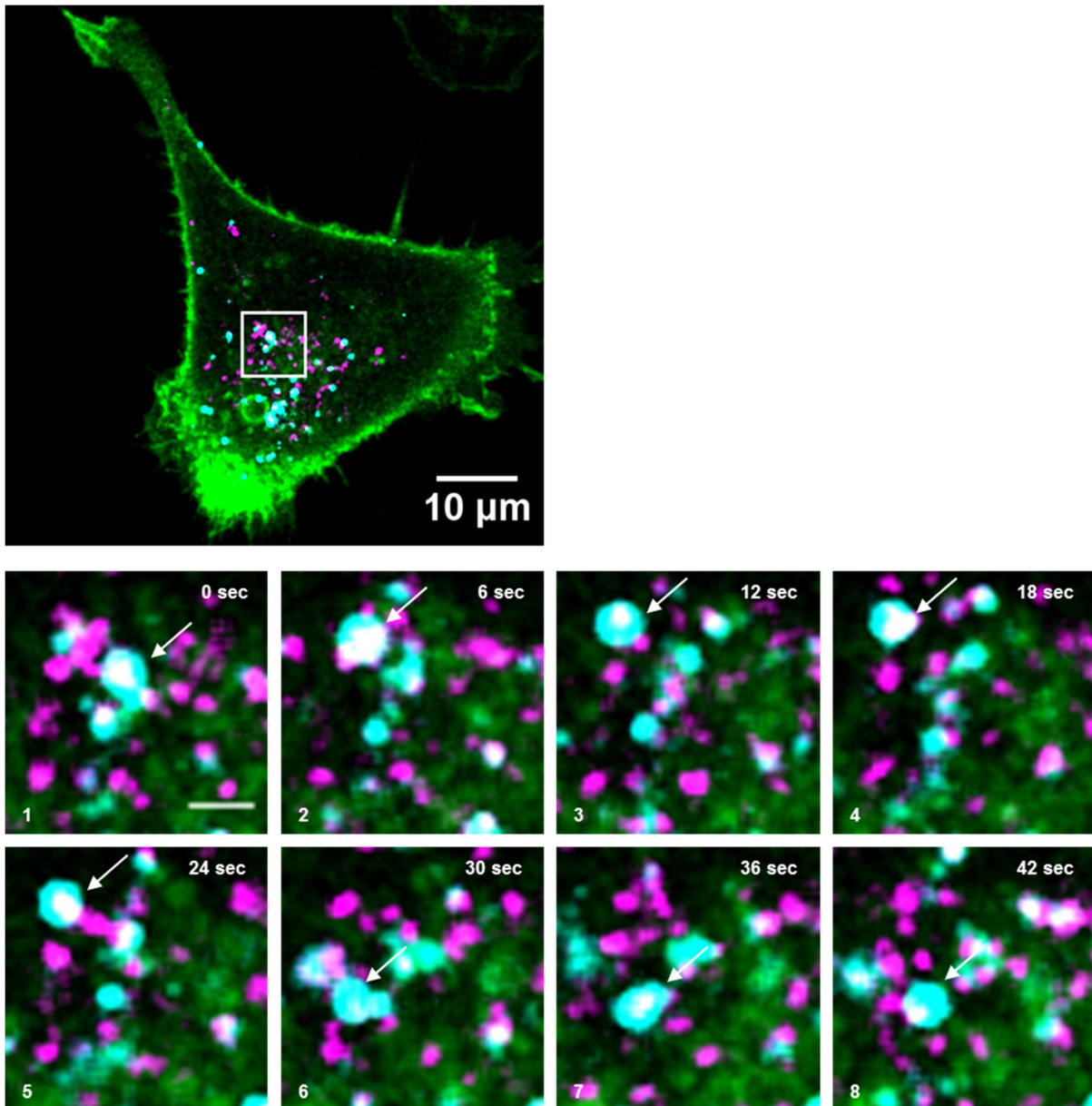


Figure 49: Simultaneous transport of dextran and gold nanoparticles.

A549 pAcGFP1-Mem cells were exposed to $0.2 \mu\text{g ml}^{-1}$ of 3 nm gold particles (7.3×10^{11} particles ml^{-1}) for 4 h. 1 mg ml^{-1} of a 70 kDa Alexa 546-labeled dextran was added to visualize macropinosomes and after 5 min an image sequence with frame intervals of 6 sec was recorded. Dextran (cyan) and gold nanoparticles (magenta) were transported simultaneously indicating nanoparticle internalization *via* macropinocytosis. Time is indicated in the top right and frame numbers are stated at the bottom left. Scale bar: $2 \mu\text{m}$. White color arises from cyan and magenta overlay. $n = 1$ with 3 technical replicates.

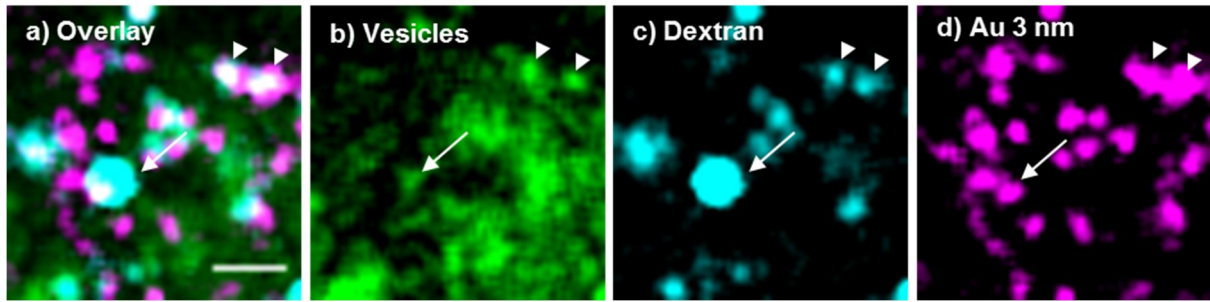


Figure 50: GFP fluorescence of internalized vesicles.

The last frame in Figure 49 was split into singles channels to allow for a precise determination of the GFP fluorescence. a) Overlay of membrane, dextran, and gold nanoparticle fluorescence. b) GFP signal of the membrane stain. c) Alexa 546 signal of dextran. d) Atto 647N fluorescence of 3 nm gold particles. The arrow indicates fluorescence arising from the vesicular structure imaged in Figure 49. Only weak GFP fluorescence was observed. Arrow heads correlate fluorescence from two other vesicles, which exhibited a very strong GFP fluorescence. Scale bar: 2 μm . $n = 1$ with 3 technical replicates.

During imaging, two other vesicles filled with dextran and gold nanoparticles were identified, which exhibited a very strong GFP signal (Figure 50). These vesicles were followed over several frames to visualize a simultaneous movement of cell membrane derived vesicles, dextran, and gold nanoparticles (Figure 51). One of the imaged structures stayed attached whereas the other compartment collapsed as indicated by the spatial separated signals of dextran and gold nanoparticles. This observation leads to the assumption that at least part of the observed vesicles, which contained dextran and gold nanoparticles, have been pinched off the cell membrane and were transported simultaneously throughout the cell. This result supports a potential macropinosome formation as well as a hypothesized gold nanoparticle uptake by macropinocytosis.

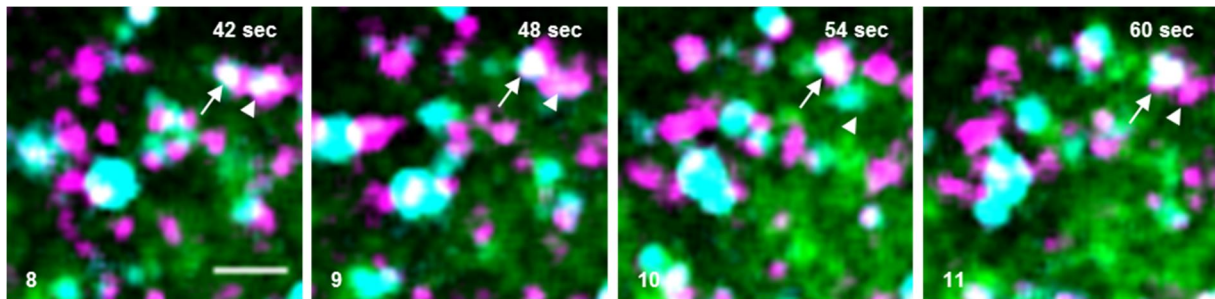


Figure 51: Simultaneous transport of vesicles, dextran, and gold nanoparticles.

The two vesicles from Figure 50 indicated by arrowheads were followed to visualize a simultaneous transport of the vesicle, the dextran, and the nanoparticles. The vesicle-dextran-nanoparticle structure marked with the arrow stayed attached, whereas the other structure did not moved simultaneously. Time is indicated in the top right and frame numbers are stated at the bottom left. Scale bar: 2 μm . White color arises from cyan and magenta overlay.

3.3.5.3 Uptake of gold nanoparticles by macropinocytosis

In the previous section, live cell data demonstrated a gold nanoparticle transport by dextran-filled vesicles that pinched off the cell membrane, presumably macropinosomes. Vesicle-mediated nanoparticle transport was studied by fixed cells as well. For this purpose, A549 pAcGFP1-Mem cells were exposed to 0.02 $\mu\text{g ml}^{-1}$ of 3 nm, 8 nm, and 15 nm gold particles for 5 h. The samples were fixed and analyzed by confocal microscopy. Z-stacks were recorded and examined concerning a nanoparticle internalization *via* vesicles. 3 nm gold particles were found inside vesicles with sizes of 1 - 2 μm (Figure 52a). The vesicles arose from membrane ruffling as already demonstrated by live cell microscopy. However, not all of the vesicles contained nanoparticles, which was also in line with the

results from live cell microscopy, where larger vesicles did not contain gold nanoparticles (*Figure 48*). One of the vesicles was densely filled with 3 nm gold particles as indicated by the very bright Atto 647N fluorescence (*Figure 52b*). The nanoparticles exclusively found attached to the cell membrane. But also vesicles filled with gold nanoparticles were observed (*Figure 52c*).

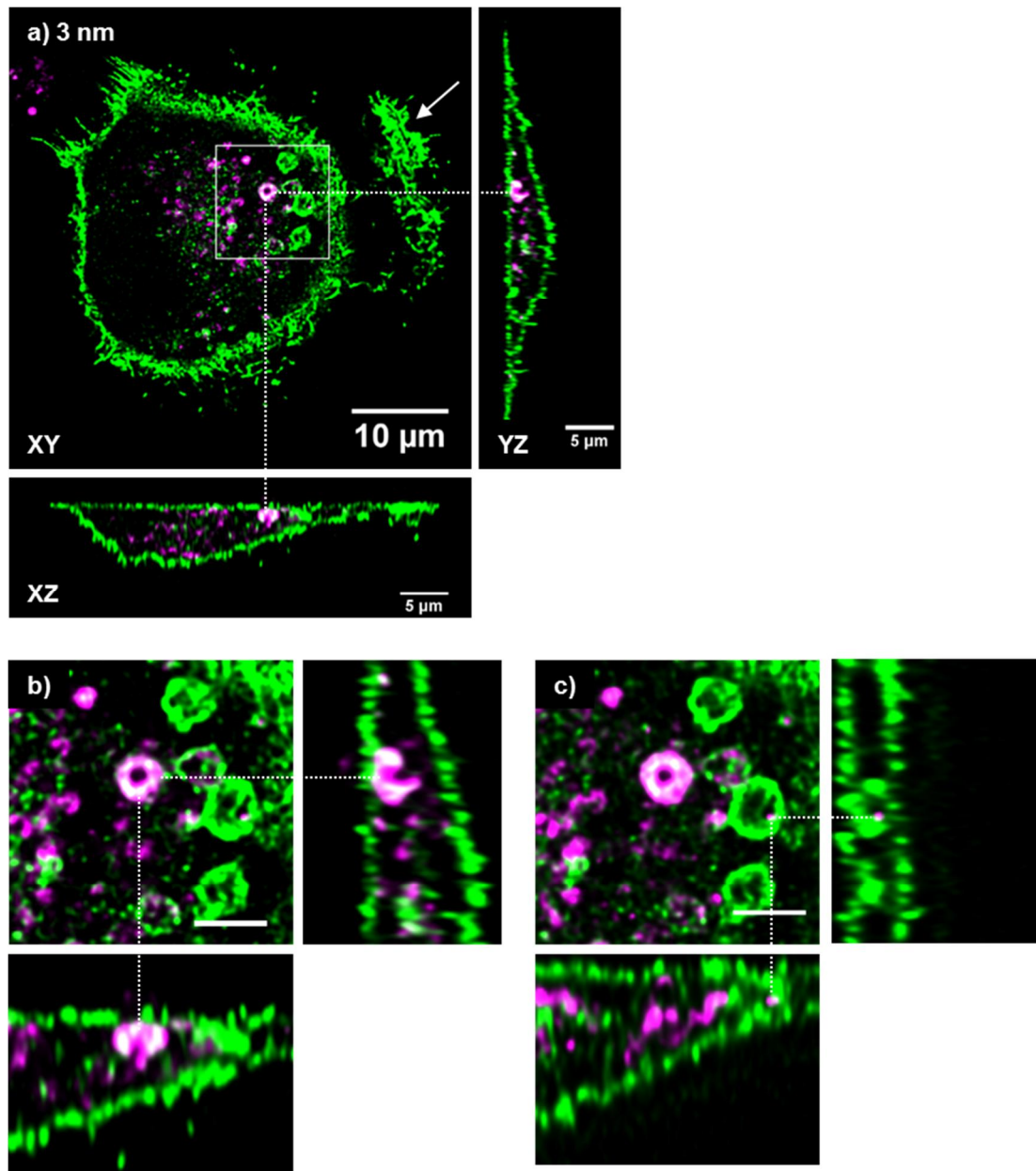


Figure 52: Vesicular uptake of 3 nm gold particles.

A549 pAcGFP1-Mem cells were exposed to $0.02 \mu\text{g ml}^{-1}$ of 3 nm gold particles for 5 h. a) Orthogonal views of a recorded z-stack demonstrated internalized vesicles that presumably arose from membrane ruffling (see arrow). Some of the vesicles contained gold nanoparticles. b) and c) Magnified view of the square drawn in a). Scale bar: $3 \mu\text{m}$. The cell membrane is displayed in green, gold nanoparticles are shown in magenta. The contrast of the images was enhanced.

A similar result was obtained from cells exposed to 8 nm gold particles (*Figure 53*). One internalized vesicle packed with nanoparticles was visualized. The vesicle had a comparable size to the vesicles shown in *Figure 52*, but was not as occupied with nanoparticles as observed previously.

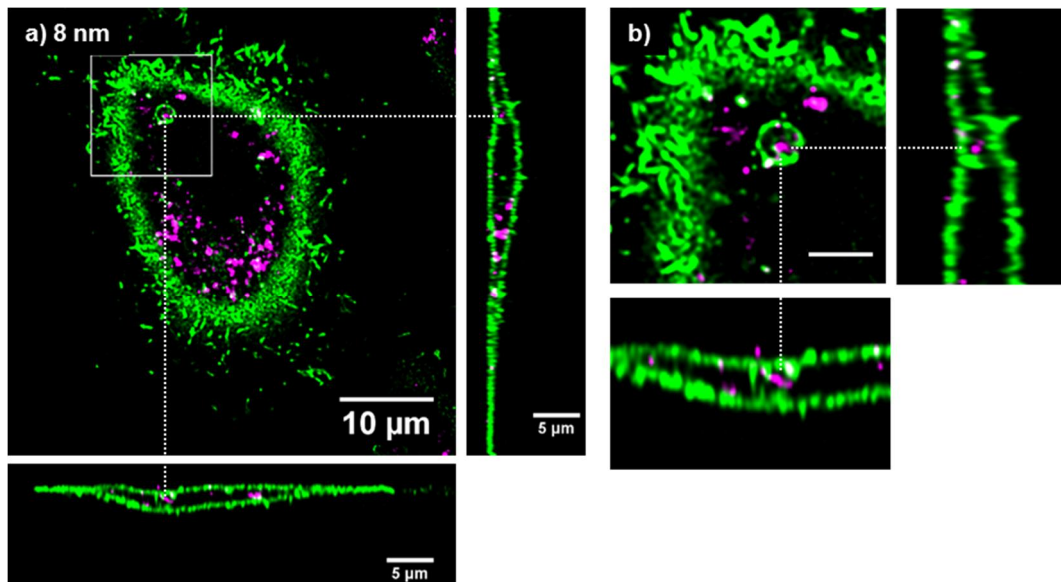


Figure 53: Vesicular uptake of 8 nm gold particles.

A549 pAcGFP1-Mem cells were exposed to $0.02 \mu\text{g ml}^{-1}$ of 8 nm gold particles for 5 h. a) Orthogonal views of a recorded z-stack demonstrated one internalized vesicles, which contained gold nanoparticles. b) Magnified view of the square drawn in a). Scale bar: $3 \mu\text{m}$. The cell membrane is displayed in green, gold nanoparticles are shown in magenta. The contrast of the images was enhanced.

Figure 54 represents results obtained from A549 cells exposed to 15 nm gold particles. One vesicle was generated during membrane ruffling and orthogonal views of the recorded z-stack revealed an enclosed nanoparticle agglomerate (Figure 54b). In comparison to vesicles filled with 3 nm and 8 nm gold particles, this vesicle was less packed. All sizes of nanoparticles were found inside the observed vesicles. The vesicle size ($1 - 2 \mu\text{m}$) as well as their formation by membrane ruffling suggests a partial gold nanoparticle uptake *via* macropinocytosis, which was in accordance with the data obtained by live cell microscopy.

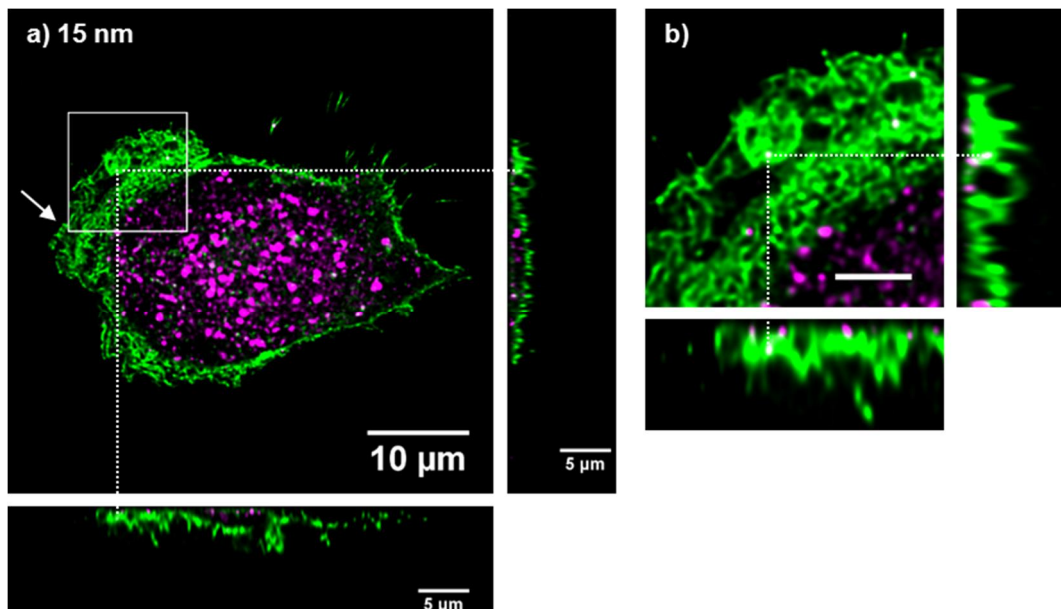


Figure 54: Vesicular uptake of 15 nm gold particles.

A549 pAcGFP1-Mem cells were exposed to $0.02 \mu\text{g ml}^{-1}$ of 15 nm gold particles for 5 h. a) Orthogonal views of a recorded z-stack showed an internalized vesicle that presumably arose from membrane ruffling (see arrow). The vesicles contained gold nanoparticles. b) Magnified view of the square drawn in a). Scale bar: $3 \mu\text{m}$. The cell membrane is displayed in green, gold nanoparticles are shown in magenta. The contrast of the images was enhanced.

3.4 Discussion

3.4.1 Cell blebbing and cell movement

Initially, blebbing of A549 cells was observed as a response to gold nanoparticle exposure and caused changes in the morphology of the tubulin cytoskeleton. The current study revealed that the blebbing also affected the actin cytoskeleton as well as the cell membrane. Especially actin is known to be responsible for cell shape and movement (Pollard and Cooper 2009; Ananthakrishnan and Ehrlicher 2007). Although cell movement is an actin-driven process, the involvement of microtubules in cell migration has been demonstrated (Ballestrem *et al.*, 2000). Hence, the observed blebbing of A549 cells after nanoparticle exposure can be explained by cell migration. During cell movement, the cell extends a protrusion, which is formed at the leading edge by actin polymerization. This lamellipodium develops new adhesion spots and the cell body moves towards the new adhesion (Ananthakrishnan and Ehrlicher 2007). The live cell data demonstrated lamellipodia formation of A549 cells after gold nanoparticle exposure. The lamellipodium showed a strong membrane ruffling and vesicle internalization was observed at the leading edge of the cell. Membrane ruffles in cell migration indicate an inefficient lamellipodia adhesion (Borm *et al.*, 2005), which in consequence hampers cell migration. A recent study of Yang *et al.* demonstrated an inhibitory effect of gold nanoparticles on the migration of PC3 cells. They concluded that settled nanoparticles reduced the grip of the substrate and thus decreased cell migration (Yang *et al.*, 2013). Although the gold nanoparticles used within the study had very small sizes and mainly diffuse freely, a sedimentation of a small particle fraction cannot be excluded. Another study by Soenen *et al.* demonstrated that the internalization of iron oxide nanoparticles negatively affected focal adhesion formation (Soenen *et al.*, 2010), which contributed to a decreased cell movement as well. The study of Yang *et al.* further suggested a nanoparticle uptake *via* the leading edge of the cell during migration followed by endocytosis at the cell body (Yang *et al.*, 2013). In the present study, vesicle formation at lamellipodia was very prominent, which might have been induced by the presence of gold nanoparticles. In summary, the extensive cell blebbing of A549 cells, which has been observed after nanoparticle exposure can be induced by cell movement. There were different indicators for an impaired cell migration as well as for a nanoparticle uptake by lamellipodia. A summary of both and a comparison with unhampered cell migration is presented in *Figure 55*. However, most of the observations require further investigations but represent promising starting points for further studies.

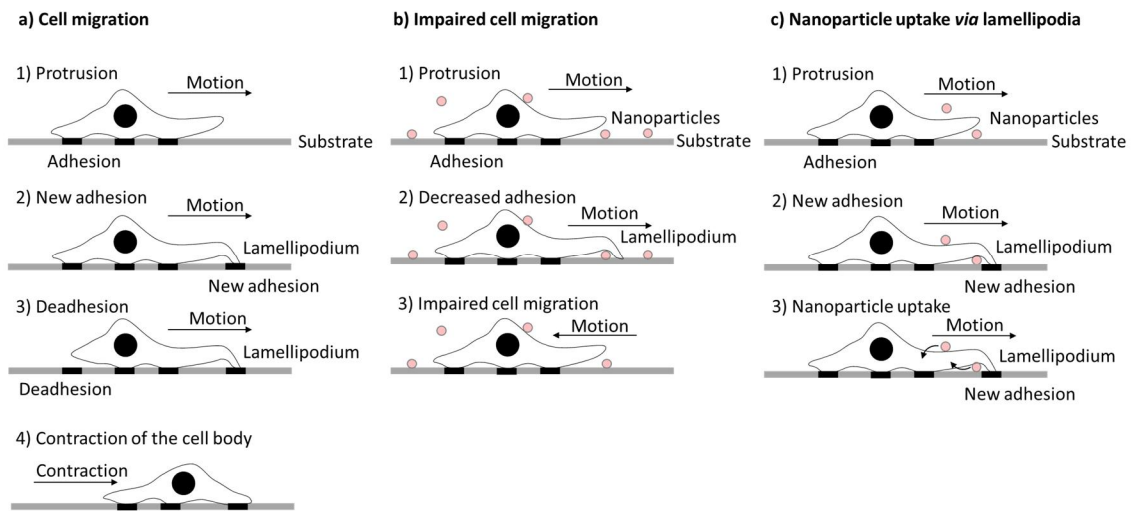


Figure 55: Comparison of unhampered cell migration and cell migration in the presence of nanoparticles. a) Unhampered cell movement through lamellipodia formation. b) Impaired cell migration due to a decreased substrate grip caused by settled nanoparticles. c) Nanoparticle uptake during cell migration. The figure was adapted from Ananthkrishnan and Ehrlicher 2007 and modified.

3.4.2 Cell blebbing and macropinocytosis

The live cell data demonstrated that cell blebbing was closely associated with vesicle formation and internalization indicating a connection of blebbing and cellular uptake processes. The internalized vesicles had sizes of 1 - 3 μm . Endocytic vesicles, which result from clathrin- or caveolin-mediated endocytosis typically have sizes of 120 nm and 60 nm respectively. Vesicles that are related to a clathrin- and caveolin-independent endocytosis exhibit diameters of about 90 nm (Conner and Schmid 2003). Vesicles with sizes above 1 μm as observed in the present study can result from macropinocytosis (Conner and Schmid 2003). Macropinosomes exhibit sizes up to 10 μm (Mercer and Helenius 2009) and can result from membrane blebbing (Mercer and Helenius 2009), usually at the margins of spreading cells (Swanson and Watts 1995). Live cell microscopy revealed a combined transport of a 70 kDa dextran, a macropinosome marker, and gold nanoparticles within vesicles, which were generated from the cell membrane. In addition, from fixed cell samples, the internalization of 3 nm, 8 nm, and 15 nm gold particles by vesicles was demonstrated. The vesicles arose from membrane ruffles and had sizes similar to that known for macropinosomes. Both experimental setups demonstrated the relationship of macropinocytosis, membrane blebbing, and gold nanoparticle uptake and transport. In contrast to cell movement, microtubules only play a minor role during macropinocytosis. A participation of microtubules in bleb formation during macropinocytosis is not known. However, macropinocytosis usually occurs at the leading edge of migrating cells (Swanson and Watts 1995). Hence, the blebbing of tubulin, actin, and the cell membrane, which was observed within this study, was caused by cell migration. Cell migration itself caused membrane ruffling, which in turn can give rise to macropinosome formation.

Generally, macropinocytosis is assumed to mediate nanoparticle uptake (Iversen *et al.*, 2011). Meng *et al.* demonstrated that A549 cells were capable to internalize SiO_2 nanoparticles by a macropinocytosis mechanism (Meng *et al.*, 2011). The present work showed similar results. Gold nanoparticle uptake by A549 cells was shown to be mediated by macropinocytosis. Internalized macropinosomes enter the endosomal-lysosomal pathway and hence undergo lysosomal degradation close to the perinuclear region (Kerr and Teasdale 2009). This transport is mediated by microtubules (Kerr 2006). Results from Chapter 2 demonstrated that internalized gold nanoparticles

reached the perinuclear region of A549 cells by microtubule mediated transport. These observations support a gold nanoparticle uptake by macropinocytosis.

Vesicles with sizes of 1 - 3 μm can also be assigned to other cellular compartments. Type II alveolar epithelial cells, like A549 cells, synthesize LB that also have sizes of 0.1 - 2.4 μm and a circular morphology (Schmitz and Müller 1991). Schumann *et al.* found SiO_2 nanoparticles associated with LB (Schumann *et al.*, 2012). LB, which are responsible for surfactant release (see 1.2.1), are known to interact with MVB, which are part of the endocytic pathway (Weaver *et al.*, 2002). Hence, further experiments on this topic should focus also on this possibility of nanoparticle transport.

3.5 Conclusion

The exposure of A549 cells to gold nanoparticles caused a cell blebbing, which affected the morphology of tubulin, actin, and the cell membrane. These morphological changes were not exclusively observed as a response to gold nanoparticle exposure; SiO_2 and Ag nanoparticles triggered blebbing as well. The cell blebbing was explained by lamellipodia formation, which occurs during cell movement. From live cell microscopy lamellipodia formation was concluded, which was characterized by an extensive membrane ruffling as well as by vesicle internalization at the leading edge. Vesicle uptake occurred partially *via* macropinocytosis, as indicated by a fluorescently labeled dextran, which was used as tracer substance for macropinosomes. It was demonstrated that the uptake and transport of 3 nm, 8 nm, and 15 nm gold particles partially followed macropinocytosis. In conclusion, increased cell migration after gold nanoparticle exposure caused cell blebbing and membrane ruffles at the leading edge gave rise to macropinocytosis. The formed macropinosomes were used to internalize a certain portion of the gold nanoparticles.

3.6 References

- Ananthkrishnan, R.; Ehrlicher, A. (2007): The forces behind cell movement. In *Int. J. Biol. Sci.* 3 (5), pp. 303–317.
- Ballestrem, C.; Wehrle-Haller, B.; Hinz, B.; Imhof, B. A. (2000): Actin-dependent lamellipodia formation and microtubule-dependent tail retraction control-directed cell migration. In *Mol. Biol. Cell* 11 (9), pp. 2999–3012.
- Borm, B.; Requardt, R. P.; Herzog, V.; Kirfel, G. (2005): Membrane ruffles in cell migration: indicators of inefficient lamellipodia adhesion and compartments of actin filament reorganization. In *Exp. Cell Res.* 302 (1), pp. 83–95.
- Bretscher, M. S. (1996a): Getting membrane flow and the cytoskeleton to cooperate in moving cells. In *Cell* 87 (4), pp. 601–606.
- Bretscher, M. S. (1996b): Moving membrane up to the front of migrating cells. In *Cell* 85 (4), pp. 465–467.
- Casciola-Rosen, L. A.; Anhalt, G. R. A. (1994): Autoantigens Targeted in Systemic Lupus Erythematosus Are Clustered in Two Populations of Surface Structures on Apoptotic Keratinocytes. In *J. Exp. Med.* 179.
- Comfort, K. K.; Maurer, E. I.; Braydich-Stolle, L. K.; Hussain, S. M. (2011): Interference of Silver, Gold, and Iron Oxide Nanoparticles on Epidermal Growth Factor Signal Transduction in Epithelial Cells. In *ACS Nano* 5 (12), pp. 10000–10008.
- Conner, S. D.; Schmid, S. L. (2003): Regulated portals of entry into the cell. In *Nat. Nanotech.* 422.
- Dausend, J.; Musyanovych, A.; Dass, M.; Walther, P.; Schrezenmeier, H.; Landfester, K.; Mailänder, V. (2008): Uptake Mechanism of Oppositely Charged Fluorescent Nanoparticles in HeLa Cells. In *Macromol. Biosci.* 8 (12), pp. 1135–1143.
- Elmore, S. (2007): Apoptosis: a review of programmed cell death. In *Toxicol. Pathol. (Toxicologic pathology)* 35 (4), pp. 495–516.
- Fackler, O. T.; Grosse, R. (2008): Cell motility through plasma membrane blebbing. In *J. Cell Biol.* 181 (6), pp. 879–884.
- Falcone, S.; Cocucci, E.; Podini, P.; Kirchhausen, T.; Clementi, E.; Meldolesi, J. (2006): Macropinocytosis: regulated coordination of endocytic and exocytic membrane traffic events. In *J. Cell Sci.* 119 (22), pp. 4758–4769.
- Gu, Z.; Noss, E. H.; Hsu, V. W.; Brenner, M. B. (2011): Integrins traffic rapidly via circular dorsal ruffles and macropinocytosis during stimulated cell migration. In *J. Cell Biol.* 193 (1), pp. 61–70.
- Hartlen, K. D.; Athanopoulos, A. P. T.; Kitaev, V. (2008): Facile Preparation of Highly Monodisperse Small Silica Spheres (15 to >200 nm) Suitable for Colloidal Templating and Formation of Ordered Arrays. In *Langmuir* 24 (5), pp. 1714–1720.
- Iversen, T.-G.; Skotland, T.; Sandvig, K. (2011): Endocytosis and intracellular transport of nanoparticles: Present knowledge and need for future studies. In *Nano Today* 6 (2), pp. 176–185.
- Kang, B.; Mackey, M. A.; El-Sayed, M. A. (2010): Nuclear Targeting of Gold Nanoparticles in Cancer Cells Induces DNA Damage, Causing Cytokinesis Arrest and Apoptosis. In *J. Am. Chem. Soc.* 132 (5), pp. 1517–1519.
- Kerr, M. C. (2006): Visualisation of macropinosome maturation by the recruitment of sorting nexins. In *J. Cell Sci.* 119 (19), pp. 3967–3980.
- Kerr, M. C.; Teasdale, R. D. (2009): Defining Macropinocytosis. In *Traffic* 10 (4), pp. 364–371.
- Koch, M.; Kiefer, S.; Cavelius, C.; Kraegeloh, A. (2012): Use of a silver ion selective electrode to assess mechanisms responsible for biological effects of silver nanoparticles. In *J. Nanopart. Res.* 14 (2).
- Lewinski, N.; Colvin, V.; Drezek, R. (2008): Cytotoxicity of Nanoparticles. In *Small* 4 (1), pp. 26–49.
- Lieber, M.; Smith, B.; Szakal, A.; Nelson-Rees, W.; Todaro, G. (1976): A continuous tumor-cell line from a human lung carcinoma with properties of type II alveolar epithelial cells. In *Int. J. Cancer* 17 (1), pp. 62–70.
- Majno, G.; Joris, I. (1995): Apoptosis, oncosis, and necrosis. An overview of cell death. In *Am. J. Pathol.* 146 (1), pp. 3–15.
- Meng, H.; Yang, S.; Li, Z.; Xia, T.; Chen, J.; Ji, Z.; Zhang, H.; Wang, X.; Lin, S.; Huang, C.; Zhou, Z. H.; Zink, J. I.; Nel, A. E. (2011): Aspect Ratio Determines the Quantity of Mesoporous Silica Nanoparticle Uptake by a Small GTPase-Dependent Macropinocytosis Mechanism. In *ACS Nano* 5 (6), pp. 4434–4447.
- Mercer, J.; Helenius, A. (2009): Virus entry by macropinocytosis. In *Nat. Cell Biol.* 11 (5), pp. 510–520.
- Mills, J. C.; Stone, N. L.; Pittman, R. N. (1999): Extranuclear apoptosis. The role of the cytoplasm in the execution phase. In *J. Cell Biol.* 146 (4), pp. 703–708.
- Mühlfeld, C.; Gehr, P.; Rothen-Rutishauser, B. (2008): Translocation and cellular entering mechanisms of nanoparticles in the respiratory tract. In *Swiss Med. Wkly.* 138 (27-28), pp. 387–391.

- Pan, Y.; Neuss, S.; Leifert, A.; Fischler, M.; Wen, F.; Simon, U.; Schmid, G.; Brandau, W.; Jahn-Dechent, W. (2007): Size-Dependent Cytotoxicity of Gold Nanoparticles. In *Small* 3 (11), pp. 1941–1949.
- Park, E.-J.; Yi, J.; Chung, K.-H.; Ryu, D.-Y.; Choi, J.; Park, K. (2008): Oxidative stress and apoptosis induced by titanium dioxide nanoparticles in cultured BEAS-2B cells. In *Toxicol. Lett.* 180 (3), pp. 222–229.
- Pollard, T. D.; Cooper, J. A. (2009): Actin, a Central Player in Cell Shape and Movement. In *Science* 326 (5957), pp. 1208–1212.
- Schindelin, J.; Arganda-Carreras, I.; Frise, E.; Kaynig, V.; Longair, M.; Pietzsch, T.; Preibisch, S.; Rueden, C.; Saalfeld, S.; Schmid, B.; Tinevez, J.-Y.; White, D. J.; Hartenstein, V.; Eliceiri, K.; Tomancak, P.; Cardona, A. (2012): Fiji: an open-source platform for biological-image analysis. In *Nat. Meth.* 9 (7), pp. 676–682.
- Schmitz, G.; Müller, G. (1991): Structure and function of lamellar bodies, lipid-protein complexes involved in storage and secretion of cellular lipids. In *J. Lipid Res.* 32, pp. 1539–1570.
- Small, J. V.; Stradal, T.; Vignal, E.; Rottner, K. (2002): The lamellipodium: where motility begins. In *Trends Cell Biol.* 12 (3), pp. 112–120.
- Soenen, S. J. H.; Nuytten, N.; Meyer, S. F. de; Smedt, S. C. de; Cuyper, M. de (2010): High Intracellular Iron Oxide Nanoparticle Concentrations Affect Cellular Cytoskeleton and Focal Adhesion Kinase-Mediated Signaling. In *Small* 6 (7), pp. 832–842.
- Swanson, J. A.; Watts, C. (1995): Macropinocytosis. In *Trends Cell Biol.* 5 (11), pp. 424–428.
- Taylor, R. C.; Cullen, S. P.; Martin, S. J. (2008): Apoptosis: controlled demolition at the cellular level. In *Nat. Rev. Mol. Cell Biol.* 9 (3), pp. 231–241.
- Thurn, K. T.; Arora, H.; Paunesku, T.; Wu, A.; Brown, E. M.; Doty, C.; Kremer, J.; Woloschak, G. (2011): Endocytosis of titanium dioxide nanoparticles in prostate cancer PC-3M cells. In *Nanomedicine* 7 (2), pp. 123–130.
- van Cruchten, S.; van den Broeck, W. (2002): Morphological and Biochemical Aspects of Apoptosis, Oncosis and Necrosis. In *Anatom. Histol. Embryol.* 31 (4), pp. 214–223.
- Yang, J. A.; Phan, H. T.; Vaidya, S.; Murphy, C. J. (2013): Nanovacuums: Nanoparticle Uptake and Differential Cellular Migration on a Carpet of Nanoparticles. In *Nano Lett.* 13 (5), pp. 2295–2302.

4. A correlative analysis of gold nanoparticles internalized by A549 cells

4.1 Introduction

The interactions of nanoparticles with human cells are of great interest with regard to safe handling and application of engineered nanomaterials in various fields including biomedicine (Borm *et al.*, 2006; Krug and Wick 2011; Oberdörster 2010; Yokel and MacPhail 2011). Current *in vitro* studies focus on uptake mechanisms and the location of nanoparticles inside different cell types by light and electron microscopy (Brandenberger *et al.*, 2010b; Johnston *et al.*, 2010; Zhang and Monteiro-Riviere 2009). Nanoparticles composed of elements with high atomic number, e.g. silver or gold, are widely used for assessing nanoparticle-cell interactions by electron microscopy (Nativo *et al.*, 2008; Pelka *et al.*, 2009; Schrand *et al.*, 2010; Uboldi *et al.*, 2009). However, the preparation of cells for electron microscopy is challenging and time-consuming and may cause shrinking or flattening of the cells or introduction of structural artifacts (Mayhew 2009; Mühlfeld *et al.*, 2007; Brandenberger *et al.*, 2010a; Elsaesser *et al.*, 2010). In contrast, fluorescence labels are commonly introduced (Al-Rawi *et al.*, 2011; Kim *et al.*, 2011) to enhance the contrast of nanoparticles for studies utilizing advanced fluorescence microscopy techniques, e.g. confocal laser scanning microscopy (CLSM) (Wang *et al.*, 2012). Fluorescence microscopy and suitable preparation techniques enable staining of a wide range of specific cellular structures, multiplex imaging, as well as live cell imaging (Merrifield *et al.*, 2002; Shaner *et al.*, 2007). In comparison to electron microscopy, fluorescence microscopy provides a larger field of view (Pawley 2010), but suffers from low lateral and axial resolution, making a differentiation between single particles or particle agglomerates difficult. Super-resolution techniques, e.g. stimulated emission depletion (STED) microscopy, in part overcome these drawbacks (Hell 2009; Hell and Wichmann 1994). STED microscopy enables an improved lateral, axial, or isotropic resolution below the diffraction barrier, typically in the range of 30 - 80 nm (Klar *et al.*, 2000; Müller *et al.*, 2012). Recently, STED microscopy was applied for the imaging of single nanoparticles and small nanoparticle agglomerates inside cells (Schübbe *et al.*, 2010; Schübbe *et al.*, 2012). However, super-resolution light microscopy techniques are not routine and limited to a small community.

Correlative light and electron microscopy (CLEM) has the power to combine advantages from both, fluorescence and electron microscopy (Giepmans 2008). CLEM comprises a wide range of potential markers. Most prominent are quantum dots, which emit light at a well-defined wavelength (Alivisatos *et al.*, 2005). Their composition, e.g. CdSe or ZnS, simultaneously allows detection by electron microscopy (Giepmans *et al.*, 2005). In other approaches, the production of free radicals from fluorophores is used to create electron dense precipitates that can be visualized by electron microscopy (Grabenbauer *et al.*, 2005; Meisslitzer-Ruppitsch *et al.*, 2010). Furthermore, fluoronanoprobes are widely used to label cellular structures for CLEM. Small colloidal metal nanoparticles, predominately gold, and fluorophores are conjugated to an antibody, enabling the imaging of cellular structures by fluorescence and electron microscopy (Takizawa and Robinson 2000). Fluorescently labeled metal nanoparticles are a common particle system to investigate nanoparticle-cell interactions by light microscopy. Their similarity to the previously mentioned fluoronanoprobes makes them a suitable substrate for CLEM. There are plenty of publications dealing with fluorescently labeled metal nanoparticles (Lehmann *et al.*, 2010; Röcker *et al.*, 2009). Generally, respective functionalizations are realized by a polymer that introduces water solubility and

carries the fluorescent dye (Pellegrino *et al.*, 2005). Although the nanoparticle shell is believed to influence uptake, intracellular delivery, and toxicity (Nel *et al.*, 2009), data regarding the stability of the nanoparticle-polymer-dye complexes in terms of a combined intracellular presence is lacking. It is known that nanoparticles agglomerate in physiological media, if not sufficiently stabilized (Schulze *et al.*, 2008). Ligand exchange reactions might cause replacement of the original coating (Mahl *et al.*, 2010). Nanoparticles might be stabilized by binding of proteins to the particle surface forming the so-called protein corona, thus acting as spacer molecules or steric stabilizer (Casals *et al.*, 2010). Cellular compartments differ in pH as well as in enzyme and protein composition from the extracellular environment. These factors have already been shown to affect nanoparticle stability (Raouf *et al.*, 2012; Sée *et al.*, 2009). The uptake of gold nanoparticles by epithelial cells has been studied recently by combining dark-field light microscopy and transmission electron microscopy (TEM) (Rosman *et al.*, 2012). Up to now there is no correlative microscopic study examining the location of fluorophores as markers for the particle coating compared to the particle core, especially after their uptake into cells. Within this study, we report the application of CLEM to monitor fluorescently labeled polymer coated gold nanoparticles inside A549 cells using CLSM and TEM. The focus of this study is on the spatial correlation of the fluorescence and the respective gold signals. For cell culture, silicon nitride microchips were used as they have already been shown to be a suitable substrate for imaging whole cells by fluorescence microscopy, scanning electron microscopy (SEM), TEM as well as CLEM (Peckys and Jonge 2011; Jonge *et al.*, 2009; Dukes *et al.*, 2010). Whole cells were prepared for TEM based on the dehydration of cells at a pressure below the equilibrium vapor pressure of water (Stokes 2003; Stokes 2008).

4.2 Experimental section

4.2.1 Gold nanoparticle synthesis

All chemicals were purchased from Sigma-Aldrich in the highest purity available and used as received unless indicated otherwise. The fluorescent dye Atto 647N-NH₂ was purchased from Atto-Tec (Germany) and stored at -20°C prior to use. Ultrapure water with a resistivity of > 18 MΩ was used for all preparation and purification steps.

8 nm lipophilic dodecanthiol-capped gold nanoparticles were prepared according to the method described by Zheng *et al.* (Zheng *et al.*, 2006). In brief, 0.31 g (0.63 mmol) AuPPh₃Cl and 313 μl (1.31 mmol) dodecanthiol were dissolved in 50 ml of toluene. After heating to 55°C, 0.54 g (6.25 mmol) tert-butylamine-borane were added under stirring. The mixture was reacted at this temperature for 60 min. The obtained gold nanoparticles were precipitated with ethanol followed by centrifugation and dispersion in 10 ml cyclohexane. Hydrophilic gold nanoparticles were prepared using a modified phase transfer protocol described by Pellegrino *et al.* (Pellegrino *et al.*, 2004). For this purpose, 100 mg of an amphiphilic polymer (Poly-maleic anhydride-alt octadecene, modified with mPEG750) were dissolved in 40 ml of water. 2 ml of lipophilic dodecanthiol-capped gold nanoparticles were added under stirring. The mixture was then emulsified for 5 min using an ultrasound disintegrator (Branson, 50% amplitude, 20 W output) and heated to 70°C to evaporate the solvent. Subsequent heating and ultrasonication yielded hydrophilic polymer coated particles in form of a wine red transparent dispersion. The particles were purified by centrifugation (20,000 x g) and again dispersed in water. Purification was repeated two times to remove non-adsorbed polymer. The obtained dispersion was filtered into sterile falcon tubes using pyrogen-free 0.22 μm hydrophilic cellulose acetate membranes and kept sterile at 5°C. Modification of the polymer coated particles with Atto 647N dye was achieved through activation of carboxylate groups on the particle surface with N-(3-dimethylaminopropyl)-N'-ethylcarbodiimide (EDC) / N-hydroxysuccinimide (NHS) and further reaction with amine-modified Atto 647N-NH₂ (Atto-Tech, Germany). To obtain nanoparticles with sufficient fluorescence for imaging an excess dye to nanoparticle ratio of 5,000 : 1 was chosen. After labeling, the particles were isolated by centrifugation (20,000 x g) and dispersed in water. This step was repeated until no dye fluorescence could be detected in the supernatant (3 - 4 cycles).

4.2.2 Characterization of gold nanoparticles

Freshly dialyzed and sterile filtered colloidal gold nanoparticle dispersions were used for characterization. The nanoparticle size, size distribution, and morphology were analyzed by TEM, using a Philips CM200 FEG (FEI Company, Eindhoven, NL) equipped with an energy dispersive X-ray (EDX) spectrometer (EDAX DX-4/Phönix, Ametek, Germany). Prior to analysis, the particle dispersion was diluted in water (1:1,000). Samples were prepared by drying the diluted nanoparticle dispersion onto a holey carbon film or a silicon nitride chip. Particle size distributions of TEM images were obtained using the free image analysis software ImageJ (<http://rsb.info.nih.gov/ij/>). In brief, after background subtraction and adjustment of brightness and contrast, the TEM images were converted into 8 bit binary images. Particle size analysis was performed by using the "analyze particle" tool, which counts the number of particles, outlines the particle boundaries and measures the Feret diameter. The gold concentration in aqueous dispersions was determined by inductively coupled plasma-optical emission spectroscopy (ICP-OES) with an Ultima 2 ICP-OES device (Horiba JobinYvon, Germany). A Cary 5000 spectrophotometer (Varian Inc., Germany) was used to record UV-Vis spectra of undiluted solutions in the range from 300 to 800 nm. Fluorescence spectra were recorded with a

Spex FluoroMax-3 (HORIBA Scientific, Germany) using diluted (1:100) particle suspensions in MilliQ water at an excitation wavelength of 647 nm. A dye concentration of 23 ± 4 Atto 647N molecules per particle was calculated based on the particle size distribution, measured fluorescence intensity and molar particle concentration in suspension. For dynamic light scattering experiments, a Dyna Pro Titan instrument (Wyatt Technology, Wyatt Technology Europe GmbH, Germany) with a laser wavelength of 831 nm was used to determine the hydrodynamic diameter of the particles in aqueous suspension. Prior to measurements, the gold nanoparticle suspension was filtered through a sterile 0.22 μm cellulose acetate membrane and adjusted to a nanoparticle concentration of 0.1 nM. Zeta-Potential measurements of the same suspensions were recorded using a Malvern Zetasizer Nano (Malvern, Germany).

4.2.3 Cell culture

The human lung carcinoma cell line A549 (ACC 107) as model for type II alveolar epithelial cells was used within this study. The cells were obtained from the German Collection of Microorganisms and Cell Culture (DSMZ, Braunschweig, Germany). A549 cells were grown in Dulbecco's modified eagle's medium (DMEM) (Gibco, Life Technologies, USA) supplemented with 10 % (v/v) fetal bovine serum (FBS) (PAN biotech, Germany) at 37 °C in a 9 % CO₂ atmosphere. After reaching ~80 % confluence, cell cultures were split using 0.05 % trypsin containing 0.02 % EDTA (PAN biotech, Germany). For experiments, cells from passage 20 were used.

4.2.4 Preparation of silicon nitride microchips and cell seeding

Custom made silicon nitride microchips (Protochips, Hummingbird, USA) were kindly provided by Protochips Inc. These microchips were used as substrates for cell culture and correlative microscopy. The chips feature a 50 x 400 μm^2 window with a thickness of 50 nm allowing transmission of the laser as well as the electron beam and are therefore suited for both, fluorescence and electron microscopy. Prior to cell seeding, the microchips were cleaned as published previously (Peckys and Jonge 2011). The cleaned chips were transferred into a 96-well plate. Each well (area: 34 mm²) was filled with 100 μl of cell culture medium and A549 cells were seeded onto the chips. An appropriate cell density of 5 - 10 cells per window (8,500 - 17,000 cells per well) was determined experimentally. DMEM without phenol red (PAN biotech, Germany) supplemented with 10 % (v/v) FBS was used as cell culture medium. Prior to nanoparticle exposure, the cells were incubated for 20 - 24 h to allow cell attachment.

4.2.5 Exposure of cells to nanoparticles

Dispersions of 0.02 $\mu\text{g ml}^{-1}$ ($3.9 \cdot 10^9$ particles ml^{-1}) were prepared freshly prior to each experiment by diluting the nanoparticle stock in cell culture medium. The colloidal dispersions were mixed using a vortex mixer and added to A549 cells grown on silicon nitride microchips. The cells were exposed to gold nanoparticles for 5 h.

4.2.6 Immunostaining

For CLSM, the tubulin cytoskeleton of A549 cells was fluorescently labeled using antibodies. In brief, the cells were rinsed with PBS and subsequently fixed using 4 % (v/v) formaldehyde (Electron microscopy science, UK). Cells were permeabilized with 0.2 % (v/v) Triton-X 100 (Roth, Germany). Blocking of unspecific antibody binding sites was carried out using 5 % (w/v) bovine serum albumin (BSA, AppliChem, Germany). α -tubulin was labeled using 1 $\mu\text{g ml}^{-1}$ mouse anti- α -tubulin IgG

(Invitrogen, Life Technologies, USA) and $3 \mu\text{g ml}^{-1}$ goat anti mouse Alexa 488 (Invitrogen, Life Technologies, USA) as secondary antibody. Both antibodies were diluted in 1 % (w/v) BSA. All solutions were prepared in PBS.

4.2.7 Confocal laser scanning microscopy (CLSM)

The Leica TCS SP5 system with a 100x / 1.4 oil immersion objective (HCX PL APO, Leica, Germany) was used for confocal imaging. Prior to microscopic analyses, the chips were transferred into cell view dishes equipped with a glass bottom (Greiner BioOne, Germany) and placed upside down onto the glass. After addition of 500 μl PBS, the samples were imaged immediately. Atto 647N was excited by using a HeNe laser with an excitation wavelength of 633 nm. An avalanche photodiode (APD) was used to detect the emitted fluorescence. Alexa 488-labeled α -tubulin was imaged using an argon laser line of 488 nm for excitation. The fluorescence emission was detected by a PMT. The pinhole size was set to 1 AU. Images and z-stacks were recorded sequentially. A z-step size of 130 nm and pixel sizes of 50 - 70 nm^2 were chosen.

4.2.8 Scanning transmission electron microscopy (STEM) of hydrated samples in the ESEM (wet STEM)

After confocal imaging, cells were additionally fixed with 1 % (v/v) glutaraldehyde (Electron microscopy science, UK) and rinsed with PBS. Samples were stored in PBS at 277 K. Prior to imaging, samples were briefly washed in water and mounted on a pre-cooled wet STEM sample holder ($T = 276 \text{ K}$). Subsequently, samples were transferred into the chamber of an ESEM Quanta 400 FEG (FEI Company, Hillsboro, USA). In order to exchange the ambient atmosphere for an atmosphere containing water at imaging conditions, the ESEM chamber was purged with water vapor five times using a pressure range of 800 - 1,500 Pa. Imaging was performed at 750 and 720 Pa and 30 keV (spot size 3) using a solid-state detector in bright field mode for the collection of transmitted electrons. At 750 Pa and $T = 276 \text{ K}$, water is at the phase boundary between liquid and gaseous water, according to the p-T phase diagram (Wexler 1976). Thus, it was assumed that the cells were in a fully hydrated state. At 720 Pa, the equilibrium is shifted just below the phase boundary. After imaging for about 10 min, the pressure in the ESEM chamber was reduced to 600 Pa for further 10 min. Under these conditions, water is in its gaseous phase, allowing for dehydration of the cells (Stokes 2003).

4.2.9 TEM imaging

Dehydrated cell samples were transferred to a TEM sample holder and investigated at room temperature using a Philips CM200 FEG (FEI Company, Eindhoven, NL) at 200 keV (gun lens 2, spot size 1) equipped with a MultiScan camera (Model 794, Gatan, Pleasanton, USA) and an EDX spectrometer (EDAX DX-4/Phönix, Ametek, Germany). An inherent property of the CM200 comprises automatic image rotation with increasing magnification. To facilitate superimposition with CLSM images, the obtained images were back-rotated.

4.2.10 Image processing

Confocal z-stacks were deconvolved with Huygens professional software (SVI, Netherlands) using the classic maximum likelihood estimation algorithm. Experimentally determined PSFs were used for deconvolution. For illustrations, intensity measurements, and orthogonal sectioning, images and stacks were further processed in Fiji (Schindelin *et al.*, 2012).

4.3 Results

4.3.1 Properties of gold nanoparticles

By use of TEM, the morphology and size of the fluorescently labeled gold nanoparticles was determined. The particles were roughly spherical with a diameter of 8.4 nm \pm 0.5 nm (Figure 56a). Hence, the nanoparticles were designated as 8 nm in size. The presence of the polymer coating surrounding the nanoparticles was monitored by depositing the particle dispersion on a holey carbon film. For gold nanoparticles laying at the edge of the carbon film, the polymer shell could be visualized by TEM analysis (Figure 56b). A shell thickness of \sim 1 nm was determined, resulting in a total particle diameter of about 10 nm. This data was in accordance with DLS measurements, indicating a hydrodynamic particle diameter of 13.2 nm \pm 4.8 nm. TEM micrographs of lipophilic dodecanthiol-capped gold nanoparticles prior to phase transfer and functionalization with the polymer shell were recorded, too. In comparison to the hydrophilic particles after phase transfer, the coating of the particles was not visible at the edge of the carbon film by TEM. (Figure 56c). Due to the large number of carboxyl groups on the polymer shell, the particles exhibited a strongly negative zeta potential (-49.7 mV). The physico-chemical parameters of the gold nanoparticles are summarized in Table 21. The particle dispersion exhibited an absorption maximum at 520 nm due to the surface plasmon resonance. The absorption maximum did not significantly shift after dispersion of the particles in cell culture medium, indicating particle stability under these conditions. UV-Vis and emission spectra of fluorescently labeled gold nanoparticles are included in the appendix (Figure S1) as well as EDX analyses of the gold particles on silicon nitride chips (Figure S2). After phase transfer and labeling, the particles were purified by repeated centrifugation steps to remove unbound dye and polymer molecules.

Table 21: Physico-chemical properties of Atto 647N-labeled gold nanoparticles.

d_{TEM} = particle diameter determined by TEM and image analysis. d_{DLS} = hydrodynamic particle diameter obtained by DLS measurements in water. The zeta potential of the particles was measured in water. The molar particle concentration (nM) was calculated based on a particle diameter of 8.4 nm and a gold mass concentration of 963 mg l⁻¹. λ_{Au} = absorption maximum of the particle dispersions due to the surface plasmon resonance. λ_{Abs} = absorption maximum related to coupling of Atto 647N, λ_{Em} = emission maximum of Atto 647N.

d_{TEM} [nm]	d_{DLS} [nm]	Zeta potential [mV]	Particle concentration [nM]	λ_{Au} [nm]	λ_{Ex} [nm]	λ_{Em} [nm]
8.4 \pm 0.5	13.2 \pm 4.8	-49.7	267	520	647	663

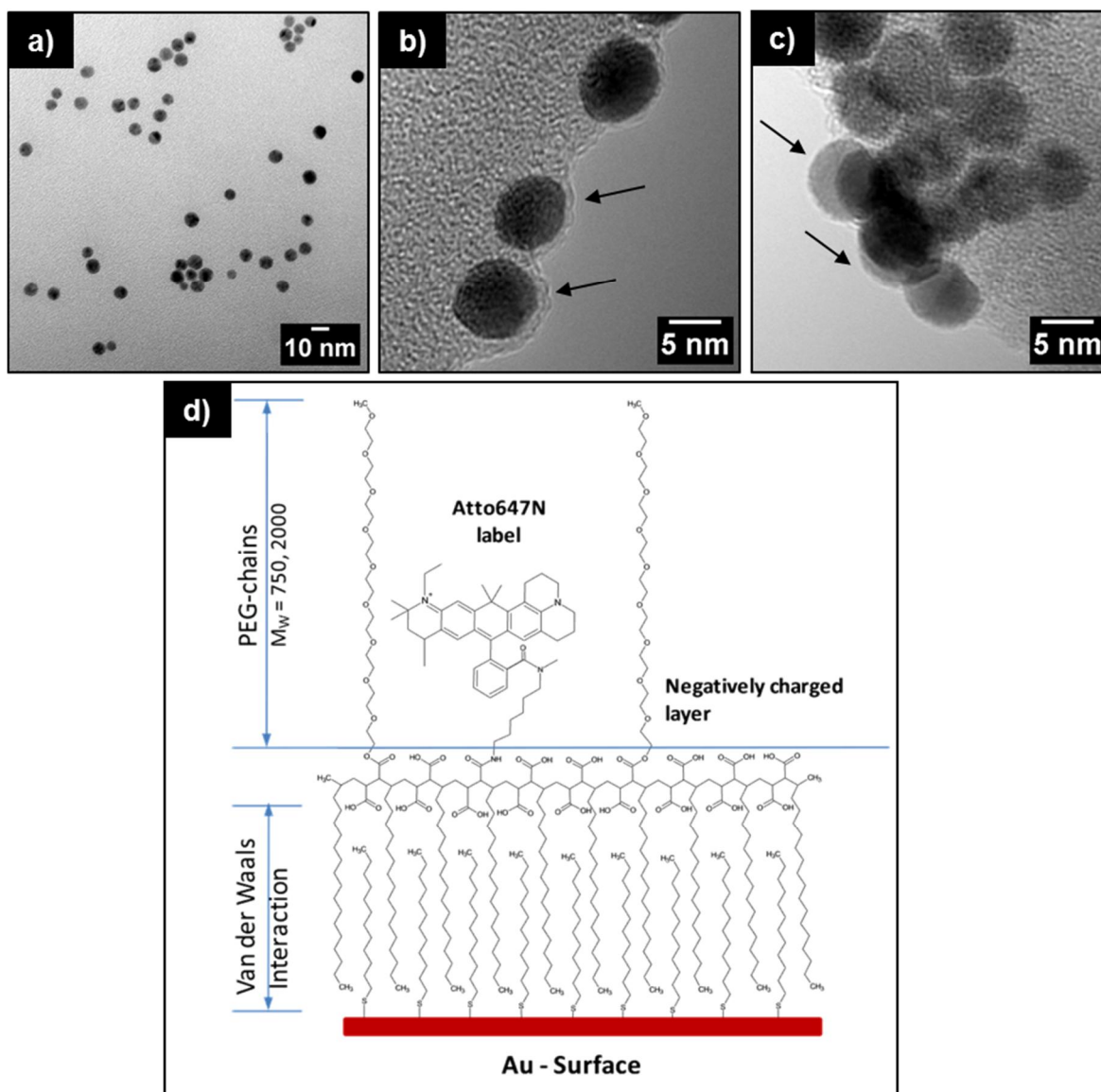


Figure 56: TEM micrographs of gold nanoparticles and scheme of the particle shell.

a) 8 nm gold particles showed a narrow size distribution and were well dispersed as indicated by the distances between adjacent particles. b) The polymer coating surrounding the particle surface was visualized at the edge of a carbon film (see arrows). c) TEM micrograph of 8 nm gold particles without polymer shell. A particle shell as seen in b) was not observed (see arrows). d) Scheme of the functionalized particle surface (Image provided by Dr. C. Cavellius). Alkylthiol linkers were covalently bound to the gold nanoparticle surface (Au, red). An amphiphilic polymer (Poly-maleic anhydride-*alt* octadecene, coupled to mPEG750) was bound via van-der-Waals interactions to the linker molecules. Negatively charged carboxyl groups were used to covalently attach the amine-modified Atto 647N-NH₂ to the polymer surface.

4.3.2 Localization of Atto 647N fluorescence signals by CLSM

A549 cells were exposed to 8 nm Atto 647N-labeled gold particles at a concentration of 3.3×10^9 particles ml⁻¹ corresponding to a gold mass concentration of $0.02 \mu\text{g ml}^{-1}$ for 5 h. The total particle number in the applied volume was 3.3×10^8 . After preparation, the cell samples were analyzed with regard to Atto 647N fluorescence signals using CLSM. Most of the observed cells exhibited signals related to Atto 647N, although the number of fluorescent spots per cell varied between cells. Typically, Atto 647N signals were distributed in a punctate pattern and accumulated in the perinuclear region of the cells, as can be seen from the image given in *Figure S3*. The correlative analysis described in the following was conducted on eight Atto 647N signals present in one cell (*Figure 57a*). Two further signals within adjoining cells were also analyzed (data not shown). For

correlative analysis, the tubulin cytoskeleton was used as a cellular marker. Microtubules radiate from the centrosome throughout the cell and extend to the plasma membrane, to which they are attached by protein linkers (Bifulco 2002; Stephens 2012). Microtubules are therefore useful to indicate the boundaries of A549 cells. In order to determine the three-dimensional distribution of the fluorescence signals, confocal z-stacks were recorded. Orthogonal sections indicated that the Atto 647N signals were located inside of the cell, as shown for positions 4 and 8 (*Figure 58*). Using the information on the z-positions of the Atto 647N signals, their distances to the upper and lower margin of the cell were determined (*Table S1*). In order to confirm that the Atto 647N signals resided inside of the cells, a marker for the cytoplasmic membrane was used in a parallel experiment (*Figure S4*). In this case, the application of a GFP fusion protein as intrinsic membrane marker, superseded permeabilization of the cells. Thus, a passive penetration of the fluorescing entities during preparation of the cells could be excluded.

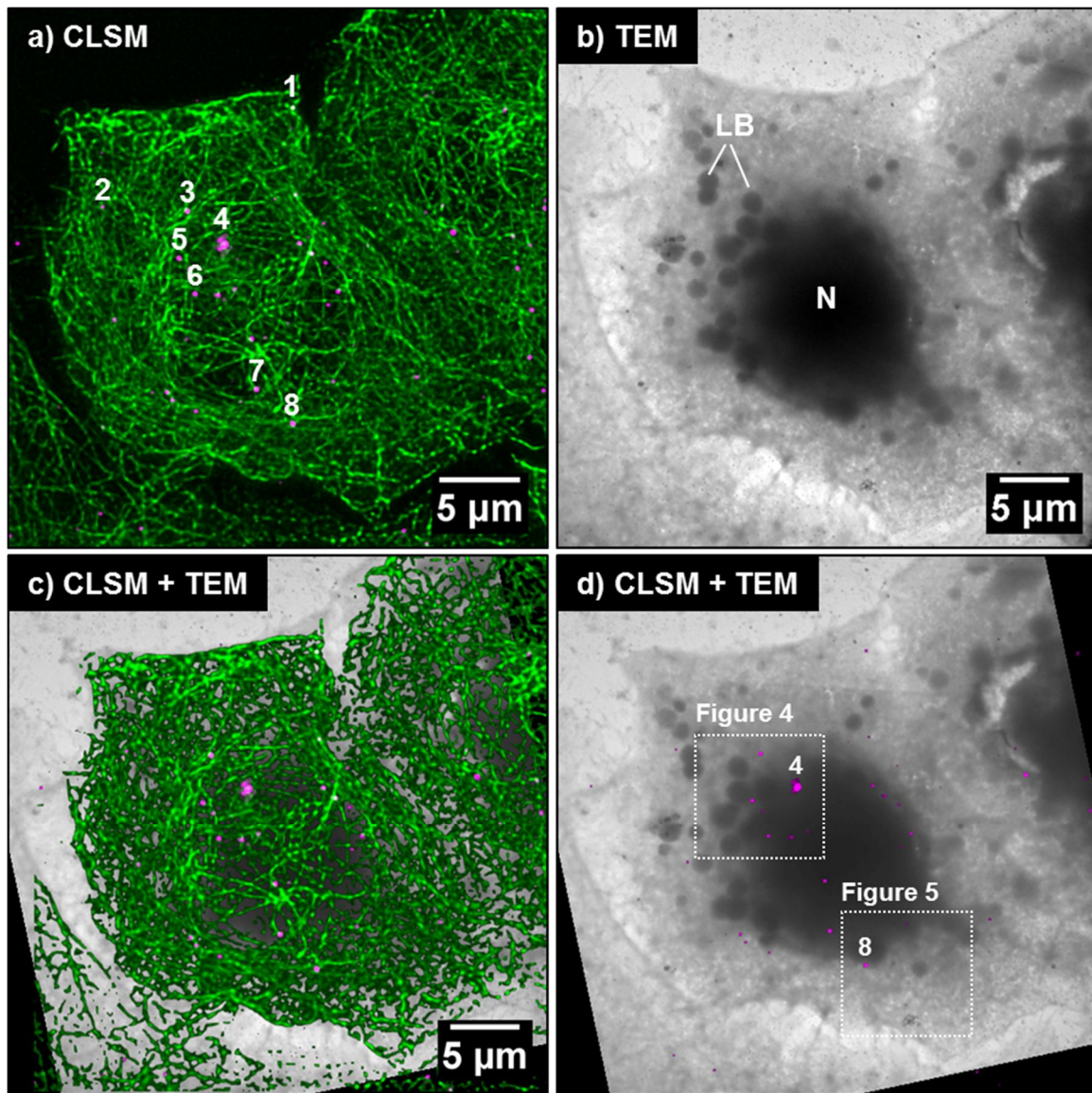


Figure 57: Correlative imaging of one cell by CLSM and TEM.

a) Maximum intensity projection of the deconvolved confocal z-stack (green: α -tubulin, magenta: Atto 647N). b) Corresponding TEM image showing the nucleus (N) and lamellar bodies (LB). c) Overlay of the maximum intensity projection and the TEM image. To facilitate superimposition, the TEM image b) was rotated. Correlation of both images was achieved by comparison of morphological features, mainly the cell edges. d) Overlay of the TEM image and Atto 647N signals (magenta). The contrast of the TEM image was adjusted to improve visibility of the Atto 647N signals in the overlay. Eight fluorescent spots (positions 1-8 in a) were analyzed by CLEM. Positions 4 and 8 were chosen as examples to illustrate further analysis (see Figure 59 and Figure 60). The squares in d) correspond to Figure 59a and Figure 60a and represent the start images of TEM analyses.

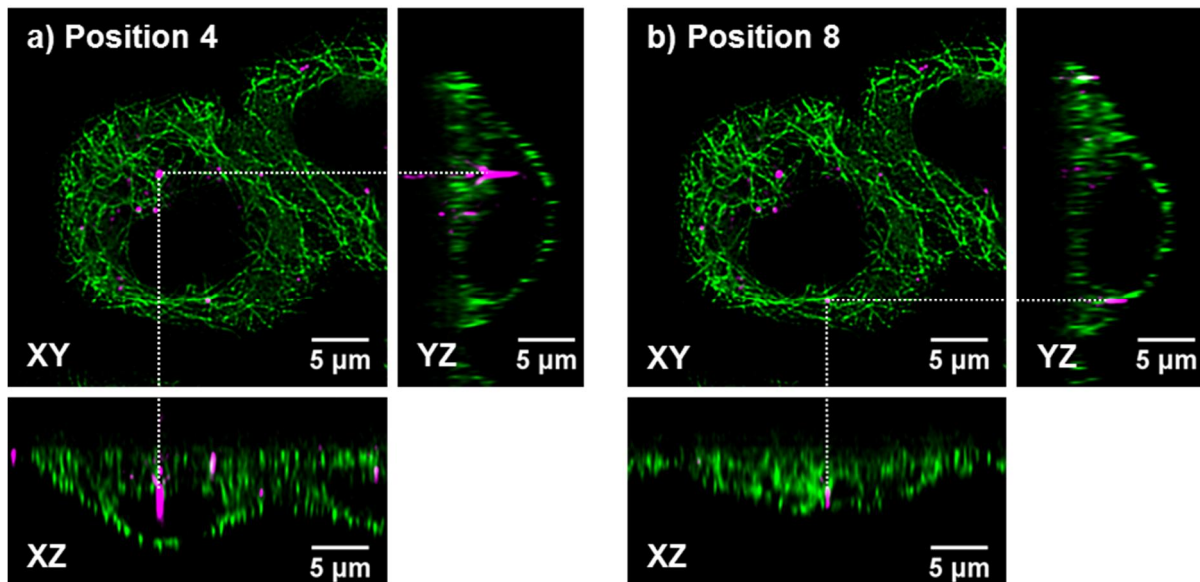


Figure 58: Localization of Atto 647N signals inside A549 cells using CLSM.

The cells were exposed to 8 nm Atto 647N-labeled gold particles for 5 h. Images were derived from confocal z-stacks and represent the top view (xy) as well as orthogonal slices (xz and yz). As microtubules are omitted from the nucleus, optical sectioning allows localization of this organelle (dark central region). The position of LB can also be derived from dark circular regions not containing microtubules. The depicted Atto 647N signals correspond to two of eight positions chosen for further TEM analysis; a) position 4 and b) position 8 (see Figure 57). α -tubulin (green), Atto 647N signals (magenta).

4.3.3 Correlative imaging of cell samples by electron microscopy

After analysis by CLSM, A549 cells were post-fixed with glutaraldehyde and samples were transferred to the SEM and imaged in transmission mode by wet scanning transmission electron microscopy (wet STEM) in a water containing atmosphere (750 Pa, 276 K) at $E = 30$ keV. Using the wet STEM mode, the cell previously analyzed by CLSM was identified based on its shape (Figure S5a). The nucleus appeared as the dark central region, but further details of the cellular structure were not readily identifiable as the cell had not been treated with contrast enhancing agents like osmium tetroxide during the preparation. At higher magnification, dark spots were detected within the nuclear region, but appeared only weakly (Figure S5b). For a clearer image, the pressure was reduced to 720 Pa (Figure S5c). Single nanoparticles could not be resolved due to the limited acceleration voltage ($E_{\text{max}} = 30$ keV). In addition, under these conditions, EDX measurements could not be applied to identify the composition of the dark spots. Immediately after imaging, the samples were dried within the ESEM chamber, applying an even lower pressure as described in the experimental section. Dehydrated samples were subsequently transferred to the TEM. The cell analyzed by CLSM was identified and imaged (Figure 57b). Besides the nucleus, LB contained within A549 cells were clearly visible. Due to the mass-thickness contrast, they appeared as dark circular structures with sizes in the range of 0.6 - 1.2 μm . Similar to the maximum intensity projection (Figure 57a), three cells were identified whereas one cell was completely visible in the center of the image. Within the cell adjacent to the right, nucleus and LB were also visible. In the electron micrograph, the border between the two cells was allocated according to the dark line between them. This border correlated with the region between the cells in the fluorescence image, containing a less dense microtubule network. The cell margin of the central cell was visible in both images and was used to superimpose the maximum intensity projection with the TEM micrograph (Figure 57c). The overlay of TEM and CLSM images based on the cell shape has been reported as a suitable method for correlative microscopy (Keene *et al.*, 2008). The positions of nucleus and LB were also used to align both images. Although

less pronounced in the maximum intensity projection shown in *Figure 57a*, in two-dimensional confocal images, the nucleus and LB were indicated by a less dense microtubule network (*Figure 58*). As mentioned above, eight Atto 647N fluorescence signals were chosen on the basis of the maximum intensity projection for further analysis by electron microscopy. Their positions were transferred to the TEM image (*Figure 57d*), defining the regions for the TEM analyses. The results are exemplified in detail for two signals only. The signal at position 4 was chosen, because it exhibited the brightest fluorescence compared to the signals at the other seven positions. The analysis of the z-stacks revealed that it resided in the inner region of the cell (*Table S1*). As indicated by TEM, position 4 was in an electron dense region containing part of the nucleus. In comparison, the fluorescence signal at position 8 was much less intense and closer to the apical side of the cell (*Table S1*). TEM analysis indicated that it resided in a less electron-dense region beside of the nucleus.

4.3.4 Correlation of fluorescence signals with positions of gold nanoparticles

In order to detect gold nanoparticles, series of TEM images were taken with increasing magnification (*Figure 59* and *Figure 60*). Gold nanoparticles were detected from a magnification corresponding to an image size of 2 μm x 2 μm . At position 4, eleven gold nanoparticles were detected within a distance of 140 nm (*Figure 59f*). Within 40 nm, seven particles formed an agglomerate close to a further single one. The other three particles resided in a distance of about 100 nm from the agglomerate. The size and shape of the particles was in accordance with the properties as determined in the cell-free system. At position 8, two single gold nanoparticles were detected in a distance of 55 nm. These particles were 3 nm and 6 nm in diameter, which was below the calculated mean diameter (*Table 21*). However, EDX analyses confirmed that the particles consisted of gold (*Figure 61*). Cu signals were generated by the sample holder; the Si and N signal by the silicon nitride substrate. C, O, S, and K signals were related to the composition of the cell.

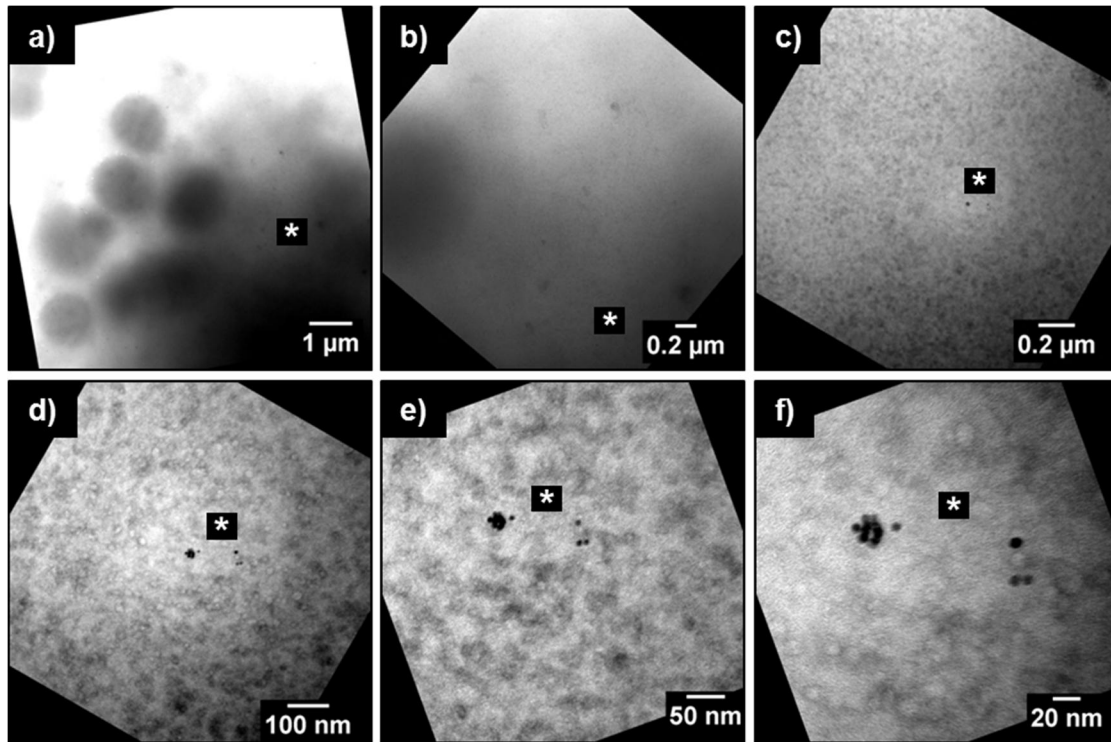


Figure 59: TEM analysis of position 4 with increasing zoom.

a-f) An agglomerate of seven gold nanoparticles was detected close to a single one and three further particles. The * symbol is used to facilitate orientation within the image series and indicates the particle position in every single image. TEM images were rotated to simplify traceability. Black rims correspond to the area outside of the images.

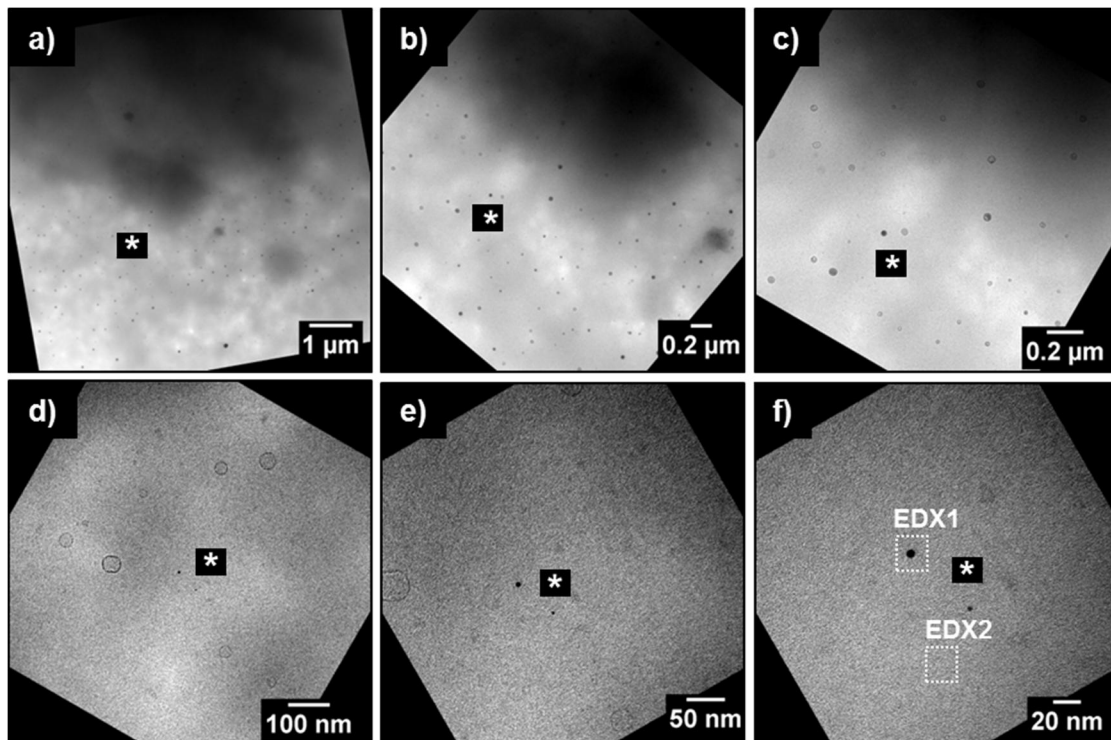


Figure 60: TEM analysis of position 8 with increasing zoom.

a-f) Two single nanoparticles with sizes of 6 nm and 3 nm were detected. The elemental composition of the 6 nm gold particle was analyzed by EDX measurement (EDX 1, Figure 61). Circular structures already visible at lower magnification (a-c) are composed of NaCl as revealed by EDX analysis (EDX 2, Figure S6). As these structures were also visible at lower magnification (a and b), they were used as markers for the correlation of gold nanoparticles with the fluorescence signals. The formation of these structures resulted from an intermediate exposition of the dried sample to air. The * symbol is used to facilitate orientation as already explained in Figure 59. Images are rotated to simplify traceability.

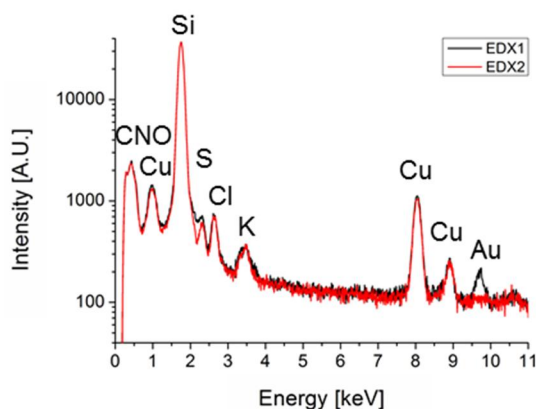


Figure 61: EDX spectra of the cell-associated gold nanoparticles detected at position 8. 8 nm gold particles (EDX1) and the cellular background (EDX2) according to Figure 60. Gold was identified by means of the distinctive L α x-ray signal (9.712 keV).

Similarly, TEM zoom series were taken at the other six positions indicated in Figure 57a. Gold nanoparticles could be detected at a magnification corresponding to an image size of $2\ \mu\text{m} \times 2\ \mu\text{m}$. At five out of eight positions, gold nanoparticles were detected by TEM analysis (Figure 62). At the other three positions, gold nanoparticles were not detected within an area of $2\ \mu\text{m} \times 2\ \mu\text{m}$ surrounding the fluorescence signal. As specified in Figure 62, the number of gold particles at each position and the intensity of the fluorescence signals were determined from the TEM and CLSM images. Interestingly, the fluorescence intensity at position 4 was five- to ten-times higher than the intensity measured at the other positions. At the same position, a multiple (four- to eleven-fold) number of gold nanoparticles was determined as compared to the other positions. Nevertheless, a quantitative relation between the number of gold nanoparticles and the fluorescence intensity could not be derived, due to a lack of positions exhibiting an intermediate number of gold nanoparticles.

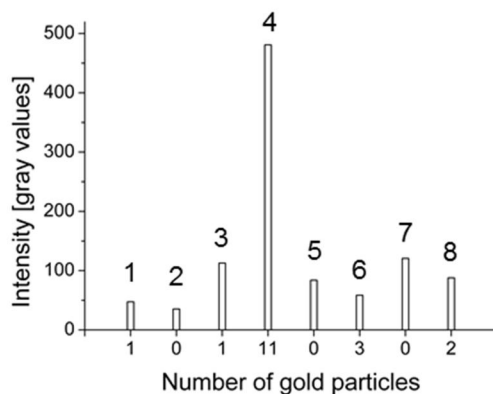


Figure 62: Number of gold nanoparticles detected by TEM compared to the fluorescence intensity detected by CLSM. For determination of fluorescence intensity, the maximum intensity projection was used. The fluorescence intensity of the Atto 647N signals was derived by analysis of the maximal gray values using the Fiji software package. The numbers written above the bars indicate the measurement position.

Finally, the distances between the correlative fluorescence signals and gold nanoparticles were determined (Table 22). Therefore, the location of the gold nanoparticles was transferred into the fluorescence image (Figure 63). As the gold nanoparticles were only resolved at higher magnification, their positions were related to markers also present at lower magnification. The particles at inner

positions (3, 4, and 6) were correlated with the margin of adjacent LB. The particles at the outer positions were related to the cell margin (position 1) and NaCl containing precipitates (position 8). The distances between the fluorescence signals at positions 1 and 8 located within the outer part of the cell and the gold particles were 830 nm and 610 nm, respectively. The particles located at inner positions exhibited lower distances to the fluorescence signals (110 - 390 nm). The precision of the given distances (Table 22) was dependent on the size of the marker and corresponded to the length of one (50 nm) and four pixel (200 nm) in the TEM images. For an evaluation of these values, the limited resolution of conventional CLSM (~300 nm at the imaging conditions used) has to be taken into account.

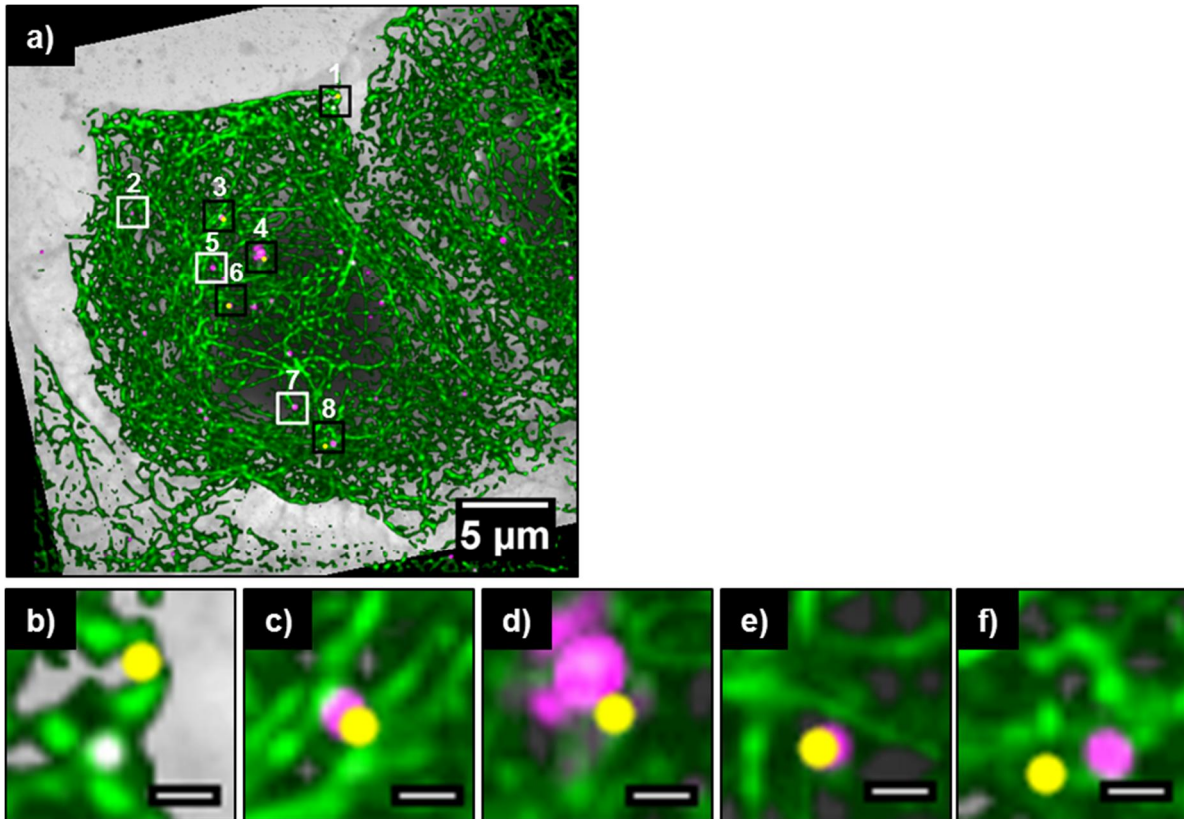


Figure 63: Correlation of gold nanoparticles detected by TEM analysis with Atto 647N fluorescence signals detected by CLSM.

The Atto 647N fluorescence signals (magenta) at positions 1 - 8 were spatially correlated with the location of the gold particles (yellow) detected by TEM. a) Overview of the cell used for the analysis. The squares correspond to TEM images with a size of 2 µm x 2 µm. The color of the frames in a) indicates either a correlation of the Atto 647N signal with gold particles (black squares) or the lack of gold particles within that frame (white squares). b-f) Magnifications of the regions within black squares b) 1, c) 3, d) 4, e) 6, and f) 8. The Atto 647N signal in b) appears white due to its weak intensity against the background of the tubulin channel. Scale bar: 500 nm.

Table 22: Distances between Atto 647N fluorescence signals and gold nanoparticles, determined by correlation of both, CLSM and TEM.

The precision of the distances corresponded to one (50 nm) and four pixel (200 nm) in the TEM images.

Position	Distances between Atto 647N signals and gold nanoparticles [nm]	Precision of the distances [+/- nm]
1	830	50
3	220	200
4	390	200
6	110	200
8	610	50

4.4 Discussion

4.4.1 Particle dosage for microscopy studies of nanoparticle-cell interactions

In our study, fluorescence and electron microscopy were applied to analyze the location of fluorescently labeled gold nanoparticles after internalization by a correlative approach. The uptake of nanoparticles into cells is an active research topic with relevance for nanobiomedicine as well as for nanotoxicology (Zhao *et al.*, 2011). The intended administration of nanoparticles for biomedical applications, such as contrast agents, facilitates an accurate estimation of the applied dose. In contrast, many *in vitro* as well as *in vivo* studies in the field of nanotoxicology are considered to exceed relevant exposure conditions (Krug and Wick 2011). In addition, incomplete characterization data hamper a comparison between studies (The dose makes the poison 2011), in particular between toxicological and microscopy investigations. In this study, the cells were exposed to a concentration of 0.02 $\mu\text{g ml}^{-1}$, corresponding to 0.0055 nM. On the one hand, this low concentration was chosen to exclude nanoparticle-induced cytotoxicity, potentially affecting uptake and target location of the particles. At the concentration chosen as well as at higher concentrations (up to 2 $\mu\text{g ml}^{-1}$), no particle-induced cytotoxicity was observed, applying a conventional cytotoxicity assay (see Chapter 2). Generally, gold nanoparticles exhibit a cytotoxic potential at high doses, which is dependent on surface charge, surface coating, and particle exposure time (Lewinski *et al.*, 2008). In comparison to other microscopy studies (Table 23), the cells were exposed to a significantly lower gold or particle concentration, in order to approach a more realistic exposure scenario corresponding to the cell type used. The narrow size distribution of the gold nanoparticles allowed calculating the number of particles at the applied concentration, accounting to 3.3×10^9 particles ml^{-1} or a molar particle concentration of 0.0055 nM. In other studies (Table 23), the cells were exposed to a 15 - 500-fold particle concentration. The concentration used here, corresponded to $1.9 - 3.9 \times 10^4$ nanoparticles per cell in five hours. Considering the liquid column above the cells (~ 3 mm), the cells residing within the lower 100 μm of this column were exposed to an average of 600 - 1,300 nanoparticles. The order of magnitude of these numbers corresponded well to 120 - 2,400 particles per hour calculated by Geiser *et al.* (Geiser and Kreyling 2010) to maximally encounter one alveolar cell after inhalation.

Table 23: Gold nanoparticle concentrations used in other microscopy studies.
ND: Not determined.

Nanoparticle size [nm]	Nanoparticle areal number density (# cm^{-2}) or nanoparticle concentration (nM)	Cell type	Cytotoxicity	Author
15	1.5×10^{10} particles cm^{-2}	A549	ND	Brandenberger <i>et al.</i> , 2010b
30	1.8 nM	Cos-7	ND	Peckys and Jonge 2011
18, 35, 65	10 - 100 $\mu\text{g ml}^{-1}$ $\sim 0.01 - 2.82$ nM	HDMEC	no ($< 250 \mu\text{g ml}^{-1}$)	Freese <i>et al.</i> , 2012
8	9.7×10^8 particles cm^{-2} 0.0055 nM	A549	no ($< 2 \mu\text{g ml}^{-1}$)	this study

It seems that for microscopic studies, high particle concentrations are chosen to facilitate detection of particles within the cellular environment. We recommend considering potential cytotoxic effects induced by high nanoparticle concentrations and relevant exposure doses for microscopic studies on nanoparticle-cell interactions. Besides nanoparticle functionalization, the low dosage used in this

study is one explanation for the detection of separated particles as well as separated particle agglomerates within the cells. Single particles and agglomerates have also been found by Brandenberger *et al.* dealing with A549 cells (Brandenberger *et al.*, 2010b). In contrast, using other types of cells Peckys *et al.* (Peckys and Jonge 2011) observed vesicles filled with particles within cells and Freese *et al.* (Freese *et al.*, 2012) detected particle agglomerates as black dots in the perinuclear region even by light microscopy.

4.4.2 The use of CLEM for investigating nanoparticle-cell interactions

Besides the dose, parameters like particle size, shape, and surface modification are regarded to determine uptake and intracellular fate of particles after uptake (Nel *et al.*, 2009). Especially, surface modification and functionalization of particles are important, influencing particle stability, specific uptake, or intracellular targeting beyond the endosomal compartment (Lévy *et al.*, 2010; Nativo *et al.*, 2008). Microscopy methods can provide insights into nanoparticle uptake and transport and are therefore a valuable tool for a quantification of nanoparticle-cell interactions (Elsaesser *et al.*, 2010). Most microscopy techniques suitable for the cellular environment enable either the detection of the particle core or the detection of the surrounding shell. In contrast, correlative microscopy facilitates spatial information on both components, even after nanoparticle internalization by cells. To evaluate the potential of CLEM for studies on nanoparticle-cell interactions, A549 cells were exposed to fluorescence labeled 8 nm gold particles. After 5 h, fluorescent spots were detected inside the imaged cell by CLSM. Only five out of eight fluorescent spots investigated correlated with gold particles, suggesting a detachment of the fluorescent dye or the polymer shell from the particle core. Reasons for the release of fluorescent dyes or drugs from nanoparticles are manifold and strongly depend on their chemical properties and on the chemical bond to the particle matrix or surface. Nonpolar dyes are for example used to label the matrix of polystyrene nanoparticles, simply by embedding. Once in contact with cells, release of dyes has been observed (Salvati *et al.*, 2011). Dye release has also been shown for particles labeled with a dye covalently attached to the polymeric particle matrix. In this case, significant leaching from particles, which had been subjected to dialysis prior to cell experiments, appeared to have caused a strong background in fluorescence microscopy (Tenuta *et al.*, 2011). A significant background due to leaching of free Atto 647N was not observed during this study. Labeling of gold nanoparticles can only be achieved by attachment of the dye to the particle surface but not by incorporation of dye into the particle core. In this study, the fluorescent dye Atto 647N was covalently attached to the polymer used for phase transfer of the particles into the water phase and for electrosteric stabilization of the particles. The polymer itself was attached *via* van-der-Waals and hydrophobic forces to alkylthiols anchored to the particle surface *via* covalent-like, high affinity thiol-gold bonds. TEM analyses of the nanoparticles at the edge of a holey carbon film demonstrated the presence of the polymer coating around the gold core. Since the alkylthiol covered particles lacking the polymer shell are not stable in water (Pellegrino *et al.*, 2004), we assume that a detachment of the polymer occurred after transfer of the particles to the cell culture medium or after uptake into the cells and that this was responsible for the reduced correlation between fluorescence signals and gold nanoparticles. It is well known that in biological environment a protein corona is formed around nanoparticles (Nel *et al.*, 2009). After transfer into cell culture medium, a blue shift of the absorption maximum of gold nanoparticles indicates particle agglomeration. Such an agglomeration was not observed for the gold nanoparticles used (data not shown). Thus, it was assumed that proteins with a high affinity to the particle surface or the covalently bound alkyl-linker molecules might have replaced the polymer shell (Cañaveras *et al.*, 2012; Zhu *et al.*, 2012). An unspecific staining of cellular structures, as has been described for the

staining of mitochondrial membranes by Atto 647N antibody conjugates (Wurm *et al.*, 2010) or for the endoplasmic reticulum by unipolar dyes (Salvati *et al.*, 2011), was also not observed, indicating that the polymer complexes do not freely diffuse throughout the cells. Nanoparticles are regarded to be taken up into the endolysosomal compartment of various cell types (Salvati *et al.*, 2011). The low pH present in these compartments was demonstrated to affect nanoparticle stability (Raouf *et al.*, 2012). Furthermore, the cellular environment is rich of protein degrading enzymes. See *et al.* showed that biological molecules attached to nanoparticles are degraded within endosomal compartments through peptide cleavage (Sée *et al.*, 2009).

The more detailed TEM analysis of position 4 and 8 suggested a relationship between the fluorescence intensity and the number of gold particles present. The very bright fluorescence signal that was observed by CLSM at position 4 could be explained by the agglomeration of several gold nanoparticles. Nevertheless, no proportional relationship between the fluorescence intensity and the number of gold nanoparticles at the other positions was found. The number of fluorophores per particle was calculated by comparison of the fluorescence of the particle dispersion compared to a solution of free Atto 647N. Statistically, every gold nanoparticle carried 23 ± 4 molecules of Atto 647N attached to the polymer. The standard deviation from this value is expected to be mainly influenced by the coupling efficiency of mPEG and the fluorophore itself, which are both coupled to free carboxylic acid residues on the PMAO backbone.

The lack of correlation between the fluorescence intensity and the number of correlating gold particles can also be explained by the limited sensitivity of CLSM at the applied conditions. For analysis, no mounting medium was used and a slight refractive index mismatch between the coverslip ($RI_{\text{glass}} = 1.51$) and the sample ($RI_{\text{water}} = 1.33$) existed. This refractive index mismatch and the accompanying light reflection might cause a decreased fluorescence yield (Pawley 2010). Additionally, the absence of antifading reagents might have promoted photobleaching of the fluorescent dye (Florijn *et al.*, 1995; Ono *et al.*, 2001). Thus, part of the nanoparticle-derived fluorescence was possibly lost during analysis. Quenching of the dye by the gold surface might also have contributed to variations in the fluorescence intensity (Mayilo *et al.*, 2009), although the fluorescence spectrum of the dye did not overlap to a great extent with the extinction spectrum of the gold particles. In addition, spots lacking gold particles did not exhibit a higher fluorescence intensity than the spots correlating with gold cores.

Regardless of the complexity of potential explanations for the imperfect correlation, more than half of the spots exhibited a correlation between the fluorescence signal and the presence of gold particles, indicating that these particles retained the shell during uptake into the cells. CLEM enabled the detection of the labeled particle shell compared to the gold cores after uptake. The application of this technique can be used to elucidate the localization of targeting molecules in relation to the particles in order to evaluate their benefit for biomedical applications as well as to further clarify the role of surface modification for the uptake of nanoparticles in the field of nanotoxicology. In addition, the fate of proteins initially bound to the particle surface can be investigated by such an approach. The applicability of fluorescence microscopy for localization of labeled particles should be tested, especially when the used label is coupled to the particle surface. In addition, the restricted resolution of conventional light microscopy might not easily allow the actual localization of nanostructures (Müller *et al.*, 2012). In comparison to light microscopy, TEM allows for an identification of the elemental composition of a sample. In this study, EDX measurements were applied to identify a single gold nanoparticle located inside the cell. Without such measurements, other structures, e.g. caused by the preparation procedure, might be misinterpreted. Furthermore, single nanoparticles located in deeper regions of the cell ($\sim 5 \mu\text{m}$) were detectable by TEM down to a

size of 3 nm. Similar results were obtained by de Jonge *et al.*, who showed the resolution of 10 nm gold particles inside whole liquid cells by scanning TEM (STEM) (Jonge *et al.*, 2009). The gold nanoparticle agglomerate at position 4 is located in the middle of the cell underneath the nucleus as indicated by CLSM. Although the electron beam is scattered on its way through the cell, individual gold nanoparticles were clearly resolved by TEM.

4.4.3 Influence of sample preparation on CLEM

The imaging of cells by electron microscopy usually requires a complete dehydration of the cellular material. Examples of techniques enabling imaging of hydrated samples are cryo-electron microscopy (Kourkoutis *et al.*, 2012), environmental SEM (ESEM) (Danilatos 1993) including wet STEM imaging (Bogner *et al.*, 2005), and liquid STEM (Jonge *et al.*, 2009; Jonge and Ross 2011). However, under the conditions used here, wet STEM imaging was not sufficient for the identification of internalized 8 nm gold particles. Therefore, the sample was dehydrated for a further analysis by TEM. Dehydration of biological material can be achieved by critical point drying or air drying after treatment of the sample with fluids of low surface tension (Braet *et al.*, 1997; Gilkey and Staehelin 1986; Reville and Cotter 1991). Such treatment of cells is often accompanied by cell shrinkage introducing artifacts (King 1998). The shrinkage of sea urchin eggs during dehydration with increasing concentrations of ethanol has been intensively studied. However, the results indicated only a slight shrinkage in diameter (4 %) and surface area (8 %) compared to living cells (Kushida 1962). For critical point drying, a much higher extent of cell shrinkage (25 - 30 %) was reported (Gusnard and Kirschner 1977). In the present study, the dehydration of cells was realized inside an ESEM chamber at a temperature of 276 K and a pressure of 600 Pa, which is below the equilibrium vapor pressure. It has been described that under these conditions, the moisture loss of hydrated specimen proceeds slowly (Stokes 2003; Stokes 2008), preventing a massive sample shrinkage. The recorded TEM images indicated no significant changes in the lateral dimensions of the cell, allowing for superimposition of the maximum intensity projection and the electron micrograph. The cell boundaries, visible in both images, matched well. Sample shrinkage in axial direction was observed after imaging of the dried cells by SEM using different tilt angles (data not shown). By the correlative analysis at five out of eight fluorescence spots, gold nanoparticles were detected indicating preservation of the particle location after drying. Especially at positions 3, 4, and 6, located in the center of the cell, the fluorescence signals and the gold particles were close to each other. The distances were less than 400 nm, a value similar to the optical resolution of fluorescence microscopy. At positions 1 and 8, closer to the cell borders, a poorer match of Atto 647N fluorescence and gold nanoparticles was observed (< 830 nm). Nevertheless, the positions of the gold particles detected could be linked to the observed fluorescence as no other gold nanoparticles were found in spatial proximity (within 2 μm x 2 μm). The area investigated by TEM comprised ~3% of the total cell area. Thus, we cannot exclude the presence of gold cores that had separated from the shell in the remaining area. We do not assume that sample preparation caused the loss of the gold cores from the fluorescent shells, because after CLSM, the cells were only post-fixed using glutaraldehyde and directly transferred to the ESEM chamber to allow drying of the sample. No dehydration by solvent exchange was carried out, potentially causing flushing of nanoparticles. As discussed in section 4.4.2, the absence of gold particles can more likely be related to a loss of the Atto 647N labeled polymer from the gold core during contact of the particles to biological components.

4.5 Conclusion

A549 cells as model for human alveolar epithelial cells were exposed to 8 nm Atto 647N-labeled gold nanoparticles for 5 h and analyzed by CLEM. The cells were exposed *in vitro* to gold particles at a low concentration relevant for an inhalative nanoparticle uptake. Atto 647N signals were detected by CLSM allowing for a diffraction-limited determination of their three-dimensional position within the cells. Eight of these signals were chosen for further correlative analyses by TEM. Five of the fluorescence signals were correlated with single gold nanoparticles or nanoparticle agglomerates. In conclusion, the correlative approach allowed for a detection of fluorescence signals in three dimensions using whole cells complemented by detection of single or agglomerated gold particles within or close to the diffraction limited fluorescent spots. Our study indicated that the polymer shell was lost from three out of eight gold nanoparticles. CLEM appears to be very powerful in the analysis of nanoparticle-cell interactions and the intracellular distribution of particle cores relative to the particle shell.

4.6 References

- The dose makes the poison (2011). In *Nat. Nanotech.* 6 (6), p. 329.
- Alivisatos, A. P.; Gu, W.; Larabell, C. (2005): QUANTUM DOTS AS CELLULAR PROBES. In *Annu. Rev. Biomed. Eng.* 7 (1), pp. 55–76.
- Al-Rawi, M.; Diabaté, S.; Weiss, C. (2011): Uptake and intracellular localization of submicron and nano-sized SiO₂ particles in HeLa cells. In *Arch. Toxicol.* 85 (7), pp. 813–826.
- Bifulco, M. (2002): 2',3'-Cyclic nucleotide 3'-phosphodiesterase: A membrane-bound, microtubule-associated protein and membrane anchor for tubulin. In *Proc. Natl. Acad. Sci. USA* 99 (4), pp. 1807–1812.
- Bogner, A.; Thollet, G.; Basset, D.; Jouneau, P.-H.; Gauthier, C. (2005): Wet STEM: A new development in environmental SEM for imaging nano-objects included in a liquid phase. In *Ultramicroscopy* 104 (3-4), pp. 290–301.
- Borm, P. J. A.; Robbins, D.; Haubold, S.; Kuhlbusch, T.; Fissan, H.; Donaldson, K.; Schins, R.; Stone, V.; Kreyling, W.; Lademann, J.; Krutmann, J.; Warheit, D.; Oberdorster, E. (2006): The potential risks of nanomaterials: a review carried out for ECETOC. In *Part. Fibre Toxicol.* 3 (1), p. 11.
- Braet, F.; Zanger, R. de; Wisse, E. (1997): Drying cells for SEM, AFM and TEM by hexamethyldisilazane: a study on hepatic endothelial cells. In *J Microsc* 186 (Pt 1), pp. 84–87.
- Brandenberger, C.; Clift, M. J. D.; Vanhecke, D.; Mühlfeld, C.; Stone, V.; Gehr, P.; Rothen-Rutishauser, B. (2010a): Intracellular imaging of nanoparticles: Is it an elemental mistake to believe what you see? In *Part. Fibre Toxicol.* 7 (1), p. 15.
- Brandenberger, C.; Mühlfeld, C.; Ali, Z.; Lenz, A.-G.; Schmid, O.; Parak, W. J.; Gehr, P.; Rothen-Rutishauser, B. (2010b): Quantitative Evaluation of Cellular Uptake and Trafficking of Plain and Polyethylene Glycol-Coated Gold Nanoparticles. In *Small* 6 (15), pp. 1669–1678.
- Cañaveras, F.; Madueño, R.; Sevilla, J. M.; Blázquez, M.; Pineda, T. (2012): Role of the Functionalization of the Gold Nanoparticle Surface on the Formation of Bioconjugates with Human Serum Albumin. In *J. Phys. Chem. C* 116 (18), pp. 10430–10437.
- Casals, E.; Pfaller, T.; Duschl, A.; Oostingh, G. J.; Puentes, V. (2010): Time Evolution of the Nanoparticle Protein Corona. In *ACS Nano* 4 (7), pp. 3623–3632.
- Danilatos, G. D. (1993): Bibliography of Environmental Scanning Electron Microscopy. In *Microsc. Res. Techniq.* 25, pp. 529–534.
- Dukes, M. J.; Peckys, D. B.; Jonge, N. de (2010): Correlative Fluorescence Microscopy and Scanning Transmission Electron Microscopy of Quantum-Dot-Labeled Proteins in Whole Cells in Liquid. In *ACS Nano* 4 (7), pp. 4110–4116.
- Elsaesser, A.; Taylor, A.; Yanés, G. S. de; McKerr, G.; Kim, E.-M.; O'Hare, E.; Howard, C. V. (2010): Quantification of nanoparticle uptake by cells using microscopical and analytical techniques. In *Nanomedicine* 5 (9), pp. 1447–1457.
- Florijn, R. J.; Slats, J.; Tanke, H. J.; Raap, A. K. (1995): Analysis of Antifading Reagents for Fluorescence Microscopy. In *Cytometry* 19, pp. 177–182.
- Freese, C.; Gibson, M. I.; Klok, H.-A.; Unger, R. E.; Kirkpatrick, C. J. (2012): Size- and Coating-Dependent Uptake of Polymer-Coated Gold Nanoparticles in Primary Human Dermal Microvascular Endothelial Cells. In *Biomacromolecules* 13 (5), pp. 1533–1543.
- Geiser, M.; Kreyling, W. G. (2010): Deposition and biokinetics of inhaled nanoparticles. In *Part. Fibre Toxicol.* 7 (1), p. 2.
- Giepmans, B. N. G. (2008): Bridging fluorescence microscopy and electron microscopy. In *Histochem. Cell Biol.* 130 (2), pp. 211–217.
- Giepmans, B. N. G.; Deerinck, T. J.; Smarr, B. L.; Jones, Y. Z.; Ellisman, M. H. (2005): Correlated light and electron microscopic imaging of multiple endogenous proteins using Quantum dots. In *Nat. Meth.* 2 (10), pp. 743–749.
- Gilkey, J. C.; Staehelin, L. A. (1986): Advances in Ultrarapid Freezing for the Preservation of Cellular Ultrastructure. In *J. Electron Microsc. Tech.* 3, pp. 177–210.
- Grabenbauer, M.; Geerts, W. J. C.; Fernandez-Rodriguez, J.; Hoenger, A.; Koster, A. J.; Nilsson, T. (2005): Correlative microscopy and electron tomography of GFP through photooxidation. In *Nat. Meth.* 2 (11), pp. 857–862.
- Gusnard, D.; Kirschner, R. H. (1977): Cell and organelle shrinkage during preparation for scanning electron microscopy: effects of fixation, dehydration and critical point drying. In *J Microsc* 110 (1), pp. 51–57.
- Hell, S. W. (2009): Microscopy and its focal switch. In *Nat. Meth.* 6 (1), pp. 24–32.

- Hell, S. W.; Wichmann, J. (1994): Breaking the diffraction resolution limit by stimulated emission: stimulated-emission-depletion fluorescence microscopy. In *Opt. Lett.* 19 (11), p. 780.
- Johnston, H. J.; Semmler-Behnke, M.; Brown, D. M.; Kreyling, W.; Tran, L.; Stone, V. (2010): Evaluating the uptake and intracellular fate of polystyrene nanoparticles by primary and hepatocyte cell lines in vitro. In *Toxicol. Appl. Pharmacol.* 242 (1), pp. 66–78.
- Jonge, N. d.; Peckys, D. B.; Kremers, G. J.; Piston, D. W. (2009): Electron microscopy of whole cells in liquid with nanometer resolution. In *Proc. Natl. Acad. Sci. USA* 106 (7), pp. 2159–2164.
- Jonge, N. de; Ross, F. M. (2011): Electron microscopy of specimens in liquid. In *Nat. Nanotech.* 6 (11), pp. 695–704.
- Keene, D. R.; Tufa, S. F.; Lunstrum, G. P.; Holden, P.; Horton, W. A. (2008): Confocal/TEM Overlay Microscopy: A Simple Method for Correlating Confocal and Electron Microscopy of Cells Expressing GFP/YFP Fusion Proteins. In *Microsc. Microanal.* 14 (04).
- Kim, J. A.; Åberg, C.; Salvati, A.; Dawson, K. A. (2011): Role of cell cycle on the cellular uptake and dilution of nanoparticles in a cell population. In *Nat. Nanotech.* 7 (1), pp. 62–68.
- King, M. V. (1998): Dimensional Changes in Cells and Tissues During Specimen Preparation for the Electron Microscope. In *Cell Biophys.* 18, pp. 31–55.
- Klar, T. A.; Jakobs, S.; Dyba, M.; Egner, A.; Hell, S. W. (2000): Fluorescence microscopy with diffraction resolution barrier broken by stimulated emission. In *Proc. Natl. Acad. Sci. USA* 97 (15), pp. 8206–8210.
- Kourkoutis, L. F.; Plietzko, J. M.; Baumeister, W. (2012): Electron Microscopy of Biological Materials at the Nanometer Scale. In *Annu. Rev. Mater. Res.* 42 (1), pp. 33–58.
- Krug, H. F.; Wick, P. (2011): Nanotoxikologie - eine interdisziplinäre Herausforderung. In *Angew. Chem.* 123 (6), pp. 1294–1314.
- Kushida, H. (1962): A Study of Cellular Swelling and Shrinkage during Fixation, Dehydration and Embedding in Various Standard Media. In *J. Electron Microsc.* 11 (3), pp. 135–138.
- Lehmann, A. D.; Parak, W. J.; Zhang, F.; Ali, Z.; Röcker, C.; Nienhaus, G. U.; Gehr, P.; Rothen-Rutishauser, B. (2010): Fluorescent-Magnetic Hybrid Nanoparticles Induce a Dose-Dependent Increase in Proinflammatory Response in Lung Cells in vitro Correlated with Intracellular Localization. In *Small* 6 (6), pp. 753–762.
- Lévy, R.; Shaheen, U.; Cesbron, Y.; Sée, V. (2010): Gold nanoparticles delivery in mammalian live cells: a critical review. In *Nano Rev.* 1 (0).
- Lewinski, N.; Colvin, V.; Drezek, R. (2008): Cytotoxicity of Nanoparticles. In *Small* 4 (1), pp. 26–49.
- Mahl, D.; Greulich, C.; Meyer-Zaika, W.; Köller, M.; Epple, M. (2010): Gold nanoparticles: dispersibility in biological media and cell-biological effect. In *J. Mater. Chem.* 20 (29), p. 6176.
- Mayhew, T. (2009): Quantifying Immunogold Localization Patterns on Electron Microscopic Thin Sections of Placenta: Recent Developments. In *Placenta* 30 (7), pp. 565–570.
- Mayilo, S.; Kloster, M. A.; Wunderlich, M.; Lutich, A.; Klar, T. A.; Nichtl, A.; Kürzinger, K.; Stefani, F. D.; Feldmann, J. (2009): Long-Range Fluorescence Quenching by Gold Nanoparticles in a Sandwich Immunoassay for Cardiac Troponin T. In *Nano Lett.* 9 (12), pp. 4558–4563.
- Meisslitzer-Ruppitsch, C.; Prikowitsch, T.; Neumüller, J.; Pavelka, M.; Ellinger, A. (2010): Correlative light and electron microscopic exploration of endocytic organelles. In *Microscopy: Science, Technology, Applications and Education*, pp. 277–285.
- Merrifield, C. J.; Feldman, M. E.; Wan, L.; Almers, W. (2002): Imaging actin and dynamin recruitment during invagination of single clathrin-coated pits. In *Nat. Cell Biol.* 4 (9), pp. 691–698.
- Mühlfeld, C.; Geiser, M.; Kapp, N.; Gehr, P.; Rothen-Rutishauser, B. (2007): Re-evaluation of pulmonary titanium dioxide nanoparticle distribution using the "relative deposition index": Evidence for clearance through microvasculature. In *Part. Fibre Toxicol.* 4 (1), p. 7.
- Müller, T.; Schumann, C.; Kraegeloh, A. (2012): STED Microscopy and its Applications: New Insights into Cellular Processes on the Nanoscale. In *ChemPhysChem* 13 (8), pp. 1986–2000.
- Nativo, P.; Prior, I. A.; Brust, M. (2008): Uptake and Intracellular Fate of Surface-Modified Gold Nanoparticles. In *ACS Nano* 2 (8), pp. 1639–1644.
- Nel, A. E.; Mädler, L.; Velegol, D.; Xia, T.; Hoek, E. M. V.; Somasundaran, P.; Klaessig, F.; Castranova, V.; Thompson, M. (2009): Understanding biophysicochemical interactions at the nano–bio interface. In *Nat. Mater.* 8 (7), pp. 543–557.
- Oberdörster, G. (2010): Safety assessment for nanotechnology and nanomedicine: concepts of nanotoxicology. In *J. Intern. Med.* 267 (1), pp. 89–105.

- Ono, M.; Murakami, T.; Kudo, A.; Isshiki, M.; Sawada, H.; Segawa, A. (2001): Quantitative Comparison of Anti-Fading Mounting Media for Confocal Laser Scanning Microscopy. In *J. Histochem. Cytochem.* 49 (3), pp. 305–311.
- Pawley, James (2010): Handbook of Biological Confocal Microscopy. 3rd ed. s.l: Springer-Verlag.
- Peckys, D. B.; Jonge, N. de (2011): Visualizing Gold Nanoparticle Uptake in Live Cells with Liquid Scanning Transmission Electron Microscopy. In *Nano Lett.* 11 (4), pp. 1733–1738.
- Pelka, J.; Gehrke, H.; Esselen, M.; Türk, M.; Crone, M.; Bräse, S.; Müller, T.; Blank, H.; Send, W.; Zibat, V.; Brenner, P.; Schneider, R.; Gerthsen, D.; Marko, D. (2009): Cellular Uptake of Platinum Nanoparticles in Human Colon Carcinoma Cells and Their Impact on Cellular Redox Systems and DNA Integrity. In *Chem. Res. Toxicol.* 22 (4), pp. 649–659.
- Pellegrino, T.; Kudera, S.; Liedl, T.; Muñoz Javier, A.; Manna, L.; Parak, W. J. (2005): On the Development of Colloidal Nanoparticles towards Multifunctional Structures and their Possible Use for Biological Applications. In *Small* 1 (1), pp. 48–63.
- Pellegrino, T.; Manna, L.; Kudera, S.; Liedl, T.; Koktysh, D.; Rogach, A. L.; Keller, S.; Rädler, J.; Natile, G.; Parak, W. J. (2004): Hydrophobic Nanocrystals Coated with an Amphiphilic Polymer Shell: A General Route to Water Soluble Nanocrystals. In *Nano Lett.* 4 (4), pp. 703–707.
- Raouf, M.; Corr, S. J.; Kaluarachchi, W. D.; Massey, K. L.; Briggs, K.; Zhu, C.; Cheney, M. A.; Wilson, L. J.; Curley, S. A. (2012): Stability of antibody-conjugated gold nanoparticles in the endolysosomal nanoenvironment: implications for noninvasive radiofrequency-based cancer therapy. In *Nanomed. Nanotech. Biol. Med.* 8 (7), pp. 1096–1105.
- Reville, W. J.; Cotter, M. P. (1991): An Evaluation of the Usefulness of Air-Drying Biological Samples from Tetramethylsilane in Preparation for Scanning Electron Microscopy. In *J. Electron Microsc.* 40 (198-202).
- Röcker, C.; Pötzl, M.; Zhang, F.; Parak, W. J.; Nienhaus, G. U. (2009): A quantitative fluorescence study of protein monolayer formation on colloidal nanoparticles. In *Nat. Nanotech.* 4 (9), pp. 577–580.
- Rosman, C.; Pierrat, S.; Henkel, A.; Tarantola, M.; Schneider, D.; Sunnick, E.; Janshoff, A.; Sönnichsen, C. (2012): A New Approach to Assess Gold Nanoparticle Uptake by Mammalian Cells: Combining Optical Dark-Field and Transmission Electron Microscopy. In *Small* 8 (23), pp. 3683–3690.
- Salvati, A.; Åberg, C.; dos Santos, T.; Varela, J.; Pinto, P.; Lynch, I.; Dawson, K. A. (2011): Experimental and theoretical comparison of intracellular import of polymeric nanoparticles and small molecules: toward models of uptake kinetics. In *Nanomed. Nanotech. Biol. Med.* 7 (6), pp. 818–826.
- Schindelin, J.; Arganda-Carreras, I.; Frise, E.; Kaynig, V.; Longair, M.; Pietzsch, T.; Preibisch, S.; Rueden, C.; Saalfeld, S.; Schmid, B.; Tinevez, J.-Y.; White, D. J.; Hartenstein, V.; Eliceiri, K.; Tomancak, P.; Cardona, A. (2012): Fiji: an open-source platform for biological-image analysis. In *Nat. Meth.* 9 (7), pp. 676–682.
- Schrand, A. M.; Schlager, J. J.; Dai, L.; Hussain, S. M. (2010): Preparation of cells for assessing ultrastructural localization of nanoparticles with transmission electron microscopy. In *Nat. Protoc.* 5 (4), pp. 744–757.
- Schübbe, S.; Cavelius, C.; Schumann, C.; Koch, M.; Kraegeloh, A. (2010): STED Microscopy to Monitor Agglomeration of Silica Particles Inside A549 Cells. In *Adv. Eng. Mater.* 12 (5), pp. 417–422.
- Schübbe, S.; Schumann, C.; Cavelius, C.; Koch, M.; Müller, T.; Kraegeloh, A. (2012): Size-Dependent Localization and Quantitative Evaluation of the Intracellular Migration of Silica Nanoparticles in Caco-2 Cells. In *Chem. Mater.* 24 (5), pp. 914–923.
- Schulze, C.; Kroll, A.; Lehr, C.-M.; Schäfer, U. F.; Becker, K.; Schneckeburger, J.; Schulze Isfort, C.; Landsiedel, R.; Wohlleben, W. (2008): Not ready to use – overcoming pitfalls when dispersing nanoparticles in physiological media. In *Nanotoxicology* 2 (2), pp. 51–61.
- Sée, V.; Free, P.; Cesbron, Y.; Nativo, P.; Shaheen, U.; Rigden, D. J.; Spiller, D. G.; Fernig, D. G.; White, M. R. H.; Prior, I. A.; Brust, M.; Lounis, B.; Lévy, R. (2009): Cathepsin L Digestion of Nanobioconjugates upon Endocytosis. In *ACS Nano* 3 (9), pp. 2461–2468.
- Shaner, N. C.; Patterson, G. H.; Davidson, M. W. (2007): Advances in fluorescent protein technology. In *J. Cell Sci.* 120 (24), pp. 4247–4260.
- Stephens, D. J. (2012): Functional coupling of microtubules to membranes - implications for membrane structure and dynamics. In *J. Cell Sci.* 125 (12), pp. 2795–2804.
- Stokes, D. J. (2003): Recent advances in electron imaging, image interpretation and applications: environmental scanning electron microscopy. In *Philos. T. Roy. Soc. A* 361 (1813), pp. 2771–2787.
- Stokes, Debbie J. (2008): Principles and practice of variable pressure/environmental scanning electron microscopy (VP-ESEM). Chichester, U.K: Wiley (RMS - Royal Microscopical Society). Available online at <http://www3.interscience.wiley.com/cgi-bin/bookhome/121497046/>.

- Takizawa, T.; Robinson, J. M. (2000): FluoroNanogold Is a Bifunctional Immunoprobe for Correlative Fluorescence and Electron Microscopy. In *J. Histochem. Cytochem.* 48 (4), pp. 481–485.
- Tenuta, T.; Monopoli, M. P.; Kim, J.; Salvati, A.; Dawson, K. A.; Sandin, P.; Lynch, I.; Vertes, A. (2011): Elution of Labile Fluorescent Dye from Nanoparticles during Biological Use. In *PLoS ONE* 6 (10), pp. e25556.
- Uboldi, C.; Bonacchi, D.; Lorenzi, G.; Hermanns, M. I.; Pohl, C.; Baldi, G.; Unger, R. E.; Kirkpatrick, C. J. (2009): Gold nanoparticles induce cytotoxicity in the alveolar type-II cell lines A549 and NCIH441. In *Part. Fibre Toxicol.* 6 (1), p. 18.
- Wang, T.; Bai, J.; Jiang, X.; Nienhaus, G. U. (2012): Cellular Uptake of Nanoparticles by Membrane Penetration: A Study Combining Confocal Microscopy with FTIR Spectroelectrochemistry. In *ACS Nano* 6 (2), pp. 1251–1259.
- Wexler, A. (1976): Vapor Pressure Formulation for Water in Range 0 to 100 °C. A Revision. In *J. Res. Natl. Bur. Stand. - A. Physics and Chemistry* 80A (5 and 6), pp. 775–785.
- Wurm, C. A.; Neumann, D.; Schmidt, R.; Egner, A.; Jakobs, S. (2010): Sample Preparation for STED Microscopy. In *Methods Mol. Biol.* 591, pp. 185–199.
- Yokel, R. A.; MacPhail, R. C. (2011): Engineered nanomaterials: exposures, hazards, and risk prevention. In *J Occup Med Toxicol* 6 (1), p. 7.
- Zhang, L. W.; Monteiro-Riviere, N. A. (2009): Mechanisms of Quantum Dot Nanoparticle Cellular Uptake. In *Toxicol. Sci.* 110 (1), pp. 138–155.
- Zhao, F.; Zhao, Y.; Liu, Y.; Chang, X.; Chen, C.; Zhao, Y. (2011): Cellular Uptake, Intracellular Trafficking, and Cytotoxicity of Nanomaterials. In *Small* 7 (10), pp. 1322–1337.
- Zheng, N.; Fan, J.; Stucky, G. D. (2006): One-Step One-Phase Synthesis of Monodisperse Noble-Metallic Nanoparticles and Their Colloidal Crystals. In *J. Am. Chem. Soc.* 128 (20), pp. 6550–6551.
- Zhu, Z.-J.; Tang, R.; Yeh, Y.-C.; Miranda, O. R.; Rotello, V. M.; Vachet, R. W. (2012): Determination of the Intracellular Stability of Gold Nanoparticle Monolayers Using Mass Spectrometry. In *Anal. Chem.* 84 (10), pp. 4321–4326.

Appendix

Absorption and fluorescence spectra of the Atto 647N labeled gold nanoparticles were recorded (Figure S1). The absorption maximum at 520 nm was caused by the SPR of the gold particles. The minor signal at 647 nm was caused by Atto 647N, attached to the nanoparticle surface. The fluorescence spectrum revealed a strong emission of the nanoparticles with a maximum intensity at 663 nm.

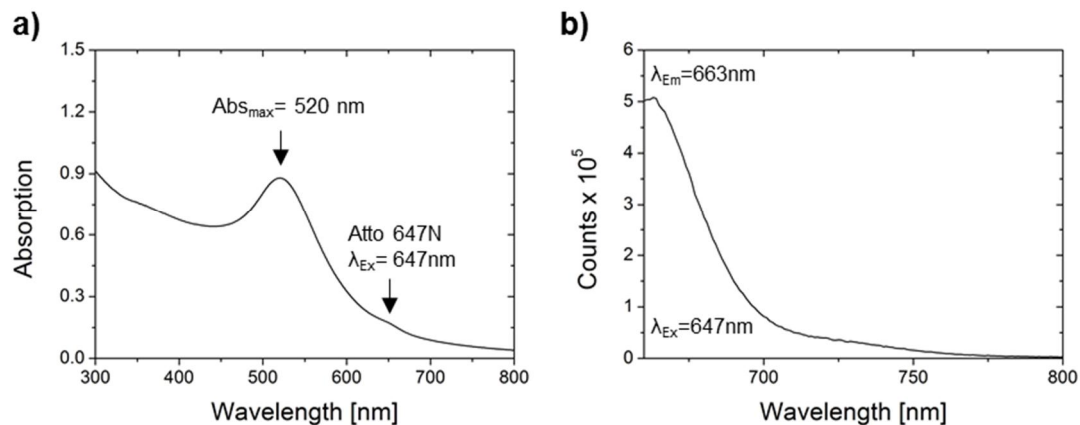


Figure S1: a) Absorption and b) fluorescence spectrum of 8 nm gold particles labeled with Atto 647N.

Gold nanoparticles were deposited on silicon nitride substrates for energy dispersive X-ray (EDX) spectroscopy. The measurements confirmed that the nanoparticles consisted of gold (Figure S2). The detected Si and N signals were assigned to the silicon nitride substrate.

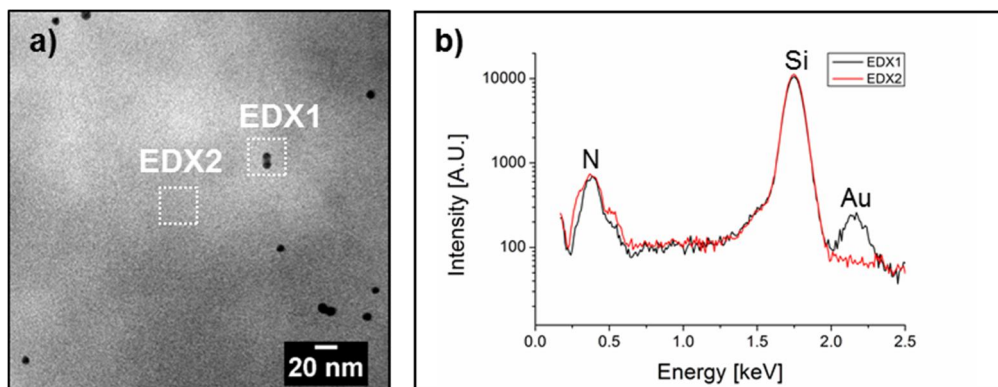


Figure S2: TEM and EDX analysis of gold nanoparticles on silicon nitride chips.

a) Atto 647N labeled gold nanoparticles were placed on silicon nitride chips and imaged by TEM. b) The subsequent EDX analysis allowed the identification of gold correlating with the presence of nanoparticles (EDX1) and differentiation from the substrate background (EDX2). The presence of gold was indicated by the distinctive M X-ray signal at 2.120 keV.

Prior to the correlative analysis, the internalization of the fluorescently labeled nanoparticles by A549 cells was studied by CLSM. The Atto 647N fluorescence signal was used as indicator for the particle location. After 5 h, cell-associated Atto 647N fluorescence signals were detected. The signals were distributed in a punctate pattern, typically including signals surrounding the nucleus (Figure S3). The perinuclear location of the detected signals was indicative for the presence of the fluorescing entities inside of the cells after internalization.

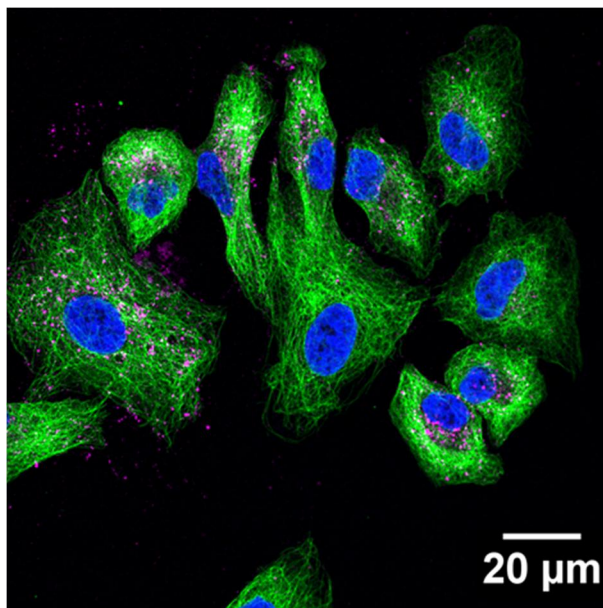


Figure S3: CLSM image of A549 cells grown on coverslips and exposed to $0.02 \mu\text{g ml}^{-1}$ 8 nm gold particles for 5 h. α -tubulin (green), cell nucleus stained with Hoechst 33342 (blue), Atto 647N used to label the gold nanoparticles (magenta).

CLSM analysis revealed the presence of Atto 647N fluorescence signals inside A549 cells. Eight of these signals in one cell were chosen for the correlative analysis (Figure 57). In addition, the z-position of these signals was analyzed with regard to the upper and lower margin of the cell defined by the tubulin network (Table S1). The axial resolution in CLSM is restricted to ≥ 500 nm, resulting in a cigar shaped PSF. For determination of the distances, the center of the axial signals were used. The analysis was performed using the image processing package Fiji.

Table S1: Distances of Atto 647N fluorescence signals to the upper and lower margin of the cell.

Position	1	2	3	4	5	6	7	8
Distance to the apical margin [μm]	0.5	1.8	0.0	3.9	7.6	4.8	1.6	1.5
Distance to the basolateral margin [μm]	2.8	3.4	7.4	5.0	1.0	4.3	4.4	4.5

To further confirm the intracellular presence of the Atto 647N labeled entities, a marker for the cytoplasmic membrane and a different staining protocol was used prior to imaging. In brief, A549 cells were transfected with pAcGFP1-Mem (Clontech) to label the cytoplasmic membrane. After exposure to 8 nm gold particles, the cells were fixed but not permeabilized and analyzed by CLSM. Orthogonal views of a recorded z-stack demonstrated that the fluorescing entities were present inside the cell (Figure S4).

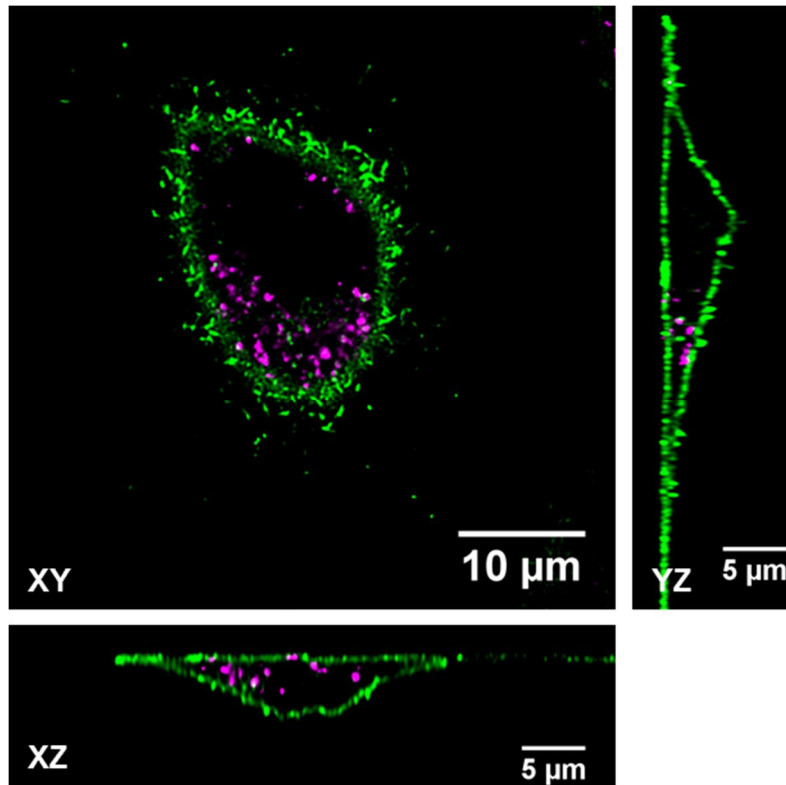


Figure S4: Orthogonal sections of a recorded z-stack of A549 cells after 5 h exposition to Atto 647N labeled 8 nm gold particles ($0.02 \mu\text{g ml}^{-1}$).

The membrane of A549 cells (green) was labeled by expression of the N-terminal membrane targeting signal of neuromodulin fused to green fluorescent protein, encoded by pAcGFP1 Mem. Atto 647N fluorescence signal (magenta).

After CLSM analysis, the sample was transferred into the ESEM to record wet STEM images of the cell. Initially, imaging was conducted at a pressure of 750 Pa (Figure S5a and b), subsequently, the pressure was reduced to 720 Pa (Figure S5c). Based on its morphology, the cell previously imaged could be retrieved (Figure S5a). At higher magnification, dark spots were detected in the nuclear region (Figure S5b and c). At lower pressure (720 Pa), they exhibited a higher contrast. The diameter of the spot detected in Figure S6c had a diameter of about 125 nm. However, the conditions applied neither allowed for resolution of single gold nanoparticles nor identification of the material composition.

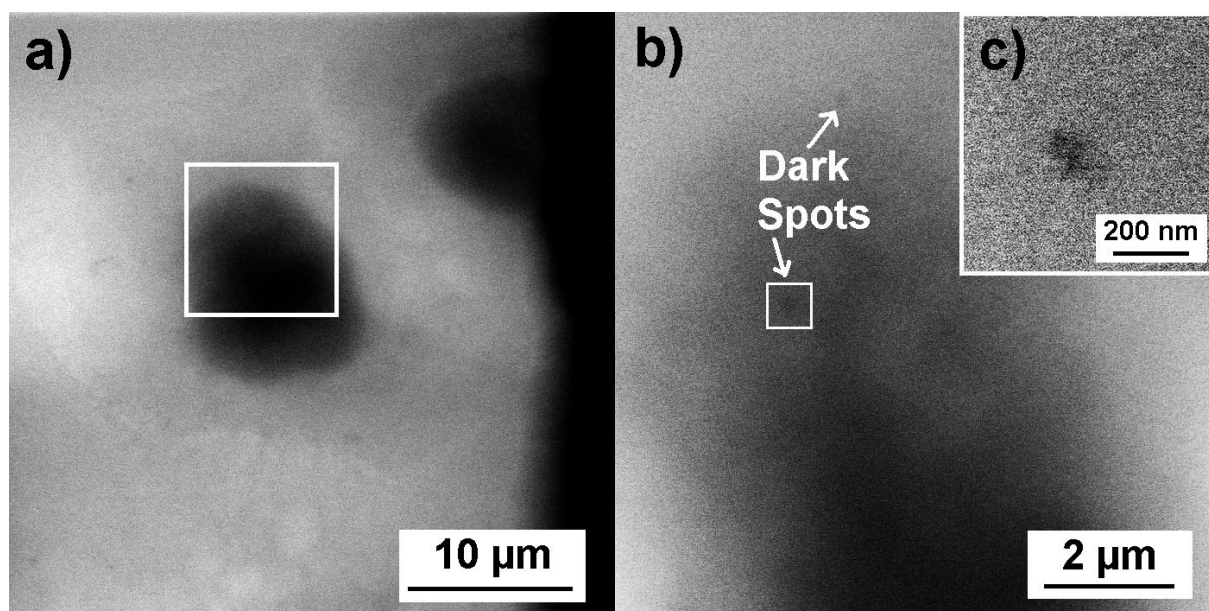


Figure S5: Wet STEM images of the cell shown in Figure 57.

Wet STEM images were taken at $T = 276$ K, $E = 30$ keV, a) and b) $p = 750$ Pa, c) 720 Pa. The squares in a) and b) indicate the magnified region in b) and c), respectively. The nucleus was visible as dark region in the center of the cell. The dark rim on the right side of the image in a) corresponded to the edge of the silicon nitride window also visible in Figure 57d. A post-fixation step was included after confocal imaging, but the samples were not exposed to contrast enhancing agents during the preparation.

After exposition of the sample to air, circular structures formed all over the sample. Although typically not desired, these structures facilitated orientation during CLEM experiments. EDX analysis revealed that the precipitates were composed of Na and Cl (Figure S6). The Si and N signals were generated by the silicon nitride substrate.

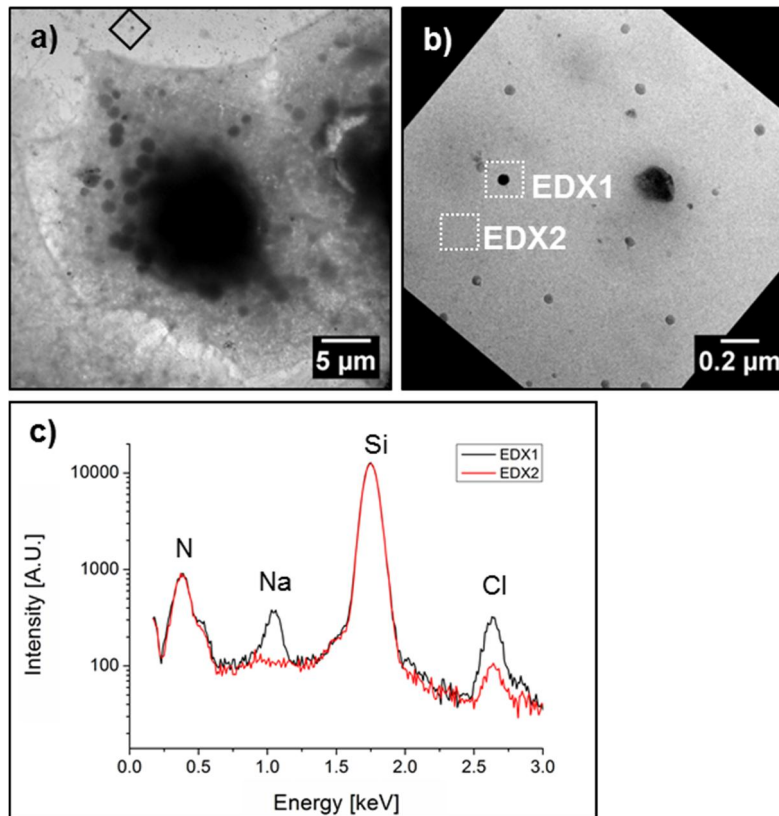


Figure S6: Circular structures detected by TEM imaging inside and outside the cellular region were used as markers for correlative microscopy.

- a) A precipitate beside the cell was chosen for detailed analysis (square). b) Magnification of the area indicated in a). c) EDX spectra of the regions labeled EDX1 and EDX2. The characteristic $K\alpha$ x-ray lines of Na (1.041 keV) and Cl (2.621 keV) indicated the presence of Na and Cl within the precipitates.

List of abbreviations

APD	Avalanche photodiode
AU	Airy unit
bp	base pairs
BrdU	5-bromo-2'-deoxyuridine
BSA	Bovine serum albumin
CLEM	Correlative light and electron microscopy
CLSM	Confocal laser scanning microscopy
DABCO	1,4-Diazabicyclo[2.2.2]octane
DLS	Dynamic light scattering
DMEM	Dulbecco's modified eagle's medium
DMSO	Dimethyl sulfoxide
dsDNA	Double-stranded DNA
EDTA	Ethylenediaminetetraacetic acid
EDX	Energy-dispersive X-ray spectroscopy
ESEM	Environmental scanning electron microscopy
EtOH	Ethanol
FBS	Fetal bovine serum
FRET	Förster resonance energy transfer
GDP	Guanosine diphosphate
GTP	Guanosine triphosphate
hCG	Human gonadotropic hormone
HMDS	Hexamethyldisilazane
ICP-OES	Inductively coupled plasma optical emission spectrometry
K	Kelvin
keV	Kiloelectron volt
LB	Lamellar bodies
MAP	Microtubule-associated protein
mPEG	Monofunctionalized polyethylene glycol
MTS	3-(4,5-dimethylthiazol-2-yl)-5-(3-carboxymethoxyphenyl)-2-(4-sulfophenyl)-2H-tetrazolium
MTOC	Microtubule organizing center

MTT	3-(4,5-dimethylthiazol-2-yl)-2,5-diphenyltetrazolium bromide
MVB	Multivesicular bodies
NA	Numerical aperture
n	Biological replicate
p	Pressure
PBS	Phosphate buffered saline
PCR	Polymerase chain reaction
PEG	Polyethylene glycol
PFA	Paraformaldehyde
PLA	Polylactic acid
PM	Particulate matter
PMAO	poly (maleic anhydride-alt-1-octadecene)
PMT	Photomultiplier tube
PSF	Point spread function
ROS	Reactive oxygen species
RT	Room temperature
SEM	Scanning electron microscopy
SERS	Surface enhanced Raman scattering
SP	Surfactant proteins
SPR	Surface plasmon resonance
STED	Stimulated emission depletion
STEM	Scanning transmission electron microscopy
T	Temperature
TAE	Tris-acetate-EDTA
TEM	Transmission electron microscopy
TNF α	Tumor necrosis factor-alpha
UFP	Ultrafine particles
UV	Ultra violet
WST-1	Water soluble tetrazolium

List of publications

Oral presentations

2012, September 4th - 7th, 6th International Conference on Nanotoxicology, Beijing, China

Katharina Narr, Marcus Koch, Alexandra K. Kiemer and Annette Kraegeloh

"A microscopic analysis of gold nanoparticle internalization in A549 cells"

2012, March 1st and 2nd, INASCON – The 6th International Nanoscience Student Conference, Saarbrücken, Germany

Katharina Narr, Alexandra K. Kiemer, and Annette Kraegeloh

"Interactions of human lung epithelial cells and different-sized gold nanoparticles"

2011, 1st - 2nd March, PhD Students Day Physic, Saarbrücken, Germany

Katharina Narr, Annette Kraegeloh, and Alexandra K. Kiemer

"Internalization of gold nanoparticles in human lung epithelial cells"

Poster presentations

2012, 29th February - 9th March, 9th International Conference and Workshop on Biological barriers, Saarbrücken, Germany

Katharina Narr, Alexandra K. Kiemer and Annette Kraegeloh

"Intracellular distribution of gold nanoparticles in human lung epithelial cells and their potential cytotoxicity"

2012, 30th - 31th January, Leibniz-Nano, Berlin, Germany

Katharina Narr, Alexandra K. Kiemer and Annette Kraegeloh

"Intracellular distribution of gold nanoparticles in human lung epithelial cells and their potential cytotoxicity"

2011, 7th - 10th June, 11th International ELMI meeting on Advanced Light Microscopy, Alexandroupolis, Greece

Katharina Narr, Marcus Koch, Annette Kraegeloh and Alexandra K. Kiemer

"Localization of gold nanoparticles within human lung epithelial cells: A microscopical analysis"

Articles in Journals

Nico Persch, Ahmed Elhayek, Martin Welk, Andrés Bruhn, Sven Grewenig, Katharina Böse, Annette Kraegeloh, and Joachim Weickert

"Enhancing 3-D Cell structures in confocal and STED microscopy: A joint model for interpolation, deblurring and anisotropic smoothing", To appear in: *Measurement and Science Technology*

Katharina Böse, Marcus Koch, Christian Cavelius, Alexandra K. Kiemer, and Annette Kraegeloh
"A correlative analysis of gold nanoparticles internalized by A549 cells", To appear in: *Particle & Particle Systems Characterization*

Acknowledgements

Die vorliegende Arbeit wäre ohne die tatkräftige Unterstützung von einer Vielzahl an Wegbegleitern niemals möglich gewesen. Mit den folgenden Worten möchte ich meinen Dank gegenüber all diesen wichtigen Menschen zum Ausdruck bringen.

Mein größter Dank gebührt meiner Betreuerin Dr. Annette Kraegelo, Arbeitsgruppenleiterin der Abteilung Nano-Zell-Interaktionen am Leibniz Institut für Neue Materialien (INM) in Saarbrücken, sowie meiner universitären Begleitung Prof. Dr. Alexandra Kiemer, Pharmazeutische Biologie der Universität des Saarlandes, die mir das Vorhaben Promotion ermöglicht und mich über den gesamten Zeitraum stets eng begleitet haben. Ich bedanke mich für die Diskussionsbereitschaft, all die konstruktive Kritik und vor allem für den Freiraum, der mir für das Anfertigen der vorliegenden Arbeit gegeben wurde. Ebenso möchte ich mich für die freundliche Zusammenarbeit und die stets nette und gute Kommunikation, auch über größere Entfernungen hinweg, bedanken.

Ebenso danke ich Prof. Dr. Ingolf Bernhardt für die sofortige Bereitschaft das Zweitgutachten zu übernehmen.

Ein großer Dank gilt der gesamten Arbeitsgruppe Nano-Zell-Interaktionen, den gegenwärtigen sowie allen ehemaligen Mitgliedern, die bei Problemen stets zur Stelle waren und zu der wunderbaren Arbeitsatmosphäre im Labor beigetragen haben.

Ich danke im Einzelnen:

- Dr. Christian Schumann, Dr. Tobias Müller sowie Dr. Thomas Ruckelshausen für ihren unermüdlichen Einsatz in der Mikroskopie, die PSF-Aufnahmen, die Unterstützung im Umgang mit der Deconvolution-Software sowie die geduldige Beantwortung aller hochauflösenden Fragestellungen.
- Dr. Christian Cavelius, Sarah Schmidt, Aljosha Jochem sowie Anika Schwarz für die Synthese und Charakterisierung der Goldnanopartikel.
- den Labormädels Dr. Melanie Kucki, Dr. Henrike „Mutti“ Peuschel und Silke Kiefer für die vielen hilfreichen Diskussionen. Ich habe gerne mit euch gearbeitet und bedanke mich für die tolle Stimmung, auch außerhalb des Labors. Silke, dir möchte ich besonders für die hervorragende Labororganisation danken, die mir das Arbeiten stets reibungslos ermöglicht hat. Ich danke dir außerdem für deine Unterstützung auf dem harten und steinigen Weg der Transfektion.
- Dr. Diana Peckys für die Unterstützung im Rahmen der Mikrochip-Experimente.
- Dr. Marcus Koch für die Hilfestellung während der elektronenmikroskopischen Experimente. Danke für die vielen Messzeiten und Aufnahmen am TEM und am ESEM und vor allem für deine wissenschaftliche Abenteuerlust, die nicht unerheblich den Fortgang und die Richtung dieser Arbeit mitbestimmt hat.

Ich danke ebenfalls allen weiteren Kollegen am INM, die mit mir ihre Zeit in der Mensa, beim Tee, beim Basketball, im PhD Seminar, beim „Schwenken“, beim „Sekt am Freitag“ oder auch im Elefanten verbracht haben... Ihr alle habt dazu beigetragen, dass ich mich immer gern an die Zeit in Saarbrücken zurück erinnern werde. Im Speziellen möchte ich meinen „Bürogeschwistern“ Robert Gralla und Jessica Kaiser danken, die stets zur Stelle waren, wenn mal wieder ein offenes Ohr von Nöten war und Freud und Leid geteilt werden mussten.

Ich bedanke mich außerdem bei Dr. Andreas Vonderheit, Direktor der Core Facility am IMB in Mainz sowie Leiter der Core Facility Mikroskopie am IMB, der mir das Zusammenschreiben der Dissertation neben meiner Arbeit ermöglicht hat und sich darüber hinaus für eine kritische Begutachtung des Manuskripts zur Verfügung gestellt hat.

Ich danke all meinen Studienkollegen aus Köthen sowie meinen guten Freunden aus Leipzig, im Speziellen meiner lieben Tina Kwapil, für die Ablenkung und den Spaß, während der endlos erscheinenden Zeit des Zusammenschreibens.

Abschließend möchte ich meiner Familie danken: meiner Mutter Kerstin Narr, meiner Schwester Marleen Narr, meinen Großeltern Horst Narr und Sieglinde Born, meinen Schwiegereltern Katrin und Andreas Böse sowie meiner Schwägerin Katja Böse. Danke, dass ihr immer da seid!

Die letzten Dankesworte will ich an meinen lieben Ehemann Thomas richten:

Thomas, du hast mir die Zeit, die Kraft und vor allem das Durchhaltevermögen gegeben, diese Arbeit zu Ende zu bringen. Deine Geduld, deine Liebe und deine Freude haben mich niemals verzweifeln lassen. Stets hast du mich aufgebaut und aufgefangen. Ohne dich wäre diese Arbeit nie zu Stande gekommen. Danke <3